DOE/ER/40646-6

PROGRESS REPORT

November 1, 1995 to October 31, 1996

for

EXPERIMENTAL PARTICLE PHYSICS AT THE UNIVERSITY OF PITTSBURGH

by

Joseph F. Boudreau

Eugene Engels, Jr.

Paul F. Shepard

Julia A. Thompson

Department of Physics and Astronomy
University of Pittsburgh
Pittsburgh, Pennsylvania 15260

May 1996

Prepared for

U. S. Department of Energy

Grant No. DE FG02 91ER40646

DISCLAIMER

Task A

1 Overview

This task started in 1982 as a collaboration with first the AFS experiment at the CERN ISR and later the NA34 (HELIOS) experiment at the CERN SPS on the subject of direct photon production. Extrapolating to lower transverse momenta, we also searched for a related directly produced component of lepton pairs and an associated enhancement of single lepton spectra. The production of such lepton pairs and low transverse momentum photons is of interest in itself if anomalies are found even in p-p or p-light nuclei collisions. But the lepton and photon production in p-p or p-light nuclei also serves as an important calibration point for comparison of such collisions to relativistic heavy ion collisions, where their presence may signal the production of a quark-gluon plasma phase of matter.

The experimental work from NA34 ended in 1994 with the completion of the thesis of Paula Pomianowski, the last HELIOS student. No anomalies are seen in the low energy photon or dilepton channels, with systematic errors of order 30-50 % of Bremsstrahlung [1] for the photons, 30 % of expected sources for the single electron and di-muon and di-electron channels and of order twice the charm contribution (90% c.l.) for the electron-muon pair data.

With the conclusion of the work on NA34, and after a 6-month stay of Thompson at the Institute of Physics in Novosibirsk in 1989-90, the focus of the task shifted to studies of kaon decays. There are two aspects to this work.

The first aspect of the rare kaon decay work is that because of Thompson's long stay at INP, there is a possibility to make a contribution to that work through continued communication and consultation, simulation and analysis at Pittsburgh, and small equipment contributions. The overall physics focus of this aspect of the Task A work is rare and semi-rare decays of the ϕ and of the short-lived kaon, with an emphasis on those aspects needed in preparation for the proposed Φ-Factory measurements of CPT violation and ε'/ε from the CP-violating decays of the $K_L K_S$ final state. The agreement for this collaboration includes continuing work on the CMD2 detector at the VEPP-2M accelerator and later work at a Φ-Factory project planned at INP. These activities are a small part of the overall budget but make a substantial contribution to the VEPP-2M work.

The second aspect of the kaon decay work is participation in one of the so-called "rare kaon decay" experiments, E865 at BNL. (spokesperson M. Zeller of Yale). This experiment is a search for $K^+ \to \pi^+\mu^+e^-$, a lepton number violating process. E865 builds on the work of the previous experiment, E777, which set the current limit for this decay mode (of 2×10^{-10}). Through a combination of a redesigned beam, larger acceptance apparatus, and longer running time, E865 hopes to push the limit for this decay down by another factor of 70, and at the same time collect a sample of $K^+ \to \pi^+ee$ decays for study, and study the asymmetries in the decays of K^+ and K^- to three charged pions, also of interest in the Φ Factory work. The 3 pion asymmetry studies might lead to a CP-violating study, depending on the level of the systematic errors encountered.

The Pittsburgh group designed and constructed two large (700 ft^3) threshold atmospheric pressure Cerenkov counters. Each of these has two cells, one filled with H_2 which has good efficiency for rejecting particles other than electrons, and one filled with CO_2 or CH4, which has good efficiency for detecting electrons (positrons) because of the relatively large index of refraction.

The design minimizes the material in the primary mirror surfaces, and in the gas envelope, since this material both introduces false signals (delta rays, secondaries from nuclear interactions), and multiple scattering. The thickness is about .12 g/cm^2/chamber, exclusive of the Cerenkov radiating gas (.01g/cm^2/ chamber H_2, .08 g/cm^2 CH_4). The mirrors contribute about 35 mg/cm^2, or about 0.1% r.l., per mirror. Reduction of interactions caused by the primary beam, which passes through the right cell of both counters, is achieved by a closed beam tube in each cell, filled with hydrogen and suspended in the region transversed by the beam.

The optical design maximizes the detection of photons generated by Cerenkov radiaton from electrons, and minimizes the detector response to photons outside the desired phase space for trajectories expected from Cerenkov photons from the K^+ decays we wish to detect.

From the 1995 data we expect to reduce the limit on $K^+ \to \pi^+\mu^+e^-$, by at least a factor of 4. We are running now for 10-12 weeks this year and expect to have a long run, 20-25 weeks, in 1997. Besides the primary lepton-violation search, we will accumulate a large sample of $K^+ \to \pi^+e^+e^-$, and will look at several other rare decay modes with electrons and photons in the final state. Whether or not the collaboration will request beam beyond 1997 is not yet decided. This depends both on the AGS schedule and our own interests, and also the systematic limits on the other processes we wish to study. One candidate for a following experiment, if the systematic errors can be controlled at the required level, would be the test of CP violation in the 3 charged pion decay of the charged kaon. Statistics would allow us to reach a level of 10^{-4} to 10^{-5}, which would allow significant tests of some models. Another experiment of interest is the absolute branching ratio of $K^+ \to \pi^0e^+\nu$. A measurement of this mode would constrain the V_{ds} matrix element in the CKM matrix. Particularly interesting may be the possibility of doing this measurement also with our Novosibirsk data.

2 HELIOS

In the past year, the collaboration has prepared a paper based on Paula Pomianowski's e-mu pair thesis data and that paper has now been submitted to Zeit. Phys. C. The limit on anomalous dielectron pairs or dimuon pairs placed by the experiment is about 30 % of the expected dielectron and dimuon events from conventional sources [2]. For the electron-muon pairs the limit on new physics decaying through a final state dilepton channel is 1.53 μbarn ($\sigma \times B.R.$), with a 30% systematic error[3].

3 K Decays and CP Violation at INP, Novosibirsk

3.1 Background

Recent ideas in accelerator physics make the construction of a ϕ-factory of luminosity of order $10^{32} - 10^{33}\ cm^{-2}sec^{-1}$ feasible [4, 5, 6, 7, 8, 9]. Such a facility would allow substantial advances in the study of K_S decays and measurements of CPT and CP-violation, including ε'/ε, which measures direct CP-violation in neutral kaon decays, at the level of 10^{-4}. This parameter can be zero in a model proposed by Wolfenstein [10, 11], but in principle is non-zero in the standard model of high energy physics interactions. The two current measurements are consistent with zero, and are inconsistent at the two standard deviation level with each other [12, 13, 14]. Another aspect, emphasized by Peccei and collaborators [6] and recently reviewed by Thompson [15], is the near-uniqueness of the ϕ-factory for CPT-tests. In addition there are quantum mechanics tests which require a coherent state such as that prepared at the ϕ factory [16, 17, 18]. Subsidiary physics goals include the measurement of e^+e^- annihilation into both the leptonic and hadronic channels, important for interpretation of the muon g-2 measurement, quark structure studies of the ϕ and f_0, and rare ϕ and η decays [19, 20, 21, 22].

Two "ϕ factories" are in the construction stage: one at Frascati, Italy, and one at the Budker Institute of Nuclear Physics at Novosibirsk (BINP).

At Novosibirsk, the ϕ Factory plans are in three steps.

1. Since 1974 the VEPP-2M collider at the Budker Institute of Nuclear Physics in Novosibirsk, Russia, has been the only machine capable of studying e^+e^- annihilation into hadrons at center of mass energies from the threshold of two pion production (280 MeV) up to 1400 MeV [23, 24, 25, 26]. During 1988-92 a new booster was installed, yielding peak luminosity $L \approx 5 \times 10^{30} cm^{-2}s^{-1}$ at the ϕ center of mass energy. Two detectors, the CMD-2 axial field magnetic spectrometer [27, 28], and the SND non-magnetic spherical NaI crystal detector, are active at VEPP-2M.

2. An upgrade of VEPP-2M, funded through the Mitterand Fund, the Soros Fund, and Russian scientific funding, will test the idea of "round beams" (in contrast to the usual "ribbon" beams) to minimize beam-beam interactions. The combined improvements in the optimum case are expected to give a total factor of 20 increase. This factor, together with the BINP depolarization precision beam energy determination, would keep Novosibirsk in the world facility class, competitive with Frascati, where "DAFNE" is expected to come on toward the end of 1996 with a luminosity of 10^{32}. As discussed below, the high resolution of the LXe calorimeter planned for the CMD2 upgrade will give BINP an edge in the short distance correlation tests, even if the BINP transition to high luminosity is somewhat behind the Frascati machine, in order to fully utilize the present facility.

   The round beams will be installed after the energy region above the ϕ has been scanned, since this region will be unavailable after the changeover, due to technical reasons of the upgrade plans.

3. A later planned facility, the "Siberian Butterfly", is hoped to give 10^{33} luminosity. The "Butterfly" also depends on the round beams idea for its full luminosity.

To reach the physics of interest requires progress on several fronts:

1. An accelerator to achieve luminosities of order 10^{33} cm^{-2} sec^{-1}

2. Control of systematic errors at the level required to measure ϵ'/ϵ.

3. An appropriate detector: at Novosibirsk we are planning a liquid xenon calorimeter upgrade of the CMD2 detector [29]. The LXe calorimeter's good spatial and energy resolution will allow the reconstruction of the kaon vertex with resolution of 2-5 mm, essential for the CPT correlation studies. The planned Frascati detector is complementary. Because of its size it emphasizes measurements such as the real part of ϵ'/ϵ which can be done well with decays further from the production vertex. The Novosibirsk group, with its better vertex resolution near production, will have an advantage in the imaginary part of ϵ'/ϵ, and in the kaon decay phase studies which emphasize short distance measurements.

4. Fast computer support, both online and off-line. The ϕ factory luminosities will yield 2-10 Mbytes/sec of useful event data. Even this heavy load assumes that only 20% of the ϕ decays are recorded. The remainder will be classified, and selected calculated information stored for later calibration and systematic studies in the delicate high statistics analysis. Cost-effective solutions to such high rates of interesting data may also be useful to other collider experiments.

As described above, the accelerator upgrades are underway. The systematic error studies follow from the current CMD2 analysis work. The liquid xenon calorimeter and DAQ system upgrades are the focus of a separate proposal to the Civilian Research and Development Fund.

3.2 Collaboration between Pittsburgh and BINP

The collaboration between J.A. Thompson and BINP was begun in 1989-90, In addition to the ϕ analysis studies, Pittsburgh has been involved in data acquisition. through Pitt students, especially Craig Valine, who completed his Master's degree in electrical engineering working on the CMD2 transputer data acquisition system upgrade [30]. Professor Steven Levitan, of the electrical engineering department at the University of Pittsburgh, became interested in the project as Valine's advisor, and will continue as a collaborator on the project. He consults with us on the DAQ system and trigger, other electronics design questions, and analysis code optimization.

Thompson travels on average one month per year to Novosibirsk (she expects to spend two months at BINP in spring, 1997) where she reviews the progress of Pitt students, works on delicate analysis points, and participates in planning. BINP personnel also travel to Pittsburgh, working with Pitt personnel on ϕ analyses using the Pittsburgh computing resources. A Pittsburgh graduate student divides time and work between Pittsburgh and Novosibirsk, and a Pitt undergraduate assists with analysis at Pittsburgh.

Pittsburgh has provided the CMD2 group with transputers and computers which were only legally exportable to Russia because of our collaboration. The group at Novosibirsk now uses a recently available complex of SGI computers, obtained through Soros grants awarded to BINP.

Previously we used DEC 5000 machines, two at BINP provided by Pitt, one in the high school classroom of our collaborator, Ivan Ober, and an ALPHA complex in the University computing facilities. The speed of event reconstruction on the Pitt ALPHA or the BINP SGI is about 60 Hz, or about 100 nb^{-1}/day.

3.3 Status of Analysis of ϕ data

During the last few years the running time has been divided between lower energies and the ϕ (where 1500 nb^{-1} of data was collected). Results from 290 nb^{-1} near the ϕ have been published [31]. The ϕ mass, width, and decay results agree with the particle data group values, with comparable statistical and systematic errors. This is the first time that all four primary decay modes (K^+K^-, K_LK_S, $\pi\pi\pi$, and $\eta\gamma$) have been measured in one experiment. The large statistics and the presence of all four main decay modes have required a careful treatment of systematics, including energy determination, interference between the ϕ and other nearby resonances, and the coulomb interaction in the K^+K^- channel.

One small difference with the PDG values is the branching ratio of ϕ to two electrons: $(2.80 \pm 0.08) \times 10^{-4}$, compared to $(3.09 \pm 0.07) \times 10^{-4}$ for the PDG branching ratio to two electrons and $(2.48 \pm 0.34) \times 10^{-4}$ for the PDG branching ratio to two muons. The previous small disagreement at somewhat less than the 2σ level between muon and electron widths had been somewhat of a puzzle, and the new measurement of the ee mode is more in agreement with expectations from lepton universality.

For the rare decays, the full sample was reconstructed at Pittsburgh using an early version of the reconstruction program, and results for a limit on the $\phi \to f_0\gamma$ as well as other rare decay modes were obtained [32, 33]. These data have now been reprocessed at Novosibirsk, with an improved reconstruction version. Some particularly interesting, but still preliminary, results are:

1. Several rare ϕ decay modes: B.R. ($\phi \to f_0\gamma$) less than 8×10^{-4} [PDG value 2×10^{-3}]; B.R. ($\phi \to \eta'\gamma$) less than 2.4×10^{-4} [PDG value 4×10^{-4}]; and B.R. ($\phi \to 4\pi$)(not through the neutral kaon channel) less than 1.0×10^{-4} [PDG value 9×10^{-4}.]

2. A check of the systematics of the detector and analysis is the previously seen decay $K_S \to \pi^+\pi^-\gamma$. Our result, from a sample of 32,340 tagged K_S decays, gives a branching ratio of $(1.82 \pm 0.49) \times 10^{-3}$ [33] [PDG value $(1.78 \pm 0.05) \times 10^{-3}$].

3. This experiment is the first to reconstruct the coupled kaon decays of interest for the CP and CPT ϕ- factory aims. In addition to studying K_L interactions in the calorimeter, we reconstructed about 1000 K_SK_L back to back decays, with the K_L decaying to its usual 3 body modes. The four pion final state, with the K_S decaying to 2 pions as usual, and the K_L decaying also to 2 pions in a CP-violating

mode, is the situation of highest interest at the ϕ factory. The sample with four charged pions, dominated by events with a K_L regenerated to K_S in the beam pipe (28 ± 6 events) emphasizes the importance of regeneration. The regeneration cross section at kaon momentum 110 MeV/c (not previously measured) was found to be 63 ± 19 mb. In our sample, this is 10 times the expected signal from the CP-violating 2 π decays of the K_L. (Low mass detectors and cuts near the beam pipe will help combat this problem in ϕ factory detectors.)

Regeneration and nuclear interactions will be particularly important in the measurement of the real part of the CP-violation parameter ϵ'. For the CPT measurements, and the imaginary part of ϵ', the events occur close to the interaction point, still within the vacuum pipe, and are less vulnerable to regeneration contamination.

Besides the final values from the analyses described above, the work should yield two results of particular interest to ϕ factory efforts: study of the K_S semileptonic decay, and study of the final state from coupled kaon decay to the $\pi^+\pi^-\ \pi^0\pi^0$ final state.

If the semileptonic branching ratio is of order 10^{-3}, there should be tens of candidates in our present sample. Suppression of the normal $\pi^+\pi^-$ decays will require studies of the differing calorimeter response to electrons, pions, and muons.

For the separation of the four pion state with two charged and two neutral pions we need 0.2-0.5 cm resolution for the two neutral pion vertex (obtainable with the liquid xenon upgrade 0.2-0.5 spatial resolution) for their full understanding. However, quite a bit can be learned even with the present 1 cm vertex resolution. As for the 4 charged pion states, the sample will be dominated by K_L regeneration events. This will be convenient in testing the vertex resolution.

In 1996 VEPP-2M will be running with both the CMD2 and the SND detectors. After background studies, and an accumulation of 2-10 pb^{-1} of data at the ϕ, scans above and below the ϕ will be completed. These regions are important for interpretation of the muon g-2, where the CMD collaboration has obligations. The lower energy runs, which require less current, are planned for the summer.

4 Rare K Decays in E865 at BNL

An overall description of the experiment was given in the general remarks in the introduction to the report. Figure 1 shows the layout for E865, very similar in design to that of its forerunner, E777.

The University of Pittsburgh primary responsibility has been the design, construction, and operation of the two large volume threshold Cerenkov counters. A summary of the counter design and construction, with an emphasis on innovative aspects, is given below.

David Kraus has overseen the construction and commissioning of the counters. Julia Thompson prepared the optical design and oversaw the construction and alignment of the optics. During this stage, several students worked with the group. These included undergraduate students who helped with the construction, as well as early help from

graduate students Paula Pomianowski and Mike Gach, and postdoc Dave Brown. Over the past year, the Pittsburgh personnel have been junior postdoc Christoph Felder, now replaced by Naipor Cheung (who joined the group in February, 1996) and part time postdoc Robin Appel (who joined the group in October, 1996). Others helped over part of the year: two visitors from the FSU (Mikhail Shubin and Vladimir Atoyan) helped with running; prospective graduate student Alexander Sher began some early activities with the experiment; a number of undergraduates have helped on a part time basis, particularly Elizabeth Battiste, from Bennett College; Rebecca Chapman and Amy Freedman from Pitt; Kent Lambert from Jackson State University; Melinda Nickelson from Bryn Mawr, and John Hotmer from Suffolk Community College. Battiste, Lambert, and Nickelson participated as part of a summer research program funded by NSF; they help with running chores and work on limited individual analysis topics while learning something about high energy physics as a whole.

The major activities of the Pittsburgh group in the past year have been

1. General running support (all personnel, coordinated by Kraus), including taking about 25% of the experiment shifts.

2. Help with the installation of an additional trigger hodoscope between the first two proportional chambers. The inclusion of this hodoscope in the trigger has reduced the number of basic ("zero level") 3-particle triggers (the basis of all our physics triggers) by a factor of 3 . The phototubes for this array were provided by Pitt, and prepared and tested by Kraus. Hotmer helped with the installation of the counter.

3. Realigning and refurbishing of the primary and secondary optics in C1 (Thompson);

4. Realignment of the optics in C2, in response to observed inefficiencies; also removal of exposed Rohacel frames from the right side of C2, to reduce scintillation light being seen by the PMT's. (Thompson); blocking scintillation light from Rohacel frames on the left in C2 (Kraus, Cheung);

5. Demagnetization of a tube with poor performance in C1, continued testing of the tubes and bases particularly their response to high rates. (Kraus, Cheung, participation by Baker and Sher);

6. Testing and monitoring the counters: demonstration of counter efficiency at the 95 - 98 percent level for C1 and C2 filled with CO_2, and 74 - 88 per cent level for the left sides of C1 and C2 when filled with hydrogen (all personnel). The higher numbers represent the best performance; the lower numbers represent overall efficiencies including cracks.

7. Development and verification of the GEANT model of the counters in the experiment Monte Carlo (Appel);

8. Installation of the ADAMO database for use in recordkeeping by the experiment (Shubin).

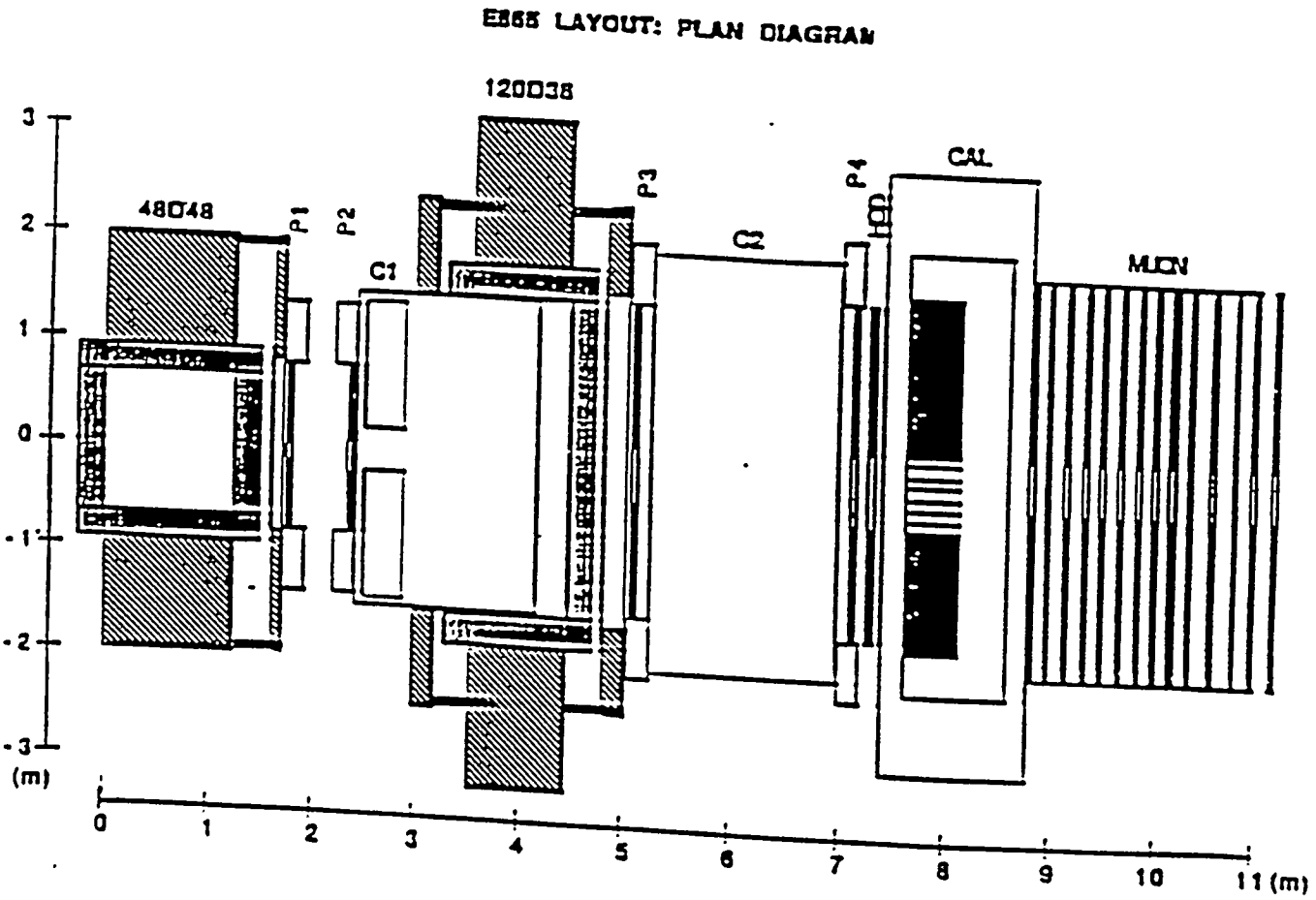

Figure 1: Layout for BNL E865, search for $K^+ \to \pi^+\mu^+e^-$

4.1 Construction of the Cerenkov Counters (C1 and C2)

The mechanical design and production of the shells, the early gas seal tests, reflectivity tests, C1 and C2 conceptual optics designs, conceptual designs of the two counters, and design and construction of the individual mirror components ("slats") and their assembly into the mirror groups as installed, are all described in previous years' reports. The most important points are summarized below, and more details are given in Appendix A.

Summary of Innovative Aspects of the Design The strategy followed in optical design has used assemblies of low-mass structures supporting thin acrylic slats each of which is a cylindrical element whose curvature and orientation may be individually specified. By judicious choice of the large-scale optical parameters, the slats may be overlapped to provide continuous coverage of those parts of the optical phase space which are of interest, without losing photons to trapping between the overlapped slats. This construction permits the direct fabrication of astigmatic mirrors needed to match the asymmetry in x and y phase space distributions of the Cerenkov light produced by particles dispersed horizontally by the magnets, and has the potential to permit the construction of more intricate optical figures, as other problems in transforming optical phase-space distributions might require.

The realization of this design required the development of a number of techniques and tools for economically fabricating these low-mass structures, and for orienting, assembling, and handling them without degrading the optical performance. The design has emphasized adaptability, both because there are a variety of other decay modes which may eventually be studied with the E865 configuration, and because uncertainties in other features of the experimental configuration made it desirable to hold options open until late in the construction cycle.

The decision to construct the mirrors from differential elements, which can be assembled inside the counter shell was initially taken to facilitate light-weight construction. It also allows:

1. Quick modification of the optics from these thin mirror elements, which do not have to be repurchased and, within limits, can be repositioned;

2. freedom in the choice of PMT and concentrator positions - parameters usually constrained by the mechanical configuration of shell;

3. increased flexibility in the arrangement of magnetic shielding and the configurations for the PMT's.

The design flexibility has also readily accomodated reconfigurations of the shell of C2 required by access to MWPC readout cards.

Construction techniques Increased attention to questions involved in the safe operation of vessels containing large volumes of flammable gases led to a number of improvements over conventional containments involving mylar windows. Adaptation of a design pioneered by the University of Washington group in BNL E777 led to the

development of a containment in which the entire stress is carried by kevlar fabric. The mylar serves only as a gas barrier, and the two gas volumes are filled and purged independently, and, if desired, in parallel. Using this system it is possible to exchange the gas volumes (from full and running, to open, to full and runing again, in about 12 hours.

We have developed effective and economical techniques for sealing extended frames and edges, using castable polyurethane gasket cast on surfaces finished with grinding and orbital sanding after welding. The performance of this technique is indicated by C1, which after the reworking of the too-thin window, has shown no leaks under helium testing at 150% of the design pressure in either gasket or window. The design for explosive gas containment does not rely on, and is not limited by, the mechanical strength of the mylar envelope, which is left slack so that the tension forces are entirely supported by the kevlar. This technique permits the use of a dual clamshell configuration, without a common containment membrane for the two compartments.

Flexibility in the optics requires, for applications involving explosive gases, in addition to the innovations in mirror fabrication, redesign of the PMT bases to secure very high reliability, and to eliminate the possibility of breakdown within the flammable gas containment. (In normal running the tubes are not powered until the gas in the cell has reached a composition in which residual oxygen has gone beneath the 0.5% limit of detectability with our chemical gas sensors, so that the gas in the cell is an order of magnitude away from a composition within explosive range, as an extra safety precaution. The reliability studies included the application of standard milspec codes and parameters, the collection of available commercial reliability parameters, and a 200 hr burn-in, which all bases survived. One failed almost immediately in service, exposing a design fault which is now dealt with by careful management of the HV turn-on/turn-off procedure. The design allowed potting the components in a cylindrical shell fitted around the neck of the inner magnetic shield which improves heat transfer and compactness, as well as easy fabrication of the photomultiplier base chain. The experience which we have acquired so far in the course of running has increased our confidence in the viability of this arrangement. No additional component failures have been experienced.

4.2 Modifications for 1996 Run

During fall 1995 and early 1996, two PMT's were replaced, one was removed and demagnetized, and others were retested for behavior in magnetic fields and at high rates.

The C1 and C2 optics alignments were rechecked and improved. Some Rohacel frames which were found cracked, probably due to rushed installation, were repaired. Measurements of the behavior of the mirror edges with humidity were made, and the primary mirrors on the left side of C1, as well as the bottom inside collector in C1, were replaced. The mirror replacements were required due to an exposure to humid air during the removal of the magnetized PMT, and testing of the mirror alignments.

For the replacement mirrors, an overcoating of SiO2 was used, instead of the usual MgFl. The advantage of the SiO2 (quartz) is that it is much more rugged as an overcoat and particularly is relatively impervious to humidity damage, which is a well

documented problem with MgFl overcoating. The mirrors were produced by the H.C. Clausing Company in Chicago. Reflectivity measurements on sample mirrors, with the MgFl and SiO2 overcoats show very similar reflectivities down to the range of 225-250 nm where our tubes lose sensitivity.

4.3 Monitoring and Performance

PMT gains and stability Because of construction in the area, and in order to improve electronic pickup problems, the cabling for the Cerenkov cables was removed after the last run. After the recabling, the single p.e. signals were checked, and the stability of pedestals and signals, as a function of time, and of run, was monitored. The events with only a few photoelectrons are the most convenient for determining the single photoelectron levels. The $\pi\mu e$ candiate events satisfy this criterion, with few photoelectrons on the left because of the low index of refraction in hydrogen, and few photoelectrons on the right because no electron is required, and muons from beam decay may be just above Cerenkov threshold in CO2 and CH4, and therefore yield only a few photoelectrons. The fitting programs for the single photoelectron peaks were begun by Vladimir Atoyan and Mikhail Shubin, continued by Christoph Felder, and have now been taken over by Naipor Cheung. The results, for 1995 running, are shown in Figure 2. In general the performance was quite stable, The automatic fitting procedure used to monitor the individual channels is not foolproof, and occasionally finds an incorrect result corresponding to a local minimum in the parameter space. Such errors are checked for, and corrected as required. The point in C1 for a run near 1647, which is at 50 ADC counts, seems to be an example of such a failure. Some other features of the plots correspond to changes in the electronics. The general small drop around Run 1710 is related to a shortening of the ADC gate. The rise by about a factor of 2 for C1F2 and C1F6 at around Run 1723 corresponds to the removal of an anode splitter with a subsequent rise in gain by of order a factor 2. Deviations from stability are identified and corrected.

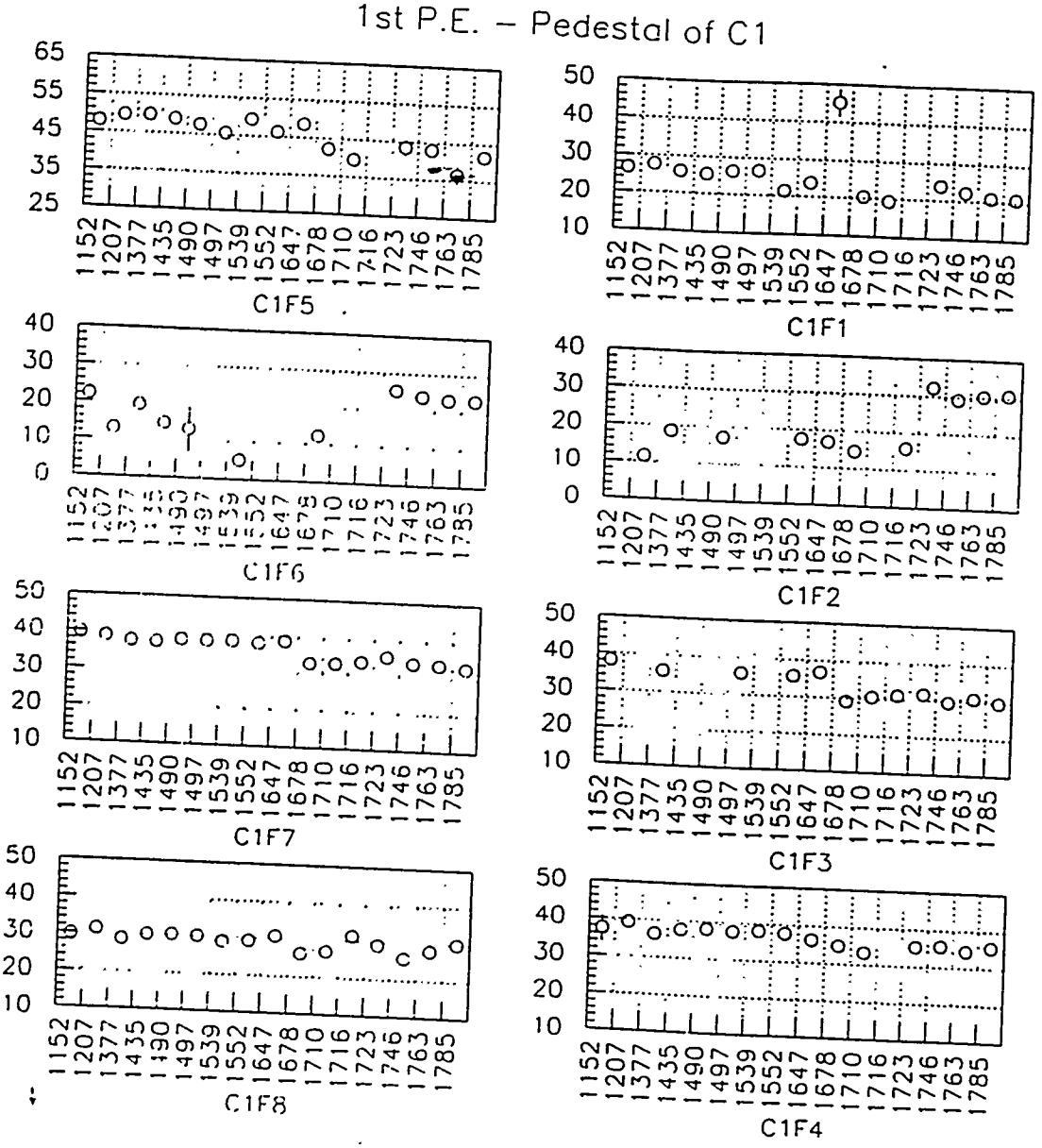

Figure 2: The single photoelectron signals, as determined from events with few photelectrons (electrons on the left, mostly muons on the right).

4.4 Counting Rates

Besides causing extra triggers, the high accidental rates in the Cerenkov counters contribute to misunderstanding of the counters' performance. The rates in the PMT's which view the mirrors near the beam are of order 5 MHz. The larger phase space of desired photons in C2 leads to a less selective optical design, and leaves the counter susceptible to accidentals from background muons or other tracks truly above Cerenkov threshold, as well as to scintillation light from charged particles below threshold. For structural reasons, the Rohacel frame had extended into the beam area, even though there were no mirrors in that region. However, after the high rates in C2 were noticed, a test by Dave Kraus demonstrated a high yield of scintillation light from Rohacel. Because of this finding, we removed the Rohacel frame near the beam line. The rates (in MHz) in several of the PMT's are shown in Figure 3. A factor of 2 decrease in the overall singles rates was seen.

In Figure 3, all rates are normalized to the ion chamber at the rear of the experiment which typically counted about 10k events/spill, or about 6MHz for the 1.6 sec. spill. Plot F (second from the bottom right) shows protons on our production target (SEC) normalized to the ion chamber. In normal running conditions this is constant. But it is higher than usual in one run, because the collimateors between the production target and the experiment were more nearly closed, lessening the beam intensity in the area but perhaps increasing the level of interactions and off-angle beam particles which reach the area. A90 (G) and Tzero (H) are respectively a counter at 90 degrees to our production target and the basic 3-particle trigger for the experiment. C1F2 (plot A) is a tube in C1 and not affected by the gas changes in C2. It can be high for other reasons, if targeting is not good, leading to larger than usual numbers of interactions by beam particles in the channel, for example.

The most striking information in Figure 3 is for C2. At Run 2000 CH4 was put into C2. CH4 was expected to have a lower scintillation yield than CO2, and the two tubes sensitive to scintillation in C2, A1 and A2, show a definite, but small, decrease in counting rates. Before Run 2160 the surgery on the Rohacel frames was done, and the subsequent drop in counting rates is clear for all C2 PMT's shown, though it is the most dramatic (a factor of 3-5) in PMTs A2 and A5. In the design, A2 is primarily for very large angle tracks from Dalitz events and therefore, for most events, sees mostly scintillation. A5 sees a large drop, since it directly faced the Rohacel frames in the beam.

The overall reduction of the rate by a factory of three for singles in C2 improves the vetoing capability of the counter.

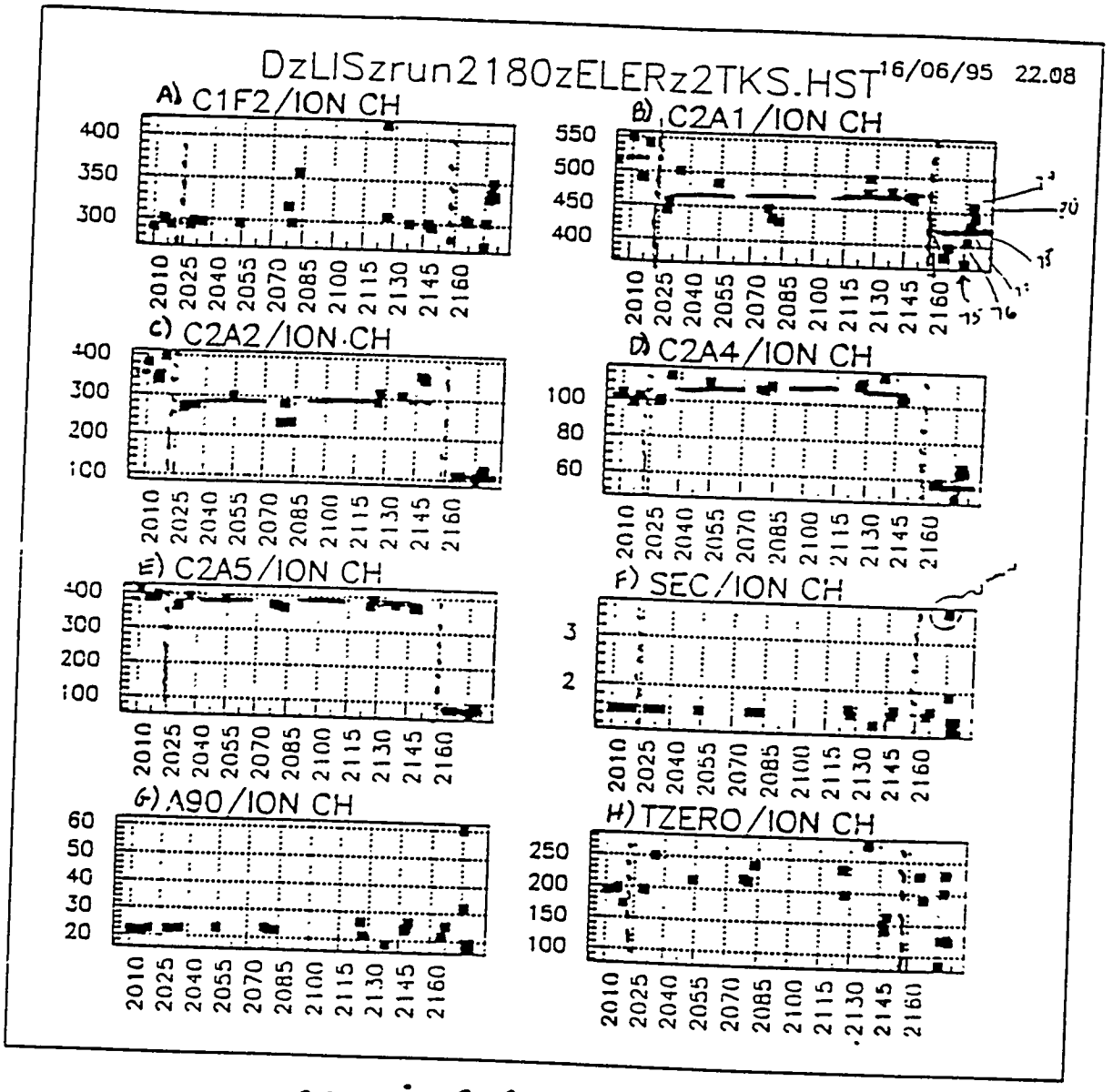

Figure 3: Rates in the Cerenkov counters as a function of run.

4.5 Efficiencies and Light Yields

After safety, the most important question concerning the counters is their efficiency.

The dependence of photoelectron yield as a function of gas (refractive index -1.) is shown in Figure 4. The photoelectron yields found, using the scale set by the PMT one photoelectron measurements, are linear with (n-1), as expected. One can also infer the photoelectron yield from the inefficiency measurements (since inefficiency = exp(-Npe_{avg})) Comparisons of the two results will give a a way to study low level residual backgrounds.

The efficiencies are shown as a function of run in Figure 5, for low mass electron pairs arising from the Dalitz decay of neutral pions. The overall efficiency in the hydrogen side of C1 is about 75% and in C2 is about 83%, and ranges to 85-90% in the parts of the counter with the best performance. For the C02 sides, for the same events, the efficiencies are $95 - 97\%$ overall, ranging to around 98% away from mirror edges. In addition to statistical errors, there is an uncertainty of a few per cent on the numbers for the hydrogen efficiencies and a per cent or less for the efficiencies on the right sides.

The last run in 1995 was Run 2200. In 1996 overall C2 efficiencies were significantly improved while C1 is about the same. Improvements in C2 include reducing the overall counting rates by removing or covering the Rohacel frames which proved a source of scintillation, improving the alignments, and (at Run 2724) replacing a dead tube.

The efficiencies as a function of position are shown in Figure 6. Some of the Cerenkov inefficiencies, especially the inefficiencies near y=0 in C1 and near y=40 cm, x = 80 cm in C2, can be traced to light sharing and cracks in the mirror surface presented to a photon. We are looking at the areas of inefficiency, in both space and phase space, to correlate weaknesses with the optics laser alignment data, and decide on possible improvements before next year's run, particularly in C1 left. Deformations of the lightweight mirrors near their edges contribute to the inefficiencies, but the modular construction allows local replacement of mirror "slats" if such replacement is indicated by our studies.

The observed efficiencies may be compared to design goals of 97-98% on the right and 85-87% on the left. The most important function of the counters is the vetoing on the right of positrons from the Dalitz decay of neutral pions from kaon decays. Removal of the most inefficient regions on the right hand side of the two counters reduces interesting event samples by a relatively modest 10%, and boosts the efficiencies to the desired 97-98% area. In addition, requiring that the 3 charged particle kaon decays (the "tau", mode, our normalization process) pass a veto on the right hand side removes another 10% of the "taus"'s. The final analysis is in progress, but these results suggest feasible lines of development.

These results seem adequate for the present requirements of the experiment. However, improvements in the efficiencies would both give us effectively more rate (on the left hand side of the counters, used for trigger identification) and better rejection for the right, where we wish to reject positrons. For the πee mode, the resulting better uniformity would facilitate the study of the form of the decay interaction. In addition, a DAQ upgrade in progress will allow us to take data at a faster rate, which will add to the importance of higher efficiency on the left. In the proposal we discuss

the improvements which are planned to give a larger margin with respect to satisfactory performance. We are presently studying the reasons for light losses in the optics and electronics. Optical scan results are being studied and compared with simulation expectations and observed inefficiencies. Replacement of some of the mirror frames, particularly in C1 left, is an option if improved performance can be shown likely to result. Replacement of the secondary mirrors and PMT collector viewing the top left of C1 is desirable, because of an exposure of the counter after the 1995 run to warm humid air. (The most severely damaged collector, on the bottom of C1, and all the primary surfaces, were replaced before the 1996 run). In C2 right, there is one area of low efficiency, near x = -80cm, y= -40cm. This area is dramatically improved this year compared to last year, and is under study to identify any possible further improvements.

Besides optics improvements, another method of improving the counter efficiencies would be to capture more of the low wavelenth light region. Preliminary tests described in our proposal indicate the possibility of significant gains from this source. We expect to make a test of wavelength shifter evaporated onto a PMT face during this run, to evaluate the possible gain in efficiency. Depending on the results of these tests and studies, we will make a final decision about improvements in the counters before next year's run.

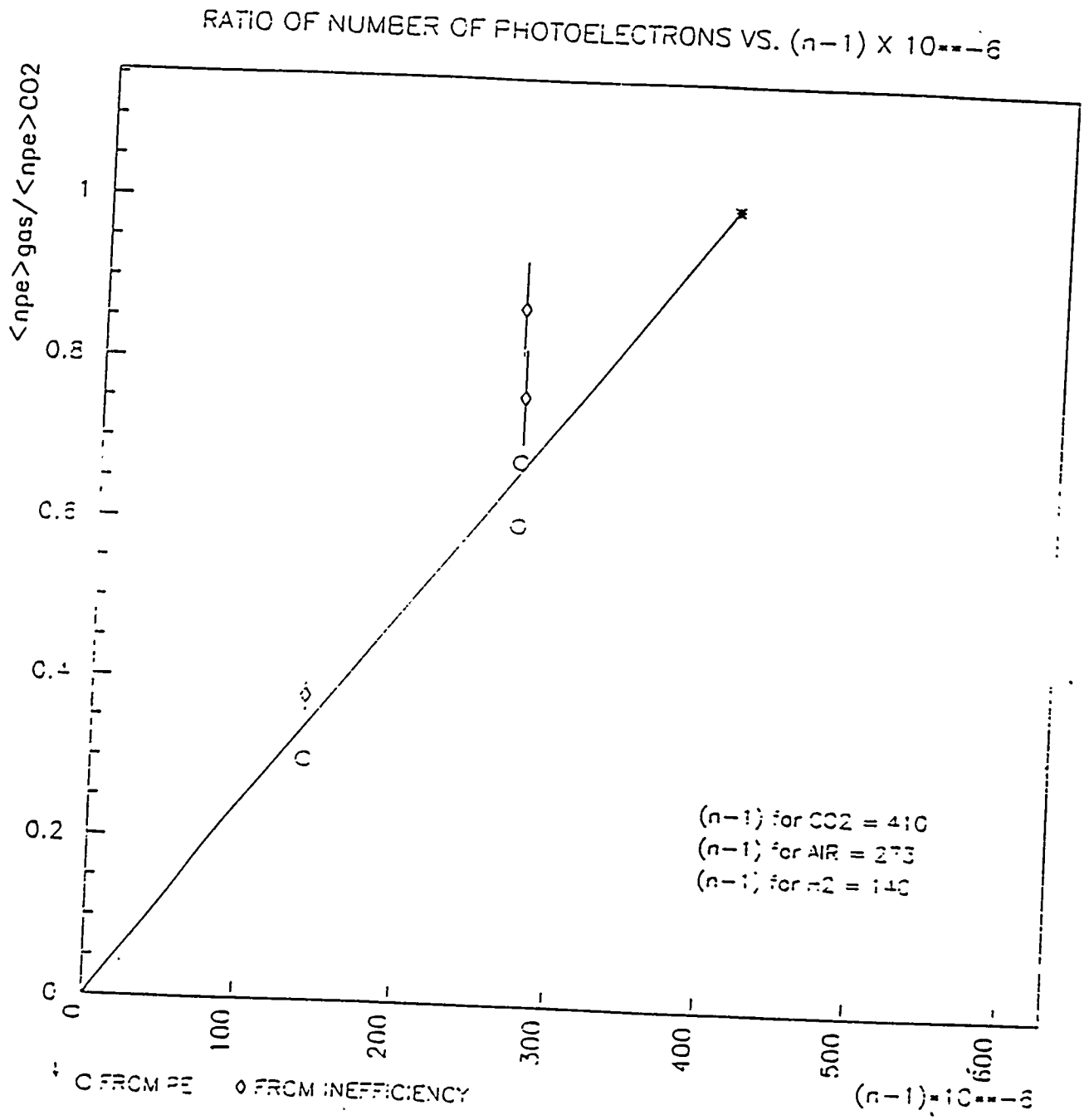

Figure 1: Photoelectron yield for the Cerenkov counters as a function of gas, normalized to the yield observed for CO_2.

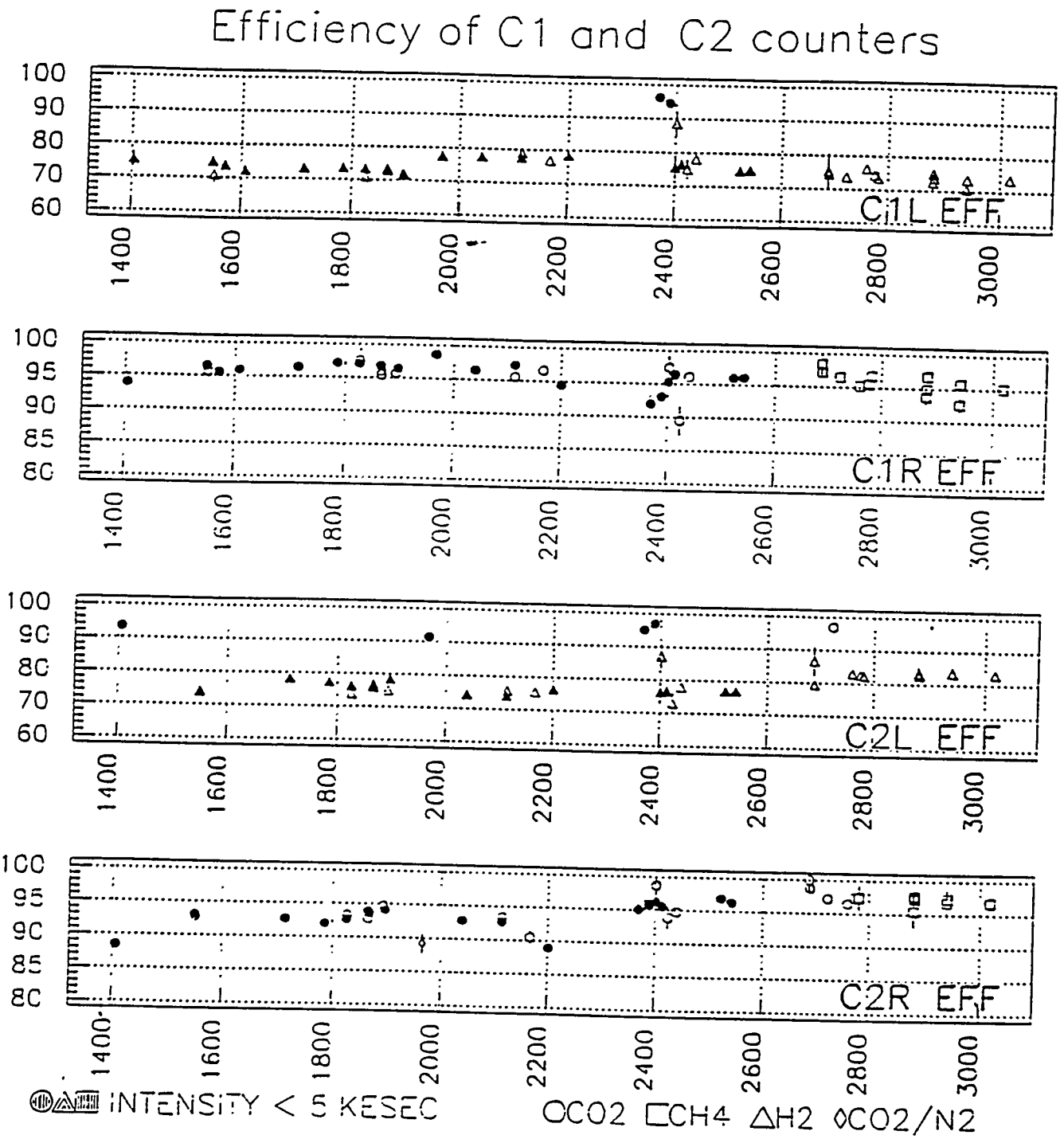

Figure 5: Efficiencies for the Cerenkov counters as a function of run number.

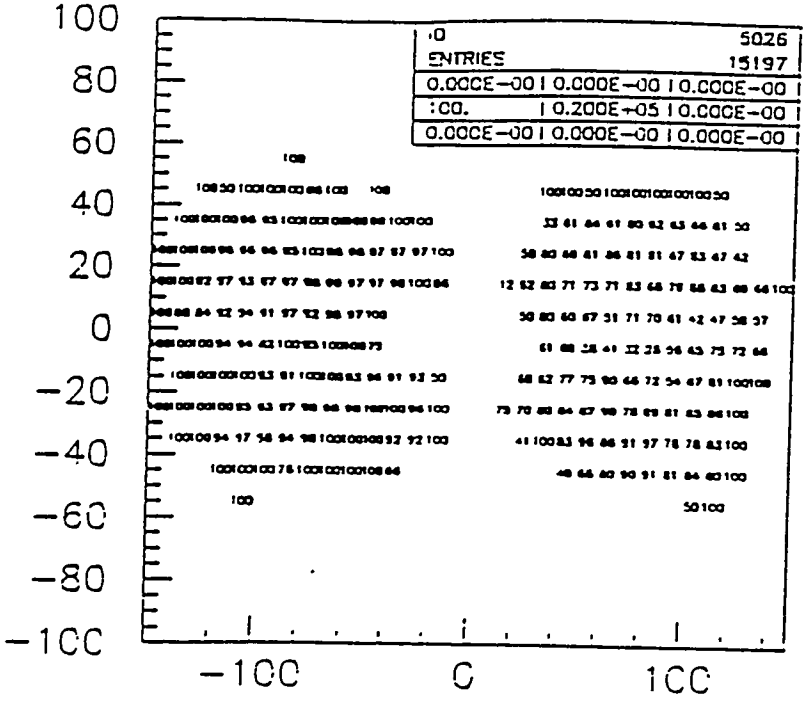

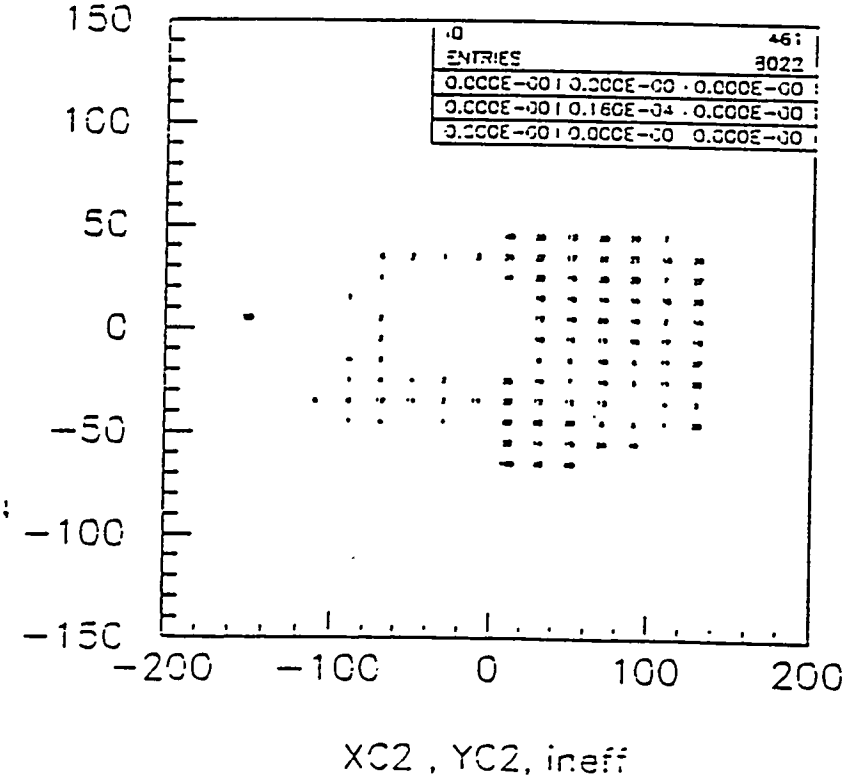

Figure 6: Efficiencies for the Cerenkov counters as a function of position at the mirrors.

4.6 GEANT Modelling of the Cerenkov Counters

A simple model of the Cerenkov counters was installed in the latest version of the E865 GEANT Monte Carlo program. The program modifications we combined GEANT-created Cerenkov radiation with the Pittsburgh ray-tracing program. As GEANT swims the particles created by decays and other interactions through the Cerenkov counters, it creates Cerenkov photons. The position, direction, and energy of each photon is input to the ray-tracing program which traces it through a model of the C1 and C2 mirrors. If the photon hits a phototube, the PMT number is saved. The known response of the BURLE 8854 tubes is folded with the wavelength dependence of the Cerenkov photons (as they are generated by GEANT). The BURLE response used is that in the BURLE specifications, which is a diode response, a factor of roughly 40% above the response of the tube used as photomultiplier, as we use it. Reflectivity losses have not yet been included. These are of order 50% for C1 (one bounce from each of the primary and intermediate mirrors, and the collector, and an average reflectivity of 80%) amd 64% for C2 (no intermediate mirrors). The ADC and TDC values of these hits are recorded.

Figure 7 shows the distribution of number of photons from electrons and positrons in C1 left and right sides. The very low number of photons comes from decays in in the volume of the counter. The high number of photons comes from low energy electrons or positrons which circle in the magnetic field. Figure 8 shows the distribution of phototube responses in C1, as expeced from GEANT and as seen in data. Only the shape of the distributions can be compared. The distribution shown is two sets of four tubes, with the first four tubes on the bottom and the second four on the top of the counter. Within each set of four, the numbers increase toward the left.

(increasing x is positive in our coordinate system). The general forms are similar, and as expected, with more hits in the two center tubes of each vertical strip. Detailed comparisons would need to include the effects of accidentals in the actual data, and known trigger biases which explain, for example, the top/bottom asymmetry seen in the data. Similar distributions are avaiable for C2. The GEANT tools are now in place. After calibration on observed data, we will be able to study the response of the counter to knock-on electrons, and other potential background processes.

Plans for the future include: inclusion of known optics imperfections and the measured counter response, the wavelength dependence of the reflectivity, and the photon polarization.

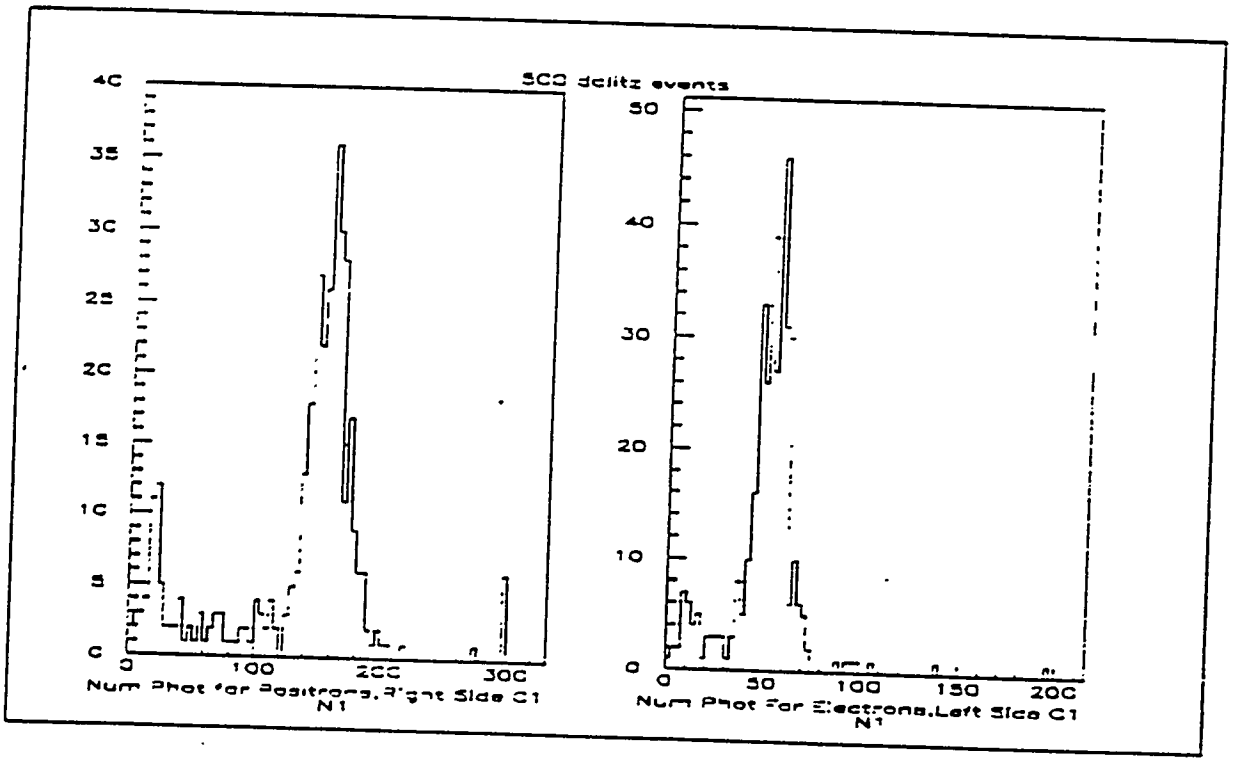

Figure 7: Number of Photons in C1 from Positrons and Electrons.

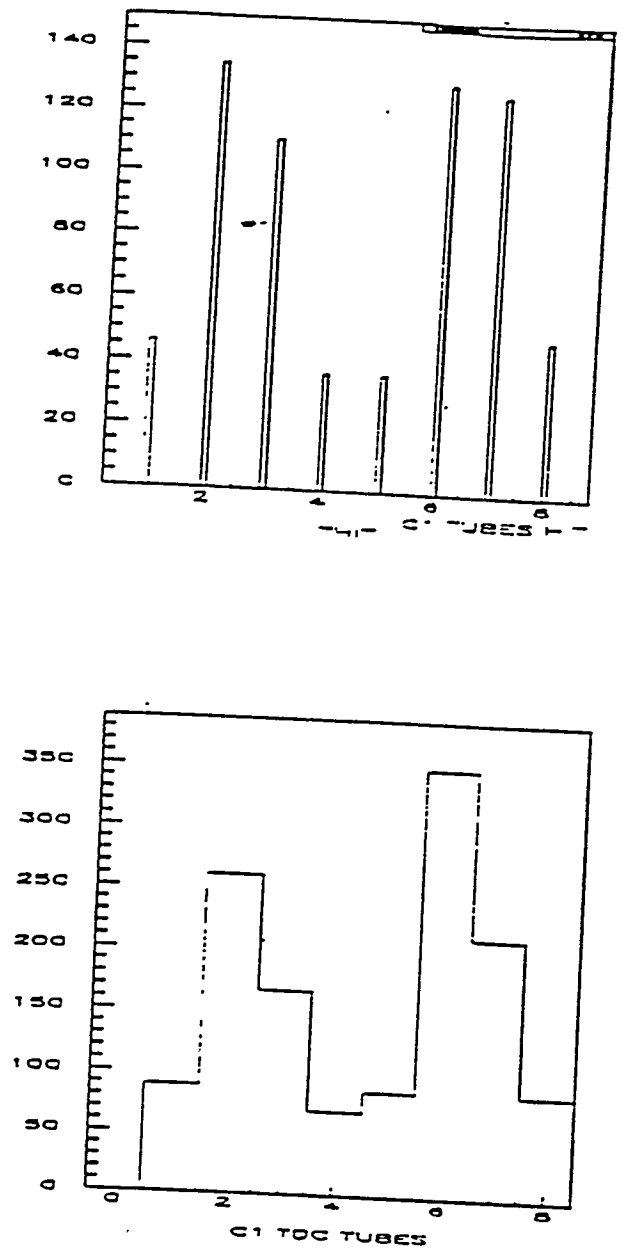

Figure 8: Number of Tubes Hit in C1 from GEANT and in E865 Run 2018 for 500 Dalitz Events (Numbering is Fastbus order in the off-line code arrays adc and itdc)

4.7 Physics Results - 1995 Run

All the data has been processed through a track reconstruction pass with loose cuts. In this first pass a 3-track vertex is required, since all our modes of interest contain three or more charged tracks, and the triggers require 3 charged particles in the hodoscope and calorimeter.

A clean sample of our normalization decay mode, $K^+ \to \pi^+\pi^+\pi^-$ has been isolated from the 1995 data. From the number of reconstructed $K^+ \to \pi^+\pi^+\pi^-$ events (shown in Figure 9) and preliminary studies of the $K^+ \to \pi ee$ events, we anticipate a single event sensitivity at or below 5×10^{-11}, compared to the present limit of 2×10^{-10}.

Thus, even with the various inefficiencies in the 1995 run we expect to improve the lepton flavor violation limit. An important part of the work now before us, however, is to demonstrate the necessary rejection in our accumulated data.

A clean sample of $K^+ \to \pi ee$ events has also been isolated as shown in Figure 10. This analysis, primarily the work of Scott Eilerts of New Mexico, shows a clean $K^+ \to \pi ee$ sample and an indication of the decay $\pi^0 \to e^+e^-$. The e^+e^- mass, shown for events with reconstructed 3-particle mass close to the kaon, shows a peak near the π^0 mass, and is interpreted as events from the $K^+ \to \pi^+\pi^0$ with subsequent decay of the π^0 to e^+e^-. The current published world sample of this mode is of order 10 events.

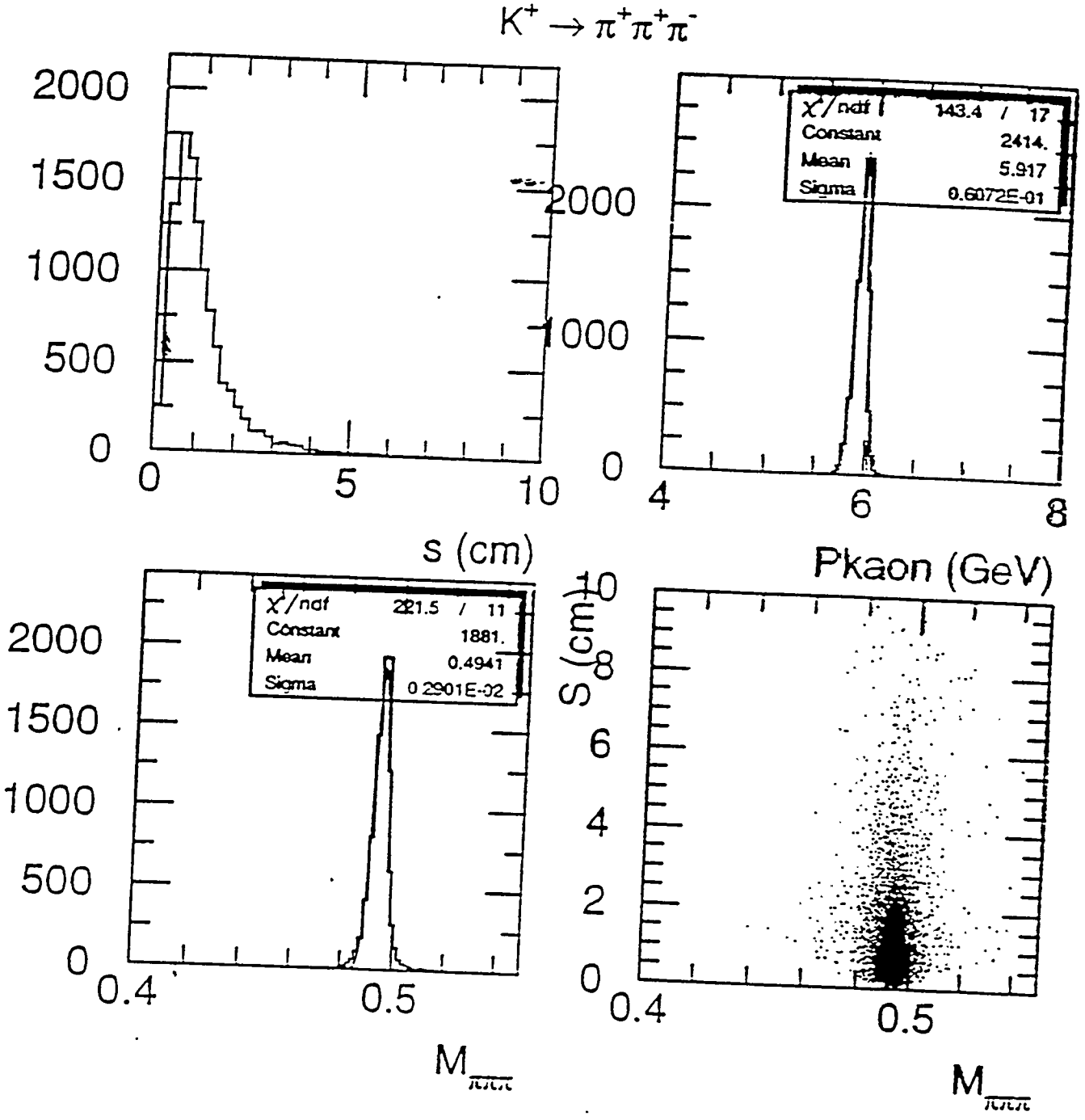

Figure 9: Reconstructed kinematic distributions for the 3 charged pion decay of the K^+.

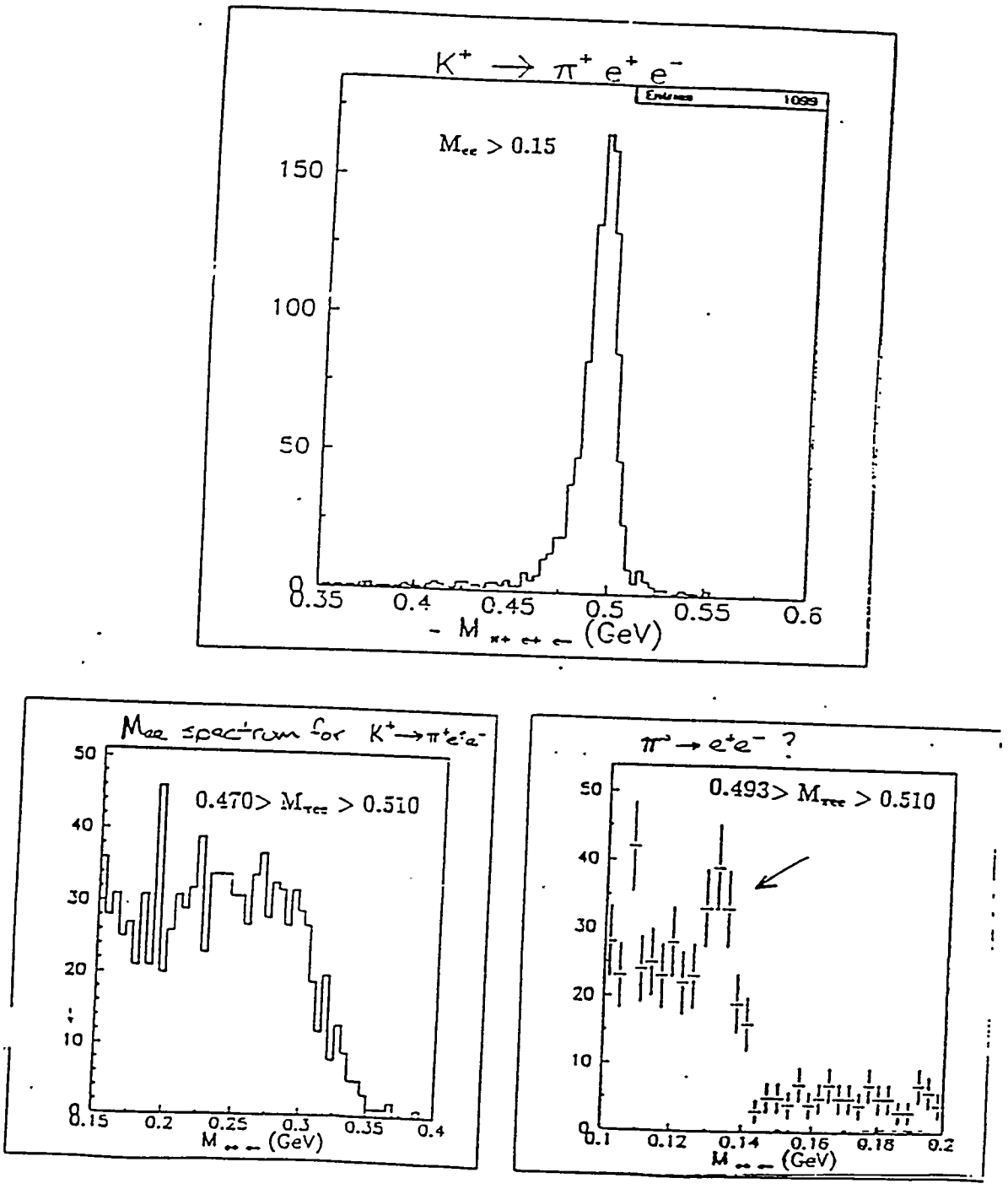

Figure 10: Plot of the K+ to pion e+ e- decay candidates, and also plot of the mass of e^+e^- candidates for events with the effective mass of $\pi^+e^+e^-$ close to the kaon mass.

4.8 Overall Experiment Improvements for the 1996 Run.

For the 1996 run, in addition to the Cerenkov counter work described above, repairs and improvements were made in the PWC's (raising the 3 track efficiency to $\approx 90\%$), and the muon chambers (repairing gas leaks and a broken wire). A trigger hodoscope was installed between the first two PWC's, to remove triggers from downstream interactions. Pittsburgh provided the PMT's for this hodoscope and assisted in its installation. The result of the hodoscope is to reduce the zero level 3 charged particle trigger by a factor of 3. This decrease is significant in allowing us to go up to higher intensities. Even with this decrease, we are presently limited by the DAQ, to about 1000 triggers per burst, about 50% less than the maximum available beam would produce. We are installing a DAQ upgrade to remove this limit.

Another upgrade in progress is the installation of a fine-grained (7mm x 7mm) scintillating pixel beam hodoscope, to give better rejection of backgrounds from off-beam particles and interactions, and also to allow us to study decay modes with missing particles (neutrinos). The interesting physics related to these decays has been discussed in conjunction with plans for the Frascati phi factory [34].

4.9 1996 Run

The 1996 run began on March 8. We are presently collecting data at a branching ratio sensitivity (from statistics) of about 7×10^{-11} per week.

The results from the 1995 run indicate that the data taken is of sufficient quality to reach our goal of a substantial improvement in the $K \to \pi\mu e$ limit.

5 Appendix A: Summary of Cerenkov Counter Design for E865

5.1 Overall Description

Schematic pictures of the optics for C1 and C2 are shown in Figures 11 and 13. The construction of the individual mirror frame cylindrical "slats" is of Rohacel with aluminized acrylic surfaces attached to the cylindrical "slat" frames by means of two small epoxy drops, and a number of low tension polyurethane bands. The phase space of photons from interesting decays is shown for C1 in Figure 12.

In C2, there is in addition a vertical division of the primary mirror assemblies, to allow for tests of low mass pairs from electrons with small vertical opening angles. The optics layout for C2 is shown in Figure 13. The phase space in C2 is shown in Figure 14. A difference from C1 is the wider divergence of the low momentum electrons and positrons from the Dalitz decay. This divergence makes the optics design problem in C2 more demanding than for C1, and led to the doubling of the collectors and photomultipliers for the high occupancy regions vertically close to the beam. A resulting problem is the additional sensitivity to scintillation and stray light.

For both C1 and C2, the lapping of the mirrors is done so that "trapping" by overlapping mirrors is minimized. This was easier in C1 because of the narrower angular distribution. In C2, a few percent of photons lying close to the edge of a mirror element may be subject to losses because the reflected ray is blocked by an adjacent mirror. However, these losses are primarily in the phase space populated only by Dalitz events, and we estimate that the additional kinematic separation available for these events makes these losses acceptable.

Because of the difference between the horizontal and vertical particle distributions, the collector outlines are different in the bending direction (ellipses) from the non-bending plane (simple slope from collector mouth to PMT photocathode). These sides come to a square at the PMT photocathode, of the same total area as the (circular) photocathode. An adiabatic transition from the 4-sided collector to a conical section near the photocathode would improve the overall collection. However, a simple transition to a conical collector does not improve collection. In the simulation, photons hitting outside the photomultiplier photocathode are simply discarded. This corresponds to a collector which may be simply built and understood. However, in order to rescue photons which would otherwise fall in the corners and be lost to the PMT, small "ears" are placed in the collector corners, near near the PMT. They convert the square end to an aperture approximately matched to the PMT area.

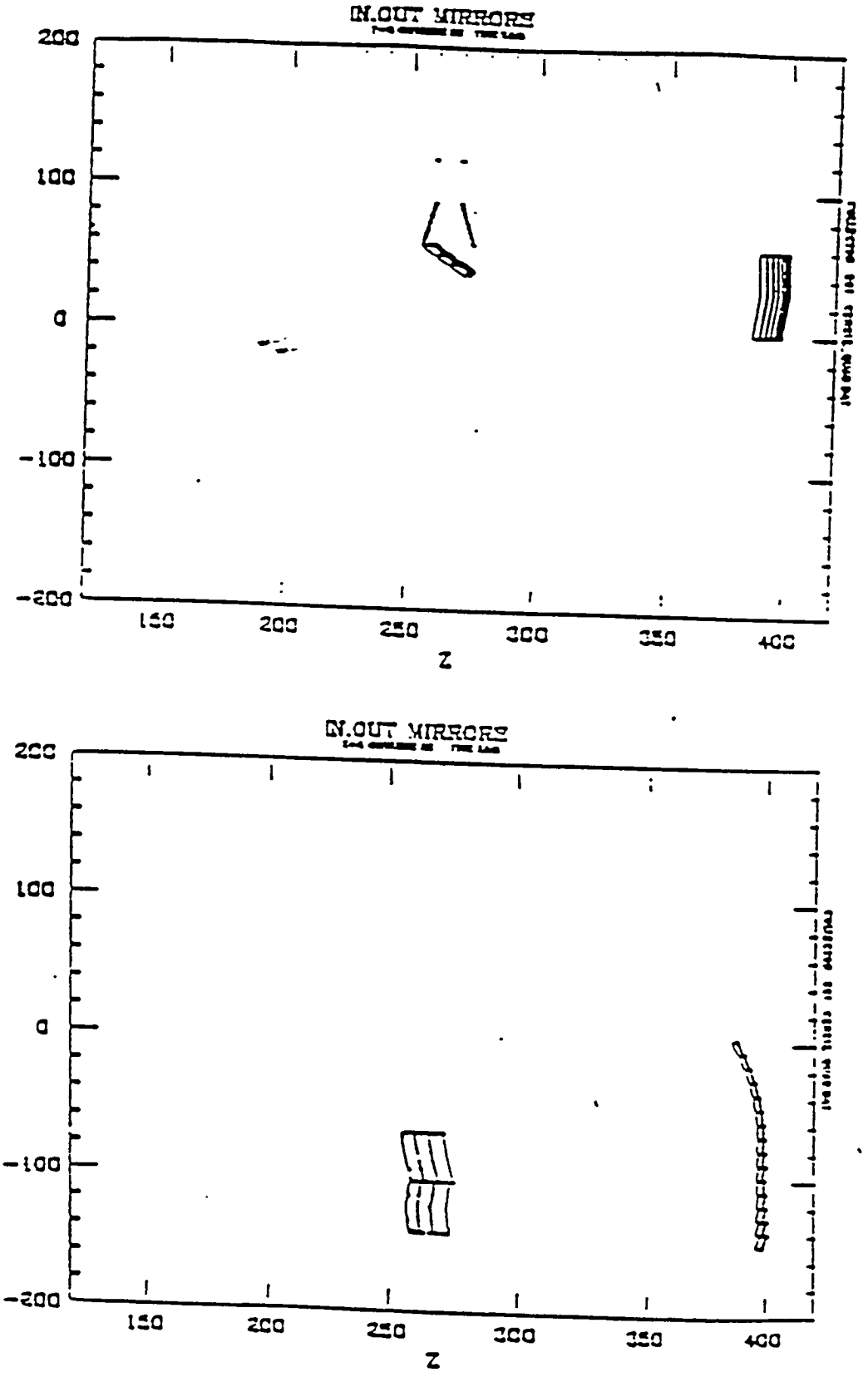

Figure 11: Outlines of the optical elements for one quadrant in C1. The top figure shows the side view, the bottom one shows a plan view.

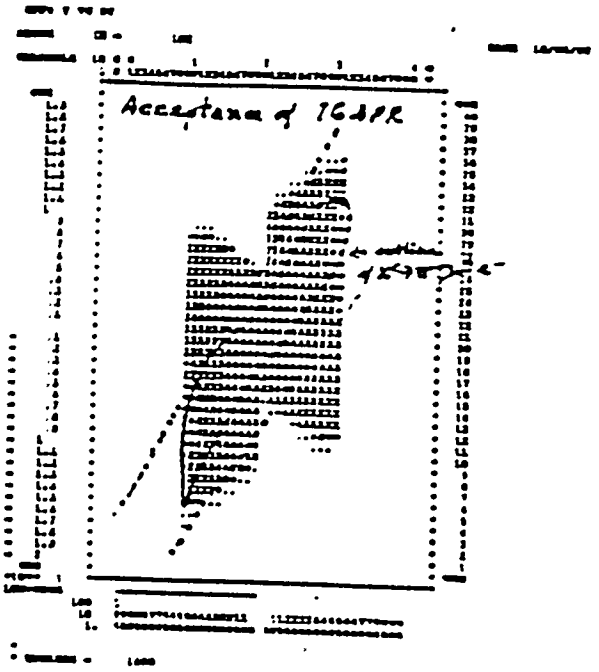

The (y,thetax) phase space plots for the expected photons and the acceptance of the CERES:IGAPR solution. a) photons from the rare, as yet unseen, decay K to pi e+ e-; b) photons from the decay K to 2 pions, with the neutral pion subsequent decay by the Dalitz mode ($\pi^0 \rightarrow \gamma e^+ e^-$); c) acceptance of the optical solution CERES:IGAPR.

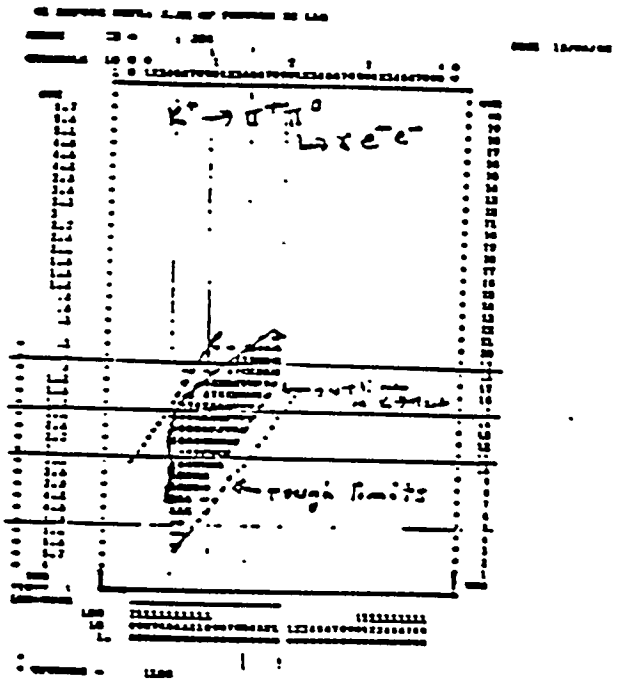

The (x,thetax) phase space plots for the expected photons and the acceptance of the CERES:IGAPR solution. a) photons from the rare, as yet unseen, decay K to pi e+ e-; b) photons from the decay K to 2 pions, with the neutral pion subsequent decay by the Dalitz mode; c) acceptance of the optical solution CERES:IGAPR.

Figure 12: Phase space for photons at the C1 mirror

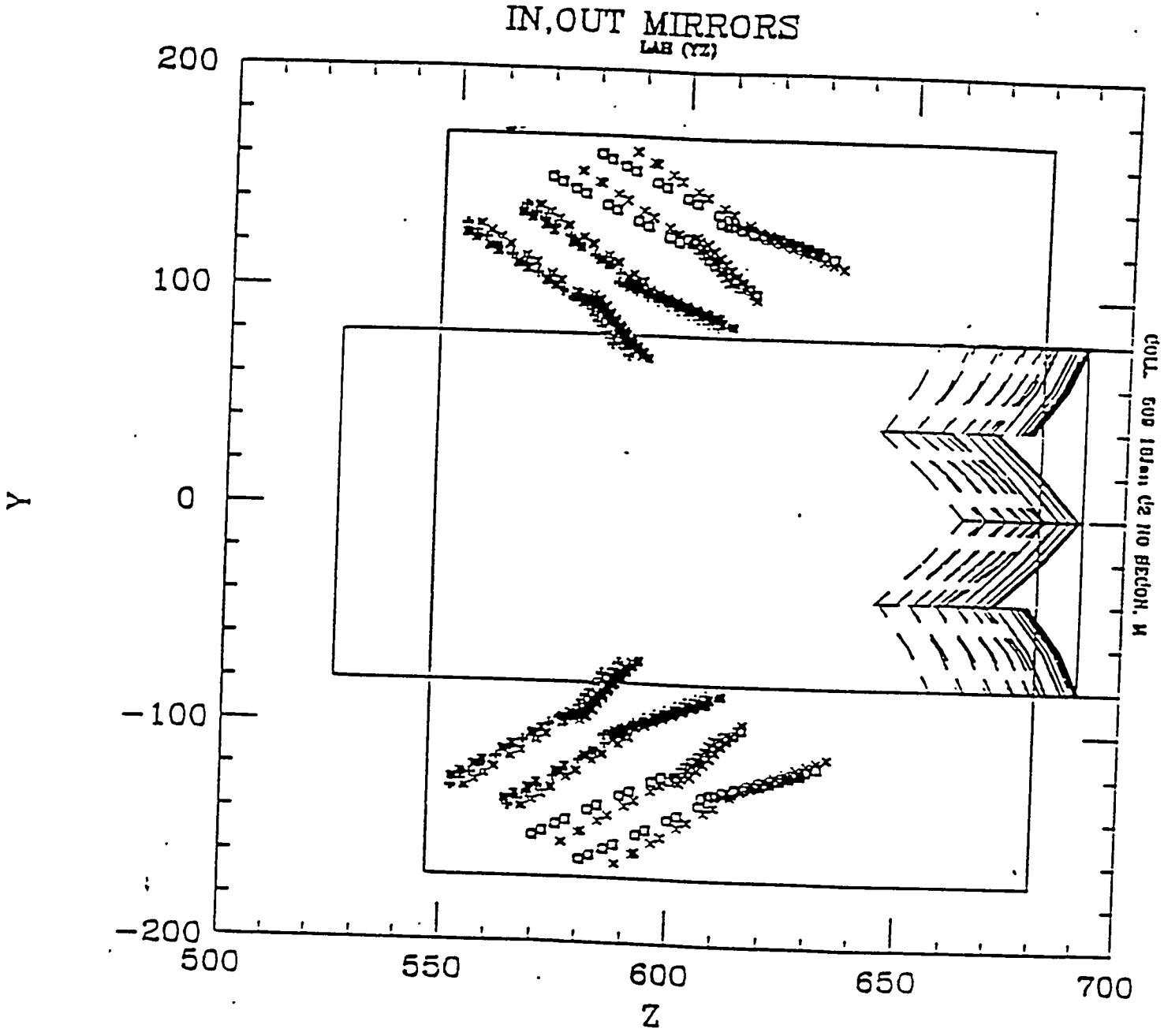

Figure 13: Outlines of the optical elements for in C2. A silhouette in y-z is shown. where y is vertical, and z is along the beam line.

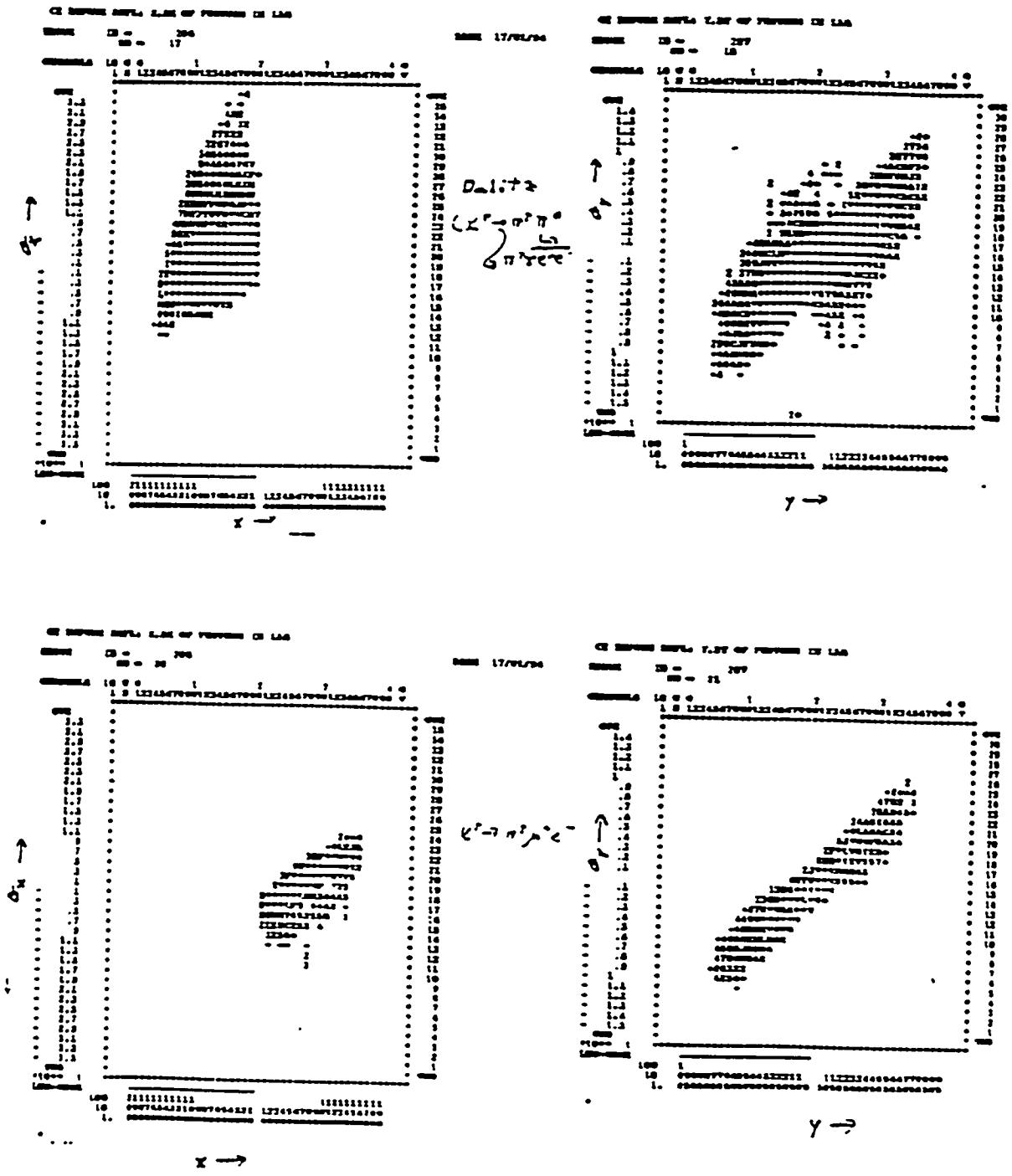

Figure 14: Phase space of the photons hitting C2

Magnetic Shielding. These optical configurations for C1 and C2 were chosen to allow simple mechanical construction, and in the case of C1 permitted positioning of the PMT's in a region of the magnetic field as predicted from TOSCA simulations to minimize the magnetic shielding problem. This property of the magnet model was confirmed in measurements of the actual magnet. At the C1 PMT position, the field is about 90 gauss in the absence of shielding, with its principal component perpendicular to the PMT axis. After installation of the magnetic shielding, (about 100 pounds per photomultiplier), the field at the PMT position was reduced to strengths which permitted the operation of the PMT's without the use of bucking coils. For C2, the photomultipliers near the beam line vertically see fields of up to 80 gauss before shielding, with the principal component at about 45° to the PMT axis, and the photomultipliers further from the beam vertically see somewhat lower fields, 35-40 gauss before shielding.

For C2 the field components were mapped, in x and y at the PMT position, and for at least one position at the location of the PMT base. The fields were less than about 0.5 Gauss at the photocathode, and about 2 Gauss at the PMT base positions. After demagnetization of the shields and tubes, performance in every position was measured to be at least 90% of the response with the magnetic field off. This conclusion was checked both for a test tube in the individual positions before the counter was closed, and for the actual ensemble used, after the closing of the counter.

5.2 Gas System

Design, Construction, Installation, and Testing of the Gas Control System. Pitt inherited responsibility for the design, construction, installation and testing of the gas flow control system for the Cerenkov counters. from the AGS Cryogenics group whose commitments did not permit them to undertake the redesign and construction which operating experience in the Summer '94 run indicated would be needed. A revised design was necessary to permit more rapid purging, and to accomodate the introduction of beam tubes. It was also desirable in order to reduce the possibility of serious error in managing the gas handling system arising from the large number of valves, complex plumbing pattern and limited visibility of the plumbing in the design inherited from E777. These hazards were compounded by the introduction of new pneumatic elements - the beam tubes, and the outer windows. The design was usefully critiqued by Don Lazarus, Dave Phillips and Ben Magurno of the AGS, and reviewed by the AGS Experimental Safety Review Committee. The central panel was constructed in the Yale Physics Dept. machine shops. The larger diameter plumbing needed to secure high flow rates at pressures below 1" H_2O was built and installed by personnel from the BNL Experimental support group and the Pitt group undergraduates, who also reworked the control panel, as necessitated by the discovery of flux residues in the plumbing.

The minimum operating relief pressure for a vessel operated at a few inches of water above atmospheric pressure is controlled by the characteristics of the relief valves. Large capacity bubblers were built to replace the mechanical relief valves of the original design. The bubblers were made in the BNL Chemistry glassblowing shop, and permit reliable operation at relief pressures of 1.5", (about half the relief pressure accessible

with commercial relief valves) at relief flow rates of 200 CFH of CO_2. They have the additional advantages of being adjustable and visible during operation, and being immune to the reseating problems of mechanical relief valves. The system now permits full purging of the C2 volume in one shift, even with the use of CO_2, which has a high viscosity, as a purge gas.

Several auxiliary testing procedures for establishing the composition of the gas have been introduced. These include direct measures of residual CO_2 and O_2 and H_2, and measurement of UV transmission in a spectrometer at the BNL Chemistry Dept. We will supplement this measurement with a one meter transmission path cell monitoring the attenuation of a deuterium lamp output whose spectral output distribution closely resembles that of Cerenkov radiation in the gases we use.

5.3 Mirror Construction and Testing

The optics construction for both C1 and C2 uses the idea of a complex mirror made of smaller components. Each component is an element of a cylinder, with a small "secondary curvature" across the narrow side of the mirror element. The mirror elements are oriented roughly vertically, with the primary curvature along the vertical direction, and the secondary curvature across the narrow part of the mirror element, in the horizontal direction. The function of the secondary curvature is to make the curvature more nearly continuous in the horizontal direction.

The optical design aims at minimizing the material introduced into the particle paths, while maintaining precision and stability of the reflecting surfaces. The Rohacel-aluminized acrylic mirrors present 35 mg/cm^2, or about 0.1 % r.l. per mirror to the detected particles. With the benefit of our substantial development work in hand, the full complement of component parts can be fabricated using about 20 hours of machining on an numerically controlled (NC) milling machine, and 20 hours on a good-quality manual milling machine. The machining of the component parts is small compared to the assembly and testing time, which was carried out at Pitt by undergraduates.

The flexibility of mirror construction of this technique may be promising for other applications in which large thin reflector surface area is required.

In spring of 1994, one full quadrant of C1 was tested for acceptance in our BNL test quad after full assembly, but before installation into the counter. Of 1000-1500 rays tested, only 15-20% of those in the Dalitz phase space were lost. This is consistent with expectations from the simulation.

5.4 Photomultiplier tests

Knowledge of the parameters of the photomultiplier tubes one uses is essential to understanding the Cerenkov counter performance. An optimum PMT design would combine windows with good transmission at least down to 180 nm and high first dynode electron multiplication (20 or better) permitting good resolution between single photoelectron signals and pulses arising from processes further down the multiplication chain. The only tube with a reliable high first dynode gain (the RCA/BURLE 8854 with a GaP first dynode) has a UV-transmitting glass which cuts off below 250 nm, but we have

decided to use this tube because of the good first dynode response and because other tubes tried did not show long term stability (Hammammatsu) or were unavailable in practice (Amperex) or were much more expensive (both Hammammatsu and Amperex).

Tests of the Burle 8854's used in E777 indicate that most of these tubes have first dynode gains of approximately 20 (necessary for the single photoelectron discrimination), and have not developed disabling after-pulsing because of helium permeation.

Some results obtained from studies in a simple monochromator test setup indicated less than a 10 % difference between light incident on the outside perimeter of the tubes and light incident on the tube centers, transit time spreads of 1.5-2 nsec, and adequate performance up to around 5 MHz, a typical counting rate for the busiest tubes at the current running conditions, which are within a factor of 2 of the full desired beam. Observation of the tubes in place at the current beam rates show satisfactory performance, both by direct observation of the pulse shapes, and by monitoring off-line the size of the single photoelectron signal as seen in the ADC's. There is built into the design of the base a booster chain of Zeners for the dynode voltages, but to date this chain has been required only in one special case.

Wave-length shifter (WLS) We have re-examined the question of using WLS, and are exploring some new possibilities. The degradation in timing performance which even the fastest efficient WLS introduces cautions against, but does not necessarily prohibit, its use in the CO_2 (pion-vetoing) cells, where the eventual data cuts will depend on tight timing agreement among the shower counters, scintillators and Cerenkov counter. Experience with p-terphenyl for photomultipliers with UV transmitting glass windows, as the Burle 8854 which we use has, is variable, and may depend on other factors such as the purity of the gas and the presence of outgassed impurities.

Helium and hydrogen poisoning. The possibility of Hydrogen permeation of the PMT envelopes is a particular concern in light of the E777 indications that its time scale might be 4 to 5 months, together with the present proposals for extended data taking runs. We have not experienced difficulties attributable to hydrogen or helium permeation to date in the present run.

Bases The bases were designed starting from the suggested BURLE configuration, with added stiffening by addition of Zener diodes in the dynode voltage distribution chain. Both bench tests and reliability calculations were done, indicating an expected failure rate of not more than one in the lifetime of the experiment. Spares are on hand in case of such failure. Because of the speed of gas turnaround in our improved gas handling system (of order half a day) and the steep incremental expense curve as one attempted to improve the lifetime using components with an official uncertainty in the calculations, this level of reliability seems adequate. We have found one fault in the design, the use of a small wattage resistor in a capacitive path to ground, which requires bringing the tube to voltage in slow (50 volt) steps to avoid large transient currents in the resistor.

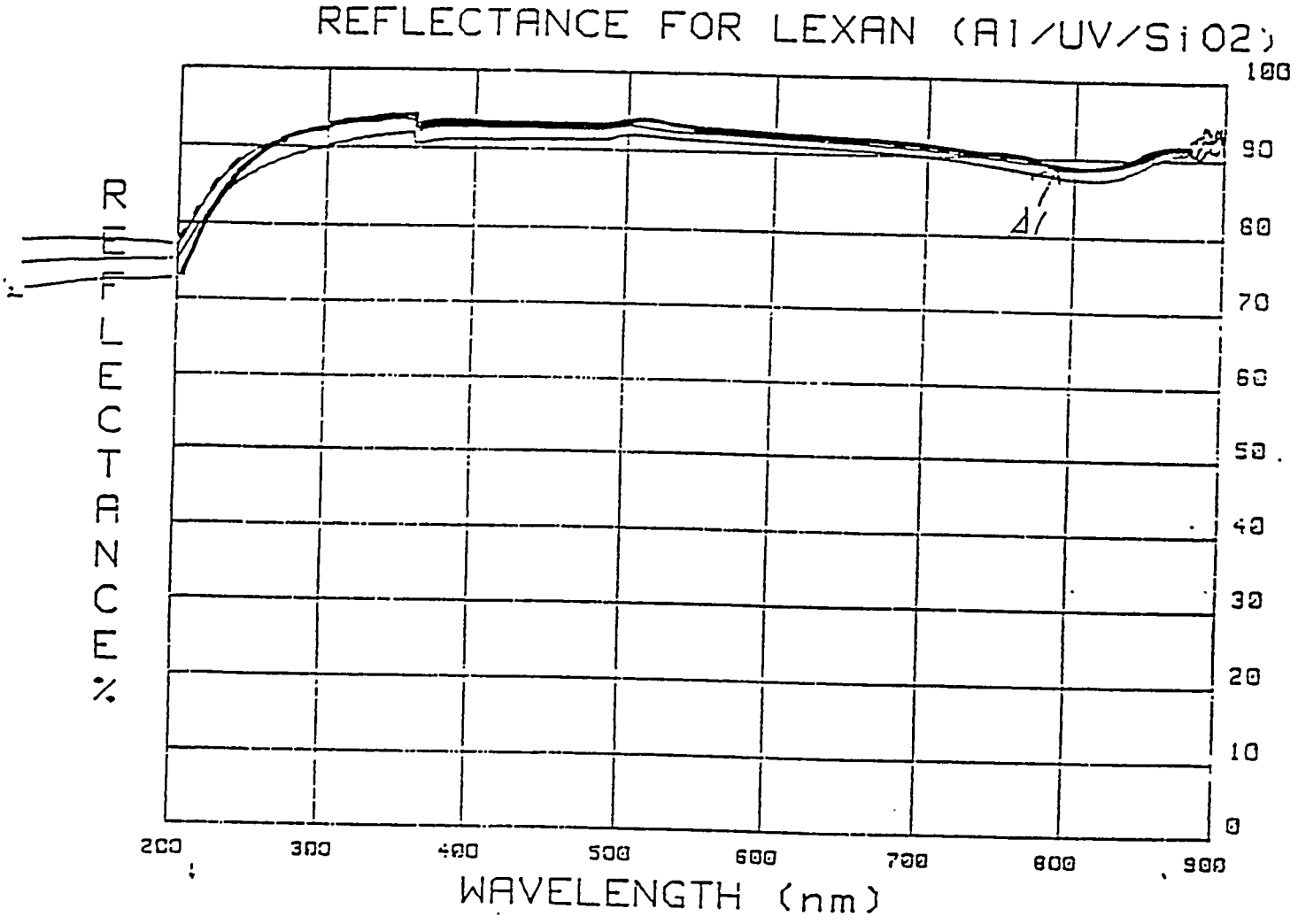

Figure 15: Reflectivity scans for mirrors prepared with a) MgFl overcoating and b) SiO2 overcoating.

References

[1] J. Antos, et al., (subset of HELIOS Collaboration), "Soft Photon Production in 450 GeV/c p-Be Collisions", Z. Phys. C **59**, 547 (1993).

[2] "Low-mass Lepton-pair Production in p-Be Collisions at 450 GeV/c", (with T. Akesson and the HELIOS Collaboration), CERN-PPE/94-140R, submitted to Z. Phys. C.].

[3] Paula A. Pomianowski, "Electron-Muon Pairs in 450 GeV/c p-Be Collisions: A Limit on Non-charm Physics Contributions Relative to Charm Production and Decay", PhD Thesis and PITT-94-06, University of Pittsburgh, January 25, 1994.

[4] I. Dunietz, J. Hauser, and J.L. Rosner, Phys. Rev. **D35**, 2166 (1987).

[5] S. Eidelman, E. Solodov, and J. Thompson, Nuclear Physics B (Proceedings Supplement) **24A** (1991) 174. (Plans for the Novosibirsk Phi Factory, contribution to the Phi Factory Workshop at UCLA, April, 1990, and PITT-90-08).

[6] C. Buchanan, R. Cousins, C. Dib, R.D. Peccei, and J. Quackenbush, "Testing CP and CPT Violation in the Neutral Kaon System at a Φ Factory", UCLA/91/TEP/44, November, 1991.

[7] G. Vignola, XXVI International Conference on High Energy Physics, Dallas, August 6-12, 1992.

[8] P. Franzini,, XXVI International Conference on High Energy Physics, Dallas, August 6-12, 1992.

[9] J. Lee-Franzini,, XXVI International Conference on High Energy Physics, Dallas, August 6-12, 1992.

[10] L. Wolfenstein, "CP Violation and $\overline{p}$ p Experiments", CMU-HEP86-5, (1986).

[11] L. Wolfenstein, Nuclear Physics B, (Proceedings Supplement) **24a** 32 (1991). (Status of CP Violation , UCLA Workshop on Testing CPT and Studying CP Violation at a Phi Factory.).

[12] K. Peach, Blois Conference on CP Violation, 1989, Phys. Lett. B**206**,169 (1988).

[13] "Measurement of the CP Violation Parameter Re $[\epsilon'/\epsilon]$", Phys. Rev. Lett. 70:1203-1206,(1993).

[14] " CP and CPT Symmetry Test from the Two Pion Decays of the Neutral Kaon with the FNAL E731 Detector", Submitted to PRD. Fermilab-PUB-95-392-E, Jan 1995 192 PP.

[15] Julia A. Thompson, "CPT-Violation: Present Status and Planned Measurements at Phi Factories", , UCLA Mini Workshop on Low Energy Signals from the Planck Scale, October 29-30, 1992, published in **Gamma Ray-Neutrino Cosmology**

and Planck Scale Physics: Proceedings of the 2nd UCLA International Conference and Other Meetings, ed. David B. Cline, World Scientific, p. 316 (1993),.

[16] P. Eberhard, Contribution to the Phi Factory Workshop at UCLA, April, 1990.

[17] Ghirardi, Plenary talk, p. 261, Proceedings of the Workshop on Physics and Detectors for DAΦNE, Frascati, April, 1991.

[18] Talks at dedicated EPR Workshop, UCLA, November 8, 1991.

[19] Summary talks of L. Maiani (p. 719) and R. Baldini Ferroli (p. 665), Proceedings of the Workshop on Physics and Detectors for DAΦNE, Frascati, April, 1991.

[20] See, for example, reviews of L. Maiani, R. Baldini, and F. Close, p. 309, Proceedings of the Workshop for Physics and Detectors at DAΦNE, April, (1991), Frascati, Italy.

[21] N.N. Achasov and V.N. Ivanchenko., Nucl. Phys. **B315**, 465, (1989).

[22] N.W. Tanner and R. Dalitz, Ann. Phys. (N.Y.),**171**, 463 (1986).

[23] V. V. Anashin et al., Preprint INP 84-114 (Novosibirsk,1984).

[24] L.M. Barkov et al., Nuclear Physics **B256**, 365, (1985).

[25] A.D. Bukin et al., SJNP **27**, 516, (1978).

[26] S.I.Dolinsky et al., Phys. Reports, **202**, 99, (1991).

[27] E.V. Anashkin *et al.*,General purpose cryogenic magnetic detector CMD-2 for experiments on the VEPP-2M collider. ICFA Instrumentation Bulletin 5 (1988), and G.A. Aksenov, *et al.*, INP 85-118.

[28] G.A.Aksenov et al., Preprint 85-118, BINP Novosibirsk, Russia.

[29] N. Ryskulov et al., Proceeding of the 5th International Conference on Instrumentation for Colliding Beam Physics, p.367. Novosibirsk,1990, Russia.

[30] C.M. Valine, "A New Data Acquisition System for the Cryogenic Magnetic Detector at the VEPP-2M Collider",M.S. thesis, University of Pittsburgh, 1995.

[31] R.R. Akhmetshin et al. (CMD2-Collaboration) Measurement of ϕ-meson parameters with CMD-2 detector at Vepp-2M collider, Preprint INP95-35, Phys. Lett. **B364**. 199-206 (1995).

[32] E. Solodov, Fifth Conference of the Intersections of Nuclear and Particle Physics, St. Petersburg, Florida, June, 1994.

[33] R.R. Akhmetshin et al. (CMD-2 Collaboration) Recent results of the f-meson with CMD-2 detector at VEPP-2M collider and relevance to future CP,CPT f-factory studies. Preprint INP 95-62, Novosibirsk 1995.

[34] J. Bijnens, G. Colangelo, G. Ecker, and J. Gasser, "Semileptonic Kaon Decays", Frascati Preprint.

6 List of Publications from Task A in 1995-96.

6.1 HELIOS

1. "A study of electron-muon pair production in 450 GeV/c p-Be collisions", (based on the thesis of Paula Pomianowski, included then Pitt undergraduate Craig Valine, along with the HELIOS collaboration as authors. CERN-PPE/96-23, Febuary 19,m1996; submitted to Z. Phys. C.

2. "Low-mass Lepton-pair Production in p-Be Collisions at 450 GeV/c", (with T. Akesson and the HELIOS Collaboration), CERN-PPE/94-140R, submitted to Z. Phys. C.

6.2 Novosibirsk

1. R.R. Akhmetshin et al. (CMD-2 Collaboration) Measurement of ϕ-meson parameters with CMD-2 detector at VEPP-2M collider. Phys. Lett. B364 (1995) 199-206 Preprint INP 95-35, Novosibirsk 1995.

2. R.R. Akhmetshin et al. (CMD-2 Collaboration) Recent results of the ϕ-meson with CMD-2 detector at VEPP-2M collider and relevance to future CP,CPT ϕ-factory studies. Preprint INP 95-62, Novosibirsk 1995

3. G.V. Fedotovich et al (CMD-2 Collaboration). Measurement of the $e^+e^- \rightarrow \pi^+\pi^-$ Cross Section in the Energy Range between ρ and ϕ mesons. Proceedings of the Second Workshop on Physics and Detectors for DAFNE, Frascati, April, 1995 199-206.

4. Aksenov et. al. A new data acquisition system for the CMD-2 detector" Proceedings 6th International Conference on Instrumentation for Experiments at e^+e^- Colliders, Novosibirsk, February 29 - March 6, 1996

5. Craig M. Valine, M.S. thesis in electrical engineering, University of Pittsburgh, August, 1995.

6.3 E865

1. H. Ma, presentation to the BNL Users' committee in 1995.

2. D. Bergman, presentation to the BNL USers' committee in 1996.

3. H.Ma, et al., presentation in preparation for DPF, August, 1996.

Task B

Contents

TASK B – FERMILAB PROGRAM

1 Program Outline

The major goals of task B are as follows: 1) participation in the analysis of the E706 data taken during the 1990-91 fixed target run at Fermilab and 2) the continuation of our work within the CDF collaboration particularly the SVX II upgrade. The E706 part of our program will involve the completion of publications reporting the results of the 1990-91 data run. The analysis of these data is now mature and physics results are emerging. Our last two students on the experiment, Woo Hyun Chung and Steven Blusk, successfully defended their theses in the summer of 1995. Chung and Blusk are now post doctoral research associates at the University of Wisconsin and the University of Rochester, respectively. During the period September 1, 1995 to April 30, 1996, Blusk was appointed as a post-doctoral research associate in our group to complete a publication on his thesis work. The publication is now essentially complete and ready for submission. One of the graduate student slots vacated by Chung and Blusk will be shifted to our CDF effort and a new graduate student, Richard Rosati, has been recruited for that effort. The CDF program involves a dedicated effort towards the design of a silicon vertex detector upgrade, SVX II, to be accomplished by the time of the Fermilab run II collider run (1999). In addition we are participating in the 1993-1995 collider run Ib and actively analyzing data from both runs Ia and Ib.

2 E706 - Direct Photon Production at the Tevatron

2.1 Introduction

Fermilab experiment E706 is designed to measure direct photon yields in the p_t range 5 -10 GeV/c with incident π/p beams between 500 - 1000 GeV/c and to study the associated jets produced in such reactions. The experiment will also measure the production of high mass ($m > 3GeV$) e^+e^- and $\gamma\gamma$ states. The experiment is being carried out by a collaboration which includes the University of California at Davis, Delhi University, Fermilab, Penn State University, Michigan State University, the University of Minnesota, Northeastern University, the University of Oklahoma, the University of Pittsburgh, and Rochester University.

Figure 1 is a plan view of the elements of the E706 spectrometer located in the Meson West Laboratory. The apparatus for E706 consists of an array of silicon strip detectors (SSD's) before and after a production target, a set of proportional chambers (PWC's) and straw tube chambers located after the analysis magnet, a large liquid argon calorimeter (LAC), and a small steel/plastic scintillator forward calorimeter. The forward calorimeter is followed by a muon system provided by E672 utilizing a toroidal magnet in conjunction with PWC's to identify muons. The LAC [1] measures the position and energy of both photons/electrons and hadrons. It has a central hole of 40 cm. diameter; this area is covered

by the forward calorimeter. The SSD's together with the PWC's and straw tubes after the analysis magnet constitute a magnetic spectrometer designed to measure the momenta of charged particles in hadronic jets associated with high p_t photons. In addition the SSD's serve as a vertex detector which accurately locates the position of primary and secondary interactions in the segmented target. One major contribution of the Pittsburgh group to E706 has been the design, construction and operation of the SSD system [2].

Figure 2 is a sketch of an E706 event viewed in the center-of-mass system of the interacting particles. The high p_t photon intercepted by the LAC provides the trigger, and this photon may be a direct photon emitted by the interacting partons or it may be a decay photon from either a π^0 or η decay in which case it is viewed as being part of a "trigger jet". Balancing transverse momentum opposite the trigger jet is a "recoil jet". In the case of both the trigger and recoil jets, the momentum of the particles assigned to those jets by a simple algorithm are summed to form the total jet momentum vectors shown in Fig. 2. The fragmentation variable z is defined as

$$z = \frac{\vec{p}_i \cdot \vec{P}_{jet}}{|\vec{p}_i||\vec{P}_{jet}|}.$$

2.2 Discussion of the 1987-88 Data Run

The 1987-88 data run was originally intended as an engineering run but actually produced a significant body of physics. A total of 5 x 10^6 events were recorded on magnetic tape. The final results of the inclusive γ production part of the analysis of the 1987-88 data run have been published [3]. In addition, the study of the γ + accompanying jet production provided the Ph.D. thesis subject for D. Weerasundara and has been published [4]. The data are compared with QCD calculations using currently accepted pion and proton structure functions.

2.3 Discussion of the 1990–91 Data Run

The 1990-91 data run represented a significant upgrade of the E706 spectrometer system and the Pittsburgh portion of the upgrade involved two reconfigurations of the target-silicon strip detector system. The target used for the first half of the run is shown in Fig. 3 while the target used for the second half is shown in Fig. 4. Presented in these figures is the distribution of interaction vertices originating in the various parts of the production target located along the beam. Apparent are peaks corresponding to interactions in the pairs of SSD's upstream and downstream of the target proper, with the prominent peaks being located in the target material being used. The data yield from liquid hydrogen in the target of Fig. 4 is a small fraction of the total yield but is deemed essential when comparing production on nuclear targets with comparable production in hadron collider experiments or other fixed target experiments using liquid hydrogen.

Table 1 shows the amount of data that has been taken to date by the E706 collaboration.

E706 RUN SUMMARY		
1988 Run		
INTERACTION	EVENTS	SENSITIVITY
π-Be @ 500 GeV/c	2×10^6	0.5 events/picobarn
(p, π^+)Be @ 500 GeV/c	3×10^6	0.75 events/picobarn
1990 Run		
π Be @ 530 GeV/c	30×10^6	8.6 events/picobarn
1991 Run		
p-Be @ 800 GeV/c	23×10^6	7.3 events/picobarn
p-H @ 800 GeV/c	23×10^6	1.5 events/picobarn
(p, π^+)Be @ 530 GeV/c	14×10^6	6.4 events/picobarn
(p, π^+)H @ 530 GeV/c	14×10^6	1.3 events/picobarn
π Be @ 530 GeV/c	4×10^6	1.4 events/picobarn
π H @ 530 GeV/c	4×10^6	0.3 events/picobarn
Total Number of Events = 76×10^6		

Table 1: Summary of the data taken by E706 during the 1988, 1990 and 1991 runs.

Apparent is that the quantity of data taken during the 1990 91 run is about 15 times the amount of data taken during the 1987 88 run. The University of Pittsburgh group had been active in all aspects of data taking and has taken responsibility for many aspects of the ongoing data analysis of the 1990-91 data. W. Chung and S. Blusk have continued during the past year to make substantial contributions to the experiment as a whole. At the time of this writing, all of the 1990 and 1991 data have been processed by the computer farm. The large production Monte Carlo runs have also been completed and the collaboration is now busily extracting physics results from the data and are preparing the corresponding publications.

2.4 Inclusive γ and π^0 Physics in the 1990-91 Data Run

Figure 5 is a plot of number of events plotted against the energy asymmetry of the two photons resulting from π^0 decay and detected by the LAC. If the LAC were completely efficient in detecting low energy γ's, then the plot would be flat over the entire range of asymmetries. The fact that the plots fall off at the larger values of the asymmetry is a measure of the LAC's inefficiency for detecting low energy γ's. The open circles on the plot represent the 1988 data while the solid circles show the improvement in the LAC's performance in the 1990-91 data run. This improvement substantially reduces the background subtraction to

the prompt γ signal, the background largely being a π^0 masquerading as a direct γ because one of its decay γ's remains undetected.

Figure 6 is a plot of the invariant π^0 production cross section comparing the E706 data using a π^- beam with results obtained from previous experiments carried out at comparable center of mass energies. The E706 and NA3 data have been scaled appropriately to account for the fact that nuclear targets were used in these two experiments. The E706 data points are somewhat higher than those of the other experiments which is to be expected given the greater center of mass energy of E706. Note that the E706 data cover a range of more than 13 decades in p_t. A comparison of the inclusive production data of direct γ's and π^0's as well as η's and ω's in the E706 energy range with Next-to-Leading Order (NLO) QCD calculations has been made. Because no calculations of higher order than NLO are available, it is necessary to select a "scale" relating the measured p_t to the QCD parameter Q. An earlier approach was the Principle of Minimum Sensitivity (PMS) which minimized the effect of the choice of scale by allowing it to vary at each point in phase space and thus allowing a predicted differential cross section. Although reasonably successful, the PMS approach has been criticized because of the large range of choice of scale and the unnaturally small values of Q vs p_t. An alternate approach and the one we employ in comparing our data to NLO calculations is a narrow choice of scale which, by itself, gives good agreement with only a fraction of the data. In order to obtain good agreement with all of our data, we must in addition introduce an intrinsic Fermi motion for partons which we parameterize in terms of an effective Gaussian smearing of the NLO calculations. This parameter is an effective k_t. We find that the best fit to all of our data is obtained by the choice of $p_t/2 < Q < p_t$ and k_t in the range 1.4 - 1.6 GeV/c [5]. Fig. 7 shows the invariant cross section plotted as a function of p_t for three sets of data. The data are compared with QCD calculations in which an appropriate scale has been chosen and for which three values of k_t have been selected. The sensitivity of the calculations to the choice of k_t is apparent in the figures shown.

2.5 γ + Jet Physics in the 1990-91 Data Run

The principal activity of W. Chung during the past year was the analysis of the γ + jet data taken during the 1990-91 run. This analysis is now nearing completion and is the subject of his Ph.D. thesis. He received his Ph.D. in the summer of 1995. [6]

Figure 8 are plots of the fragmentation function 1/N dn/dz for the 1990 (515 GeV/c π^- beam) data and 1991 (800 GeV/c proton beam) data. N is the total number of γ + jet or π^0 + jet events and dn/dz is the number of particles in the recoiling jet per unit of z. The data shown in either plot have been fitted with the form $\frac{1}{N}\frac{dn}{dz} = Az^{-B}e^{-Cz}(1-z)^D$. The γ + jet data have been background subtracted. The outer Monte Carlo generated curves on both figures represent the fragmentation functions that are expected if the recoiling jet is entirely a fragmenting gluon jet or entirely a fragmenting quark jet. Figure 8a) shows a clear difference between the γ + jet and π^0 + jet data. The comparison of these fragmentation functions is consistent with the expectation that γ + jet events produced by a π^- beam are

very rich in gluon jets, yielding a steeper z dependence of the fragmentation function. This is not to be expected in the case of jets produced by incoming proton beams. These latter jets are largely fragmenting quarks. Figure 8b) shows the γ + jet and π^0 + jet fragmentation functions which appear to be identical.

Figure 9 is a plot of the angular distribution in the interacting parton-parton rest frame of a) the γ + jet events and b) π^0 + jet events using a 515 GeV/c π^- beam (1990 data). Plotted are number of events vs. $\cos\theta^*$ where θ^* is the angle which the trigger γ or π^0 particle makes relative to the incoming beam axis in the parton-parton rest frame. No data are plotted above $\cos\theta^*$ greater than 0.5 in order to present an unbiased data sample. There appears to be a distinct difference between the two production processes in that the π^0 + jet data are more steeply rising than the γ + jet data. These results are compared with QCD predictions and with fully detector-simulated Monte Carlo results. Figure 10 is a plot of the $\cos\theta^*$ distribution using an 800 GeV/c proton beam (1991 data). Again, the π^0 + jet and γ+ jet data show a difference in their angular distributions and are in reasonable agreement with the simulated data. The enhanced event yield at small values of $\cos\theta^*$ for γ + jet compared with π^0 + jet data results from the large contribution of the Compton process to the γ + jet data.

Finally, the azimuthal correlation of the two jets produced in heavy nuclei has aroused considerable interest. One would expect that the two outgoing partons emerging from a collision between two incoming partons would subtend an azimuthal angle about the beam axis of 180 degrees with respect to one another. k_t effects of the interacting partons within their nucleons and Fermi motion within the nucleus would result in a broadening of the azimuthal distribution about 180 degrees. Any broadening of the distribution as a function of the nuclear mass might be interpreted as a rescattering of the outgoing partons in the nuclear matter before fragmenting. Figure 11 is shows plots of the quantity k_{to} where k_{to} is defined by the expression

$$k_{to} = \frac{Pt_1 + Pt_2}{2} \sin\Delta\Phi$$

P_{t1} and P_{t2} for this experiment are the transverse momenta of the γ and its accompanying jet or the π^0 and its accompanying jet, and $\Delta\Phi$ is the azimuthal angle between particle and jet. Apparent in the figure is that $< k_{to}^2 >$ increases with nuclear mass, in agreement with previous experiments [7]. One might expect the γ + jet data to differ from the π^0 + jet data because the γ might be expected to rescatter less than either a quark or gluon represented by the outgoing π^0. No such effect is observed.

2.6 Studies of the Charm Content in the Trigger and Recoiling Jets

The subject of S. Blusk's Ph.D. thesis is the study of the charm content of the E706 data. [8] Of interest is the production mechanism both in leading order and next-to-leading order

for charm in hard hadron-hadron collisions. Because of the presence of the SSD system in the experiment, Blusk put great effort into refining the secondary vertex finding and reconstruction capability of the experiment and extracted an unambiguous charm signal from the data.

Figure 12 is a plot of the $\pi^+\pi^-$ mass for pion pairs produced just downstream of the production target and still within the silicon system. The location of the peak at the K^0_S mass along with its narrowness demonstrates that the energy scale of the charged particle spectrometer is well understood. The data compare well with a Pythia Monte Carlo simulation. Figure 13 is a plot of the $K\pi\pi$ mass associated with secondary vertices produced downstream of a primary interaction vertex in an event. A requirement is placed that the secondary vertex be located a distance of at least 3 millimeters downstream of the primary vertex in order to eliminate as much background relative to signal as possible. Figure 14 is a plot of the $K\pi$ mass in the same data sample, clearly revealing a D^0 signal.

During the past year, considerable work by S. Blusk went into determining the efficiencies for observing the above decay modes of charm in order to arrive at the value of the total cross section for charged D production by E706. Shown in Fig. 15 is a comparison of the $D^\pm$ differential cross section per nucleon with the NLO predictions. Shown in the upper left hand plot is the calculated NLO unfragmented $c\bar{c}$ p_t distribution along with the $D^\pm$ data points. As expected, the unfragmented $c\bar{c}$ quarks have a stiffer p_t distribution than the data. The remaining plots compare the data with predictions using a Peterson fragmentation function along with varying values of $< k_t^2 >$.

Figure 16 shows the integrated $D^\pm$ cross section per nucleon, with other recent experimental results measured at different beam energies. Also shown is the NLO prediction for the total charm quark cross section using appropriate parton distribution functions for the incident pion and target nucleon. The curves shown in the figure indicate the sensitivity of the calculation to the choice of normalization scale. The various triggers used in E706 are to some degree sensitive to the semi-leptonic decay of charm and require an understanding of how these triggers respond to a low p_T lepton from D decay. Correcting the data for trigger efficiencies, tracking and reconstruction efficiencies and branching modes, one arrives at a value for the total charged D production cross section shown in Fig. 16 This result is sensitive to the choice of k_T of the incident partons because the low p_T turn-on of the relevant experimental triggers strongly influences the efficiency for triggering on the decaying D meson.

2.7 E706 Physics in Collaboration With E672

Fermilab experiments E706 and E672 share the same beamline as shown in Fig. 1. Although the two experiments have their own individual spokespersons and physics missions, the data of the two can be combined when that is of physics interest. E672 is a dimuon experiment with a toroidal magnet muon spectrometer flanked by proportional wire chamber planes, and is particularly sensitive to high mass muon pairs. Combining the J/Ψ capability of E672

with the precision vertexing capability of the E706 silicon microstrip detection system, the group was able to study the production of B mesons which subsequently decay into J/Ψ mesons and either a $K^{\pm}$ or a K^{0s} for which the B can be fully reconstructed.

This study has been published [9]. Studies of charmonium states that decay into $J/\Psi + \gamma$, the γ being detected by the LAC, are also underway and a paper reporting the production of J/Ψ and $\Psi(2S)$ mesons in π^--Be-collisions at 515 GeV/c has just been published [10].

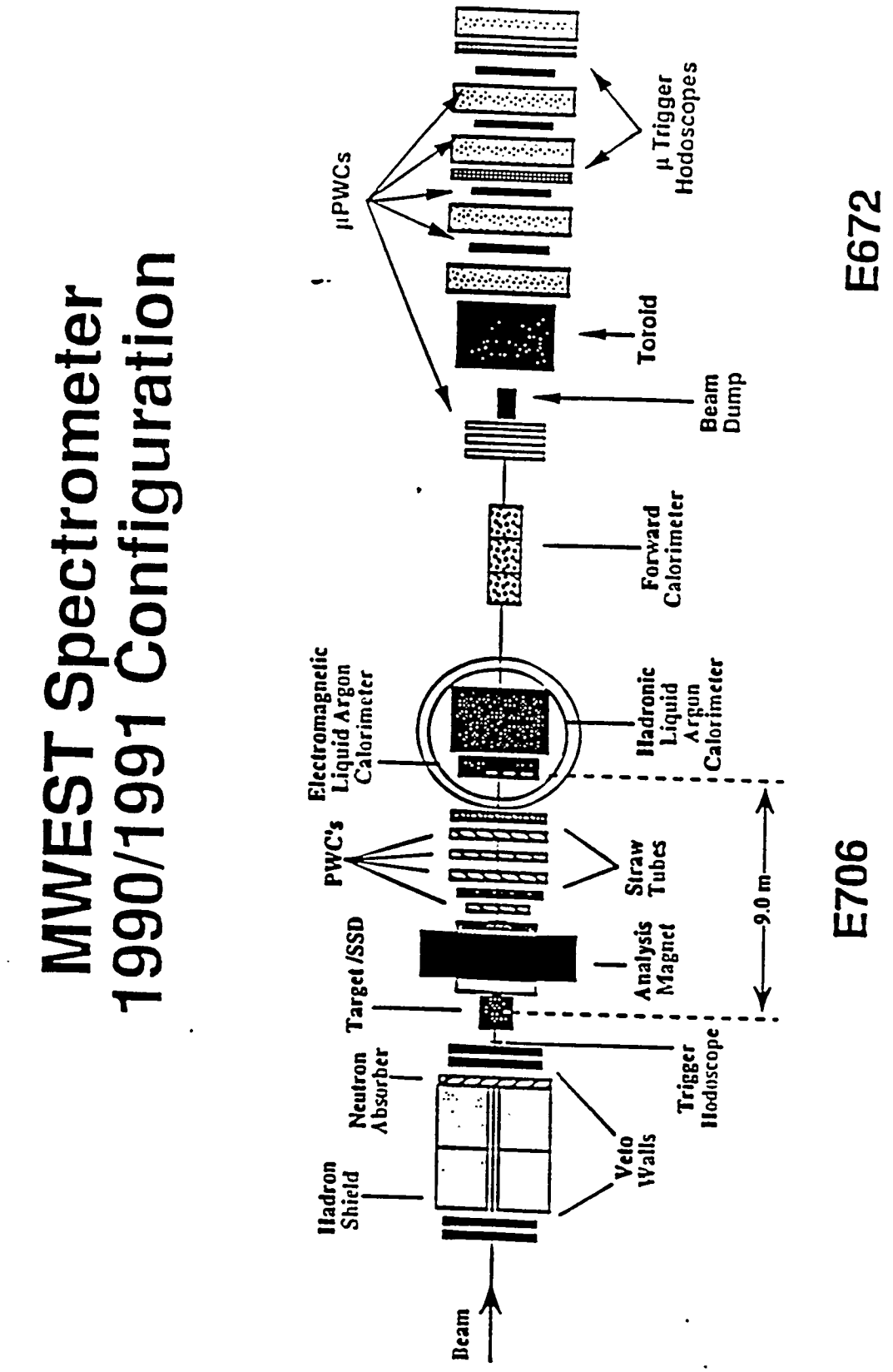

Figure 1: A Plan View of the E706 Spectrometer. Downstream of the E706 spectrometer is the E672 apparatus.

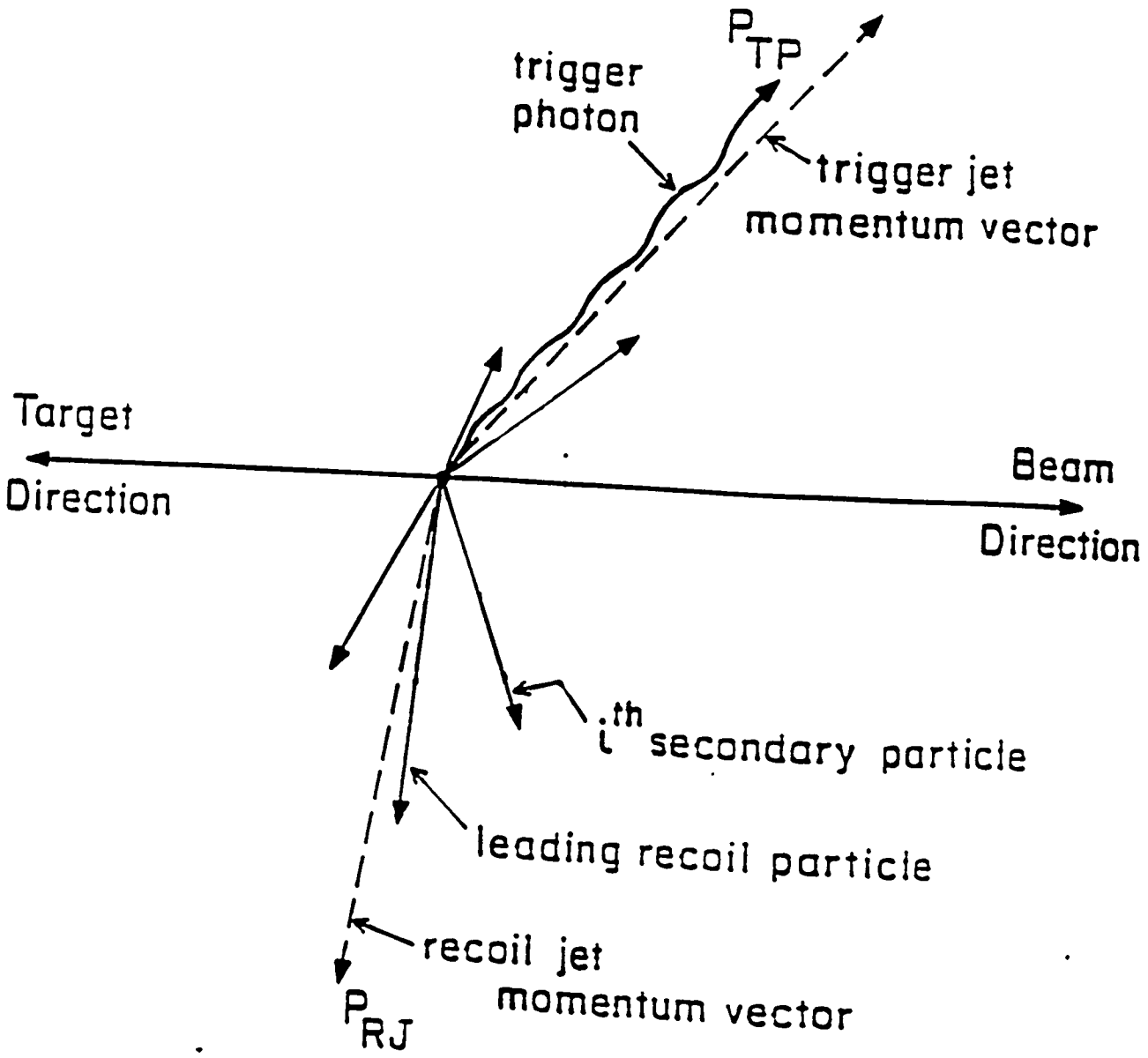

Figure 2: A sketch of a γ + jet event in the center-of-mass system of the interacting hadrons.

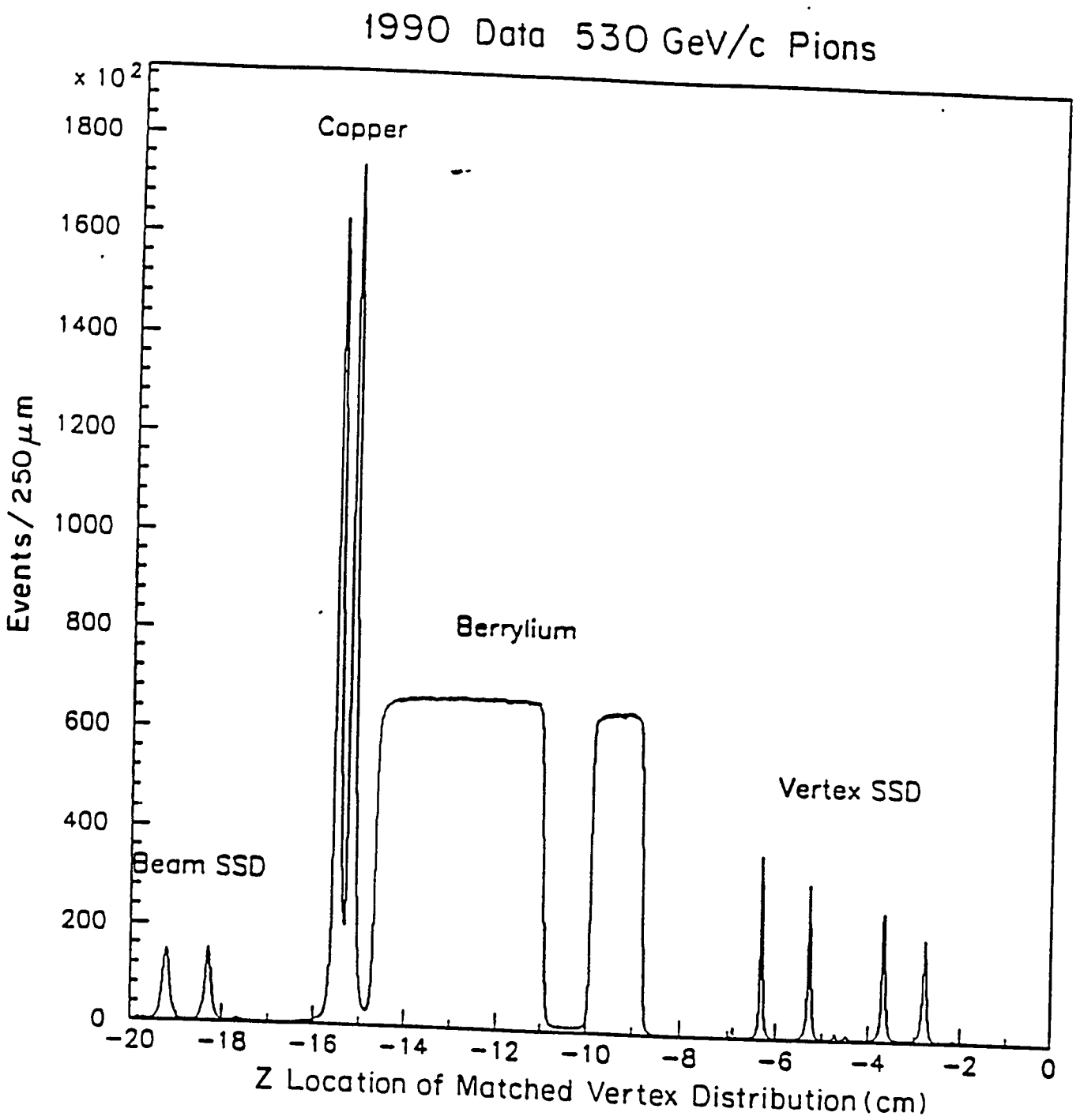

Figure 3: A plot of the vertex distribution along the beam line of the events produced in the target region during the 1990 data run.

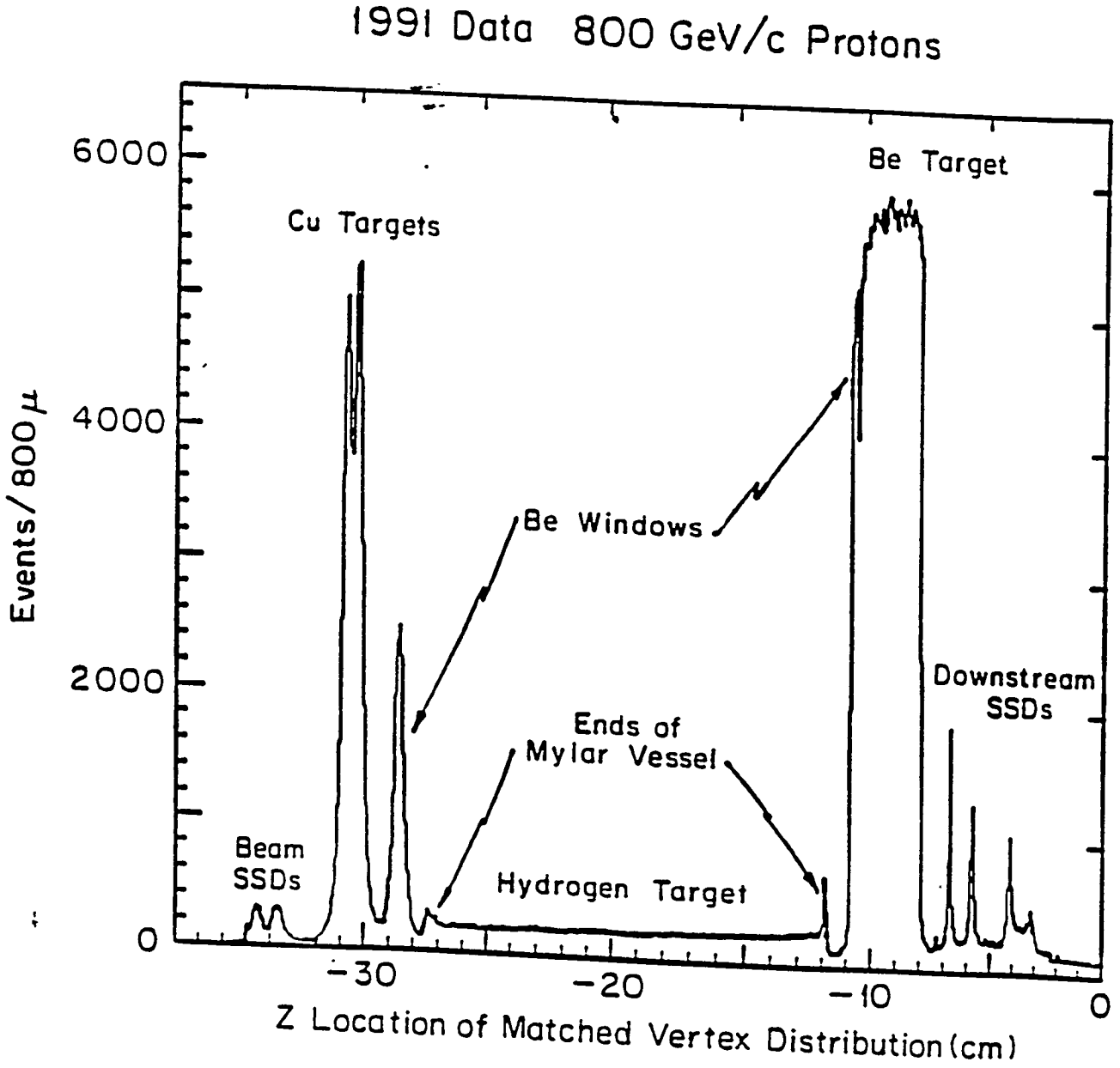

Figure 4: A plot of the vertex distribution along the beam line of the events produced in the target region during the 1991 data run.

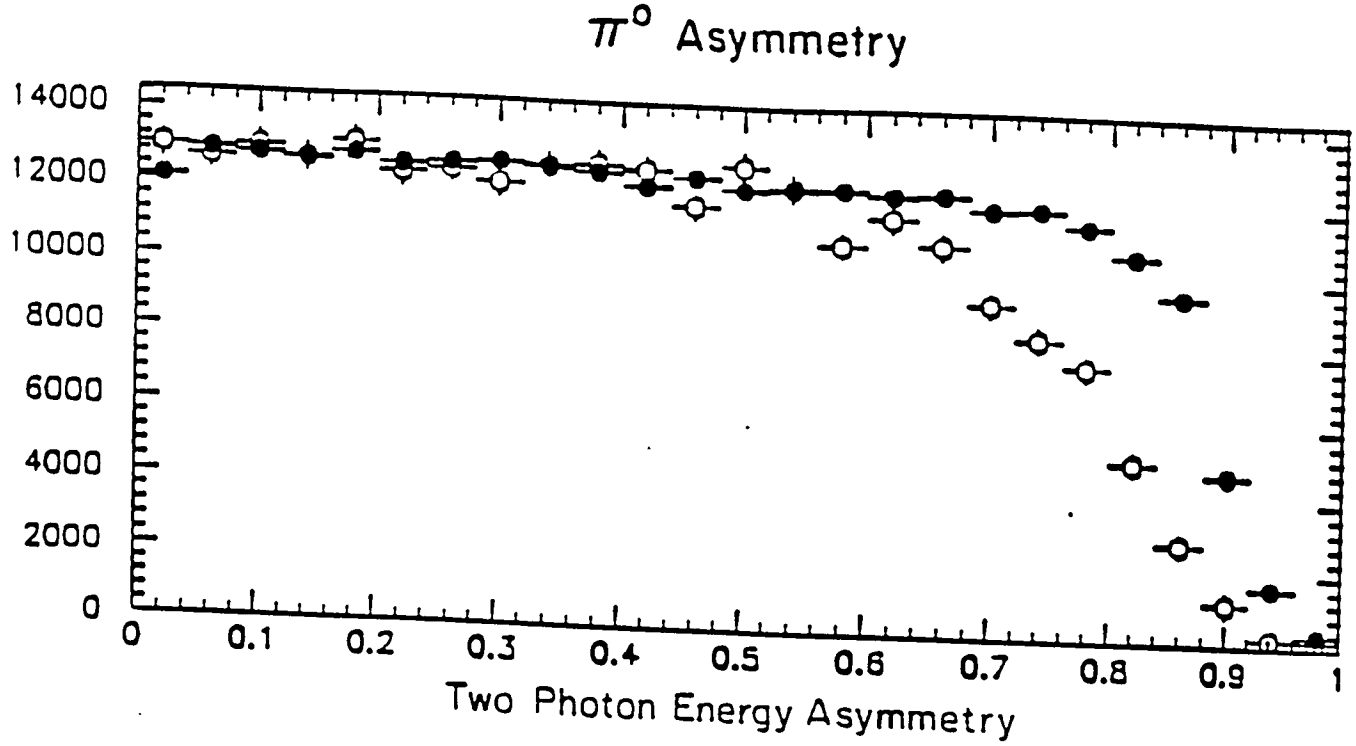

Figure 5: Number of events vs. the energy asymmetry of the 2 γ's from π^0 decay. The open circles show the 1987-88 data while the solid circles show the 1990-91 data.

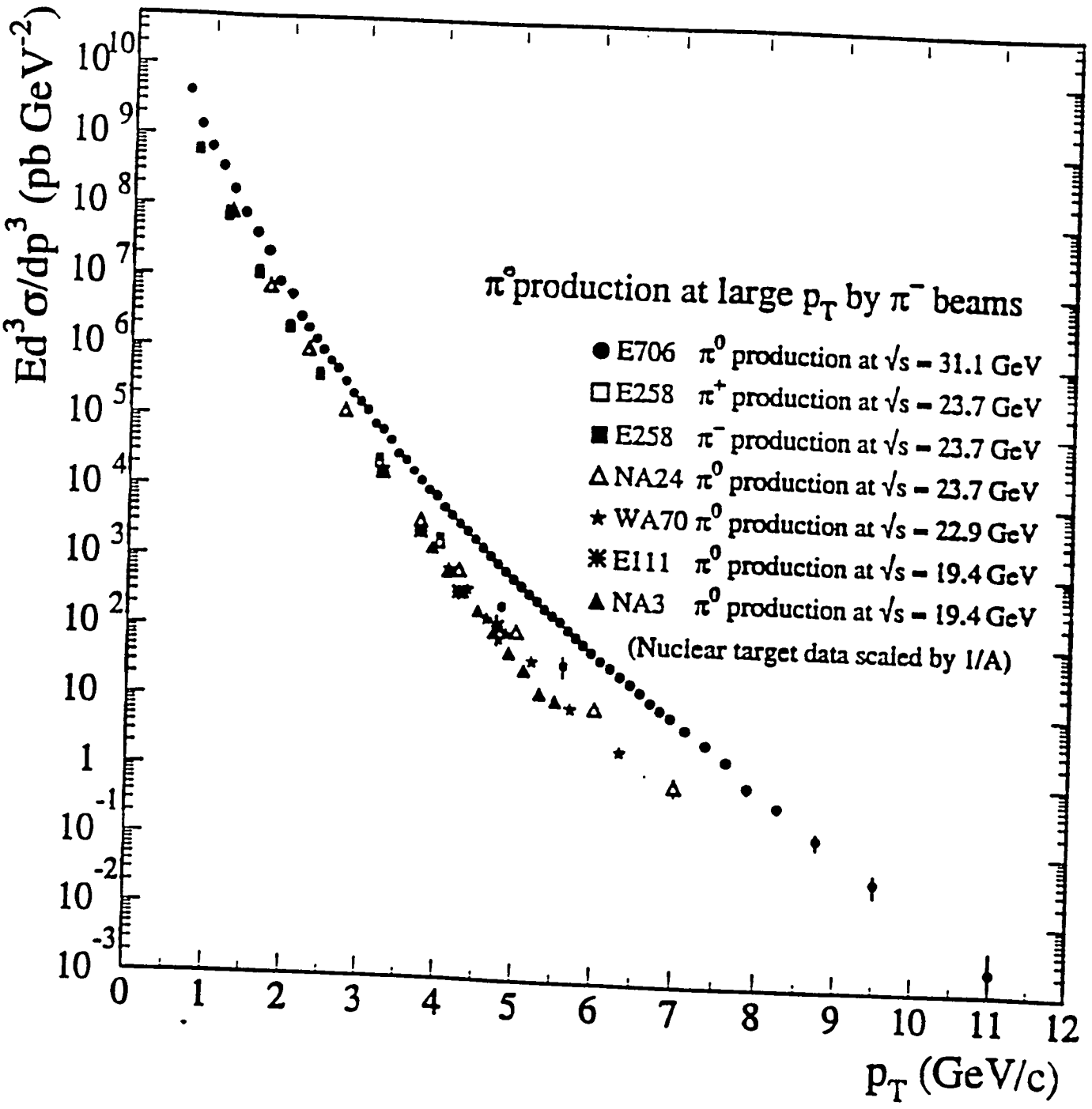

Figure 6: Inclusive π^0 production cross section plotted as a function of p_t of the π^0. The data are compared with previous experiments at comparable center-of-mass energies.

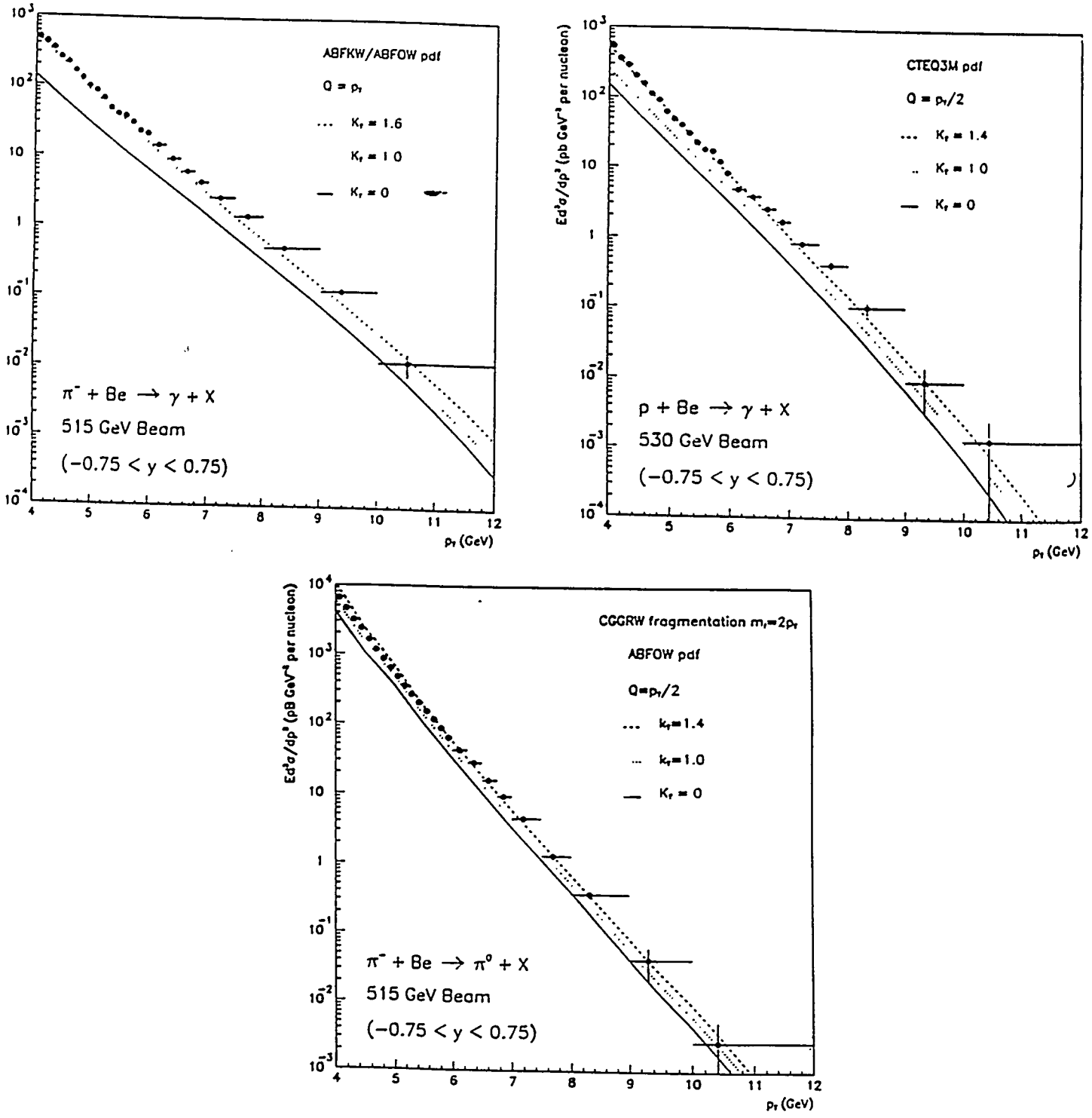

Figure 7: A comparison of the inclusive γ and π^0 production data with QCD calculations. Shown on each figure are three curves corresponding to three choices of k_t and the choice of scale indicated.

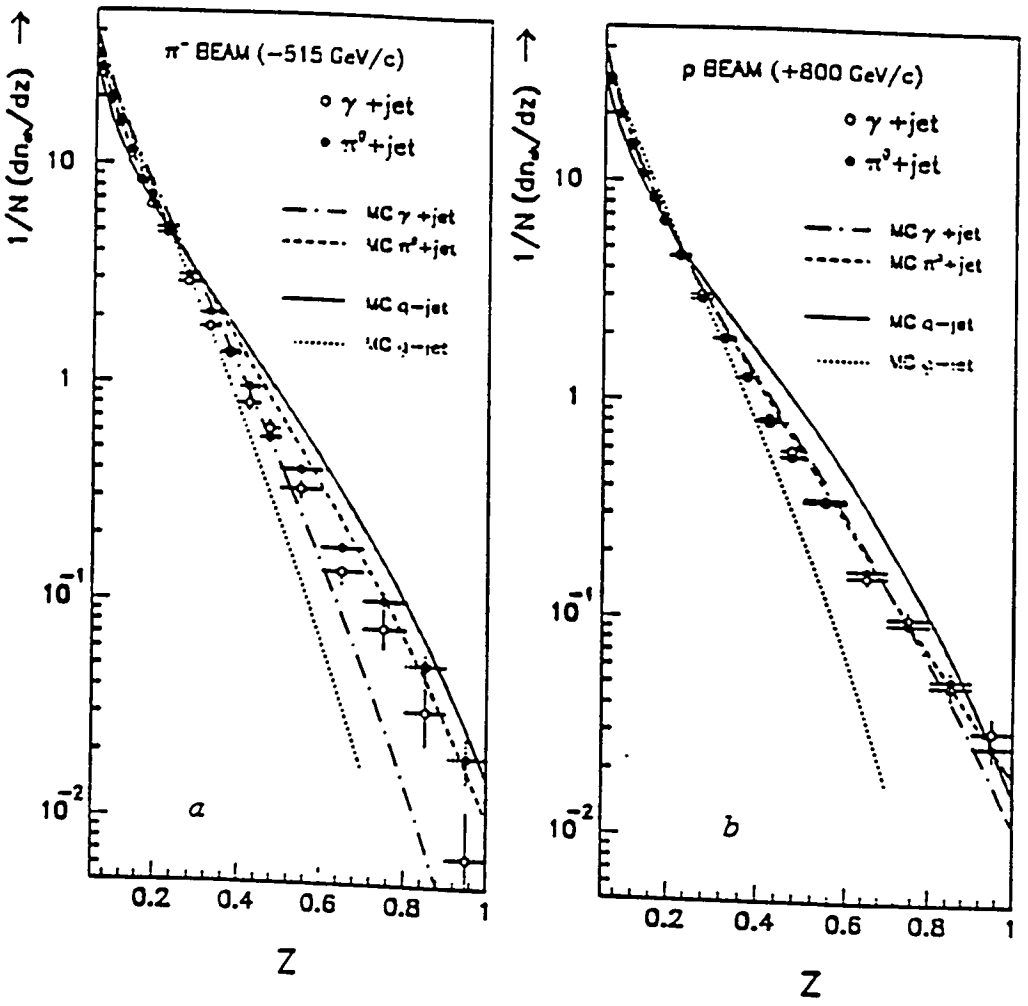

Figure 8: The jet fragmentation functions for π^0 + jet and γ + jet using a) a 515 GeV/c π^- beam and b) an 800 GeV/c proton beam. The data are compared with fully detector-simulated Monte Carlo data.

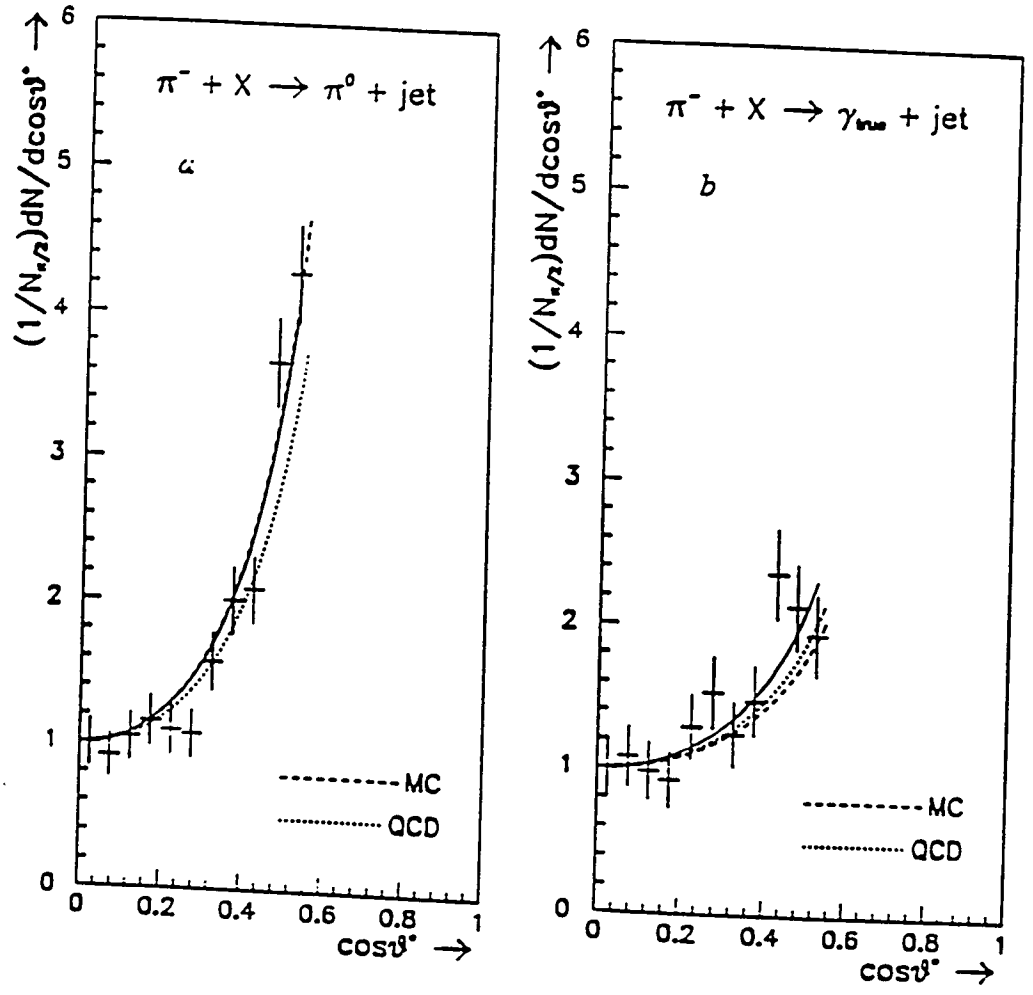

Figure 9: Plot of number of events vs. $\cos\theta^*$ for γ + jet and π^0 + jet events.

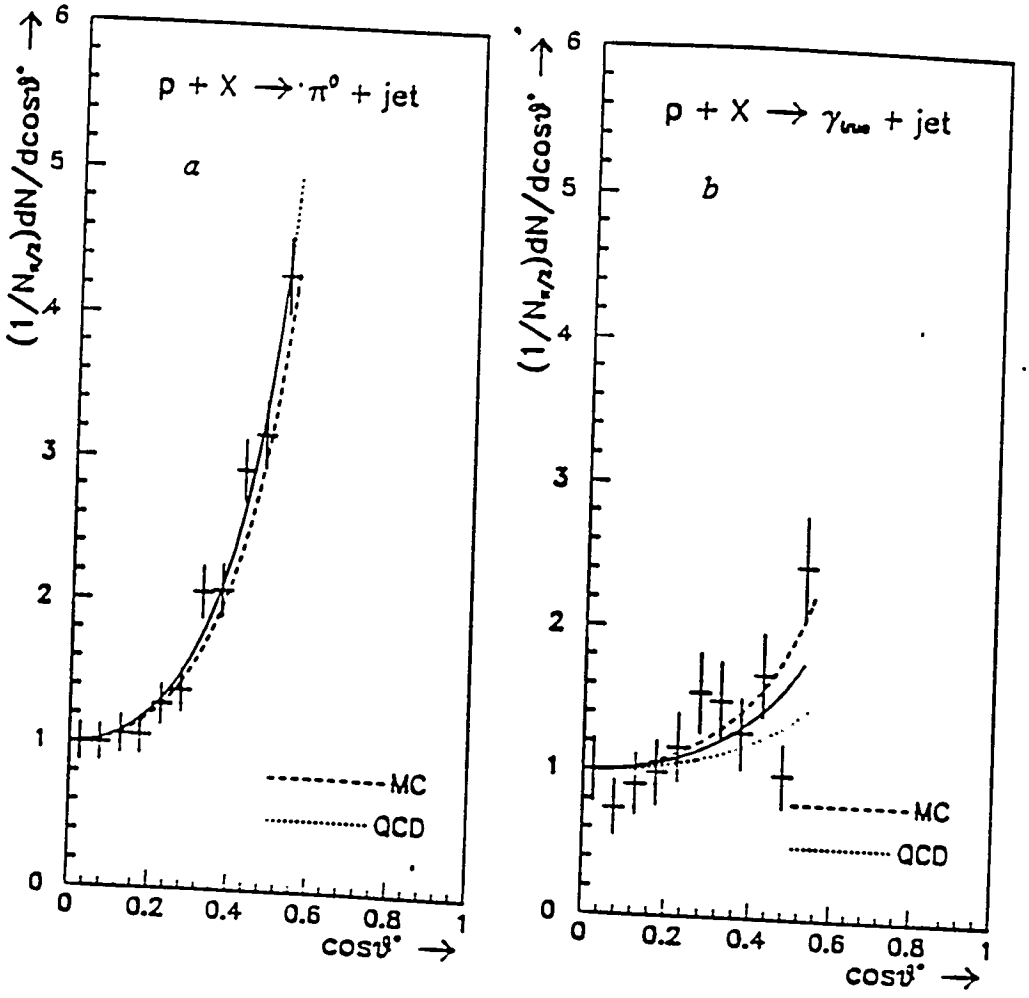

Figure 10: $cos(\theta^*)$ plots of a) π^0 + jet and b) γ + jet events using an 800 GeV/c proton beam. Comparison is made between data and QCD predictions and also with fully detector-simulated Monte Carlo results. The γ + jet data are background subtracted.

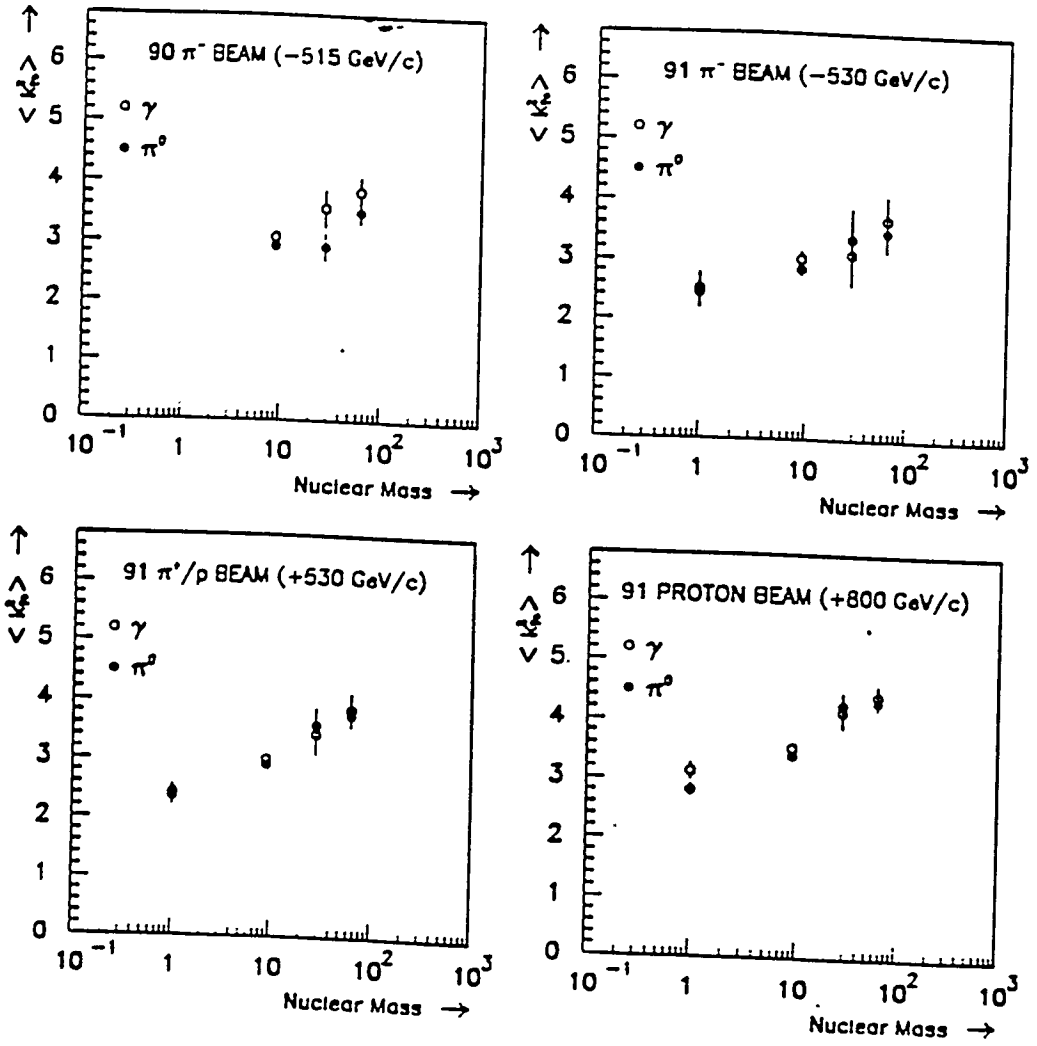

Figure 11: $\langle k_{to}^2 \rangle$ as a function of atomic mass for π^0 + jet and γ + jet events produced with various beam types and beam energies. Be, Cu and Si were used as targets in the 1990 data run and liquid hydrogen was added in the 1991 data run.

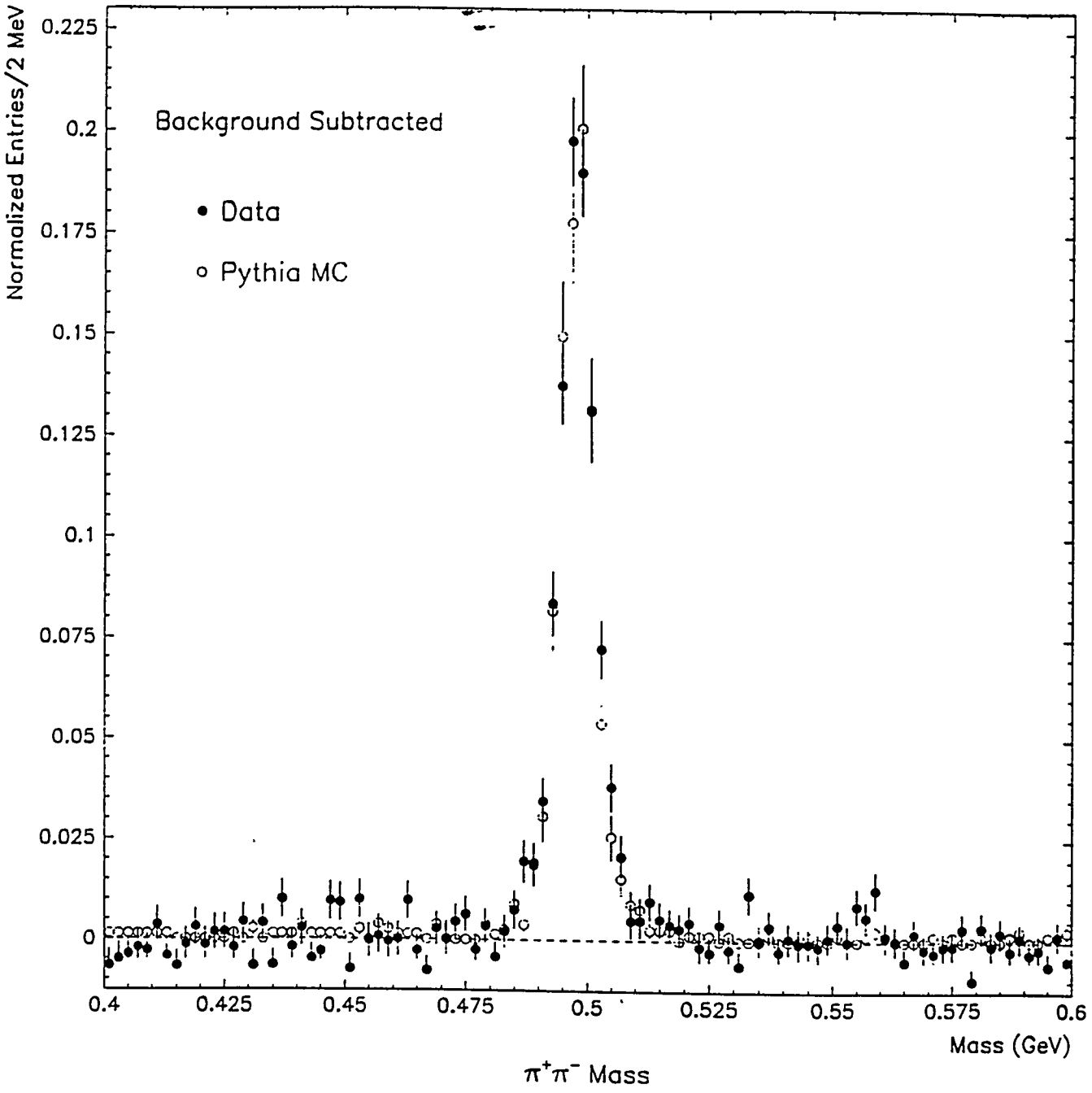

Figure 12: $\pi^+\pi^-$ mass plot for secondary vertices originating in the SSD system. The peak of the curve appears at the K^0_S mass. Also shown is a Monte Carlo simulation of the data.

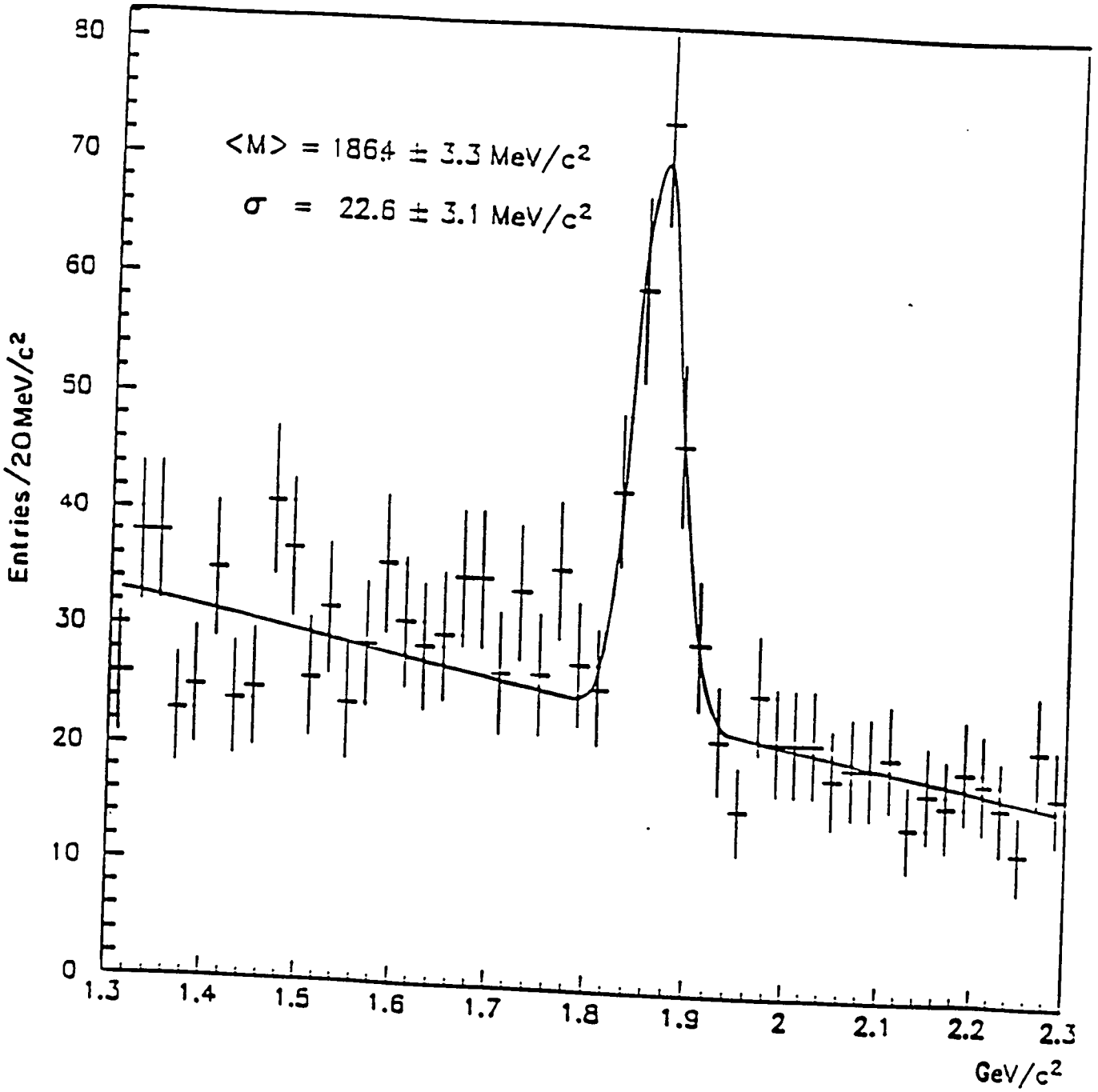

Figure 13: Mass plot of three-track secondary vertices, showing the decay $D^+ \to K\pi\pi$.

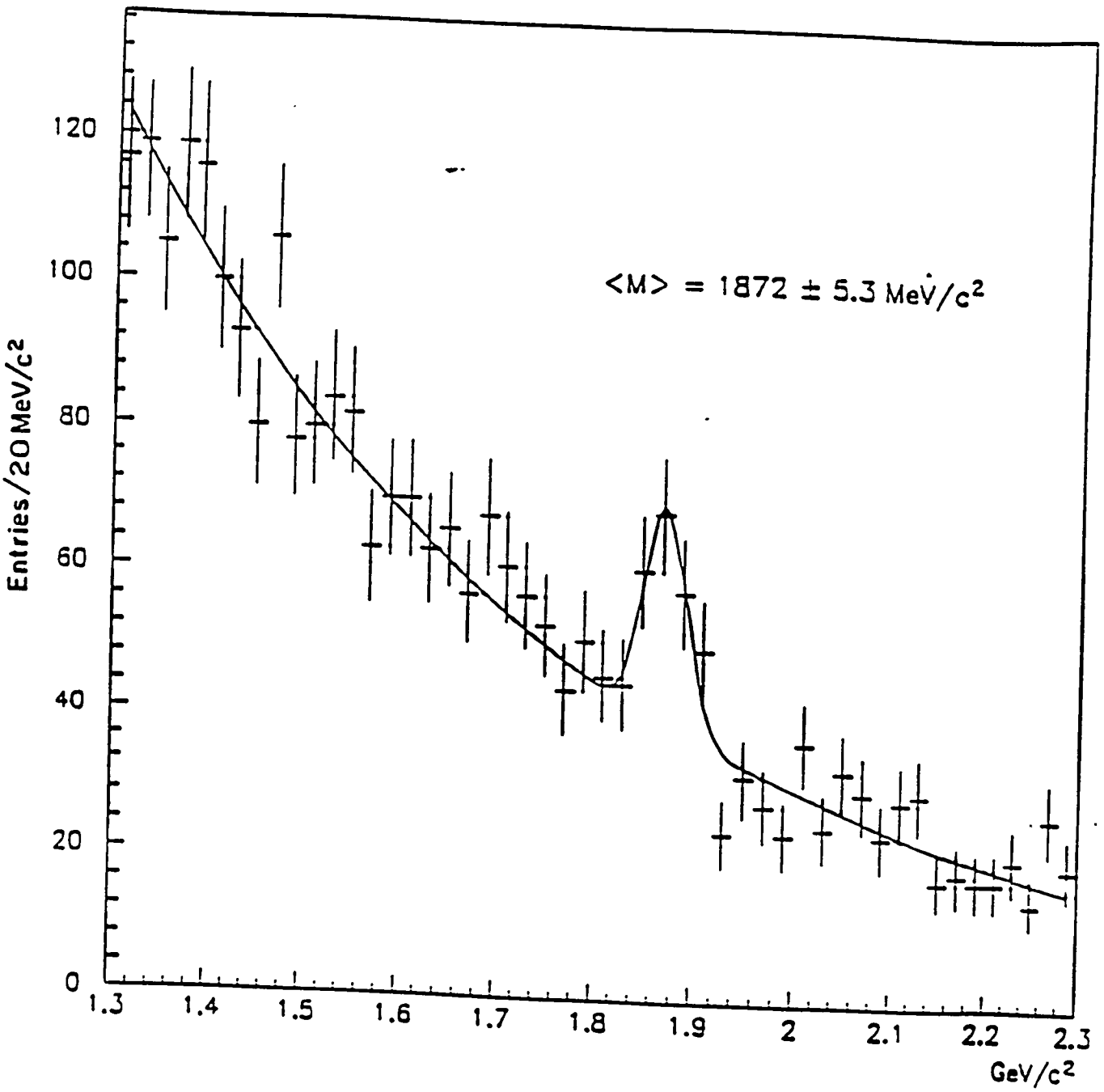

Figure 14: Mass plot of two track secondary vertices showing the decay $D^0 \to K\pi$.

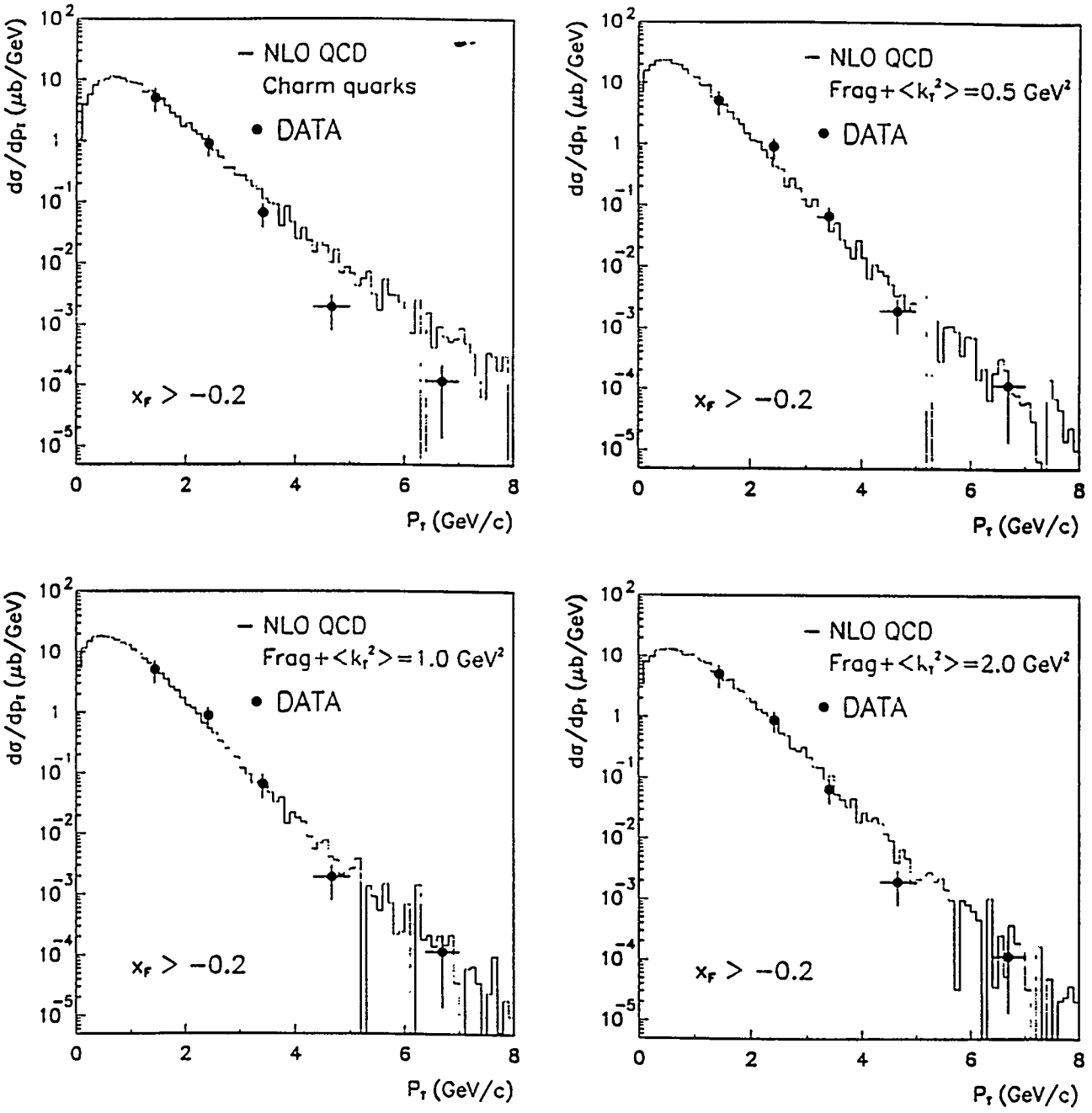

Figure 15: A comparison of the $D^{\pm}$ differential production cross section per nucleon and NLO calculations. Input to the calculations include a Peterson fragmentation function and a range of values of $< k_T^2 >$

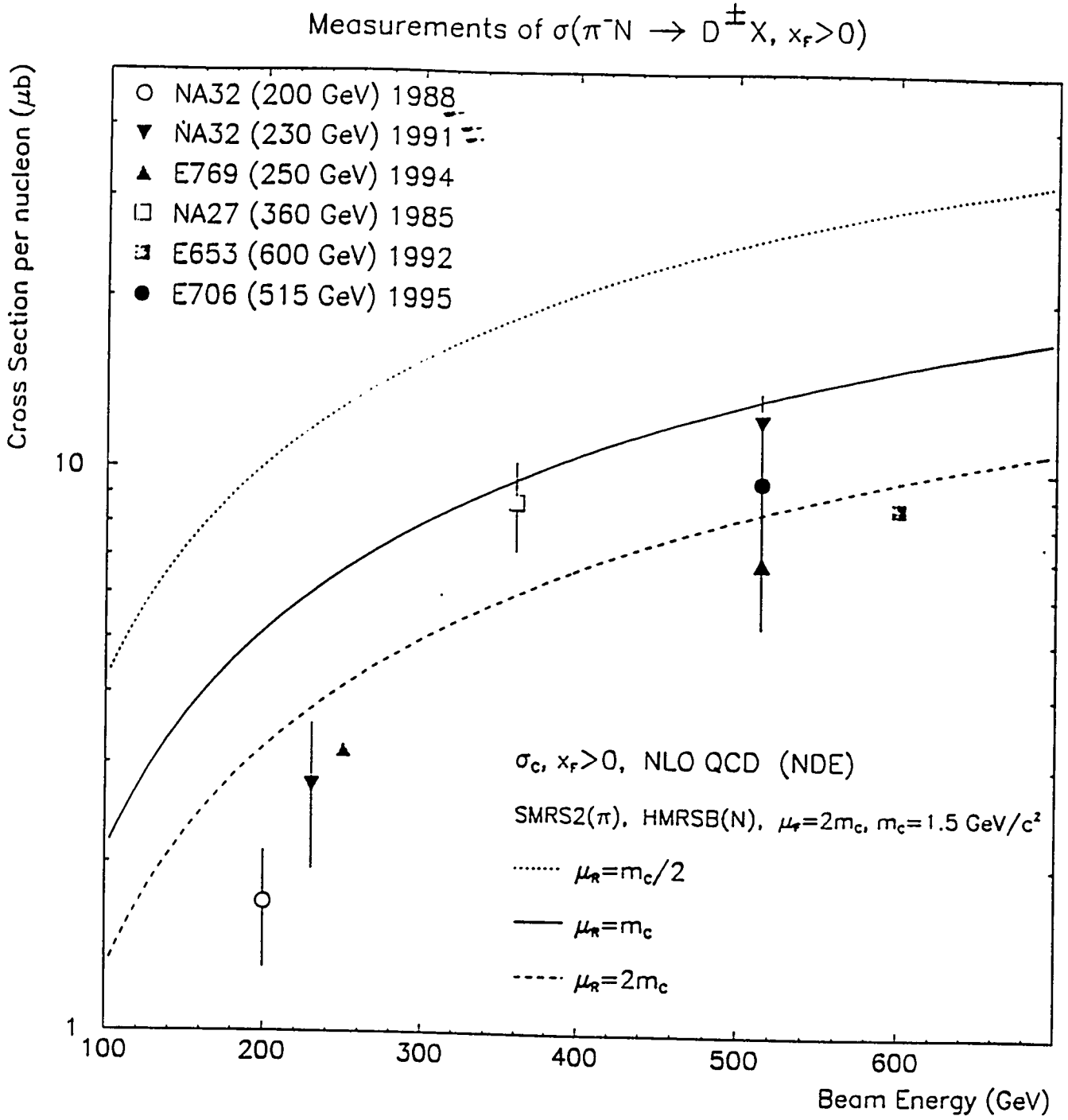

Figure 16: The total cross section for $D^{\pm}$ production per nucleon compared with other recent experimental results. Also shown is the NLO prediction using appropriate parton distribution functions for the incident pion and target nucleon.

3 CDF - $p\overline{p}$ Collisions at 1.8 TeV

During the past year the group from the University of Pittsburgh working on CDF has consisted of Joseph Boudreau, Eugene Engels, Todd Huffman, Richard Rosati, Prem Singh, Paul Shepard, and Stephan VandenBrink. Dr. Boudreau is a relatively new arrival having come to the University of Pittsburgh as an Assistant Professor in January, 1994. Our activities over the course of the past year have included the following topics:

- Monitoring of pedestals, gains, thresholds and leakage currents for the SVX′ detector during Run Ib and Run Ic data taking. (Prem Singh)
- Co-coordinator of the SVX II upgrade project. (Shepard)
- Development of the baseline design for the SVX II detector subsequent to its receiving stage I approval in May, 1993. Redesign of the SVX II to accommodate a fifth layer.(all)
- Design studies and prototype work for the SVX II data acquisition system. (Shepard, Huffman)
- Continued development and use of a special purpose SVX2/3 test station (Huffman, Shepard)
- Continued development of VME based DAQ test stand (Huffman, Shepard)
- Assembly of test stand modules including test portcards and test fiber interface boards. (Boudreau, Rosati, Shepard)
- Software development. (Boudreau)
- Analysis of test beam data for prototype SVX II detectors. (Boudreau)
- Analysis of CDF Run I data. (all)
- Maintenance of HV monitoring for the CDF detector. (Todd Huffman)
- Run Ib ACE. (Stephan VandenBrink)

3.1 The SVX′ Detector

Because the SVX detector which was installed in the B0 collision hall for the 1992 collider run (run Ia) was too radiation soft to last for both run Ia and Ib, it was replaced with a radiation hard detector, SVX′. Our group worked on the evaluation of critical features of the AC-coupled detectors from Micron Semiconductor which were used for this upgrade. [11, 12] One of our graduate students, Prem Singh, has worked full time on the construction and the installation of the silicon vertex detector upgrade, SVX′. He was responsible for the mechanical construction and inspection of the SVX′ ladders and the barrels. He also

participated in the electrical testing of the ladders and the barrels. Once the SVX′ detector was built, he was involved in installing the VTX-SVX′ module in the CTC. During the Run I data taking which has just ended he was responsible for monitoring the pedestals, gains, thresholds and leakage currents of the SVX′ detector.

3.2 SVX II Upgrade - Overview

During the past year the University of Pittsburgh has continued a leading role within the CDF collaboration in the development of the SVX II detector for run II. At the present time the project is being co-led by Paul Shepard from the University of Pittsburgh along with Jeff Spalding from Fermilab. In January, 1993 the SVX II upgrade proposal was given to the laboratory and considered by the PAC at their February, 1993 meeting. [13] It received stage I approval by the Fermilab director in May, 1993. In January, 1995 the scope of the project was expanded to include a 5th layer and a redesign of the readout chip.

The accumulated CDF data make it clear that high resolution vertex detection is a key tracking component in the CDF program of high p_T physics, specifically the top search, and b physics. The planned increase in the number of p and $\overline{p}$ bunches in the accelerator by 1999, and the resulting shorter bunch spacing (132 ns or 395 ns) requires a replacement for the SVX and SVX′ detectors.

The design goals for the SVX II upgrade are:

1. Accommodate improvements to the accelerator which necessitate replacement of the SVX′, specifically shorter inter-bunch spacing and higher radiation levels. This is required for Run II which is the first run with the reduced bunch spacing.
2. Improve performance for vertex detection in high p_T physics, in particular to tag b decay vertices in top events.
3. Enhance the b physics capabilities of the present detector.
4. Provide a detector and electronic readout capable of supporting a Level 2 vertex trigger processor.

The principal features of the SVX II barrel detector at the time we received stage I approval are given below:

- A set of three barrels which approximately double the length of the present SVX.
- Four layers of double-sided detectors with 90 degree stereo. The proposed detectors 7-bit analog to digital conversion should attain a resolution of $\approx 10\mu$m in r-ϕ and $\approx 25\mu$m in r-z.
- A pipelined readout chip which will support operation at either 395 ns or 132 ns between beam crossings.

- High speed digitization and readout of the SVX II analog data in $\approx 10\mu s$ in response to a Level 1 trigger. The high speed of the readout is required in order to use the SVX II data in a Level 2 vertex trigger processor.

- Support for a Level 2 microvertex trigger processor (SVT). [14] This is a separate project which is being developed by the CDF collaboration. The ability to trigger on the impact parameters of reconstructed tracks will greatly extend the physics capabilities of the CDF detector.

- A new data acquisition system (DAQ) employing a highly parallel fibre optic readout and control utilizing low power optic drivers and receivers.

We expect the top physics program and other high p_T physics topics to be helped by increasing the length of the vertex detector in order to improve coverage of the luminous region in z at the interaction point. Doubling the length and adding z information will increase the b tag efficiency for top events by a factor of 1.6 to 2.0 In combination with an increase in luminosity, this increased efficiency gives a dramatic improvement to the overall physics capabilities of the detector.

The capability of using impact parameter information obtained from a vertex detector in the level 2 trigger to select events with secondary vertices will be of fundamental importance for any experimental program of b physics in a hadron collider environment. Having an impact parameter trigger implemented for SVX II will significantly increase the size of the b sample on tape. The experience gained in installing and running this trigger will help us to design more ambitious triggering systems in the future.

Since receiving stage I approval both the collaboration and the laboratory have reassessed the scope of the SVX II project. First, the design luminosity of the main injector upgrade has been re-evaluated upward to a starting luminosity of 10^{32} $cm^{-1}sec^{-1}$. Second, the required Level 1 trigger rates in Run II are now projected to be 50 kHz rather than 5 kHz. The response to these challenges was as follows:

1. A decision to redesign the 4-layer SVX II to accommodate 5-layers with 2-layers of small angle stereo to permit stand-alone tracking.

2. A decision to add an intermediate tracking system built on a scintillating fiber technology.

3. A decision to redesign the pipelined readout chip to accommodate both a longer pipeline and simultaneous data acquisition, digitization and readout. This last change will permit the SVX II detector to run with a small deadtime with Level 1 trigger rates as large as 50 kHz.

All of these decisions were tentatively made at a Fermilab Director's review of the CDF upgrades in January, 1995. The SVX II upgrade group is responsible for implementing both

the 5-layer SVX II and the deadtimeless readout which is being designed as a two chip set. Subsequently in June, 1995 these decisions were confirmed and a decision was also made to replace the CDF central tracker (CTC). At first it appeared that the choice for a new tracker would be straw tubes. However, after extensive technical and cost review, the collaboration has decided to use an open cell geometry similar to the present CTC, but with smaller cells so as to accommodate the higher luminosity expected in Run II. During the past year considerable effort has been made to incorporate the changes in scope in the SVX II project into the overall project plan.

The decision to replace the SVX2 chip (already far advanced in its development) with the deadtimeless SVX3 chip set is the most critical change, and carries a significant risk of delaying the overall completion of the upgrade.

3.3 SVX II Design/R&D

The baseline design for a 4-layer SVX II detector with some exceptions was completed in 1994. The decision to add a 5th layer has reopened the design process to some extent. During the past year this redesign has been accomplished, and we discuss the salient features below.

Mechanical

The initial 4-layer design consisted of 4 double-sided silicon layers with 0-90° stereo. The new design consists of three 0-90° layers and two small angle (1.2°) stereo layers. Layers 0,1 and 3 will be 0-90° and Layers 2 and 4 are small angle. Table 2 shows the parameters for the new 5-layer system. For comparison the parameters for the SVX′ are also included. A cross section of the bulkhead region of one of the barrels is shown in Fig. 17. Table 3 shows the radial locations of the numbered indicators in Fig. 17.

The ladders for all of the layers consist of four silicon detectors each with an active length of 7.24 cm in length mounted end to end and supported by a carbon fiber re-enforced rohacell support. The signals from the detectors are readout at both ends of the ladders so a ladder consists of two electrical units each composed of two silicon detectors. Since the silicon detectors are double-sided (r-ϕ and r-z for 0-90° stereo or r-ϕ and r-ϕ' for small angle stereo), there is a multilayer hybrid circuit assembly on both sides of the ladder ends to connect and support the fully integrated CMOS readout chips. The hybrid is inboard to the ends of the ladder and located on the silicon detector faces in order to minimize the gaps between the barrels.

Three dimensional perspective views of the r-ϕ and r-z sides of a Layer 0 ladder are shown in the left and right hand plots of Fig. 18, respectively. In every case the r-ϕ side of the silicon detectors is on the side away from the beam (outside). Both the bulkhead and ladder designs are the outgrowth of detailed cooling model studies and finite element analysis. In addition to theoretical studies, actual models were made and measured. [15, 16, 17, 18] Given the significant heat load of the readout chips (approximately 400 mW per chip) an integrated design of the SVX II ladder has been a challenging problem.

Detector Parameter	SVX′	SVX II
Readout coordinates	r-ϕ	r-ϕ; r-z
Number of barrels	2	3
Number of layers per barrel	4	5
Number of wedges per barrel	12	12
Ladder length	25.5 cm	29.0 cm
Combined barrel length	51.0 cm	87.0 cm
Layer geometry	3° tilt	staggered radii
Radius innermost layer	3.0 cm	2.44 cm
Radius outermost layer	7.8 cm	10.6 cm
r-ϕ readout pitch	60:60:60:55 mm	60:62:60:60:65 mm
r-z readout pitch	absent	141:125.5:60:141:65 mm
Length of readout channel (r-ϕ)	25.5 cm	14.5 cm
r-ϕ readout chips per ladder	2:3:4:6	4:6:10:12:14
r-z readout chips per ladder	absent	4:6:10:8:14
r-ϕ readout channels	46,080	211,968
r-z readout channels	absent	193,536
Total number of channels	46,080	405,504
Total number of readout chips	360	3168
Total number of detectors	288	720
Total number of ladders	96	180

Table 2: Comparison of SVX′ and 5-layer SVX II.

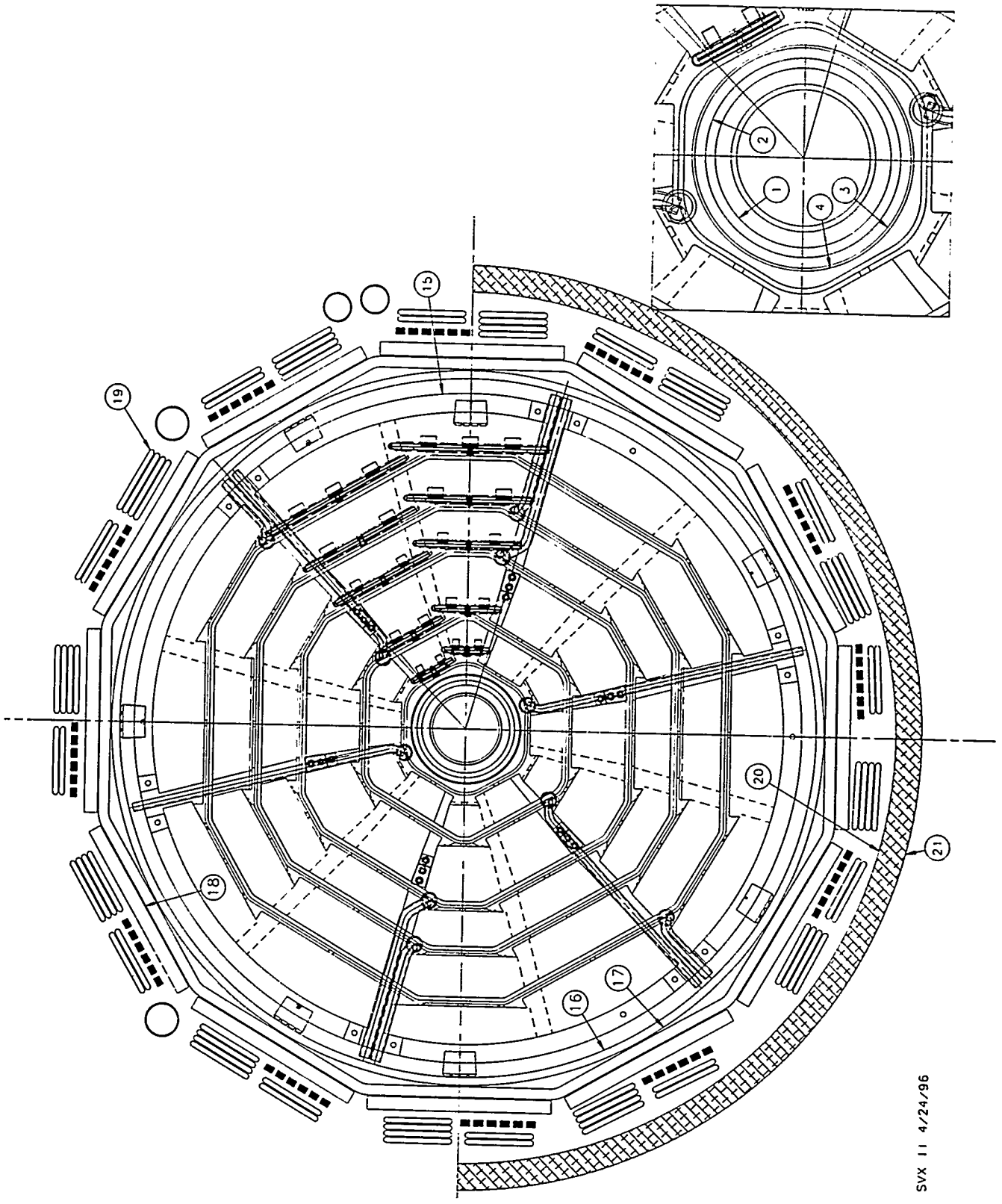

Figure 17: The SVX II bulkhead design

	Description	R (cm)
1	Beam pipe outer radius	1.6700
2	Beam pipe flange outer radius	1.8542
3	Inner screen inner radius	2.0500
4	Bulkhead inner radius	2.1000
5	Layer 0a *	2.5450
6	Layer 0b	2.9950
7	Layer 1a	4.1200
8	Layer 1b	4.5700
9	Layer 2a	6.5200
10	Layer 2b	7.0200
11	Layer 3a	8.2200
12	Layer 3b	8.7200
13	Layer 4a	10.0950
14	Layer 4b	10.6450
15	Bulkhead outer radius	12.9000
16	Outer screen inner radius	12.9000
17	Outer screen outer radius	13.2500
18	Port card inner radius	14.1000
19	Cables	16.1000
20	Half cylinder inner radius	16.3000
21	Half cylinder outer radius	17.3000
	IFT inner radius (not shown)	19.5000

* All layer radii are relative to center of silicon.

Table 3: SVX II Bulkhead Information

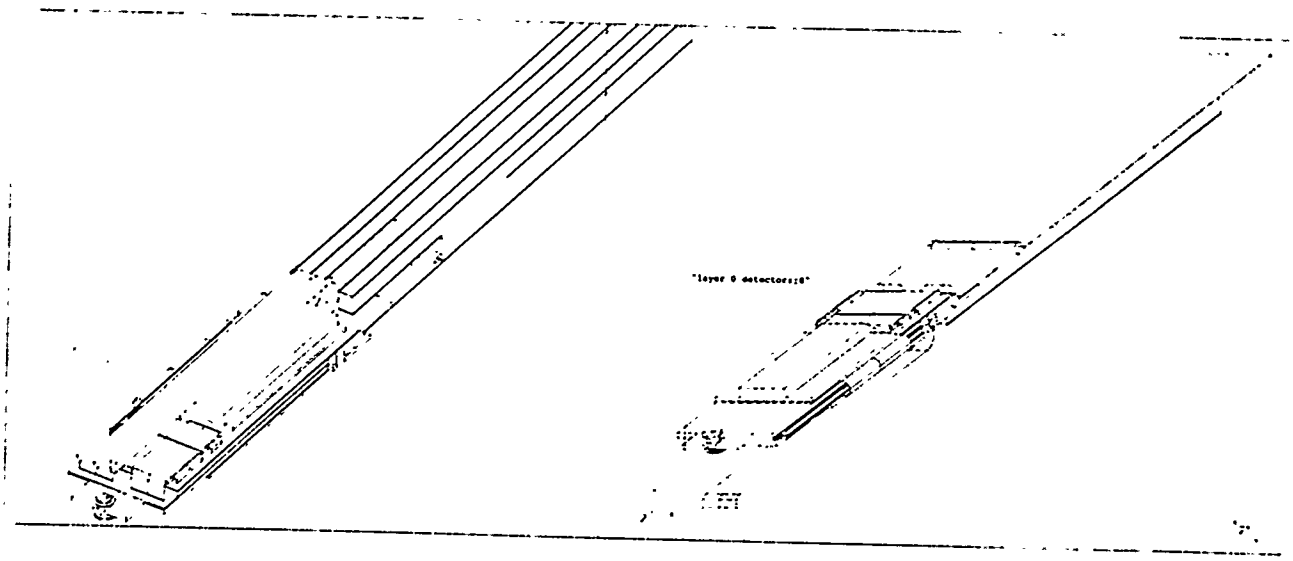

Figure 18: Three dimensional perspective views of the r-ϕ and r-z sides of a Layer 0 ladder are shown in the left and right hand plots, respectively.

Detectors

Prototype double-sided detectors from SI, Micron, and Hamamatsu have now been extensively studied in two beam tests at KEK and two radiation exposures at Triumf. [19, 20, 21, 22, 23, 24, 25] [26, 27, 28] Since our last report, there has been both a second radiation exposure at Triumf and a second beam test at KEK. Joe Boudreau made major contributions to the analysis of the data from both beam tests at KEK and his work is discussed in Section 3.6.1. Based on this extensive detector R&D program, the entire production quantity of both small angle and double-metal detectors has been specified, bid, and contracts awarded. Hamamatsu is the vendor for Layers 0, 1, and 3 which are the 0-90° stereo double-sided double-metal detectors, and Micron is the vendor for Layers 2 and 4, the small angle stereo double-sided detectors.

DAQ

A simplified schematic of the design of the SVX II DAQ is shown in Fig. 19. The original design for the DAQ used the SVX2 chip. Because the SVX2 chip has a single ported pipeline and incurs deadtime for every level 1 accept, we have changed the design to utilize the SVX3 chip set which is essentially deadtimeless. This change has been motivated because we would like to use the SVX II detector with Level 1 accept rates of 50 kHz, and also be compatible with the overall CDF electronics upgrade which is deadtimeless. Starting officially in January, 1995 (actually earlier), extensive work was begun on the development of the SVX3 chip set.

Both the SVX2 or 3 chips are capable of very rapid digitization and readout of their analog data. After receiving a Level 1 trigger the chip digitizes the analog data in the corresponding pipeline cell. One can select either 7 or 8 bit accuracy which corresponds to digitization times of 1.2 μs and 2.4 μs respectively. This time is independent of the number of hit channels because all of the channels are digitized in parallel. Once digitization is complete the digital information is readout over an 8 bit parallel bus at a speed of 53 Mbytes/s. For a 10 chip bus with an average occupancy of 7% this takes 3.4 μs. The occupancy is expected to be higher in the r-z chips and for this reason they will be readout after the r-ϕ chips in order that the data can be presented to the SVT trigger processor in the minimum time.

For each wedge there will be 5 high density interconnects (HDI's), one for each layer. These 5 buses will control and readout the 44 SVX3 chip sets in each wedge. In addition to power and ground each HDI carries the control signals and the data lines from the portcard (PC). The PC's are located at the periphery of the detector as close as possible to the detector wedge which they control. Each PC will control the entire 44 chips of single wedge. The PC in turn is controlled from the fiber interface board (FIB) over a Cu control bus. The control signals from the FIB are decoded and sent on to the chips by the PC. Data from the chip are converted at the PC into light signals for transmission to the FIB. Each HDI drives a dense optical interface module (DOIM) consisting of a clock and 8 data lines. The data are transmitted at 53 MHz. Thus each DOIM transmitter makes an optical connection to a ribbon fiber consisting of 9 fibers which go to the FIB board. There are a total of 72 PC's, one for each wedge.

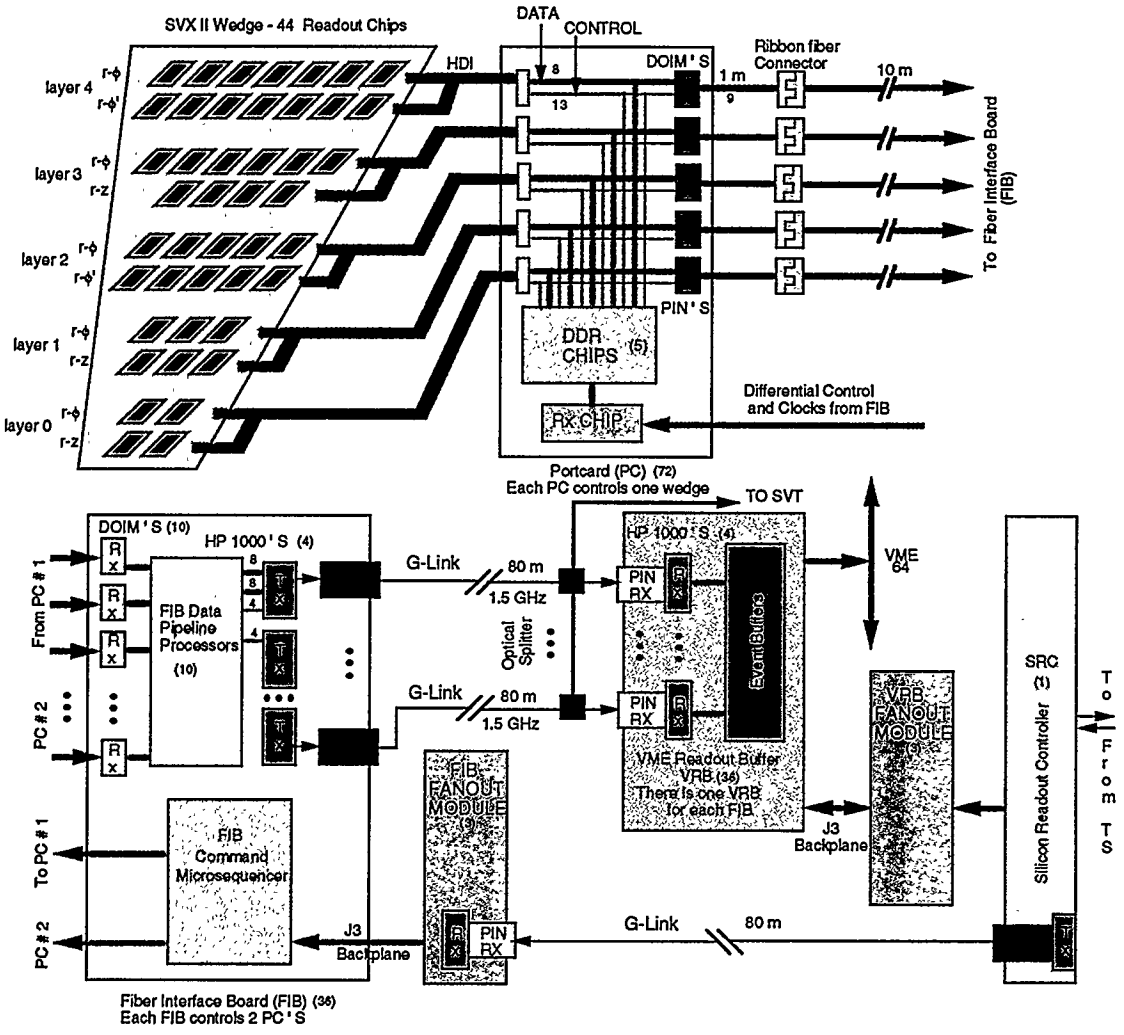

Figure 19: Simplified schematic design of the SVX II DAQ system.

The FIB's are located in 3 VME crates on the face of the CDF detector. We are presently planning to use 1 FIB's for every 2 PC's or 36 FIB's in all. The FIB's are controlled by the silicon readout controller (SRC) located in the B0 counting house over a high speed optical link. The SRC is responsible for the necessary communication with the CDF trigger supervisor (TS).

The data being readout from the detector is further multiplexed at the FIB. Five DOIM receivers are multiplexed by two HP1000 G-link transmitters and the 20 parallel lines for each transmitter are sent serially over a single fiber driven by a laser diode at approximately 20 x 53 = 1060 MHz. The G-link system is capable of serial transmission up to 1.5 GHz. At the VME readout board (VRB) the signals are received by an HP-1000 G-link receiver and demultiplexed. The design calls for 4 such receivers per VRB. The VRB board has two principal functions. First it serves as the port to pass the SVX II data to the SVT trigger processor. Second it provides the event buffering during the Level 2 trigger processing. If the event fails the Level 2 trigger, the buffer is cleared; and if it passes, it is then passed on to Level 3 over the VME backplane through the crate CPU.

To prove many of the features of this design a VME based test stand consisting of a test PC, test FIB and combined VRB-SRC (called a STAR) has been built. This test stand is now being used with the SVX2 chips. It was used in noise tests at Fermilab following the second radiation exposures at Triumf in April, 1995 and during the beam test at KEK last June. Ultimately about 12 of these test stands are planned to support component testing during the construction phase of the project. Our group at Pittsburgh has finished the assembly of the remaining test PC's and test FIB's during this past year. Modifications of these test stand components is presently in progress so that they can be used with the SVX3 chip set when it becomes available.

3.4 The SVX2 and SVX3 Integrated Circuits

Below we give an overview of the SVX2 and SVX3 chips and discuss the contributions the University of Pittsburgh is making to the design and testing of the SVX3 chip set.

SVX2

The design of the SVX2 and SVX3 chips are quite similar. A discussion of the main features of the SVX2 chip [29] will be followed by a discussion of the points making the SVX3 chip set different. Shown in Fig. 20 is a functional diagram of a single channel of the SVX2 readout chip.

The SVX2 readout chip is an integrating amplifier with a pipeline and in-situ digitization and data sparsification. Each chip has 127 channels. The integrating amplifier has an adjustable bandwidth so it can be optimized for the varying conditions of accelerator running (either 132ns or 396ns bunch spacing and input capacitances less than 30pf). The amplifier can be either inverting or non-inverting for use on either the N or the P side of a silicon detector and has a dynamic range of $\simeq$ 500fC (130 times minimum ionizing in 300μm of

silicon).

Also one wants to use as much of the time between beam crossings as possible for integration time. A large dynamic range is required because more than 1μs is needed to reset the preamplifier. So the pre-amplifier is only reset during the abort gaps of the accelerator and not between every beam crossing.

The difference in charge between the current beam crossing and the previous crossing is amplified again and placed on the pipeline capacitor. The pipeline length can be arbitrarily set up to the total number of cells. In the final system, it will be set to the equivalent Level 1 trigger formation time. This time is specified to be 4.1μs and will require 32 cells with an additional 10 cells added for contingency. When an accept from the trigger is received, data taking ceases and the correct cell is connected to the digitization and readout sections of the chip. When the chip is finished digitizing and reading out that cell, data taking resumes.

Digitization proceeds using a Wilkinson ADC. The voltage on the cell is compared to the voltage on a capacitor with a constant current source. The rise of the voltage on the current source will be linear. While this is happening a Grey Code counter is counting on both clock edges at a fixed rate. When the voltage on the ramp surpasses the voltage on the pipeline data cell, the comparator changes state. This latches the counter value into an asynchronous FIFO. The value is compared to a digitally downloaded threshold before latching, however, so the user can elect to only latch in channels above a threshold. CDF intends to digitize to 7 bits with a 53MHz clock. Thus it will require 1.25μs to digitize the data.

The data and channel numbers are held in their locations in the FIFO until digitization is complete. Then the FIFO is allowed to collapse. Collapse takes 600ns at which time readout can proceed. The chip is read out over an 8 bit bus. The user-defined chip ID is read out on the first high clock when the chip has priority. The low clock causes the status word to be presented on the bus. After this, every high clock presents the channel number and the low clock is the data associated with that channel number. When the last channel with data is clocked out, the chip will pass priority to the next chip which will present its chip ID.

Since the data is sparsified, the readout time is variable. Based on Monte Carlo simulations of data events along with additional minimum bias events we have determined that the detector occupancy should be dominated by real tracks and not noise hits. This has led us to a scheme where each layer of the SVX has its own bus.

SVX3 motivation

The SVX2 device described above has some problems in an environment where the trigger rate is greater than about 5KHz. As stated before, when the SVX2 chip receives a trigger, data taking must cease while digitization and readout commence. During this time events are being missed, so deadtime is incurred. Additionally, the trigger system as it is specified will not be able to recover events waiting in the pipeline. So an additional number of events equivalent to the Level 1 formation time are lost.

If the readout time is 5-6μs, and the Level 1 formation time is 4μs, then 10μs of deadtime

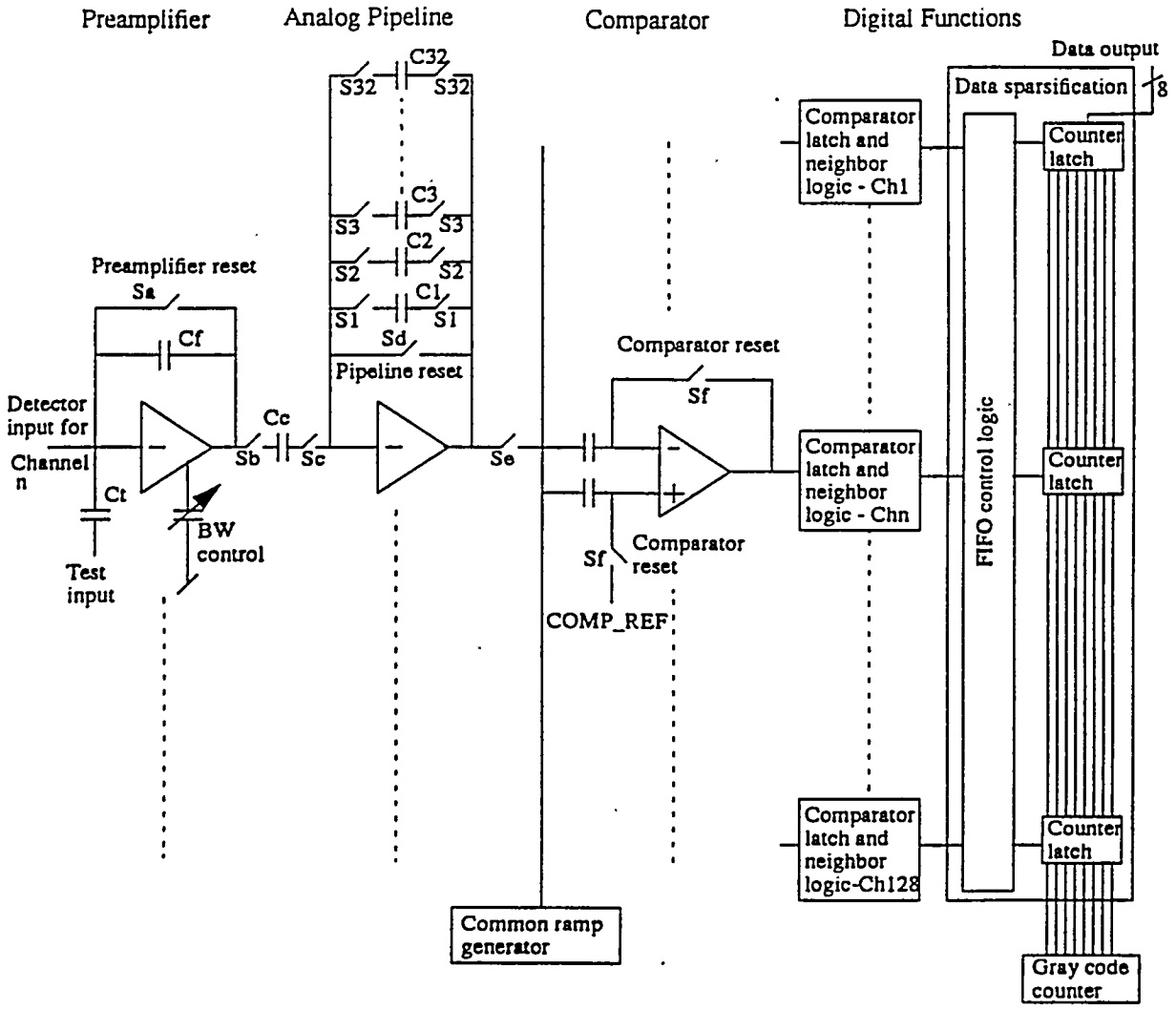

Figure 20: A functional block diagram of the SVX2 chip.

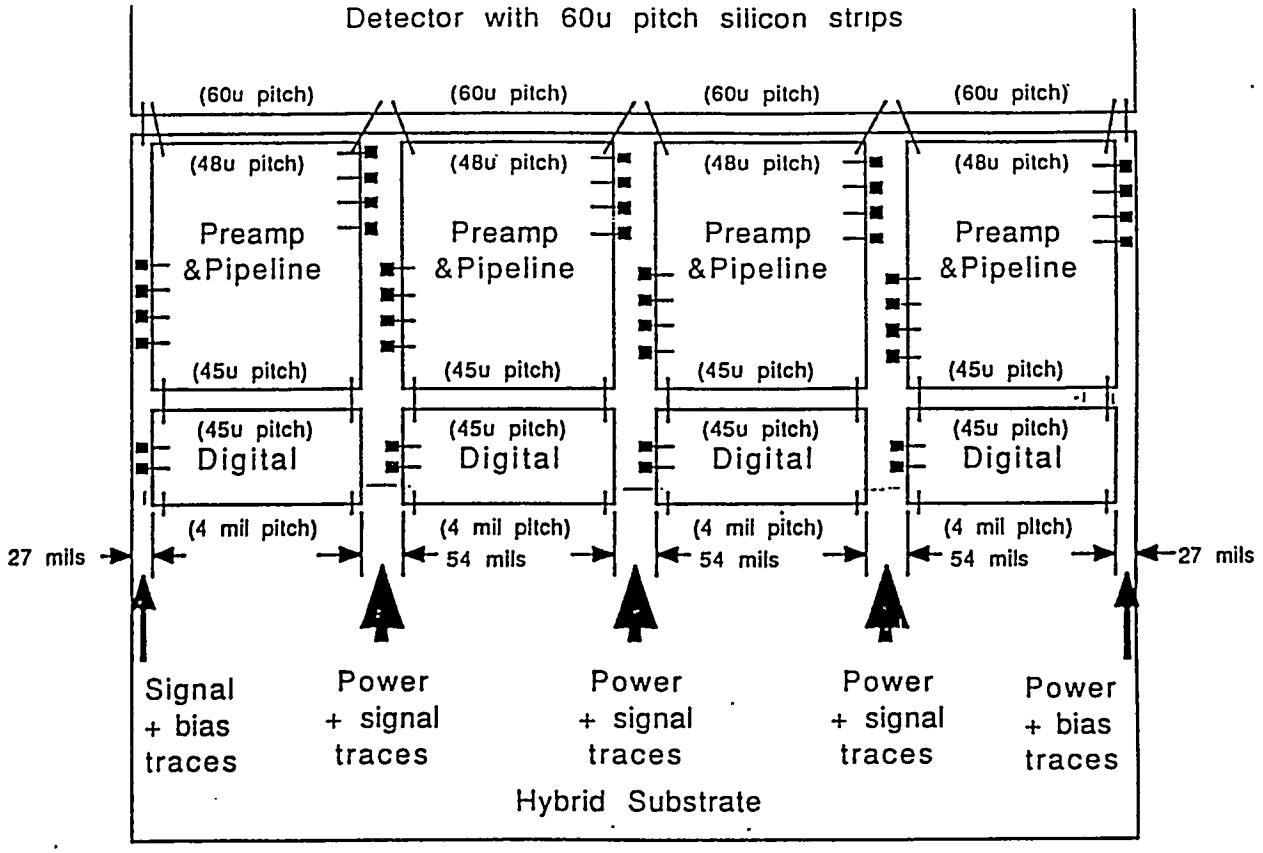

Figure 21: A conceptual layout of the SVX3 chip set. Shown is a row of chip pairs with power for the analog chip running between the sets. Digital input and output enter the set from the bottom. The chip set uses wire bonds to transmit signals between chips.

are associated with every Level 1 trigger. Our design trigger rate is 50KHz or on average, one event every 20μs. This implies a deadtime percentage on the order of 40%. This can be prevented if one changes the architecture of the SVX2 chip such that it is buffered as well as pipelined. In this way the data on a cell of interest can be removed from the pipeline on the fly without interrupting data taking. With enough additional cells to act as buffers the chip can become effectively deadtimeless.

SVX3 chip set

The SVX3 chip is going to be a two chip set. The two devices are called the frontend (SVX3FE) and backend (SVX3BE) chips. The SVX3FE chip has all the analog operations of amplification and contains the pipeline and skip logic while the SVX3BE device has the comparator the ADC, sparsification, and readout drivers. The operation of the readout proceeds identically to the SVX2 chip with one important difference. It is possible to continue data taking during digitization and readout. Shown in Fig. 21 is a schematic drawing of several chip sets on a hybrid. The chips will use wire bonds on a 45μm pitch to pass signals between them.

When a Level 1 trigger is received, the cell at the correct pipeline depth is marked by a read pointer and data taking continues. When the data taking pointer encounters that cell

again it will skip that cell. The pipeline depth pointer is automatically adjusted to account for the fact that a cell is being skipped (up to four cells can be marked for readout at any given time). The data on the cell being skipped is connected to the digital comparator and the process of digitization and readout proceeds. When the cell has been read out, it is placed back in the pipeline and the skip marker removed. During this entire exercise, the data were still accumulating on the other cells in the pipeline. Up to four pending Level 1 triggers can be accommodated in this manner. Deadtime is only incurred if all four additional cells are marked. Then the trigger must be inhibited until a cell is freed.

Whenever one intends to take data during digital readout there are concerns of coherent noise coupling into the input and corrupting the data. These concerns require a prototype chip before we can begin to address them fully; however, in anticipation of this difficulty the SVX3 chip set will have features that should minimize such coupling. First, the decision to make SVX3 a two chip set was driven mainly by the concern that the digital operations of the chip would couple through the substrate if it were one large chip. Another consideration was yield of the chips, since the physical size of a single chip would have been quite large, about the area of a nickel. Second, the data drivers that place the data on the bus will be differential and can have a level difference as small as 100mV. Differential signals not only allow for high noise immunity but are inefficient generators of noise as well. Last of all, an effort is being made to confine all the digital operations and input of the digital signals to the back-end, digital chip. Any digital signals needed by the analog chip would be passed by the digital chip since a chip-to-chip driver does not need as much power as the bus drivers. Additionally, analog power and ground will pass between the chip sets and never connect to the digital chip. Further measures may be necessary, but it is hoped that these steps will help maintain data integrity during readout cycles.

3.5 Development of a Chip Test Station

The University of Pittsburgh is extensively involved in the testing and characterization of the early SVX3 prototypes and has had a major impact in moving that project forward and effecting the design of the device. Additionally the Pittsburgh group has diverted its SVX3 testing efforts to aid in the characterization of the first radiation hard prototype SVX2 IC which will be used by the D0 collaboration.

Three years ago the University of Pittsburgh purchased a Tektronix stimulus system capable of providing input signals to an arbitrary digital circuit at speeds up to 630MHz. This equipment was sent to Fermilab in 1994 and used as the key component in a full IC test station assembled and maintained at Fermilab by one Pittsburgh and one Harvard Post doctoral research associate. A block diagram of the test station is shown in Figure 22.

The University of Pittsburgh provided the stimulus system and a post-doctoral assistant to build a test station that would be able to run the chip at speed and fully characterize its performance. A block diagram of the test station is shown in Fig. 22. The waveforms are downloaded from the PC to the stimulus system which can generate patterns up to 630 MHz.

The patterns for 12 channels from the stimulus system are distributed by the EPLD board to the chip inputs (depending on the mode the chip is in). In the readout mode the EPLD outputs for the data-buses are tri-stated and the data-buses are read into a FIFO on the EPLD board. The cycle (acquire, digitize, and readout) can be repeated with a 4 kHz rate. After up to 100 cycles the data is readout from the FIFO to the PC for further analyses. Charge can be injected into the chip in two ways: Either by the internal calibration capacitor using a calibration voltage controlled by the computer, or externally using surface mount capacitors on the chip board and a pulser triggered by the stimulus system. The signals on the lines between the chip and the stimulus system are monitored by a 1 GHz logic analyzer. Not shown in the figure is an Alessi probe station which allows direct probing of test pads placed on the IC by the chip designers. This allows access to internal chip functions to aid in determining where the performance of the chip is marginal.

3.5.1 Progress on Development of the SVX3BE

The SVX3BE chip was submitted to MOSIS in May of 1995 and was received from the foundry and ready for testing by September of 1995. This device was then extensively characterized on the chip test station without an analog front chip. Our tests indicate that the SVX3BE behaves very closely to the manner expected from the design. Additionally, no SVX-3BE chip from the MOSIS submission was inoperable from the wafer.

During the months subsequent to testing of SVX3BE it became clear to the DAQ group that some additional changes are needed to the SVX3BE chip so that the remaining sections of the data acquisition system can reliably handle the data streaming out at 53Mbytes/s. These changes are:

- The SVX3BE chip draws the same power when the output drivers on the data lines are tri-stated. The drivers should be turned off during tristate.
- An additional output signal called Data Valid should follow the data path and qualify the data. Additionally this is needed to determine when valid data appears at chip boundaries.
- A null clock cycle will be added in the passing of priority between chips. This will allow smooth transitions on the data bus as the chips trade bus control during data readout.
- A pair of Digital to Analog converters will be added to the SVX3BE chip to allow for the internal setting of the pedestal voltage. This voltage is currently set externally and had to be supplied from a source at the outer radius of the SVX II barrel. There is not enough room to supply all the needed DACs for a wedge at this location.

All of these items have been requested by the D0 collaboration as well and have been already implemented in the SVX2c and rad-hard SVX2d chips. They have been tested by

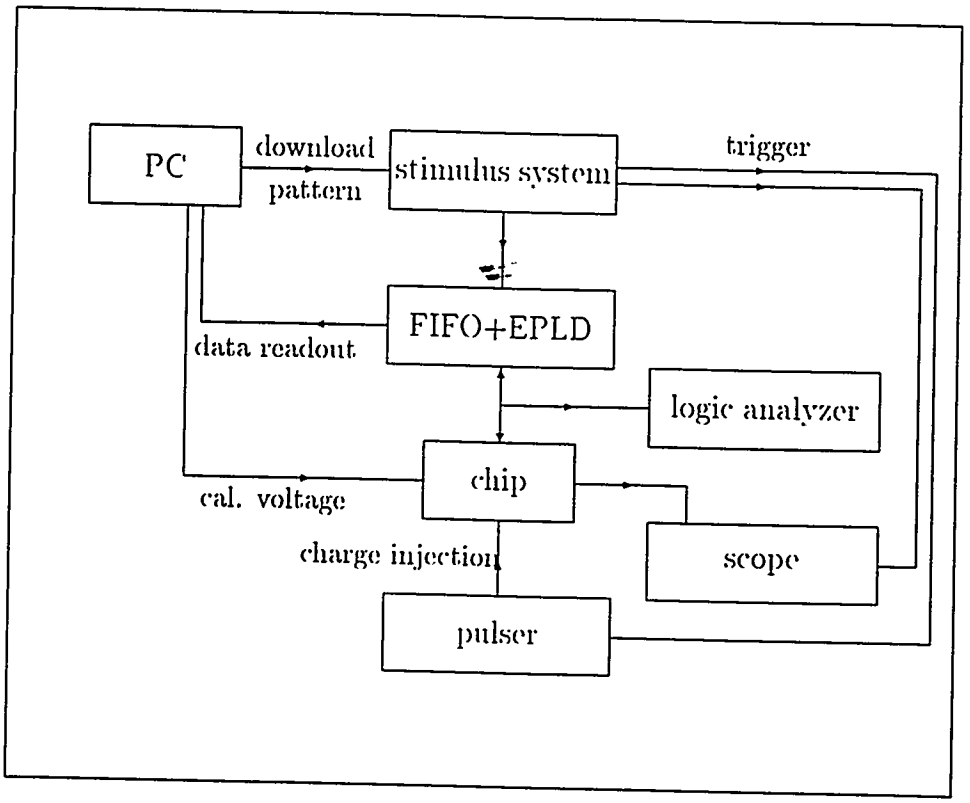

Figure 22: Block diagram of the integrated circuit test station.

the Pittsburgh test station and found to operate satisfactorily. Since the submission in May, 1995 there have been no chip designer resources available for the SVX3BE effort.

3.5.2 Progress on the SVX3FE

The first version of the SVX3FE chip was submitted to MOSIS in July, 1995 and was received in October, 1995. It was clear very shortly afterward that this device had severe problems, most of which were associated with the skip logic section of the IC. Additional engineering support was requested and received in November, 1995. Working in tandem with Fermilab engineers the following items were identified as errors in the design of the SVX3FE chip.

- The write pointer logic passes a token from cell to cell in response to the beam crossing clock indicating which cell is currently taking data. There was a missing connection between cell 44 and cell 45 in the passing of this token causing the token to be lost after one pass through the pipeline.
- There was a metal layer missing from the design in the write address encoder. This missing metal had the effect of only sending the address of cell 0 to the write address shift register no matter what cell the token was actually on. Consequently, only cell 0 could be read out into the the BE chip.

- The driver at the output of the write address shift register was not powerful enough to drive the skip address decoder and the read address FIFO at speed.
- An additional connection was made in the pre-amplifier circuit which shorted a bias voltage to VCC. This effectively prevented proper operation of the pre-amplifier.

Approximately 10-12 of these IC's were sent to Accurel for focused ion beam (FIB) surgery to try to fix some of these problems and allow continued testing. This effort met with limited success. By March, 1996 only one SVX3FE chip had enough successful FIB changes made that would allow running in a limited deadtimeless mode.

This test was done in order to try to understand what kinds of problems we might encounter with noise coupling in the deadtimeless SVX3 chip set. Tests with this chip indicated that there is no measurable increase in noise at the 1000e^- level when the BE chip is digitizing or reading out during data taking. However there is a periodic and large (20 counts) pedestal shift present during readout and digitization.

The changes identified were implemented and a second submission of the SVX3FE chip was made in late January, 1996. This device (now called SVX3FE2) was received on April 10, 1996. Preliminary tests indicate that this device is fully functional and that it properly operates with the SVX3BE chip. Tests continue in an attempt to learn more about the coupling issues of deadtimeless operation of this chip set.

There are also two additional changes required on this device. The first is a series of special pads on the FE chip outputs that will facilitate wafer testing of SVX3FE with a probe card. The current pitch of the output pads (45μm) is too small for conventional wafer probe card technology. The additional pads will connect to one of 4 outputs depending on switch settings in the chip.

The second change involves the protection diode scheme. Studies done by CDF and D0 have shown that the breakdown of one of the strip coupling capacitors on an AC coupled silicon detector will turn on the protection diodes at the input to the IC's. As these diodes draw more current and it diffuses through the chip, neighboring channel's protection diodes also activate. This removes up to 6-8 channels for each broken coupling capacitor. The effect is termed a 'black hole'. The SVX2d IC has a new protection diode scheme that seems to limit the effect of black holes to the channel with the broken capacitor and no where else. We have requested this be implemented on SVX3FE as well.

SVX2d testing

During the month of September, 1995 UTMC announced that it was selling its radiation hard process foundry to Rockwell International. This sale meant that this facility would no longer be available for the fabrication of radiation hard electronics after August 1996. The closest alternative in terms of performance of the process appears to be from Honeywell corporation which is 3 times more expensive.

The D0 collaboration decided to go ahead and attempt to finish its rad-hard production in the UTMC process in the hope of completing their production run prior to the closing of the UTMC process. The first prototype rad-hard IC arrived on April 15, 1996 with only one month of testing available before a decision has to be made about submitting the production device to UTMC. During this month the Pittsburgh test station and the time of the CDF post-docs has been made available to D0. Thus far, no fatal problems have been discovered in the SVX2d chip though the top speed (58Mbytes/s) is uncomfortably close to the design specification of 53Mbytes/s.

Future testing activities

There are two efforts that will continue in the near future with the test station. The current version of the SVX3 chip set is functional but has not been thoroughly tested for noise and pedestal variations during deadtimeless operation. This is our main priority starting before the end of May, 1996. The current plan is to submit the first rad-hard prototypes of SVX3BE and SVX3FE to Honeywell by the end of June, 1996. The arrival of those devices will also be subject to these tests.

Additionally, the test station is a general system that can work on any type of digitally operated electronics. This system will be used to characterize the new prototype SVX3 port card which will allow the testing of SVX3 hybrids and detectors in test stands at Fermilab and remote institutions.

3.6 SVX II Simulation and Reconstruction

In addition to construction activities for the future SVX II silicon vertex detector, the Pittsburgh group is active in designing algorithms for exploiting this detector. By attacking this problem well in advance of installation we expect to have in place well tested reconstruction programs, which uses every advantage of 3-D precision tracking, at the time that the detector starts taking data. In addition to readiness for data taking, developing this software at an early stage will allow us to learn any lessons affecting the design of the detector in a timely fashion. We have used some of the algorithms during beam tests of sensor prototypes and hope to integrate elements of the reconstruction with all future tests of sensors, ladders, and wedges so that the hardware + software can be simultaneously brought under scrutiny.

In 1994 a class library for sophisticated object-oriented track reconstruction was publicly released. This class library, called SLT [30], is a Toolkit containing the basic building blocks of pattern recognition algorithms, including Kalman Filter methods for track fitting and for vertex fitting. The Toolkit does not represent a finished application but should facilitate the development of a variety of reconstruction and analysis applications, in an object-oriented environment. It is not tied to the CDF experiment in any way but in principle can be used in other experimental settings such as D0. In 1995, this library was updated and in 1996 it is being used to develop pattern recognition and alignment code for the SVX II detector.

The importance of this class library is twofold: first, the SVX II detector has a very

high potential for pattern recognition, as we discuss later; however, the task of exploiting it will be difficult if one doesn't have a flexible, powerful toolkit which allows experimentation and visualization. Second, CDF and Fermilab in general have realized the shortcomings of the current software environment and are looking to solutions for the second run of the collider. An object-oriented environment is a serious possibility and is now being studied. This project (track reconstruction in SVX II) is perhaps the most advanced object-oriented software project at the laboratory. It will provide valuable feedback about techniques that are mostly unknown to the particle physics community by solving a real problem in a real experiment. Thus, although this project has been carried out in the absence of a firm decision on the language environment, it is providing valuable input to that very decision.

The SLT Tracking Toolkit is primarily for track and vertex reconstruction and four-vector analysis. However it provides enough support for simulation to allow development of pattern recognition code. Using the tracking toolkit, we have developed a fast simulation of the SVX II detector, a fiber tracker, and straw tracker. The fast simulation generates reconstructed hits, ignores particle interactions and smears the hits with a Gaussian resolution function. To use this as the basis for physics simulation would be wrong; however CDF is currently examining the issue of physics simulation in Run II, paying particular attention to the possibility of standardizing to GEANT4, CERN's object-oriented toolkit for detector simulation [31]. In the meantime this fast simulation provides what is required to begin development of the pattern recognition.

The simulation generated the image of the SVXII detector shown in figure 23, which shows a top plus minimum bias event in the SVX II. The yellow helices are simulated tracks, and the light blue lines in the detector represent hits. The image illustrates the functionality of the simulation, which consists of about 500 non-reusable lines of C++ in addition to the tracking toolkit. This illustrates one of the benefits of the object-oriented approach to software, code re- use. The simulation is steered through graphical user interfaces so that configuring and running the simulation is fast and easy and requires no programming.

The work on track finding is ongoing. The tools we have developed make this task as convenient as possible. Small programs in a high-level language means that programmers can concentrate on small sections of the problem at a time. Use of the Standard Template Library[32] trivializes the task of storing these objects in memory which in the past has consumed an astounding amount of programmer's time and effort. Several in-house and free data persistence packages [33] are in use for storing the objects on files. Visualization tools built-in to the SLT Toolkit assure that the developer can conveniently see the state of his program as it executes by adding a line here and there to write the objects to a VRML[34] viewer. In particular, the developer can view complicated events, such as the one shown in figure Figure 23, in stereo and on arbitrarily sophisticated hardware, including regular workstations, desktop VR (available at Pittsburgh and soon at Fermilab), VR caves (a partial system available soon at Pittsburgh), and head-mounted devices (which no physics group currently owns). At least the desktop VR system is nearly indispensable when viewing complicated events such as the one in figure 23

The simulation so far consists of the following components:

- An editable, browsable data base containing the structures describing the detector and used by the program
- A GUI-wrapped event generator (pythia)
- The simulation program

The user types

```
xpythia | z-sim Database
```

where xpythia is the event generator, z-sim is the simulation program, and Database is the data base. The generator and simulator pop X-windows GUI's[1] allowing users to set parameters of the event generation and detector simulation. Currently the output of z-sim is only graphical. The problem of importing its output into another program is the data persistence issue: this issue is being taken up by other groups and should be solved soon.

Combining reconstructed hits to form reconstructed tracks is the problem we are currently working on. The procedure that does this can be made embeddable into any software environment, but we prefer to use the simple and easy-to-use environment described here to develop the pattern recognition. This environment will be soon be installed publicly so that others may participate in the development of object-oriented reconstruction algorithms with as much ease as possible.

As one sees above the program has three components: the event generator, the database, and the simulator. The **simulator** is used exclusively for this task and has no other outside application. The **database** is developed from free components, notably the gnu database, and adds to this a browser so that one can see what's in the database and change it, allowing for a quick reconfiguration of the detector under study. This capability is vital and we don't want to do without it how ever ideally the functionality could come with whatever future database CDF decides upon for Run II. If not, we will re-use the prototype with the future persistence mechanism to insure that all CDF collaborators can see what is in their datafiles. The gnu database is a swappable component: any other relational or object-oriented database can replace it, with a minimum of effort.

The **event generator** (xpythia) program should be useful to a wide community outside of CDF as well as inside. We believe there is no better way of interacting with an event generator. It leaves the whole CERN application library undisturbed. It simply is an interface to pythia's input and output. There are many advantages of this approach, to list a few:

[1] A professional X-windows GUI builder was purchased to minimize the manpower used to develop GUIs.

- It gains support even from software conservatives
- Nice way of interfacing event generators to FORTRAN, C, or C++
- Event generator libraries can be dropped from link lists
- Run-time redirection of output to files or to processes (like simulators)
- Easy site management of configuration files
- Run-time connection to simulator, viewer, browser...
- Easy parallel multiprocessing (via rsh)
- Protects the substantial investment in existing event generators

The coming year should see rapid progress towards the full SVX II reconstruction and alignment. By the end of summer 1996 we would like a 3-D segment finder to work. The current status of the pattern recognition is shown in figures 24, 25, 26; these plates also illustrate the philosophy behind the pattern recognition.

Figure 24 shows one wedge of one barrel of the SVXII. The tracks come from a single $b\bar{b}$ event. The true intersection points are shown by white crosses, while the measured hits are shown as blue lines. Notice the "ghost" hits in the first, second, and fourth layer: because of a multiplexed SVX II readout, a hit aliases several times into other regions of the detector. Confusion occurs for two reasons: 1) ambiguous assignment of $r\phi$ hits to z hits, and 2) the presence of the ghost hits, which also exacerbate the previous problem. Notice also that the third and fifth layer have a different geometry: the stereo angle in these layers is 1.2 degrees. There is substantially less confusion in these layers as one can see from the diagram, so they will form the starting point for a track search.

In Figure 25, the two hits in the low-angle stereo layers have been combined to form three dimensional hits in these layers. These three dimensional hits have an elongated shape due to the geometry of the two low-angle stereo hits that constitute them, and appear as red flecks in plate 3 (a closer view reveals elongated ellipsoids). Once this step is taken (in this event) one can practically pick out the true particle trajectories by eye. In a follow-up step, these hits will be combined with a hit between the two layers and if the transverse momentum of the resulting track is not too low, the "stub" is accepted as a candidate. Figure 26 shows that even at this primitive level already, we have picked out the correct three tracks for this part of the detector.

The next stage of reconstruction will involve finding all reasonable candidates that incorporate hits in the inner layers, and computing their χ^2. We expect that in a high multiplicity event that some confusion will occur. We have experimented with one way of resolving this confusion that works well in two dimensions, and probably better in three. This is minimization of a cost function (mostly just the χ^2, but with a penalty for unassigned tracks), subject to constraints (for example, "hits may not be used twice"). This method comes

from the field of integer programming, and free packages can be obtained to perform the minimization[35]. We cannot yet give performance figures for this method.

The SVX II detector has other strengths that can be brought to bear on the problem of pattern recognition besides its geometry. In z, a low-angle track may leave a hit consisting of at least 12 fired strips. The length of the hit in z then correlates with the track angle. Furthermore, the measured pulse height on the z side of the detector varies with angle is highly correlated to that on the $r\phi$ side (in the absence of detector noise they would be equal). These characteristics will be useful in track finding. We will be examining these issues as the pattern recognition develops.

A summer student from Harvard has been "donated" to our group for the task of developing the pattern recognition: this individual is gifted in both mathematics and object-oriented programming, and the friendly programming environment will allow us to take advantage of these skills. By the end of the summer one will have the capability of interacting with the graphical objects. This will form the basis of the first iteration of SVX II internal detector alignment. Physicists will have the capability of viewing detector elements, with reconstructed hits and tracks, and moving them interactively into place so as to minimize residuals. Note that automatic detector alignment algorithms must also be developed, and that this is simply our first line of attack . Adding interactivity to the graphics can be handled elegantly by combining the Tracking Toolkit with the Open Inventor Graphics Toolkit and using the Standard Template Library "Map" class to establish a mapping between physics object and graphical representation. In short, this has an easy implementation in an object-oriented language.

The beam test, scheduled for November of this year, will involve a full wedge of SVX II in a test beam at Fermilab. This beam test will require both hardware and software to be mature. A wire will be placed upstream of the SVX II this will allow us to test vertex finding. Track finding and alignment are all necessary for interpretation of the beam test.

The elements discussed above, alignment and track-finding, must come together with clustering algorithms developed for last year's beam test, and at a least a prototype data persistence package, must come together as an integrated "offline" environment for performing the analysis of the SVX II beam test by November of this year. These packages must be available as installation kits that can be installed at other institutions with a minimum of hassle. The beam test will provide us with an opportunity to understand an improve our algorithms. Further improvement and bench marks will require Monte Carlo studies with a full detector simulation.

Admittedly the program of developing reconstruction software for the SVX II has been carried out with a mind towards proving object-oriented technology to skeptics within the collaboration. On result of tackling this as a effort has been that the analysis and design of the project has been done somewhat rapidly, though with good results so far. Hopefully, in an object-oriented CDF all tracking detectors use common classes to describe their tracking objects–and possibly they share these classes with other major experiments, like BaBar, D0, and the LHC detectors, for example. This would be a great benefit to the students and

post-docs who invest time and effort into learning how to work with a particular software environment.

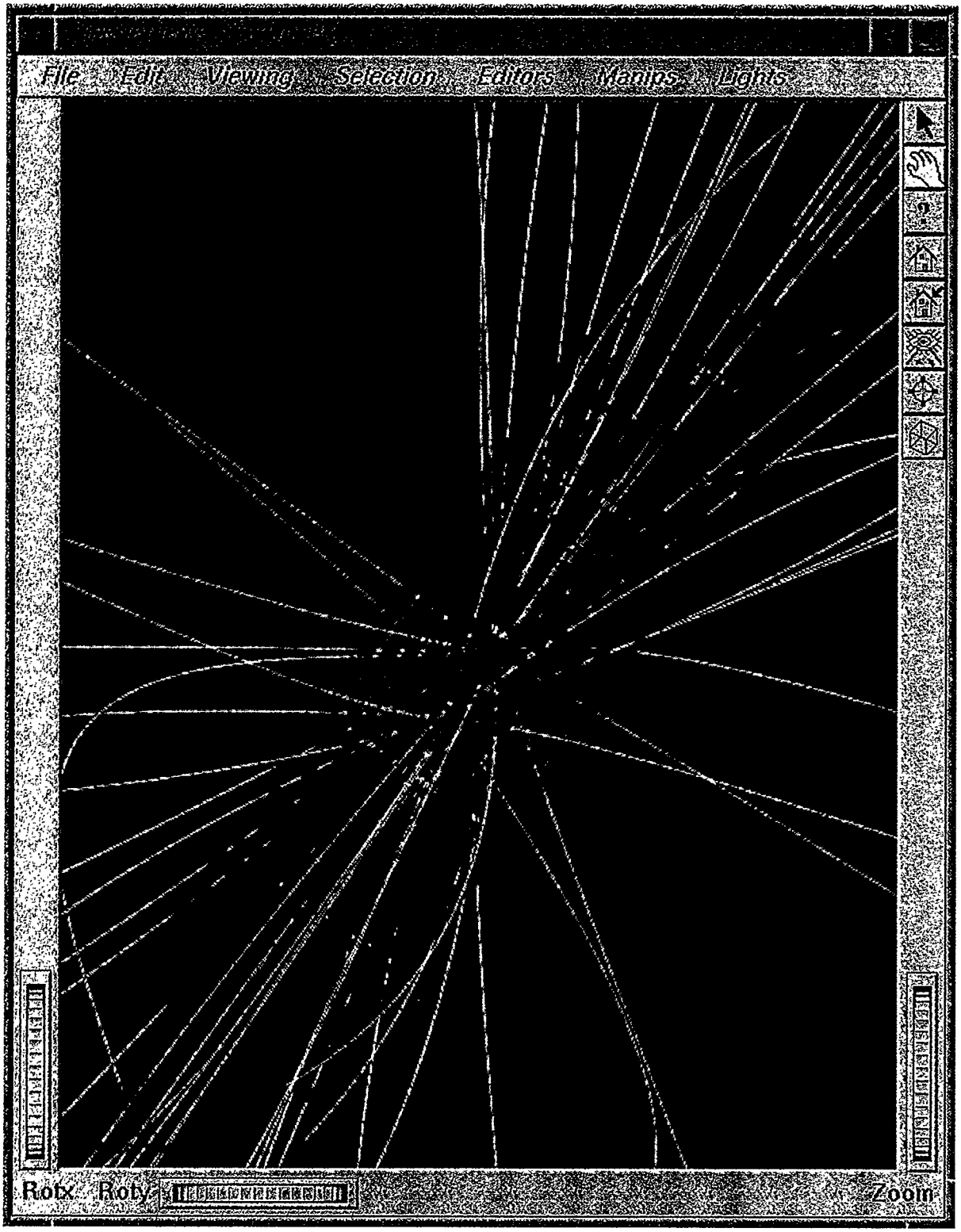

Figure 23: Full top + minimum bias event in fast simulation. The light blue lines represent reconstructed hits in the SVX II detector. Yellow lines are generated particle tracks.

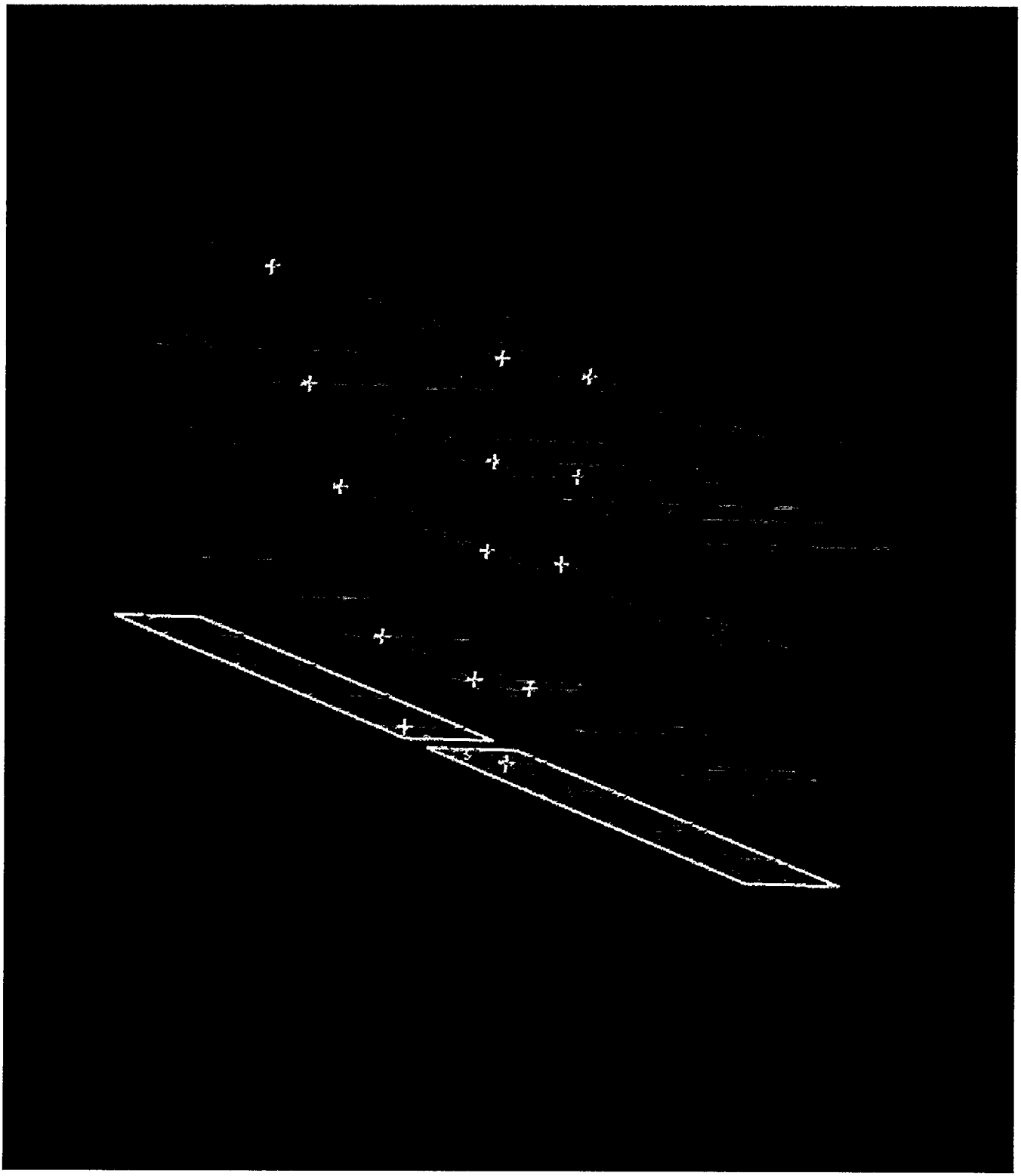

Figure 24: Hits in one wedge of SVX II prior before any pattern recognition. The white crosses show actual intersection points and are not known to the pattern recognition. The third and fifth layers have small angle stereo strips.

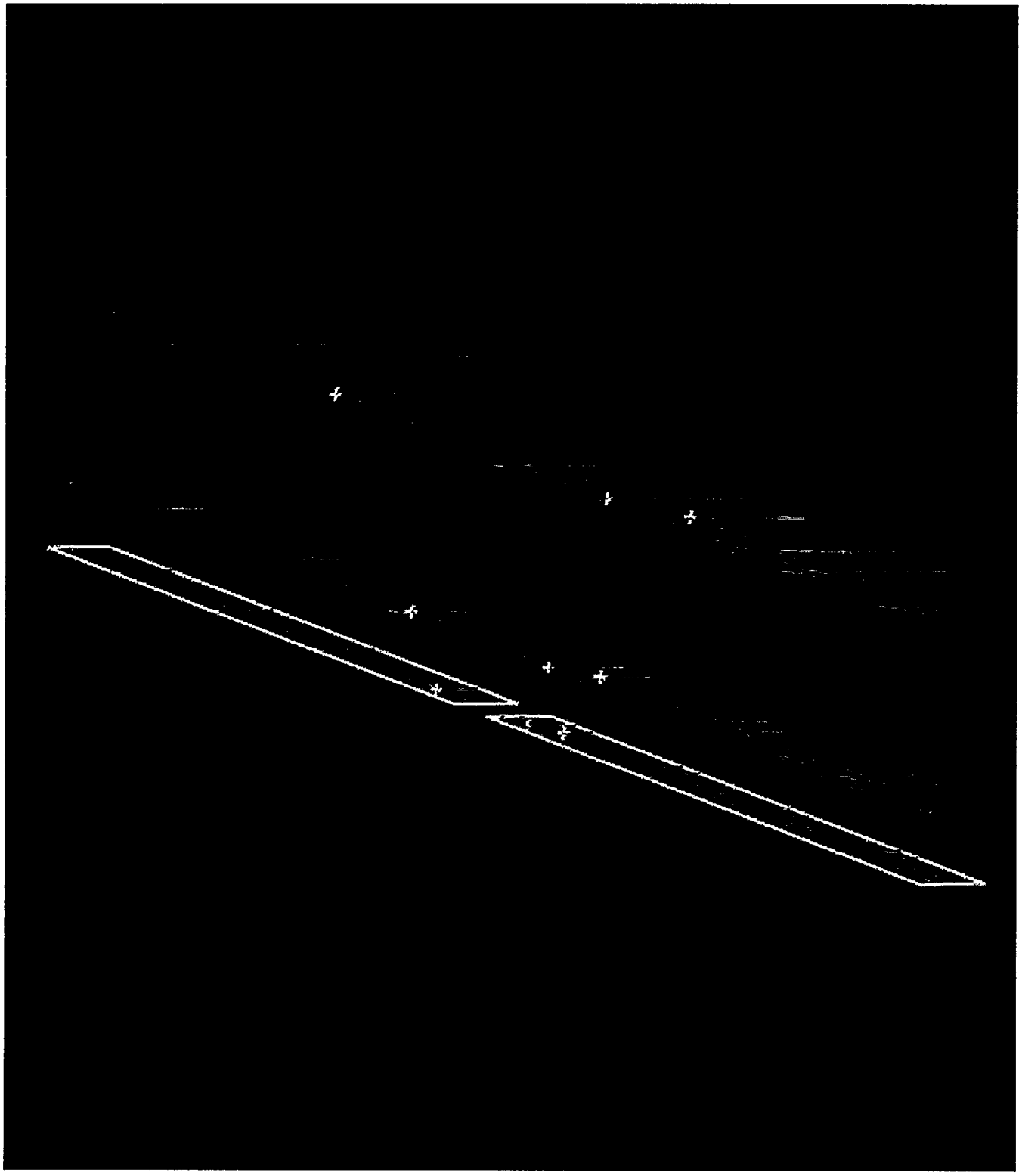

Figure 25: As a starting point in the pattern recognition, the hits in the small angle stereo layers (third and fifth) are combined to form three dimensional hits.

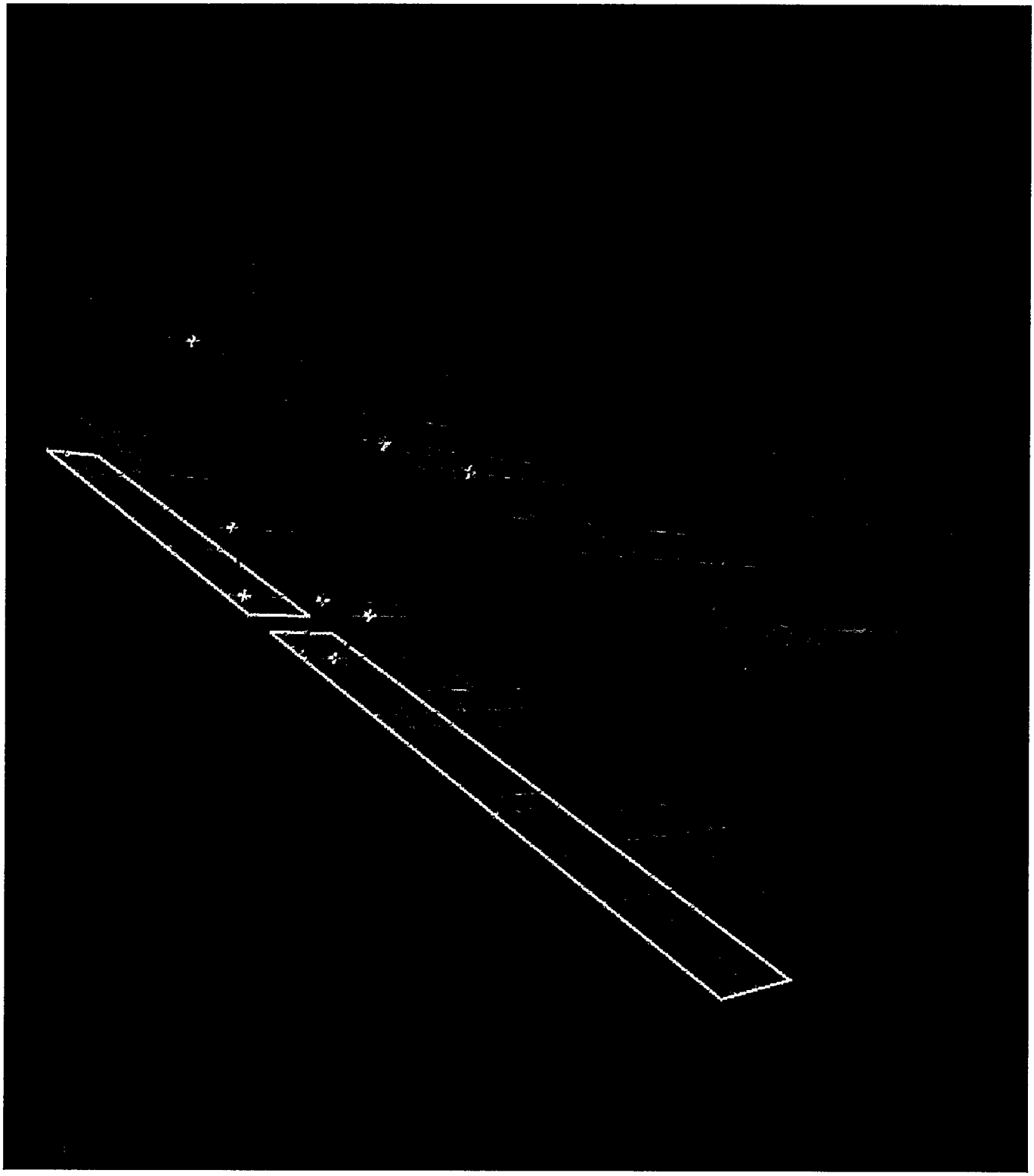

Figure 26: Three candidate tracks are found by requiring an additional hit in the fourth layer. This is a humble beginning that we hope to develop into a robust track finder in SVXII.

3.6.1 Analysis of the 1995 SVX II Beam Test

In 1994, prototype SVX II wafers were tested in a proton beam at KEK. This beam test did not use the SVX2 chip, but instead used older, well-understood electronics. The Pittsburgh group participated in the analysis of this beam test; the results were reported in [27].

In June 1995, a second beam test was carried out at KEK. The major difference between this beam test and the previous one was that the SVX2 chip was used in the readout. The sensors under test were a mix of double-metal detectors and low-angle stereo detectors from SI, Micron, and Hammamatsu. The data was analyzed for signal-to-noise ratio, for resolution, and for the variation of resolution with track angle. This analysis was carried out by the Pittsburgh group; an independent analysis of signal-to-noise ratio was carried out by the New Mexico group and confirms the Pittsburgh analysis. The beam test shows that signal-to-noise ratios as high as 15:1 and resolutions of under 20 microns on the r-ϕ side can be obtained. Resolution on the z-side varies with rapidity but remains under 80 microns even at the highest rapidities.

This analysis is described in CDF note number 3547 and is included as appendix A of this report.

3.7 Data Analysis

3.7.1 Search for the Exclusive Decay $B_c \to J/\psi\pi$

The B_c meson is a bound state of the bottom and charm quarks. It is predicted by potential models to have a mass of $6.26 \pm .02$ GeV/c^2 but has not been observed in any experiment. [36] Estimates of B_c production indicate that it could be produced at up to 10^{-3} the rate of b quark production. [37] The University of Pittsburgh has been conducting a search for this particle in the CDF run Ia and Ib data in two decay modes: (1) The exclusive mode $B_c^{\pm} \to J/\psi + \pi^{\pm}$; (2) the inclusive mode $B_c^{\pm} \to J/\psi + \mu^{\pm} + X$.

The exclusive mode search has been presented at previous meetings of APS [38] and is featured in this section. In the exclusive mode search we compare the results of a $B_c^{\pm} \to J/\psi + \pi^{\pm}$ search to the signal $B^{\pm} \to J/\psi + K^{\pm}$ which is kinematically similar and makes a highly effective control sample. Since last year the completion of run Ib has permitted the collection of approximately four times the J/ψ data sample over run Ia. The run Ia J/ψ data contains 19pb^{-1} while the run Ib data has 110pb^{-1}. A smaller run period called run Ic was completed in Feburary, 1996 and we are currently looking into the possibility of including this data as well.

The CDF detector triggers on J/ψ particles that decay to $\mu^+ \mu^-$ pairs. This trigger imposes a lower limit on the transverse momentum of the muons of 1.5 GeV/c. Additionally the silicon vertex detector (SVX) is capable of resolving displaced vertices greater than 60 μm from the primary in the r-ϕ plane. The cuts applied to the B_c candidates are listed below.

Somewhat less restrictive cuts were applied to the B_u meson to increase the sample size in the comparison channel.

Tracks in muon chamber correspond to good CTC tracks
At least two of the three tracks must be in the SVX
The three tracks must form a good vertex (fit $P(\chi^2) > 0.01$)
$P_T(\pi) > 2.5$ GeV/c
$P_T(B_c) > 6.0$ GeV/c
Proper decay length greater than 150 μm
for $\tau(B_c) > 0.8$ *ps*

A Monte Carlo was developed for Run Ia using different models of b quark fragmentation into B_c and this was simulated in the detector. [37] This Monte Carlo was used as an aid in determining the cuts and also for determining the relative efficiency of detecting $B^{\pm} \rightarrow J/\psi + K^{\pm}$ as opposed to $B_c^{\pm} \rightarrow J/\psi + \pi^{\pm}$. The Monte Carlo was run for a B_c lifetime similar to the B meson lifetime. The detector resolution was parameterized and convoluted with $c\tau$ distributions for other B_c lifetimes to correct the relative efficiency. Since all of the data have been collected we are currently working to publish a Physical Review Letter on the results.

There is no evidence in the data for a B_c meson decaying through the exclusive channel. The values of the relative efficiency R_c between $J/psi + /pi$ and $J/\psi + K$ are shown in Table 4. The B_c lifetime is unknown so the limit is set as a function of that lifetime.

The results of the cuts are shown in Fig. 27 which are histograms of the 3 track invariant masses for the $\psi + \pi$ and $\psi + K$ mass regions respectively. $\sigma \cdot \mathrm{BR}(B_c^{\pm} \rightarrow J/\psi + \pi^{\pm})/\sigma \cdot \mathrm{BR}(B^{\pm} \rightarrow J/\psi + K^{\pm})$ can be obtained as a function of the B_c lifetime and is shown in Fig. 28.

To set a limit, the number of signal candidates $N_{\psi+\pi}$ and the expected background $\overline{N_{Bkg}}$ are needed. [39] For $N_{\psi+\pi}$, the largest 4 consecutive bins in the mass range from 6.1 to 6.4 GeV/c^2 were used while $\overline{N_{Bkg}}$ was determined by fitting a straight line over the full plot. The number of $B^{\pm} \rightarrow J/\psi + K^{\pm}$ events was obtained from Fig. 27 and is 325 ± 20 events. Table 4 contains all the information for a range of B_c lifetimes and Fig. 28 shows the limit as a function of $\tau(B_c)$. [40]

Work in this area continues and preparation of a Physical Review Letter is in progress.

Table 4: This is a table showing the $c\tau$ cut used, the chosen B_c lifetime, the relative efficiency of the cuts, R_ϵ, the largest number of data events in 4 consecutive bins from 6.1 to 6.4 GeV/c^2, $N_{c+\pi}$, and also the fit to the data for the expected number of background events in those 4 bins, $\overline{N_{Bkg}}$. The data from both Run-1a and Run-1b are combined in this table.

CDF Preliminary *Combined Run Results at various B_c Lifetimes*				
$c\tau$ cut	B_c lifetime	$R_\epsilon \equiv \frac{\epsilon(B_u)}{\epsilon(B_c)}$	$N_{c+\pi}$	$\overline{N_{Bkg}}$ (stat)
60 μm	0.17 ps	$2.50 \pm 0.15 \pm 0.10$	40	29.2 ± 2.6
85 μm	0.33 ps	$2.10 \pm 0.12 \pm 0.09$	25	16.5 ± 2.0
100 μm	0.5 ps	$1.84 \pm 0.11 \pm 0.07$	18	12.7 ± 1.7
150 μm	1.0 ps	$1.80 \pm 0.10 \pm 0.04$	10	5.9 ± 1.2
150 μm	1.0 ps	$1.61 \pm 0.09 \pm 0.04$	10	5.9 ± 1.2
150 μm	1.3 ps	$1.43 \pm 0.08 \pm 0.04$	10	5.9 ± 1.2
150 μm	1.55 ps	$1.35 \pm 0.07 \pm 0.04$	10	5.9 ± 1.2

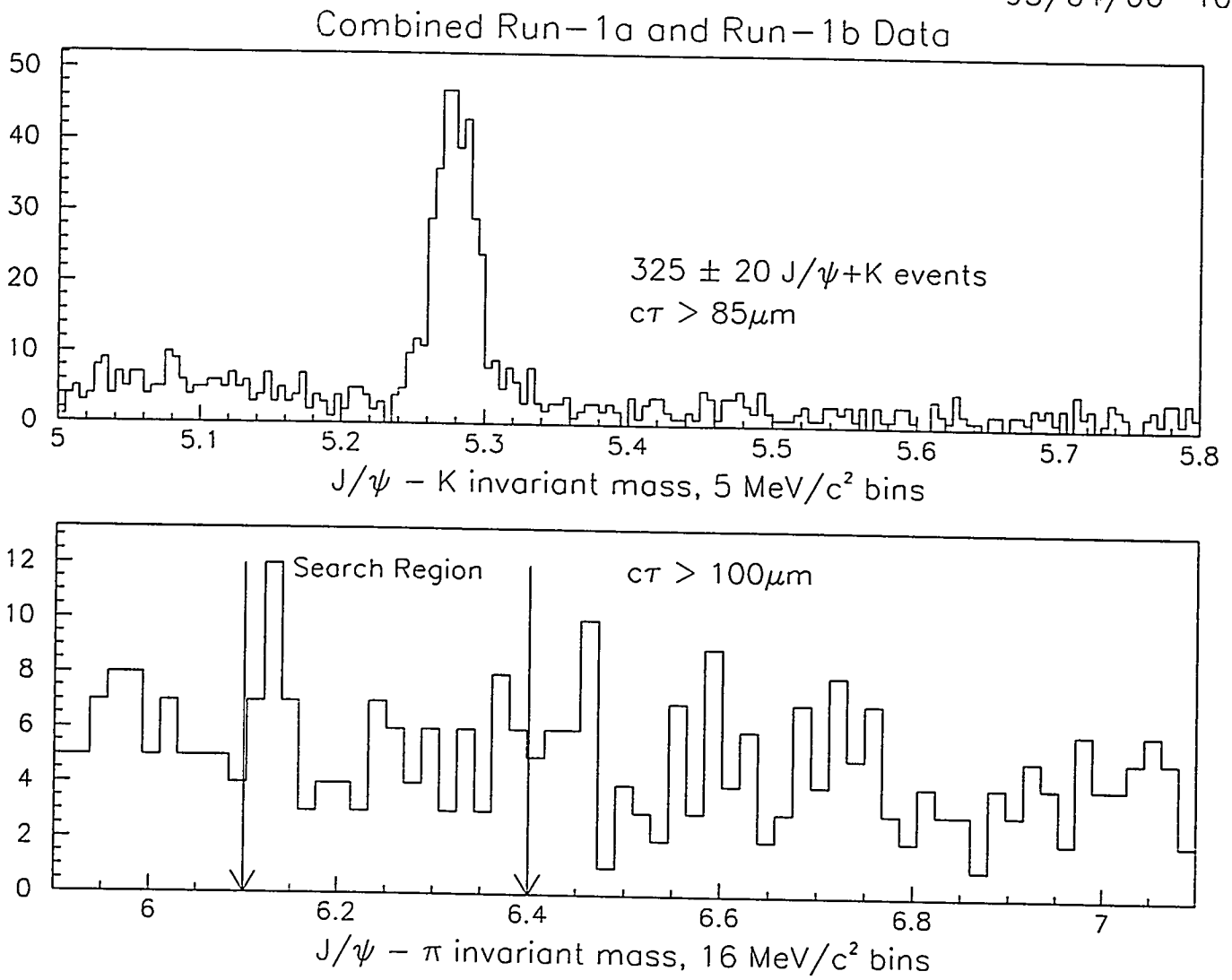

Figure 27: The upper plot shows the three track invariant mass region from 5.0 to 5.8 GeV/c^2 for the mode $B^{\pm} \to J/\psi + K^{\pm}$. The lower plot shows the three track invariant mass region from 6.0 to 7.0 GeV/c^2 for the mode $B_c^{\pm} \to J/\psi + \pi^{\pm}$. The search region is marked on the $J/\psi + \pi$ histogram. These plots use the combined data sets for Run-1a and Run-1b.

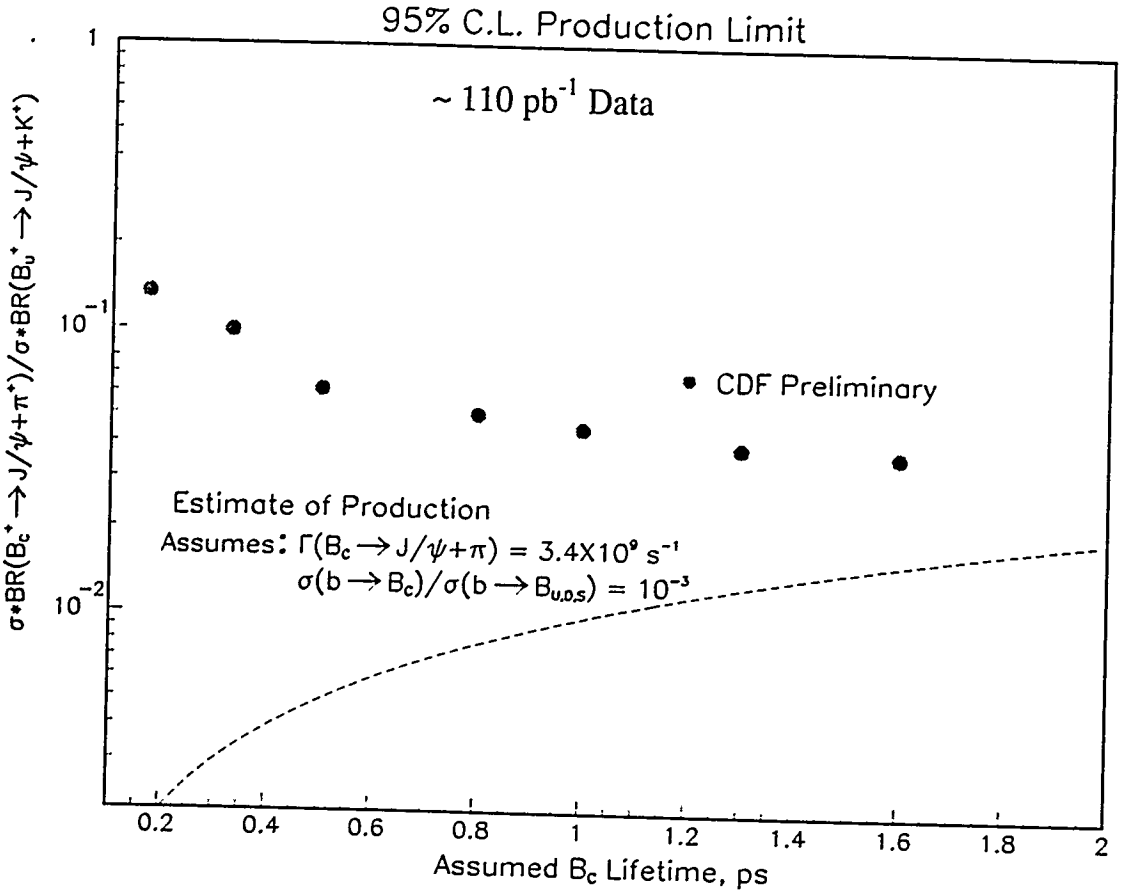

Figure 28: Each solid triangle shows the 95% confidence level limit on the production of $B_c^{\pm} \rightarrow J/\psi + \pi^{\pm}$ relative to $B_u^{\pm} \rightarrow J/\psi + K^{\pm}$ as a function of the B_c lifetime.

3.7.2 Inclusive B_c Analysis

We have also searched for the decay $B_c \rightarrow J/\psi+\mu+X$ in the Run I dataset with an integrated luminosity of 110 pb^{-1}. A detailed description of the analysis is contained in Appendix B which is a copy of our CDF Note on the subject. [41] Here we present a summary of the work.

The signature of the B_c in the decay channel $B_c \rightarrow J/\psi + \mu + X$ is three muons coming from a vertex that is displaced from the primary vertex. Figure 29 shows the three muon invariant mass distribution for the Run Ia and Run Ib data. It should be noted that because of the missing energy due to the neutrino in the decay the distribution is quite broad. Monte Carlo studies show that due to the missing energy the B_c signal would populate the mass region from 3.8 to 6.3 GeV/c^2. Based on this fact and the shape of the background distribution the search region for the B_c was defined to be between 4 and 6 GeV/c^2.

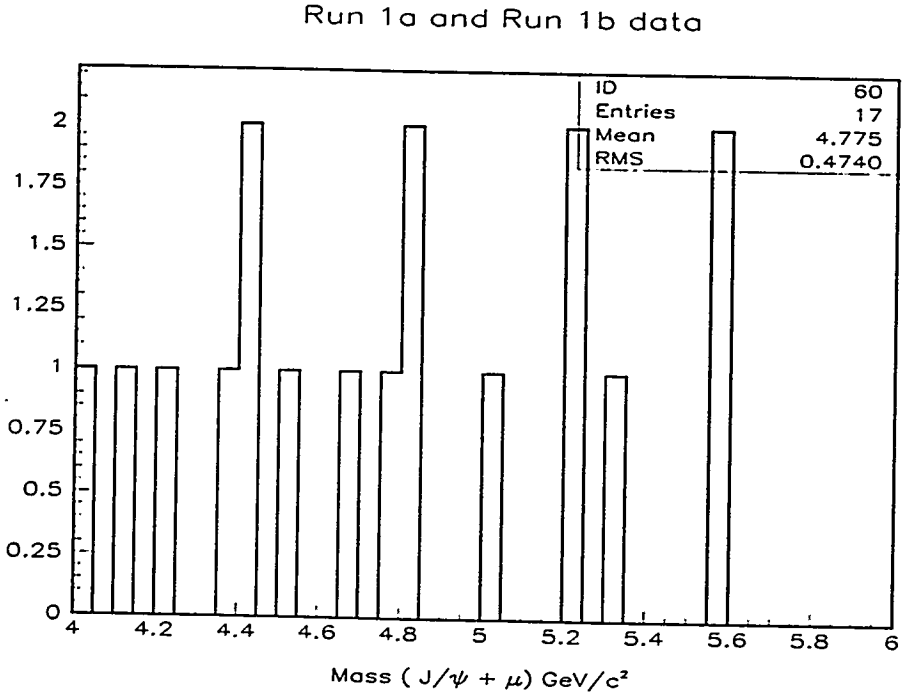

Figure 29: The three track invariant mass plot for Run Ia and Ib. There are 17 events in the signal region. The $c\tau^*$ cut is 60μm.

Background

The irreducible background in this inclusive decay channel comes from fake muons and

$B\bar{B}$ events. Muons can be faked either by a hadron punch-through or from a pion or a kaon decay in flight. An event with a J/ψ may have other tracks that might travel through the calorimeter and the steel upstream of the central muon chambers, without showering. If such a track makes a good vertex with the two muons from the J/ψ and passes the other analysis cuts, then it will fake the $B_c \rightarrow J/\psi + \mu + X$ signal. Similarly a pion or a kaon in an event with a J/ψ may decay in flight. The daughter muon from such a decay may show up as a good muon in the muon chambers. If it passes the analysis cuts, it will fake a B_c event. The decay in flight background can come either from pions or kaons that orginate from a $B \rightarrow J/\psi + X$ and subsequently decay in flight, or the decay of pions and kaons from the primary vertex.

A $B\bar{B}$ background event may result when one B in an event decays into $J/\psi + X$ and the other B into $\mu + X$. The J/ψ and the muon in the event could pass the analysis cuts and fake a B_c. Table 5 shows the estimate of the various backgrounds for this search.

Table 5: Background for Run Ia and Run Ib at $c\tau > 60\mu$m.

Background type	Run Ia	Run Ib	Run Ia + Run Ib
$B\bar{B}$	0.23±0.16	1.07±0.62	1.30±0.64
Punch-through	0.43±0.17	1.77±0.69	2.20±0.71
Decay in Flight from Prompts	0.14±0.10	0.64±0.49	0.78±0.50
Decay in Flight from B's	0.79±0.23	3.87±1.12	4.66±1.14
Total Background	1.59±0.34	7.53±1.53	8.94±1.57
Data events	3	14	17

Limit on B_c Production

The results presented in Table 5 show that the number of observed events in the data do not have a statistically significant excess over the expected background. The upper limit of the ratio of $\sigma \times \mathrm{BR}(B_c \rightarrow J/\psi + \mu)$ to the $\sigma \times \mathrm{BR}(B \rightarrow J/\psi + K)$ at the 95% C.L. was calculated as a function of assumed B_c lifetimes and is shown in Fig. 30.

Future Plans for the Inclusive B_c Analysis.

The search for the B_c meson at CDF in the inclusive J/ψ mode was conducted in two of its decay channels. The Pittsburgh group studied the $B_c \rightarrow J/\psi + \mu + X$ channel and another group from Tsukuba studied the $B_c \rightarrow J/\psi + e + X$ channel. The results from each of the above channels independently showed only a slight excess of events over the expected background. Table 3.7.2 shows the probability for the background to fluctuate to the number of events observed for the two analyses. Combining the results of the two searches yields an excess which is inconsistent with the background hypothesis at the level of three sigma. This excess raises two major questions:

- Are the background estimates for each of the two channels reliable?
- If the background estimates are reliable, then is it possible to get a higher significance?

Table 6: Significance of the results from the $B_c \to J/\psi + \mu$ and $B_c \to J/\psi + e$ analysis.

Channel	Data Events	Estimated Background	Probability for the background to fluctuate to the observed events	Significance
$B_c \to J/\psi + \mu$	17	8.94±1.57	1.04%	2.56
$B_c \to J/\psi + e$	16	9.6 ±1.30	3.62%	2.09
Combined	33	18.54±2.04	0.21%	3.07

These questions motivate the type of work that will have to be done for this analysis. Initially the major thrust will be on running additional cross checks to further establish the reliability of the background estimates. At the same time work will be done to re-optimize the analysis cuts to get a better signal squared to background ratio and to study other ways of increasing the significance.

Cross checks on the Background Estimates.

An accurate estimate of the background is crucial to this search. There are several ways by which the background estimates can be verified. One way to verify the background estimates is to compare the number of events observed below 4.0 GeV/c^2 and the number of predicted background events in the same region. The events in this region come primarily from the background. This exercise will be a good cross check on the reliability of the background estimate, but it will be limited by statistics. To increase the statistics one can relax the $c\tau^*$ cut on the three track vertex.

This exercise can be repeated for events observed with effective mass values above 6.3 GeV/c^2. In this case the observed events will be pure background. This region will also not have any contributions from decays in flight of particles originating from B's. The comparison of the observed events and the expected background in this region would give an estimate of the backgrounds labeled $B\bar{B}$, punch through, and the decay in flight from the prompts, listed in Table 5. Here also the statistics could be increased by relaxing the $c\tau^*$ cut.

Table 5 shows that the major background in this search comes from fake third muons. The fake muon background due to the punch through is determined by using data. However, the decay in flight background from B's is estimated using a Monte Carlo simulation. The validity of the Monte Carlo predictions needs to be verified. The verification can be done by looking at a sample of data which contains B's. We have a dataset in which the B's were tagged by looking for high impact parameter tracks in the jets in an event. This data set comes from the single muon trigger. If we take this data set and apply strict cuts (e.g. an impact parameter cut) on the muon that triggered the event then we will be able to select a very pure sample of B's. In this sample we can look for the same sign $\mu\mu$ events which come from the same secondary vertex. The second muon in such an event will be a fake muon.

It can either be a punch-through or a decay in flight. We can estimate the number of fake muon events in this dataset using the same method that was used in the B_c search. The estimated number of events can then be compared with the observed number of same sign $\mu\mu$ events in the data set. This procedure will be an extremely good check of the reliability of the Monte Carlo simulation for the decay in flight estimate. It will also check the way the punch-through background is estimated.

The checks listed above will confirm the reliability of the background estimates that were made in the B_c search. The other issues which subsequently have to be addressed are an increase in the Monte Carlo statistics for the data samples that were used to estimate the background. Some additional work will have to be done on reducing the systematic errors in the background estimates.

Increasing the Significance

Once the reliability checks are done and the current background estimates are stable, we will work on ways to see if the significance of the excess can be increased to something that suggests a discovery. This will be done by re-optimizing the signal squared over background by changing the present cuts or by introducing new cuts. We will also study the shape of the $J/\psi + \mu$ invariant mass plot from data and compare it to the background and the signal shapes which may give us additional significance.

Conclusion

When the search in the muon and the electron channel is combined there is evidence of B_c production at CDF, but there are many checks to be done before the evidence is firmly established. Our efforts will be to complete the tasks listed above in a fairly small time frame so that we can converge on the results of this analysis as soon as possible.

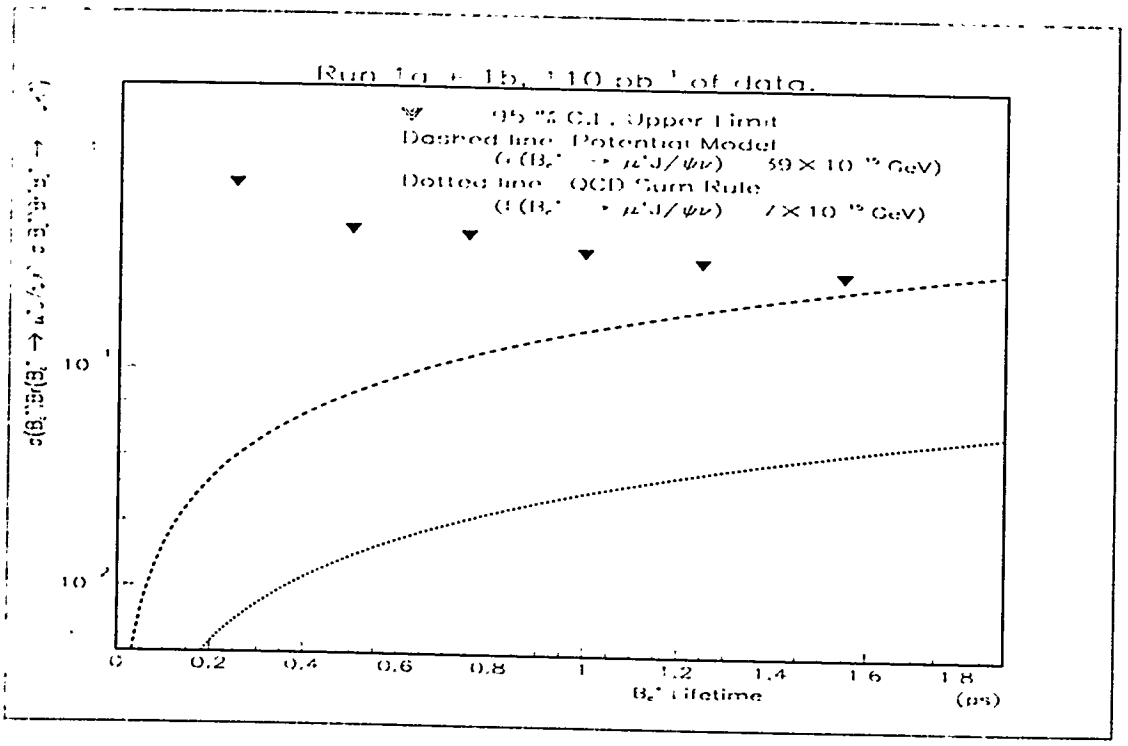

Figure 30: 95% C.L. upper limit on $\sigma \times Br(B_c \to \nu\mu X)/\sigma \times Br(B \to \nu X)$ for the Run Ia and Ib data.

3.7.3 Analysis of B^0 Mixing through D^{*+} - Lepton Correlations

The Pittsburgh group has a long-term interest in investigating neutral B_s mixing at the hadron collider. The oscillation in the neutral B_s sector is controlled by the parameter $X_s = \Delta M/\Gamma$ where ΔM is the mass difference between the two B_s mass eigenstates and Γ is the decay width. The reason to study B_s oscillation is that a measurement of the oscillation parameter X_s can constrain the magnitude of the CKM matrix element $|V_{td}|$.

This happens as follows: The oscillation parameter X_s is related to $|V_{ts}|$ through poorly known constants, including the the B_s meson bag parameter, the weak B_s decay constant, and QCD corrections. Alternately, since $|V_{ts}|$ is constrained by unitarity, one can use the measured value of

$$\frac{X_d}{X_s} = \frac{|V_{td}|^2}{|V_{ts}|^2} \frac{B_d}{B_s} \frac{f_d^2}{f_s^2} \frac{\eta_d}{\eta_s} \frac{\tau_d}{\tau_s} \tag{1}$$

in which many theoretical uncertainties cancel, plus the value of $|V_{ts}|$, to constrain the magnitude of V_{td}. Of course this CKM matrix element is of great interest because in the standard model it represents the length of one side of the unitarity triangle, and thus is important in CP violation.

Unlike the B^0, The B_s oscillation will be rapid: current experimental constraints correspond to a limit of $X_s > 10$[42]. It is not known whether observation of mixing is within the experimenter's reach: the limiting factors are statistics, and the resolution of one's vertexing system. There are two ways of looking for B_s oscillations: 1) looking for a second frequency component in a flavor-tagged sample of generic $B \rightarrow lepton$, such as a dilepton sample, and 2) looking at exclusive final states such as $B_s \rightarrow D_s l\bar{\nu}$. Our investigations into the former method were discouraging, so we are now investigating the possibility of studying B_s mixing with exclusive final states. There are several reasons that these channels are interesting. First, the high-frequency component in a sample of reconstructed B_s will be the only Fourier component in the oscillation. Second, the kinematics of the tertiary vertex is closed leading to a much more accurate extrapolation to the B_s vertex. Third, the D_s has a short lifetime compared to some charm states so the extrapolation from D vertex to B vertex is less. One must weigh these factors against the lower statistics in these channels.

As a warm-up exercise for the B_s into exclusive final states, and also as a potentially interesting measurement of B^0 mixing in its own right, Stephan Vandenbrink, a graduate student, is now investigating mixing in the decay channel $B^0 \rightarrow D^{*+}X$, in a sample of D^{*+}s reconstructed opposite a lepton. The lepton's flavor tags the B^0 at production, while the sign of the D^{*+} tags the flavor at decay. A charged D opposite a lepton of the same sign is the signature of an unmixed event, while a charged D opposite a lepton of the opposite sign is the signature of a mixed event. The results shown here are very preliminary, since this is an ongoing analysis.

As a first step in this analysis, a D^{*+} is reconstructed opposite to a lepton (either an electron or a muon), leading to a mass peak in the expected region. There are 1153 events in the signal region. Figure 31 shows the mass peak.

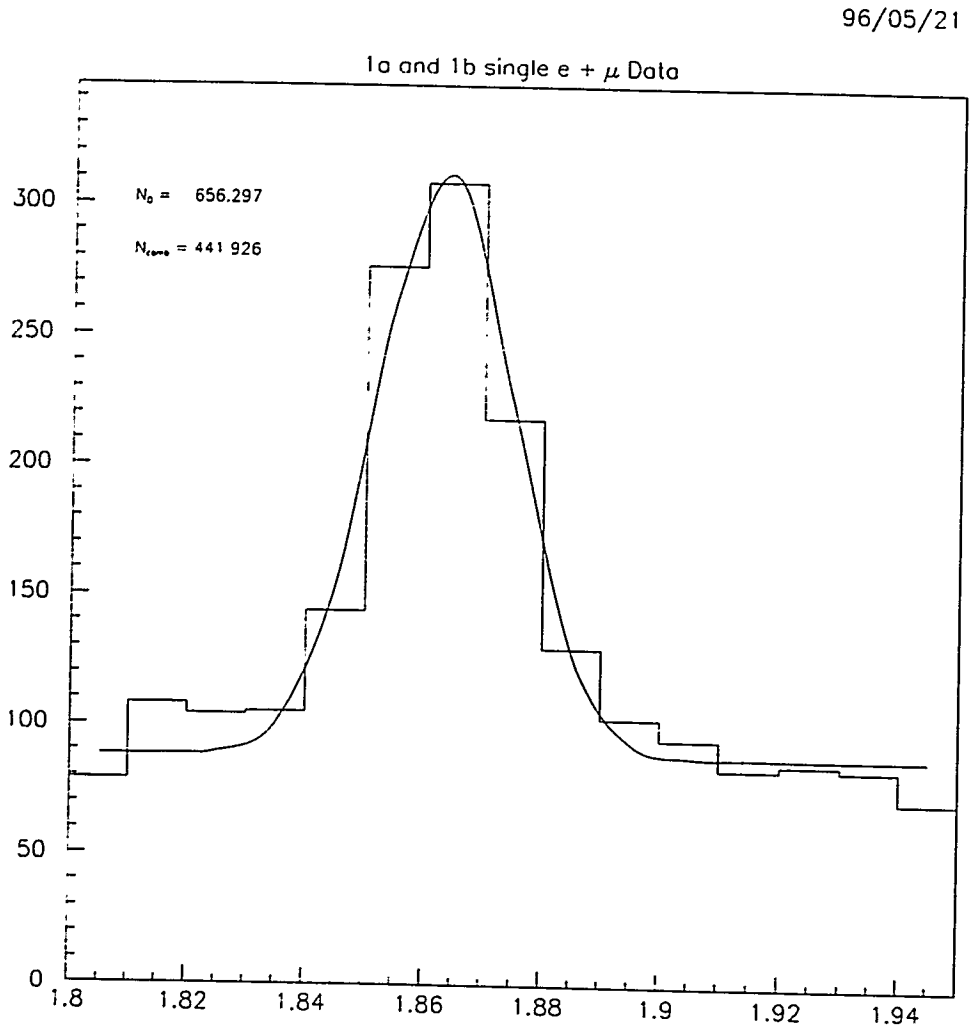

Figure 31: D^{*+} mass peak in the B^0 mixing analysis

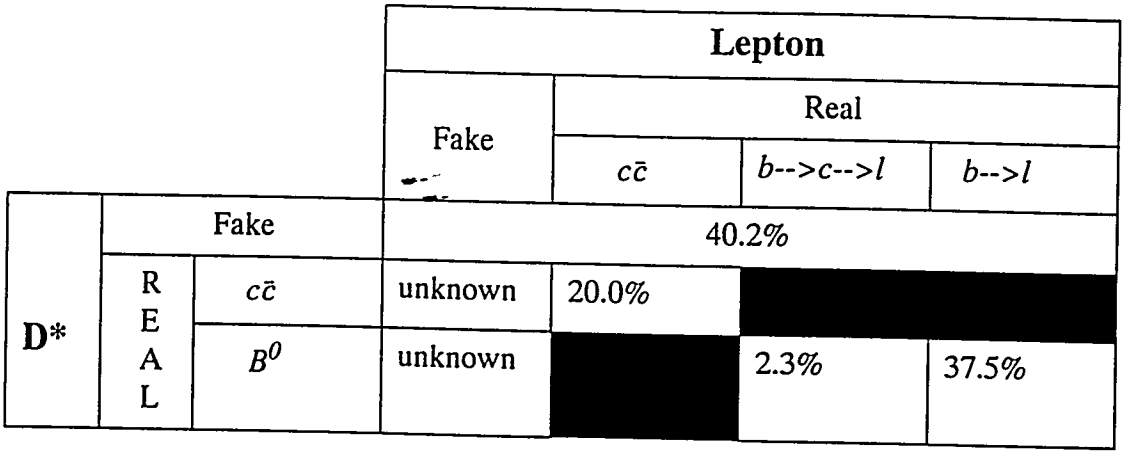

Figure 32: Composition of the lepton-D^{*+} sample. The categories labeled "unknown" are the subject of current investigation

In addition to the D^{*+} + lepton from B^0 decay, there are several sources of background:

- fake D^{*+} from combinatorial background,
- fake leptons with real D^{*+},
- real D^{*+} + lepton from direct $c\bar{c}$ production, and
- real D^{*+}s with wrong-sign leptons that arise from cascade decays $b \to c \to l$.

The contribution from the first source can be estimated from the sidebands in the mass peak. The contribution from the second source is expected to be small, and is currently under investigation. The contribution from the remaining two sources can be understood by looking P_t^{rel}, the component of the lepton's momentum relative to the nearest jet. The distribution of this variable is harder for leptons from a b quark than for those from direct $c\bar{c}$ production or $b \to c \to l$ decays. The shape of the P_t^{rel} distribution is studied for $b \to l$, $c\bar{c}$, and $b \to c \to l$ using the Pythia Monte Carlo, then the data is fit for the background fractions. This fit includes a fixed fraction of combinatorial background whose shape and normalization is obtained from the data in the sideband region of the mass plot. The composition of the sample is displayed in Fig. 32.

Knowing the composition of the sample, the reconstructed proper decay distance for both like (unmixed) and unlike (mixed) events is examined and which is shown in Figs. 33 and 34. In Fig. 35, the excess over background is shown. This shows signs of mixing; however at this stage in the analysis the shape of the distributions indicate other sources of background. This must be understood before proceeding further. We are beginning now to study the contribution from fake leptons.

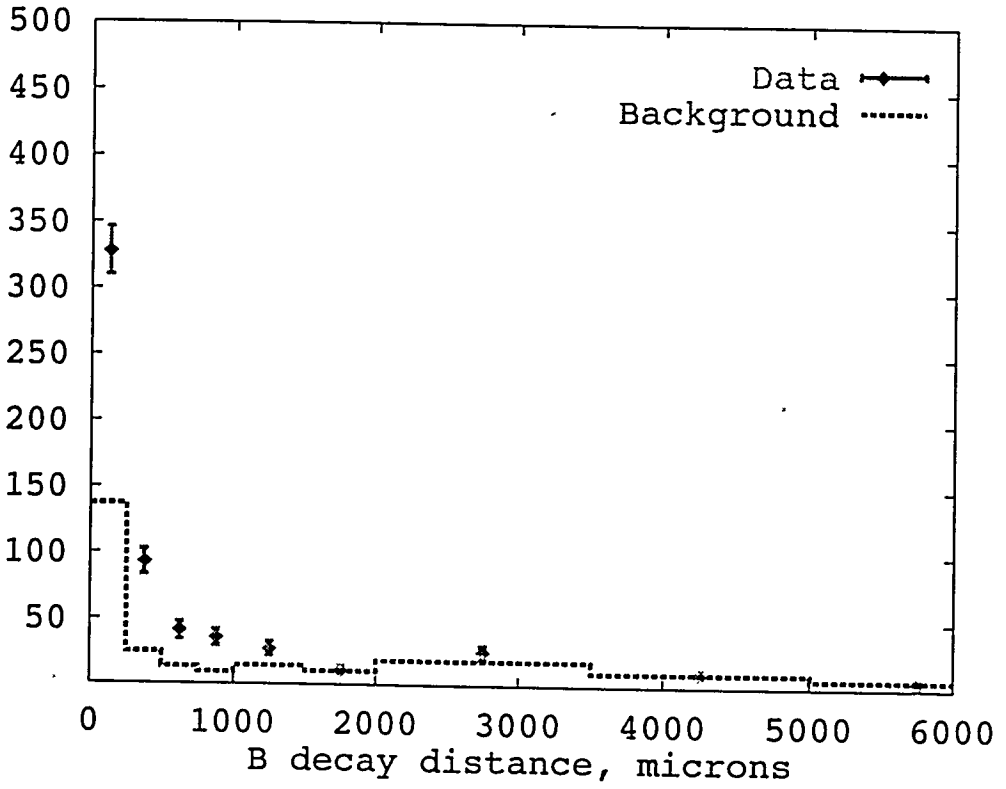

Figure 33: Proper decay distance distribution for like-sign events. Solid line: expected background distribution. Points: data

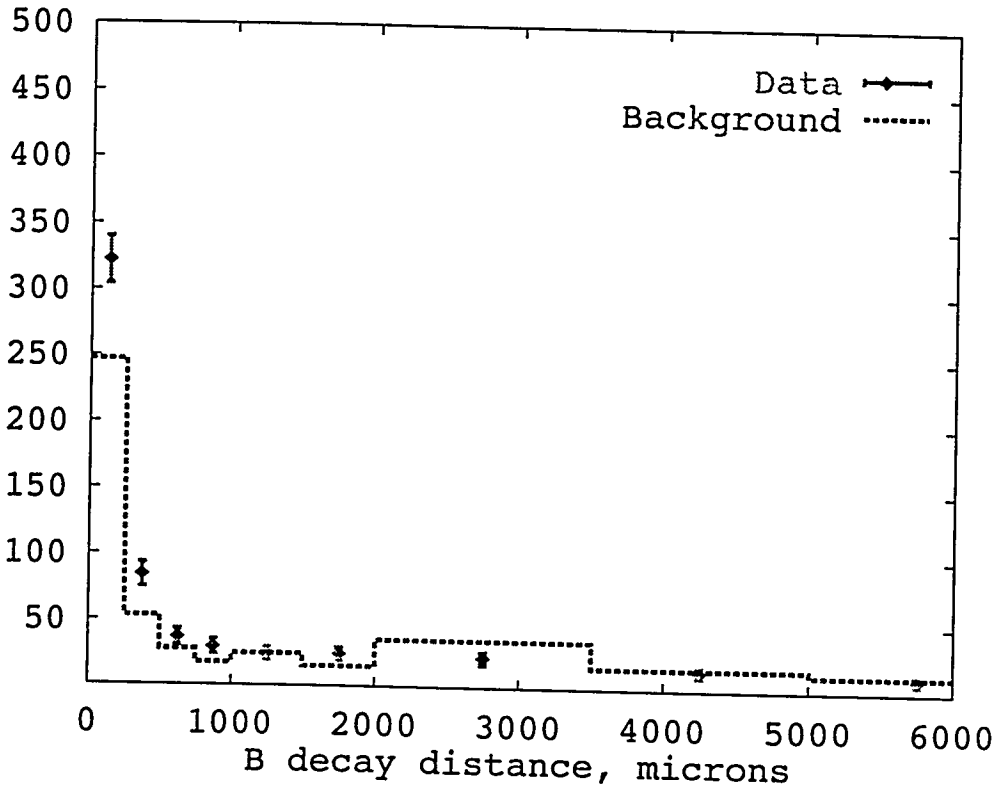

Figure 34: Proper decay distance distribution for opposite-sign events. Solid line: expected background distribution. Points: data

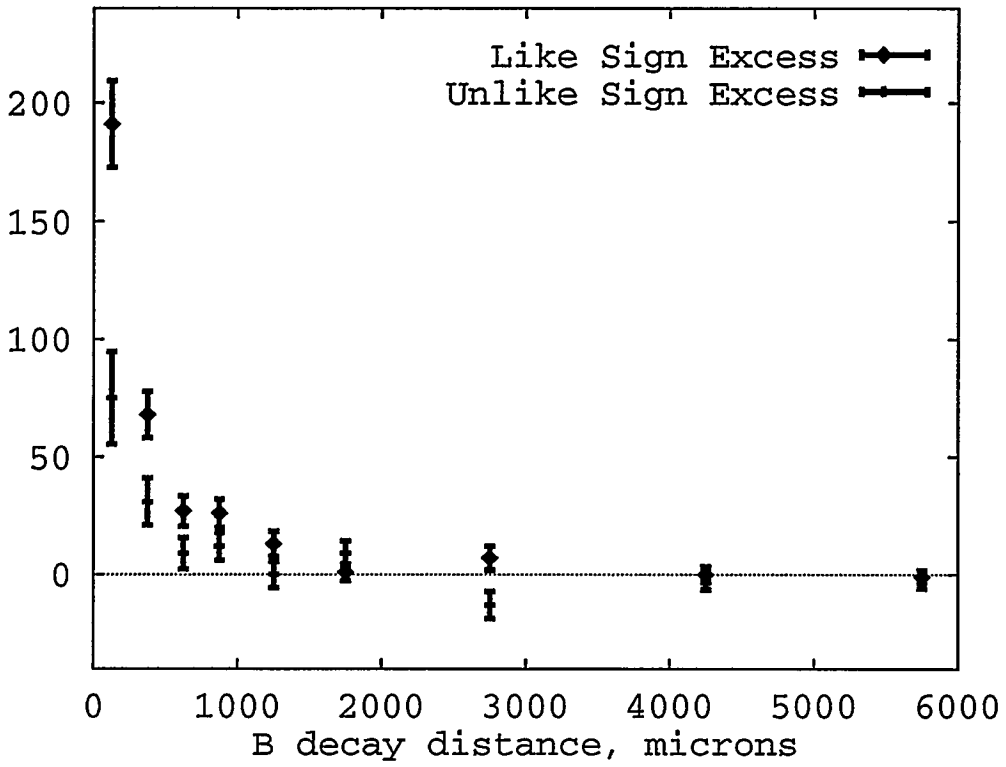

Figure 35: Proper decay distance for the excess over background in the previous two plots, for like-sign and opposite-sign events

Another analysis in CDF is similar in spirit to this one: A charged D^+ is reconstructed, rather than the charged D^{*+}. This is more difficult because no "bachelor pion" exists to help reconstruction of the D^+. The second analysis is being carried out independently from our efforts at the University of Pittsburgh. These two analyses are likely to be combined at some point in the future.

We anticipate that the analysis being developed at the University of Pittsburgh will not only lead to a measurement of B^0 mixing, but may be useful if a sample of B_s plus opposite side lepton can be obtained.

4 Papers

We include a list of papers which have appeared in the literature since our last report.

1. "Direct-photon and Meson Production in a QCD-inspired Phenomenological Framework" in *QCD and High Energy Hadronic Interactions*, Proceedings of the XXXIst Rencontre de Moriond, Les Arcs, Savoie, France, 23-30 March, 1996.

2. "Production of J/ψ and $\psi(2S)$ Mesons in π^--Be Collisions at 515 GeV/c", FERMILAB-Pub-95/298-E, Phys. Rev. D **53**, May 1, 1996.

3. "Measurement of $W\gamma$ Couplings with CDF in $p\bar{p}$ Collisions at $\sqrt{s} = 1800$ GeV," F. Abe et al., The CDF Collaboration, Phys. Rev. Lett. 74, 1936 (1995). FERMILAB-PUB-94/236-E.

4. "Search for Charged Bosons Heavier than the W in $p\bar{p}$ Collisions at $\sqrt{s} = 1800$ GeV," F. Abe et al., The CDF Collaboration. Phys. Rev. Lett. 74, 2900 (1995). FERMILAB-PUB-94/268-E.

5. "Limits on $Z\gamma$ Couplings from $p\bar{p}$ Interactions at $\sqrt{s} = 1800$ GeV," F. Abe et al., The CDF Collaboration. Phys. Rev. Lett. 74, 1941 (1995). FERMILAB-PUB-94/304-E.

6. "The Charge Asymmetry in W-Boson Decays Produced in $p\bar{p}$ Collisions at $\sqrt{s} = 1800$ GeV," F. Abe et al., The CDF Collaboration, Phys. Rev. Lett. 74,850 (1995). FERMILAB-PUB-94/313-E.

7. "Kinematical Evidence for Top Pair Production in W + Multijet Events in $p\bar{p}$ Collisions at $\sqrt{s} = 1800$ GeV." F. Abe et al., The CDF Collaboration. Phys. Rev. D 51, 4623 (1995). FERMILAB-PUB-94/411-E.

8. "Search for New Particles Decaying to Dijets in $p\bar{p}$ Collisions at $\sqrt{s} = 1800$ GeV," F. Abe et al., The CDF Collaboration, Phys. Rev. Lett. 74, 3538 (1995). FERMILAB-PUB-94/405-E.

9. "Measurement of the B_s Meson Lifetime," F. Abe et al., The CDF Collaboration, Phys. Rev. Lett. 74, 4988 (1995). FERMILAB-PUB-94/420-E.

10. "Measurement of the W Boson Mass," F. Abe et al., The CDF Collaboration, Phys. Rev. D., 4784 (1995). FERMILAB-PUB-95/035-E.

11. "A Measurement of the Ratio $\sigma \cdot B(p\bar{p} \to W \to e\nu)/\sigma \cdot B(p\bar{p} \to Z^0 \to ee)$ in $p\bar{p}$ Collisions at $\sqrt{s} = 1800$ GeV," F. Abe et al., The CDF Collaboration, Phys. Rev. D 52, 2624 (1995). FERMILAB-PUB-95/025-E.

12. "Properties of High-Mass Multijet Events at the Fermilab Proton-Antiproton Collider," F. Abe et al., The CDF Collaboration, Phys. Rev. Lett. 75, 608 (1995). FERMILAB-PUB-95/038-E.

13. "Limits on WWZ and $WW\gamma$ Couplings from WW and WZ Production in $p\bar{p}$ Collisions at $\sqrt{s} = 1800$ GeV," F. Abe et al., The CDF Collaboration, Phys. Rev. Lett. 75, 1017 (1995). FERMILAB-PUB-95/036-E.

14. "Measurement of the B Meson Differential Cross-Section, $d\sigma/dp_T$, in $p\bar{p}$ Collisions at $\sqrt{s} = 1.8$ TeV," The CDF Collaboration, Phys. Rev. Lett. 75, 1451 (1995). FERMILAB-PUB-95/048-E.

15. "A Search for Second Generation Leptoquarks in $p\bar{p}$ Collisions at $\sqrt{s} = 1800$ GeV," F. Abe et al., The CDF Collaboration, Phys. Rev. Lett. 75, 1012 (1995). FERMILAB-PUB-95/050-E.

16. "Observation of Top Quark Production in $p\bar{p}$ Collisions with CDF Detector at Fermilab," F. Abe et al., The CDF Collaboration, Phys. Rev. Lett. 74, 2626 (1995). FERMILAB-PUB-95/022-E.

17. "Identification of Top Quarks using Kinematic Variables," F. Abe et al., The CDF Collaboration, Phys. Rev. D, Rapid Communications, 52, R2605 (1995). FERMILAB-PUB-95/083-E.

18. "Study of $t\bar{t}$ Production in $p\bar{p}$ Collisions Using Total Transverse Energy," F. Abe et al., The CDF Collaboration, Phys. Rev. Lett. 75, 3997 (1995). FERMILAB-PUB-95/149-E.

19. "Search for the Rare Decay $W^{\pm} \to \pi^{\pm} + \gamma$," F. Abe et al., The CDF Collaboration, submitted to Phys. Rev. Lett. December 5, 1995. FERMILAB-PUB-95/386-E.

20. "Upsilon Production in $p\bar{p}$ Collisions at $\sqrt{s} = 1800$ GeV," F. Abe et al.,The CDF Collaboration, Phys. Rev. Lett. 75, 4358 (1995). FERMILAB-PUB-95/271-E.

21. "Measurement of Correlated $\mu - \bar{b}$ Jet Cross Sections in $p\bar{p}$ Collisions at $\sqrt{s} = 1800$ GeV," F. Abe et al., The CDF Collaboration, Phys. Rev. D, 52 (1995). FERMILAB-PUB-95/289-E.

22. "Measurement of the Polarization in the Decays $B_d \to J/\psi K^{*0}$ and $B_s \to J/\psi\phi$," F. Abe et al., The CDF Collaboration, Phys. Rev. Lett. 75, 3068 (1995). FERMILAB-PUB-95/270-E.

References

[1] F. Lobkowicz, *et al.*, "A Large Liquid Argon Photon/ Hadron Calorimeter at FNAL," Nucl. Instr. and Meth. **A235** (1985), 332.

[2] E. Engels, Jr., *et al.*, "A Silicon Microstrip Vertex Detector for Direct Photon Physics," Nucl. Instr. and Meth. **A253** (1987), 523.

[3] G. Alverson *et al.*, "Production of Direct-Photons and Neutral Mesons at Large Transverse Momenta by π^- and p Beams at 500 Gev/c," Phys. Rev. D48, 5(1993)

[4] G. Alverson *et al.*, "Structure of the Recoiling System in Direct-Photon and π^0 Production by π^- and p Beams at 500 GeV/c," Phys. Rev. D49, 3106 (1994)

[5] T. Ferbel et al.,"Direct-photon and Meson Production in a QCD-inspired Phenomenological Framework" (to appear in the proceedings of the XXXIst Rencontre de Moriond, Les Arcs, Savoie, France, 23-30 March 1996

[6] Woo-Hyun Chung, "A Study of the Event Structure in High P_T Direct Photon and π^0 Production by 515 GeV/c π^- and 800 Gev/c Proton Beams Incident on Nuclear Targets," Ph.D. Thesis. University of Pittsburgh, 1995.

[7] D. Naples et al., (E683 collaboration), Phys. Rev. Lett. 72, 2341 (1994).

[8] "Measurement of the Production Cross Section of Charm Mesons at High Transverse Momentum in 513 GeV/c π^--Nucleon Collisions," Ph.D. Thesis. University of Pittsburgh, 1995.

[9] R. Jesik, et al., (E672 and E706 collaboration), Phys. Rev. Lett. 74, 495 (1995).

[10] A. Gribushin et al., "Production of J/Ψ and Ψ(2S) Mesons in π^--Be Collisions at 515 GeV/c". (to be published in Phys. Rev. D53, May 1, 1996).

[11] M. Laakso, P. Singh, E. Engels, Jr. and P. F. Shepard, "Operation and radiation resistance of a FOXFET biasing structure for silicon strip detectors." Nucl. Instr. and Meth. in Phys. Res., **A326** (1993), 214.

[12] M. Laakso, P. Singh, P. F. Shepard, "Field oxide radiation damage measurements in silicon strip detectors." Nucl. Instr. and Meth. in Phys. Res., **A327** (1993), 517.

[13] SVX II Upgrade Proposal and Simulation Study. CDF/DOC/SEC_VTX/CDFR/1922. Proposal submitted to the Fermilab Directorate on January 13, 1993 and approved in May, 1993.

[14] G. Punzi and L. Ristori, "SVT: The Silicon Vertex Tracker," Version 3.4, CDF 1872, December, 1992.

[15] P. M. Ratzmann, Analysis of Ladder Support Fiber Options, December 2, 1993, CDF Note 2393.

[16] P. M. Ratzmann, Ladder Thermal Analysis for CDF with SVX III Chips, June 5, 1995, CDF Note 3507.

[17] P. M. Ratzmann, SVX II Ladder Thermal Analysis, January 5, 1996, CDF Note 3508.

[18] P. M. Ratzmann, Thermal Analysis of the CDF SVX II Silicon Vertex Detector, FERMILAB-Pub-96/031-E, submitted for publication to Nuclear Instruments and Methods March, 1996.

[19] D. Bortoletto, *et al.*, Evaluation of single metal SVX II prototypes manufactured by Micron Semiconductor, CDF/DOC/SEC_VTX/ CDFR/3259.

[20] D. Bortoletto, *et al.*, Irradiated SVX II prototype probing results, CDF/DOC/SEC_VTX/CDFR/3295.

[21] D. Bortoletto, *et al.*, Capacitance measurement of double metal double sided silicon microstrip detector, Proc. Second International Symposium on Development and Application of Semiconductor Tracking Detectors, Hiroshima, 1995, to be published in Nucl. Inst. and Meth.

[22] A. Patton, *et al.*, Electrical Characterization of SINTEF/SI Prototype Double-sided Silicon Microstrip Detectors, CDF/DOC/SEC_VTX/CDFR/2835.

[23] M. A. Frautschi, *et al.*, Capacitance Measurements of Double-sided Silicon Microstrip Detectors, FERMILAB-PUB-96/008-E, submitted to Nucl. Instr. and Meth.

[24] S. C. Seidel, *et al.*, Studies of Double-sided Silicon Microstrip Detectors, Proc. Second International Symposium on the Development and Application of Semiconductor Tracking Detectors, Hiroshima, 1995, FERMILAB-CONF-96/049-E, to be published in Nucl. Instr. and Meth.

[25] K. Hoffman, *et al.*, Laser Studies of Charge Collection Efficiency in SVX II Prototype Sensors, CDF/DOC/SEC_VTX/PUBLIC/3438.

[26] G. Bolla *et al.*, Double Metal SVX II Prototype Probing Results, CDF Note 3288 (1995).

[27] N. Bacchetta, *et al.*, Resolution of Double-Sided Silicon Microstrip Sensors, CDF/DOC-/TRACKING/PUBLIC/3277.

[28] N. Bacchetta, *et al.*, Results of the KEK Beam Test of SVX II Prototype Detectors. CDF/DOC/TRACKING/PUBLIC/3547.

[29] R. Yarema *et al.*, "A Beginners Guide to the SVXII." FERMILAB-TM-1892.

[30] Joe Boudreau, SLT: A Class Library for Charged Particle Tracking in a Solenoidal Magnetic Field, CDF Note 2991, February 1995.

[31] "Geant4: an Object-Oriented toolkit for simulation in HEP", CERN/DRDC/94-29. Also http://asdwww.cern.ch/img/asd/pl/geant/geant4.html

[32] A.A. Stepanov and M.Lee. The Standard Template Library. ISO Programming Language C++ Project. Doc. No. X3J16/94-0095, WG21/N0482, May 1994.

[33] "The Trybos Document", R. D. Kennedy, CDF Note 3494.

[34] VRML is a modeling language for exchanging geometry between programs or over the internet. See http://www.vrml.org., especially the final VRML Specification 1.0.

[35] "A Davis-Putnam Based Enumeration Algorithm for Linear Psuedo-Boolean Optimization", Peter Barth, MPI I 95 2-003, January 1995.

[36] E. Eichten and C. Quigg, "Mesons with beauty and Charm: Spectroscopy." FERMILAB-PUB-94/032-T.

[37] E. Bratten, K. Cheung, and T.C. Yuan, Phys. Rev. D 48, R5049 (1993).

[38] B. T. Huffman *et al.*, "Search for B_c in the channel $B_c \to J/\psi + \pi$ at $\sqrt{s} = 1.8$ TeV $p\bar{p}$ collisions at CDF." APS/AAPT Meeting, Crystal City, Virginia, 18-22 April, 1994.

[39] G. Zech, Nucl. Inst. and Meth., **A277**, 608, (1989).

[40] B.T. Huffman, CDF/ANAL/BOTTOM/CDFR/2521.

[41] P. Singh *et. al.*, "Search for $B_c \to J/\psi + \mu$ in the Run Ia and Run Ib Data." CDF Note 3393, April 26, 1996.

[42] D. Buskulic *et. al.*, "Study of the $B_s^0 \to \bar{B}_s^0$ oscillation frequency using $D_s l^+$ combinations in Z decays", CERN PPE/96-030, submitted to Phys. Letters B.

Appendix A

/CDF/DOC/TRACKING/PUBLIC/3547
February 15 1995

Results of the KEK Beam Test of SVXII Prototype Detectors

N. Bacchetta, B. Barnett, D. Benjamin, G. Bolla, D. Bortoletto, J. Boudreau, N. Bruner, M. Frautschi, M. Garcia-Sciveres, A. Garfinkle, C. Gay, M. Gold, C. Haber, T. Handa, A.Hardman, T. Huffman, K. Hoffman, Y. Iwata, T. Keaffaber, T. Kohriki, K. Kurino, J. Mathews, E. Moore, M. Nakao, T. Ohmoto, Y. Unno, T. Oshugi, A. Patton, S. Seidel, N. M. Shaw, P. Shepard, A. Sill, J. Skarha, W. J. Spalding, L. Spiegel, M. Spiropulu, G. Stanley, R. Stroehmer, N. Tamura, M. Takahata, R. Takashima, N. Tamura,T. L.Thomas

Abstract: Results of the beam test of SVXII prototype detectors at KEK in June of 1995 are discussed. The main results are the signal-to-noise ratio of the prototype detectors, and the resolution for both the $r\phi$ and z sides. A signal-to-noise ratio of less than 12 is characteristic of the prototype detectors used in this test. This appears to be due to a loss of signal rather than an increase of noise. The noise measurements may be valuable in understanding detector capacitance.

The Detectors

The second beam test of SVXII prototype detectors took place in June 1995. Unlike the first beam test[1], this test used the SVXII chip to read out the prototype detectors, though the SVXH chip continued to be used to read out the "anchor" detectors. The physical layout was similar to that of the first beam test: four anchor detectors at x=10 cm, x=11.475 cm, x=22.652 cm, and x=24.127 cm, and the protype detector at 16.954 cm.

The double metal detectors for which at least some useful results have been extracted are listed in Table 1. Results are available from Micron, Hammamatsu, and SI double metal detectors. Also some stereo angle detectors from Hammamatsu were tested; they are listed in Table 2. Some of the detectors had been previously given a dose of radiation at Triumf in May of 1995. The amount they received is indicated also in the tables[2].

Table 1: Double metal detectors

Board	Vendor	Type	rϕ pitch	rϕ interstrip	z pitch	Dose
DB15	Micron	D	50 μ		158 μ	
DB1	Micron	A	50 μ	Yes	103 μ	0.7 MR
DB20	Micron	B	50 μ		103 μ	0.5MR
DB17	Micron	B+Be	50 μ		103 μ	0.5MR
DB8	SI	D	50 μ		160 μ	
DB19	SI	A	50 μ	Yes	103 μ	
DB21	SI	B	50 μ		103 μ	
DB12	SI	B	50 μ		103 μ	0.1 MR
DB29	SI	B+Be	50 μ		103 μ	0.6 MR
DB25	Hammamatsu	H	50 μ	Yes	84 μ*	?

*The Hammamatsu detectors have strips separated by 42 μ, which are connected pairwise to the readout electronics.

Table 2: Stereo Detectors

Board	Type	Dose
DB23	SDC-DEEP	0.8 MR
DB13	SDC-2NDPRO	0.7 MR

The Measurements

The data taken while the prototype and anchor detector assembly together were within the KEK beam was used to measure the pedestals in a first pass and then re-used to search for clusters in a second pass. During the pedestal measurement, the noise on each channel was also determined. The noise is usually taken to be the RMS of the (non-zero-suppressed) signal on any one strip; however, with beam in the detector there are long tails in this distribution for most strips. A gaussian fit removes the effect of the tails. The noise and D-noise profile for an SI-B-Type detector is shown in Figure 1.

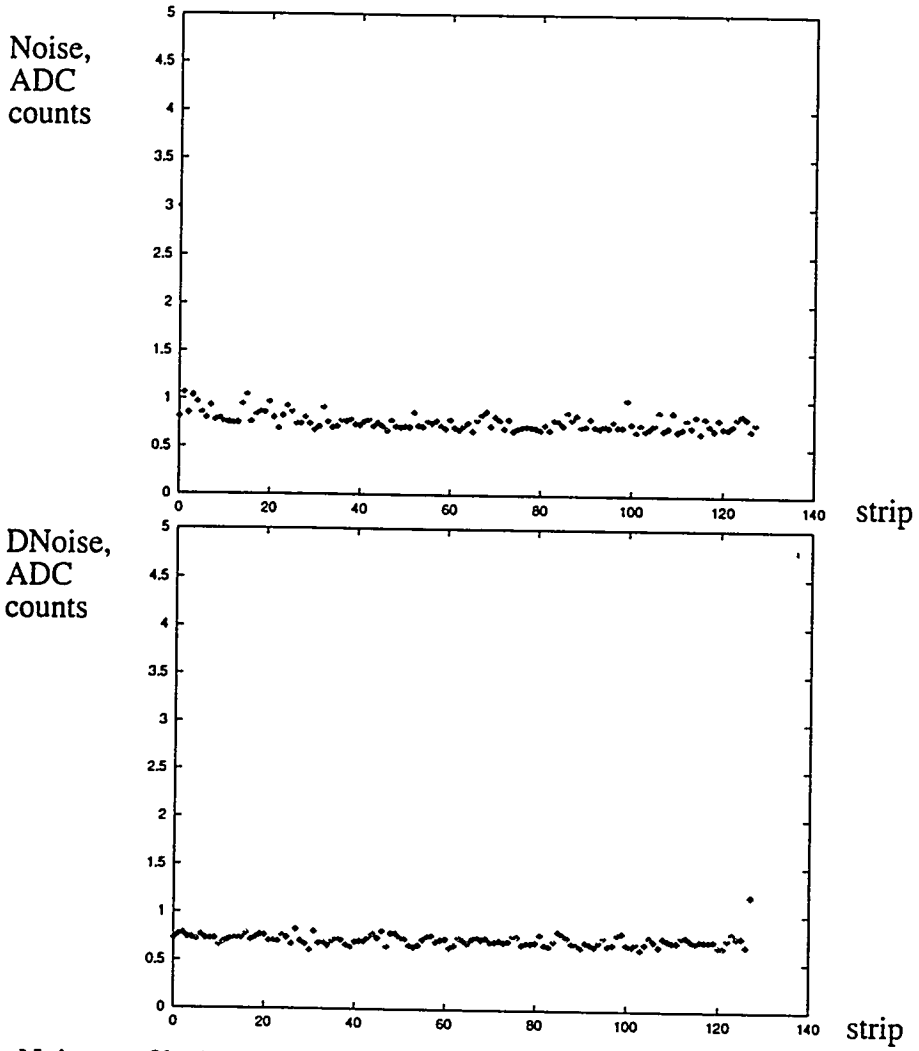

Fig 1. Noise profile (top) and D-noise profile (bottom) over a detector.

The peak value of Noise and D-noise are determined for each run. The D-noise is useful because it represents an irreducible detector noise not due to pickup, poor grounding, & cetera. , and is also used to determine the Signal-to-Noise ratio for the detector. The noise rather than D-noise is used for noisy strip suppression because it depends on only an individual strip rather than also on the neighboring strip like D-noise. Any strip whose noise is over 1.5 ADC counts after common-mode correction (half of the threshold) is suppressed for cluster finding.

Hits in the prototype detectors were found using a very simple clustering algorithm, which clusterered all neighboring strips if their signal was above 3 ADC counts (1 ADC count ~ 1330 electrons), after a common-mode suppression was performed. Because of the low signal in this test beam run, the tuning of sophisticated algorithms on this data was not judged worth the effort.

The anchor detectors had a large signal, low noise and no noticeable noisy regions requiring special treatment. By contrast all prototype detectors had a low signal, and often had noisy regions which needed to be masked off. The data analysis required that one and only one hit was found in the prototype detector for every reconstructed track through the anchor detectors. For highest efficiency, we consider only hits lying within a 200 μ window (100 μ for ϕ scans) of the fitted track. This in addition to the suppression of noisy strips discussed above avoided vetoing good events because of noise activity elsewhere in the detector.

The anchor detectors measure the position of a charged track in the vertical direction. The four coordinates are combined to form a fitted track, using a Kalman filter method[3] in which the curvature is constrained to zero. The precision of the track's position measurement can be calculated from the data itself by looking at the unbiased residual distributions of the four anchor detectors which are shown in figure 2.

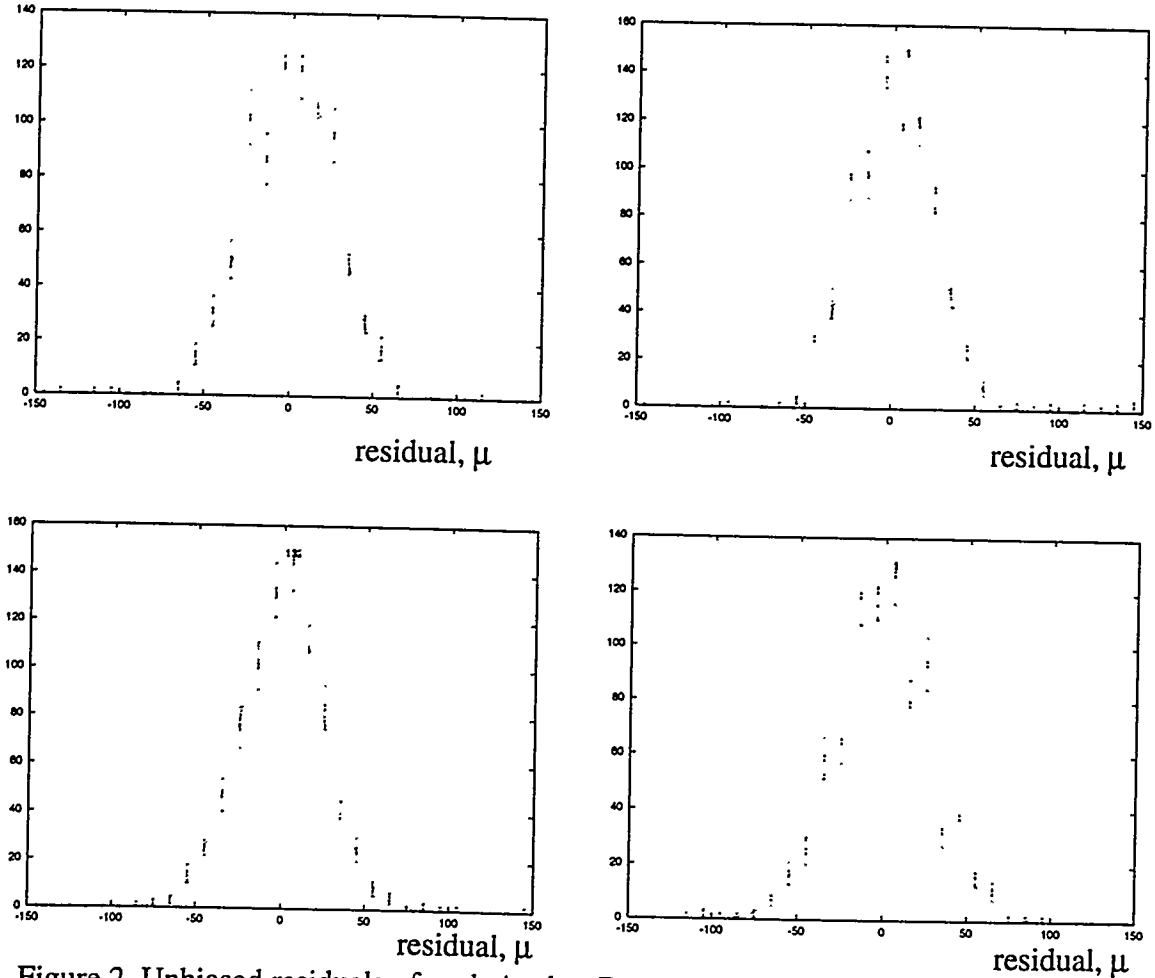

Figure 2. Unbiased residuals of each Anchor Detectors w.r.t fitted tracks.

To interpret these residual distributions, note that (as shown in figure 3, bottom) a track fitted to just three of the four hits will go through the average position of one pair of hits and directly through the remaining hit. Thus the unbiased residual will have a width the intrinsic detector resolution times $\sqrt{2}$. The average unbiased residual of one anchor hit with respect to the track fitted in the other three anchor detector is 24 μ, so one obtains that the resolution of each detector is 17μ (the expected figure is $60\mu/\sqrt{12}=17\mu$). So these distributions give us a cross check on the extracted detector resolutions.

The top of figure 3 shows what happens when a track is fitted to all four anchor plane detectors. The fit selects a track trajectory that passes through the average position of the two hits in each set of anchor plane detectors. The resolution in the vertical position of the track would normally be $17\mu/2.0 = 8.5\mu$.

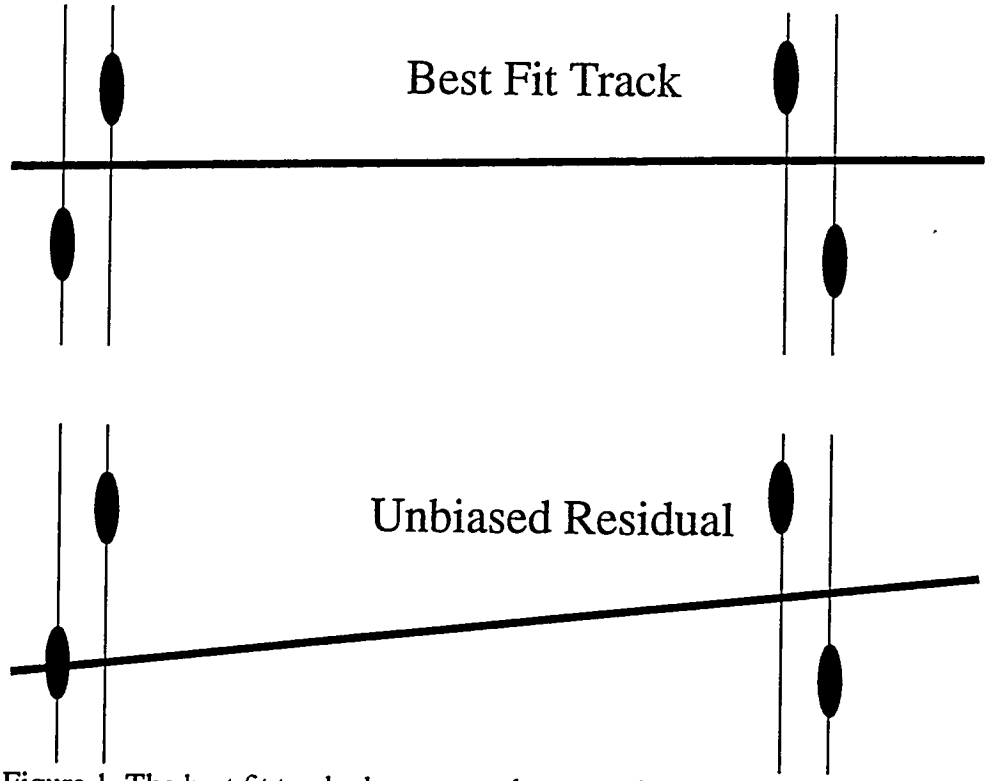

Figure 1. The best fit track always goes between the two hits on each end (top). Unbiased resduals of the anchor detector always have a width equal to the sum in quadrature of the individual anchor detector resolutions.

However, both anchor plane detectors have a step-like relationship between track position and reconstructed hit position and one cannot simply divide by $\sqrt{2}$ when combining measurements. Two pairs of detectors can give anwhere between the same resolution to half the resolution of a single detector. The actual resolution will depend on uncontrollable features of the arrangement, such as the strip-to-strip alignment, the beam angle, or the beam width. It should vary between 6 and 12 μ however. 6 μ would be a small uncertainty, however 12 μ would be a rather large one when one is talking about measuring resolutions as low as 15 μ or less. In other words, for this configuration it is rather difficult to predict the resolution of the tracker. In the resolution measurements quoted here, 8.5 μm track error has been has been "subtracted in quadrature" from the DUT residual in order to determine detector resolution.

Signal, Noise, and Signal-to-Noise Ratio: For those clusters lying within the 200 μ window (100 μ for ϕ scans) , the pulse height is plotted for both rϕ and z sides. The resulting pulse height distribution is fitted to a Landau distribution. Convolution with a Gaussian was found to affect the results very little and so was dropped. The path length is normalized to 300 μ and then the cluster pulse height is divided by the detectors peak D-noise to get the signal to D-noise value. Exact values for each of the runs is given in Appendix A. A summary for each detector is given in table 3. The values given in Table 3 for signal to noise are averages over all runs at full bias. The signal-to noise ratio could not be determined for DB17 (Micron B-type) because it was impossible to recognize the pulse-height distributions as Landau, for DB15 (Micron D-type) on the z-side because the pulse height was too low, possibly due to underdepletion, also for the z-side of DB12 (an SI B type detector) and the ϕ side of DB13 (a SDC stereo detector) because of low pulse height.

Table 3: Summary of Signal-to-Noise Measurements

Detector	Runs	rϕ Signal	rϕ Noise	rϕ S:N	z Signal	z Noise	z S:N
DB8	143, 145-9,151	11.0	.91	12.1	11.3	1.06	10.7
DB1	178,214-7	10.1	0.95	10.6	10.6	1.19	8.9
DB20	290,296	6.8	0.90	7.5	10.1	0.99	10.2
DB17	286-7	----	1.18	----	----	1.14	----
DB15	59,62-65	5.4	.99	5.5	----	1.15	----
DB19	303,307,309	9.4	0.78	12.0	12.6	0.90	14.0
DB21	200,205-9,225,227	10.9	0.72	15.2	11.0	1.10	10.0
DB12	274-5	6.8	0.89	7.6	----	0.92	----
DB29	162,164-7,169,171	9.9	1.24	8.0	9.8	1.00	9.8
DB25	108-112	8.6	1.19	7.2	9.6	1.31	7.3
DB23	239, 241	10.1	1.14	8.9	11.1	1.09	10.2
DB13	248-9	----	0.95	----	9.5	0.94	10.1

Resolution vs Angle: The unbiased residuals of each detector was calculated for each run. This unbiased residual is the distance in 3-D space between the hit centroid position and the track, as shown in figure 3, and so differs from the usual definition by a factor of 1/cosθ. The width of the unbiased residual distribution gets a contribution from the fitted track uncertainty taken to be 8.5μ; this 8.5 μ is "subtracted in quadradure" from the width of the unbiased residual distribution in order to get the resolution of the detector. A full set of resolution measurements can be found in the Appendix; however; Figure 4 shows the resolution vs η of all detectors in which an η scan

was performed and Table 4 shows the resolution vs. ϕ angle for detectors in which a ϕ scan was performed. It should be remembered that the track position resolution is not well known and the values in table 4, in particular, suffer from large errors.

Table 4: Resolution vs. ϕ angle

Detector	resolution 0^o	resolution 15^o
DB23	20	19
DB13	21	-----
DB21	30	27
DB12	19	19
DB19	13	14
DB20	17	14
DB17	17	16

Conclusions: The principal results of the test beam are contained in table 3, table 4, and figure 4. The signal-to-noise measurements indicate disappointing values, expected to be much higher for the small detectors used in the beam test. Is this due to a low signal or a large noise?

The gain of the SVXII chip was determined by pulsing the front end electronics through a known calibration capacitance. This was performed on several detectors, and also through external capacitors, in order to check the stability of the method. This consistently gave gain figures of about 1330 counts with an error of about 10%.

Independent attempts to predict the noise from probe station measurements of capacitance combined with SVXII chip characteristics show a gain of the SVXII chip, operating at the same ramp as during the KEK run of 1 ADC count/1330 electrons. The expected noise is of course detector dependent, and includes contributions from the chip noise, the shot noise, and the Johnson noise of the bias resistor. Three of the detectors (DB1, DB20, and DB25) have been probed after the beam test at Fermilab and at Purdue; the measurement of leakage current, bias resistance and detector capacitance can be used to predict the detector noise, and the numbers are found to agree well on the z side, and to within about 20% on the rϕ side. The comparison is shown in Table 5.

Table 5: Comparision Noise Expecation to Measurement

	$Noise_{Expected}/Noise_{Measured}$	
Detector	rϕ	z
DB1	81%	89%
DB20	83%	102%
DB25	87%	101%

These measurements and calculations generally confirm the noise figures on the z-side and are close to explaining the noise on the rϕ side. The signal however is a mystery. One would expect that all detectors should have given a signal of ~18.8 ADC counts, whereas 12.6 was the highest observed signal in any detector. Monte Carlo Studies

One potential source of low charge collection efficiency is the late arrival of particles within the time window of the trigger, so that the signal has insufficient time to rise. This has been studied with a simple Monte Carlo[4] and it is found that this effect is unlikely to account for more than about 14%.

The conclusion about signal to noise is that no single effect accounting for low signal-to-noise can be identified at the present time, although it is possible that several 10% effects all contribute. test-stand studies with laser, source, and/or cosmic rays are now critically needed for an understanding of this basic detector spec.

The resolution numbers speak for themselves. At normal incidence they are determined by the strip pitch alone. Off-normal incidence, the charge sharing and ultimately the quality of the signal-to noise figure influences the resolution. So under the hypothesis that the detectors were operated in an abnormal mode, one cannot claim that the measured resolutions are typical of these detectors. In a more optimal mode, they would be better.

References:

1) Resolution of Double-Sided Microstrip Silicon Sensors, N. Bachetta et. al, CDF/DOC/TRACKING/PUBLIC/3277

2) Lenny Spiegel, private communication.

3) "SLT: A Class Library for Charged Particle Tracking in a Solenoidal Magnetic Field", Joe Boudreau, CDF/DOC/TRACKING/PUBLIC/2991

4) "Anatomy of the SVXII Pipeline and the KEK Beam Test", Colin Gay, CDF/DOC/SVXII/CDFR/3514

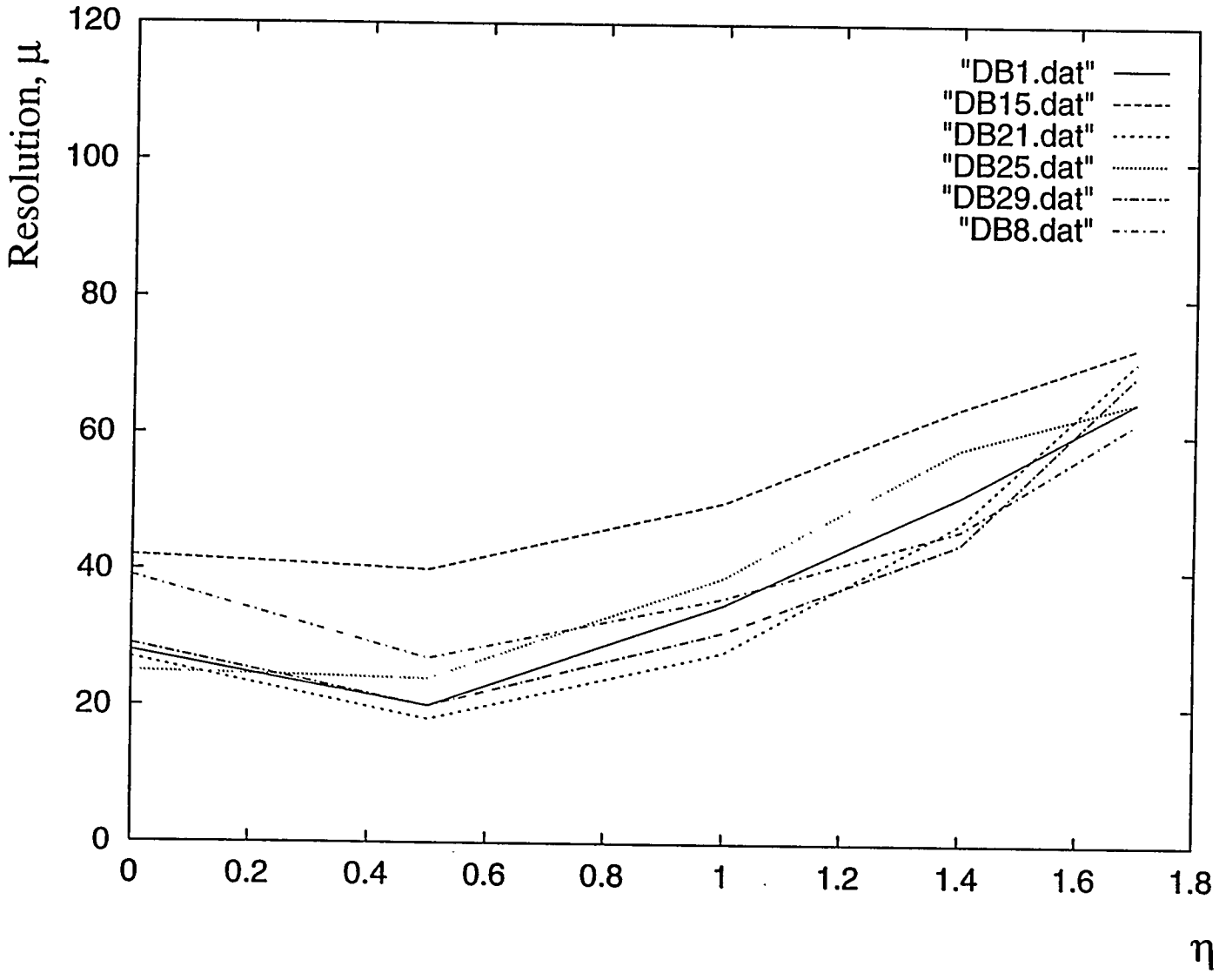
Resolution, μ
120
100
80
60
40
20
0
0
0.2
0.4
0.6
0.8
1
1.2
1.4
1.6
1.8
η
"DB1.dat"
"DB15.dat"
"DB21.dat"
"DB25.dat"
"DB29.dat"
"DB8.dat"

Appendix: Independent measurements of signal-to-noise ratio:

An independent set of measurements of signal-to-noise was done, using the same set of data, at New Mexico. Due to differences in clustering algorithms, common-mode suppression and pedestal measurements, one expects cluster charge depend upon details of the algorithm, and in addition the New Mexico results include a Gaussian smearing term in the Landau fit. Nonetheless, these measurements show general agreement with those discussed in detail in this note. The two measurements of noise agree much more closely.

Table 6 shows the comparison between the signal extracted as explained in this note, and Figure 5 shows a histogram of the deviation between the two sets of measurements.

Table 6: Independent Signal Measurement

Run	Side	Signal (Pitt)	Signal(NM)	% Deviation
145	N	12.7	12.3	3.3
145	P	11.7	11.2	4.5
146	N	12.8	13.0	-1.5
146	P	13.2	13.1	0.8
147	N	17.2	15.5	11.0
147	P	18.6	17.8	4.5
148	N	25.1	23.1	8.7
148	P	27.2	25.8	5.4
151	N	34.7	30.5	13.8
151	P	35.7	34.2	4.4
209	N	12.1	11.6	4.3
209	P	11.1	10.5	5.7
208	N	13.0	11.6	12.1
208	P	12.6	11.9	5.9
207	N	16.4	16.1	1.9
207	P	16.8	17.4	-3.4
200	P	33.8	32.0	5.6
274	P	8.4	7.0	20.0
162	P	9.8	9.5	3.2

Table 6: Independent Signal Measurement

Run	Side	Signal (Pitt)	Signal(NM)	% Deviation
164	P	9.8	9.5	3.2
165	N	11.3	10.8	4.6
165	P	9.7	9.0	7.8
166	P	10.9	10.6	2.8
167	P	15.6	15.3	2.0
169	N	15.2	19.9	-23.6
169	P	22.7	22.1	2.7
171	P	30.8	29.4	4.8
239	N	11.6	11.1	4.5
239	P	11.5	10.0	15.0
248	N	9.8	9.6	2.1
178	N	12.5	10.6	17.9
178	P	10.0	9.5	5.3
290	N	10.8	10.2	5.6
290	P	7.9	6.9	14.5
108	N	11.7	11.1	5.4
108	P	8.1	8.1	0.0
109	N	15.3	11.1	37.8
109	P	9.3	8.6	8.1
110	N	15.8	15.1	4.6
110	P	13.7	13.0	5.4
111	N	14.6	17.1	-14.6
111	P	20.5	18.5	10.8
112	N	14.7	17.4	-15.5
112	P	29.6	26.4	12.1

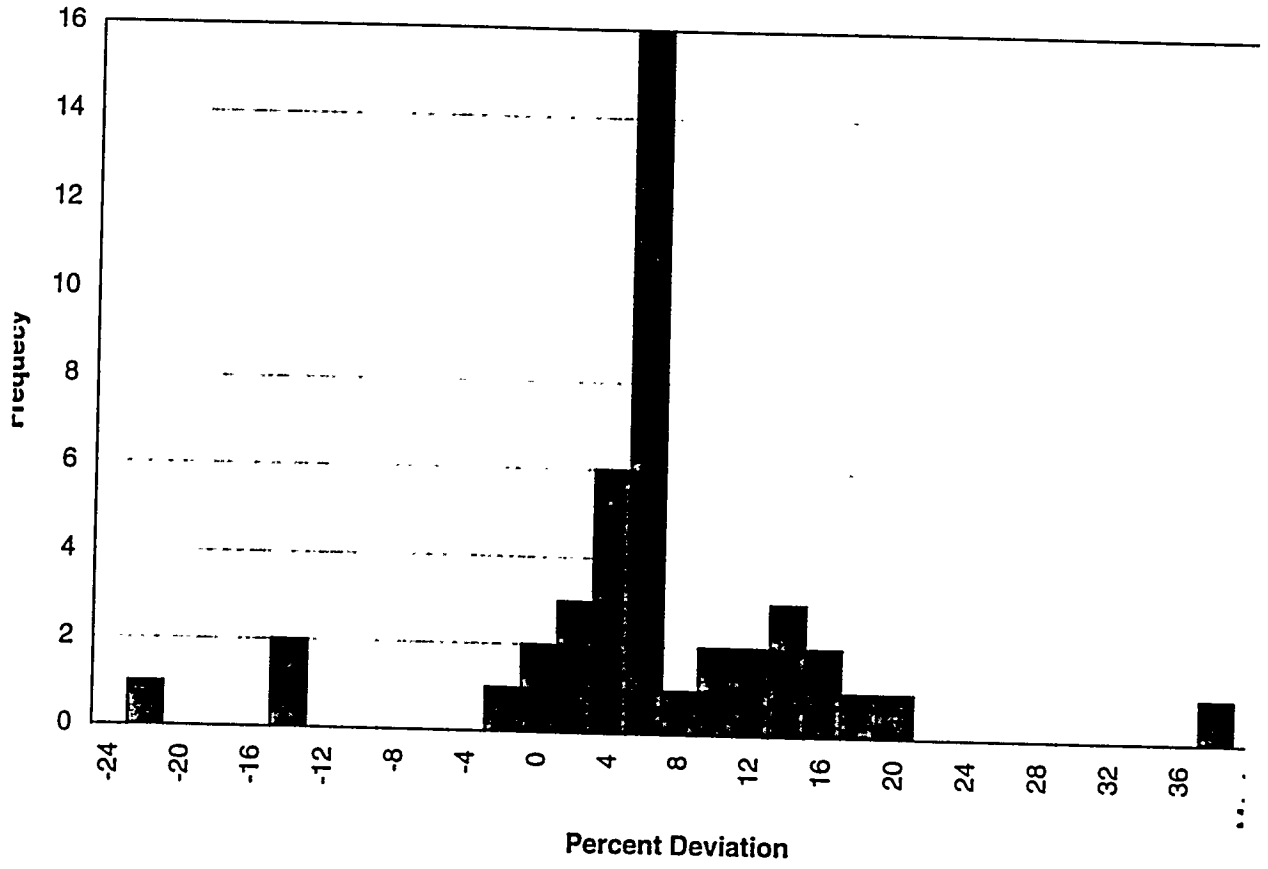

Figure 5: Deviation between the Pittsburgh and New Mexico signal measurements.

Appendix: Raw Measurements Run-by-Run

The following page contains the raw data used in tables throughout this note. The following is a key to the informatio contained therein:

Run:	Run Number
Type:	Type of scan and angle
Detector:	Detector name
Bias:	Bias voltage
#Ev:	Number of events in run
#TR:	Number of tracks found in anchor detectors
REff:	Efficiency of detector under test on rϕ side
RSig:	Fitted peak of Landau distribution on rϕ side
RNoi:	Peak fitted noise on rϕ side
RDN:	Peak fitted differential noise on rϕ side
RS:N:	Signal to differential noise on rϕ side
ZEff:	Efficiency on z side
ZSig:	Fitted peak of Landau distribution on z side
ZNoi:	Peak fitted noise on z side
ZDN:	Peak fitted differential noise on z side
ZS:N	Signal to differential noise on z side.
Resl:	Resolution for this measurement. The side that this applies to depends on the type of scan (η or ϕ)
RFN:	Fraction of channels on rϕ side flagged as noisy
ZFN:	Fraction of channels on z side flagged as noisy

s	Run	Type	Detector	Bias	#Ev	#TR	REff	RSig	RNoi	RDN	RS:N	ZEff	ZSig	ZNoi	ZDN	ZS:N	Resl	RFN	ZFN
0	143	Eta scan 0.0	SI-D-DM-0MR	90.0	3566	1422	0.88	11.2	1.05	0.97	11.5	0.88	12.3	1.22	1.04	11.8	40.0	0.00	0.05
1	145	Eta scan 0.0	SI-D-DM-0MR	90.0	2037	912	0.87	11.2	1.08	0.96	11.7	0.88	12.3	1.26	1.06	11.6	38.7	0.00	0.04
2	146	Eta scan 0.5	SI-D-DM-0MR	90.0	1030	433	0.88	13.1	1.11	0.97	12.0	0.90	13.0	1.24	1.05	10.9	27.2	0.00	0.04
3	147	Eta scan 1.0	SI-D-DM-0MR	90.0	980	385	0.90	17.8	1.07	0.96	12.0	0.86	15.5	1.23	1.06	9.5	35.5	0.00	0.05
4	148	Eta scan 1.4	SI-D-DM-0MR	90.0	3068	975	0.89	25.8	1.12	0.98	12.3	0.83	23.1	1.26	1.07	10.0	45.8	0.00	0.05
5	149	Eta scan 1.7	SI-D-DM-0MR	90.0	2041	685	0.87	33.8	1.12	0.98	12.1	0.78	30.2	1.25	1.08	9.9	65.1	0.00	0.04
6	151	Eta scan 1.7	SI-D-DM-0MR	90.0	5013	3062	0.88	34.2	1.13	0.98	12.4	0.67	30.5	1.21	1.06	10.2	61.3	0.00	0.04
ERAGE:										0.97	12.1				1.06	10.7			
7	59	Eta scan 0.0	MI-D-DM-0MR	40.0	5127	2963	0.77	5.0	0.98	0.98	5.0	0.64	***	1.47	1.15	***	42.0	0.01	0.12
8	62	Eta scan 0.5	MI-D-DM-0MR	40.0	1028	601	0.80	5.3	1.00	1.00	4.8	0.67	***	1.49	1.13	***	40.0	0.00	0.12
9	63	Eta scan 1.0	MI-D-DM-0MR	40.0	1011	597	0.82	8.1	1.01	0.98	5.3	0.67	***	1.48	1.16	***	50.6	0.02	0.12
0	64	Eta scan 1.4	MI-D-DM-0MR	40.0	3057	1777	0.85	11.9	1.00	1.00	5.6	0.66	***	1.54	1.16	***	64.0	0.02	0.14
1	65	Eta scan 1.7	MI-D-DM-0MR	40.0	5124	2807	0.83	16.6	1.02	0.99	6.0	0.62	***	1.55	1.15	***	73.0	0.02	0.14
ERAGE:										0.99	5.5				1.15	***			
2	239	Phi scan 0.0	SDC-DEEP-1MR	120.0	4765	1355	0.86	10.0	1.28	1.14	8.8	0.77	11.1	1.27	1.09	10.2	20.0	0.05	0.02
3	241	Phi scan 15.0	SDC-DEEP-1MR	120.0	1016	206	0.91	11.3	1.28	1.15	9.5	0.75	11.3	1.21	1.07	10.2	19.0	0.04	0.05
ERAGE:										1.14	8.9				1.09	10.2			
4	248	Phi scan 0.0	SDC-2NDPRO-1MR	100.0	5006	1416	0.47	***	1.11	0.95	***	0.63	9.6	1.08	0.93	10.2	21.2	0.02	0.05
5	249	Phi scan 15.0	SDC-2NDPRO-1MR	100.0	1033	197	0.35	***	1.07	0.95	***	0.56	8.4	1.09	0.94	8.7	32.8	0.02	0.05
ERAGE:										0.95	4.0				0.94	10.1			
6	108	Eta scan 0.0	HAM-Delphi-1MR	100.0	5132	3167	0.63	8.1	1.22	1.20	6.7	0.68	11.1	1.45	1.31	8.5	26.2	0.02	0.10
7	109	Eta scan 0.5	HAM-Delphi-1MR	100.0	1040	583	0.71	8.6	1.22	1.18	6.5	0.74	11.1	1.45	1.33	7.4	24.9	0.02	0.18
8	110	Eta scan 1.0	HAM-Delphi-1MR	100.0	1028	515	0.72	13.0	1.22	1.19	7.1	0.67	15.1	1.46	1.32	7.4	40.0	0.02	0.13
9	111	Eta scan 1.4	HAM-Delphi-1MR	100.0	3100	1395	0.74	18.5	1.22	1.17	7.3	0.45	17.1	1.42	1.32	6.0	59.9	0.02	0.14
0	112	Eta scan 1.7	HAM-Delphi-1MR	100.0	5018	2371	0.79	26.4	1.24	1.19	7.9	0.29	17.4	1.44	1.31	4.7	74.9	0.02	0.14
ERAGE:										1.19	7.2				1.31	7.3			
1	200	Eta scan 1.7	SI-B-DM-0MR	100.0	4872	3007	0.98	32.0	0.77	0.73	15.4	0.57	28.5	1.22	1.06	9.6	70.8	0.00	0.02
2	205	Eta scan 1.4	SI-B-DM-0MR	100.0	3163	1723	0.98	24.2	0.78	0.72	15.6	0.76	21.9	1.28	1.16	8.8	47.2	0.00	0.02
3	206	Eta scan 1.0	SI-B-DM-0MR	100.0	1070	534	0.99	17.6	0.77	0.73	15.6	0.92	16.4	1.30	1.19	8.9	26.7	0.00	0.04
4	207	Eta scan 1.0	SI-B-DM-0MR	100.0	1038	508	0.98	17.4	0.77	0.73	15.5	0.92	16.1	1.29	1.19	8.7	28.3	0.00	0.04
5	208	Eta scan 0.5	SI-B-DM-0MR	100.0	1068	503	0.99	11.9	0.77	0.72	14.6	0.91	11.6	1.29	1.21	8.5	17.7	0.00	0.05
6	209	Eta scan 0.0	SI-B-DM-0MR	100.0	5209	2400	0.98	10.5	0.76	0.72	14.6	0.85	11.6	1.30	1.19	9.8	26.9	0.00	0.04
7	225	Phi scan 0.0	SI-B-DM-0MR	100.0	1050	613	0.93	11.3	0.74	0.70	16.0	0.94	12.0	1.00	0.88	13.6	29.7	0.00	0.00
8	227	Phi scan 15.0	SI-B-DM-0MR	100.0	1475	865	0.94	10.3	0.71	0.69	14.3	0.94	12.2	1.03	0.89	13.3	26.9	0.00	0.00
ERAGE:										0.72	15.2				1.10	10.0			
9	274	Phi scan 0.0	SI-B-DM-0.25MR	95.0	4850	2636	0.91	7.0	1.31	0.89	7.8	0.05	***	3.35	0.94	***	18.8	0.02	0.34
0	275	Phi scan 15.0	SI-B-DM-0.25MR	95.0	1006	470	0.91	6.2	1.20	0.91	6.6	0.16	***	3.16	0.90	***	18.9	0.01	0.34
ERAGE:										0.89	7.6				0.92	***			
1	178	Eta scan 0.0	MI-A-DM-1MR	80.0	1014	601	0.86	9.5	0.94	0.94	10.1	0.92	10.6	1.27	1.18	9.0	28.3	0.00	0.01
2	214	Eta scan 0.5	MI-A-DM-1MR	100.0	1042	643	0.79	11.0	0.92	0.95	10.3	0.94	12.0	1.30	1.20	8.9	20.4	0.01	0.01
3	215	Eta scan 1.0	MI-A-DM-1MR	100.0	1023	658	0.82	15.1	0.95	0.96	10.3	0.93	16.5	1.31	1.20	8.9	34.7	0.01	0.01
4	216	Eta scan 1.4	MI-A-DM-1MR	100.0	2296	1434	0.82	22.0	0.96	0.95	10.8	0.80	22.8	1.32	1.19	8.9	50.8	0.01	0.01
5	217	Eta scan 1.7	MI-A-DM-1MR	100.0	3143	1322	0.82	29.2	0.95	0.94	10.9	0.60	29.7	1.32	1.20	8.8	65.0	0.01	0.01
ERAGE:										0.95	10.6				1.19	8.9			
6	303	Phi scan 0.0	SI-A-DM-0MR	87.0	951	200	0.82	9.5	0.89	0.77	12.4	0.90	12.9	1.03	0.90	14.3	13.3	0.00	0.00
7	307	Phi scan 0.0	SI-A-DM-0MR	87.0	1886	424	0.77	9.2	0.90	0.78	11.8	0.89	12.4	1.03	0.90	13.8	13.5	0.00	0.00
8	309	Phi scan 15.0	SI-A-DM-0MR	87.0	1011	229	0.73	9.7	0.89	0.78	12.0	0.86	13.0	1.00	0.89	14.0	13.7	0.00	0.00
ERAGE:										0.78	12.0				0.90	14.0			
9	162	Eta scan 0.0	SI-B-DM-1MR-Be	95.0	1049	447	0.59	9.5	1.22	1.24	7.6	0.73	11.4	1.23	0.99	11.5	29.0	0.00	0.09
0	164	Eta scan 0.0	SI-B-DM-1MR-Be	90.0	967	416	0.60	9.5	1.24	1.26	7.6	0.68	11.0	1.20	0.99	11.1	30.0	0.00	0.09
1	165	Eta scan 0.0	SI-B-DM-1MR-Be	90.0	2051	889	0.58	9.0	1.24	1.25	7.2	0.70	10.8	1.23	1.00	10.8	29.2	0.00	0.09
2	166	Eta scan 0.5	SI-B-DM-1MR-Be	90.0	1052	426	0.60	10.6	1.25	1.24	7.6	0.68	10.8	1.23	0.99	9.6	19.8	0.00	0.09
3	167	Eta scan 1.0	SI-B-DM-1MR-Be	90.0	1020	422	0.58	15.3	1.24	1.23	8.0	0.69	14.5	1.23	1.00	9.4	31.2	0.00	0.09
4	169	Eta scan 1.4	SI-B-DM-1MR-Be	90.0	2962	1165	0.64	22.1	1.26	1.25	8.2	0.59	19.9	1.22	1.01	9.1	44.3	0.00	0.09
5	171	Eta scan 1.7	SI-B-DM-1MR-Be	90.0	4863	1851	0.65	29.4	1.24	1.23	8.5	0.44	24.5	1.25	1.02	8.5	69.0	0.00	0.10
ERAGE:										1.24	8.0				1.00	9.8			
6	290	Phi scan 0.0	MI-B-DM-1MR	80.0	923	161	0.77	6.9	0.88	0.91	7.6	0.69	10.2	1.16	1.01	10.1	17.4	0.04	0.04
7	296	Phi scan 15.0	MI-B-DM-1MR	80.0	911	200	0.69	6.9	0.89	0.90	7.4	0.62	10.5	1.17	0.98	10.3	14.1	0.04	0.04
ERAGE:										0.90	7.5				0.99	10.2			
8	286	Phi scan 0.0	MI-B-DM-1MR-Be	100.0	2971	882	0.85	****	1.24	1.19	****	0.15	***	1.33	1.14	***	16.7	0.02	0.11
9	287	Phi scan 15.0	MI-B-DM-1MR-Be	100.0	946	288	0.81	***	1.25	1.18	***	0.08	***	1.34	1.14	***	15.6	0.01	0.16
ERAGE:										1.18	***	1.14	***						

Appendix B

April 26, 1996
CDF/ANAL/BOTTOM/CDFR/3393
version 1.1

Search for $B_c^{\pm} \to J/\psi + \mu^{\pm}$ in the Run 1a and Run 1b Data

P. Singh, T. Huffman, E. Engels Jr. and P. Shepard
University of Pittsburgh
Pittsburgh PA 15260

Abstract

The bottom-charm meson B_c is predicted by the Standard Model. If it exists the decay mode $B_c \to J/\psi + \mu^{\pm} + X$, where $J/\psi \to \mu^+\mu^-$ would result in copious tri-muon events from a secondary vertex. A search for the B_c in this decay channel in Run 1a and Run 1b data is presented in this note with a limit on $\sigma \times BR(B_c^{\pm} \to J/\psi + \mu^{\pm})/\sigma \times BR(B^{\pm} \to J/\psi + K^{\pm})$ @ 95% C.L. for various assumed B_C lifetimes.

1 Introduction

The Standard Model predicts the existence of the bound state of the bottom and the charm quark; the B_c meson. Its mass is calculated to be in the range of 6.194 – 6.292GeV/c^2[1]. The production of B_c is dominated by the b quark fragmentation. The calculated fragmentation probabilities for $\bar{b} \to B_c$ and $\bar{b} \to B_c^*$ are approximately 3.8×10^{-4} and 5.4×10^{-4} [4]. The B_c decay final state with J/ψ is prominent. Although theorists differ on their calculations of the branching ratio, the branching ratio for $J/\psi + \mu +$ X is at least 1.5% [2][5].

2 Monte Carlo Studies

The monte-carlo study of the B_c was done by generating B_c's using BGENERATOR [6] and decaying them using the CLEOMC Monte Carlo [16]. BGENERATOR was forced to produce 100% B_c (50% B_c^+ and 50% B_c^-). All the B_c's were forced to

decay to $\psi + \mu + \nu$. The detector was simulated using QFL, and the trigger simulation was done using DIMUTG [13]. In BGENERATOR the minimum b quark P_t was required to be greater than 5 GeV/c. The B_c mass was set to 6.258 GeV/c^2 .

The difficulty in searching for $B_c \to J/\psi + \mu + X$ decays is that there is at least one neutrino which is undetectable. Therefore the invariant mass distribution of the three muons is very broad. Figure 1 shows such a mass plot made from the GENP information (i.e. before the detector simulation). In order to extract signal from background, we studied the transverse mass distribution. Assuming B_c's momentum is $\vec{P}_b$, the three muons have momenta $\vec{P}_1, \vec{P}_2$ and $\vec{P}_3$, the transverse mass is

$$M_T = E_1 + E_2 + E_3 + E_\nu$$

where,

$$E_i = \sqrt{(\vec{P}_i - \frac{(\vec{P}_i \cdot \vec{P}_b)\vec{P}_b}{{P_b}^2})^2 + m_\mu^2}, \quad E_\nu = \sqrt{(\Sigma\vec{P}_i - \frac{(\Sigma\vec{P}_i \cdot \vec{P}_b)\vec{P}_b}{{P_b}^2})^2}, i = 1, 2, 3.$$

The transverse mass for B_c calculated with GENP bank information is shown in Fig. 2. This plot shows that there is a sharp cutoff at the B_c mass. However if the GENP bank is not used and the same plot is made using the data after the detector simulation, then $\vec{P}_b$ is unknown in the reconstructed events. In this case it is replaced by $\vec{L}_b = \vec{X}_{sec.} - \vec{X}_{prim.}$ where $\vec{X}_{prim.}$ and $\vec{X}_{sec.}$ are the primary and secondary vertices. Figure 3 shows the transverse mass distribution after the detector simulation. In this plot the sharp cutoff at the B_c mass as in Fig. 2 disappears. This is due to the poor resolution on the z-position of the vertex measurement. Thus the conclusion was made that the transverse mass distribution in $B_c \to J/\psi + \mu + X$ search will not be helpful with the current detector.

Next we tried to remove the z component from the transverse mass calculation to see if we could improve the signal spectrum. This was done by defining one dimensional transverse mass as follows:

$$M_{TT} = E_T(1) + E_T(2) + E_T(3) + E_T(\nu)$$

where,

$$E_T(i) = \sqrt{(\vec{P_T(i)} - \frac{(\vec{P_T(i)} \cdot \vec{P_T(b)})\vec{P_T(b)}}{{P_T(b)}^2})^2 + m_\mu^2}$$

and

$$E_T(\nu) = \sqrt{(\Sigma\vec{P_T(i)} - \frac{(\Sigma\vec{P_T(i)} \cdot \vec{P_T(b)})\vec{P_T(b)}}{{P_T(b)}^2})^2}, i = 1, 2, 3.$$

Figure 4 shows the M_{TT} distribution from GENP information and Fig. 5 shows the M_{TT} distribution after QFL simulation in which $\vec{P}_T(b)$ was replaced with $\vec{L}_{xy}$. First we noticed there is no sharp cutoff in the M_{TT} distribution. Second we saw a lot of smearing after QFL simulation. This is partly because we replaced $\vec{P}_T(b)$ with $\vec{L}_{xy}$ and our resolution on $\vec{L}_{xy}$ magnitude and direction is not good enough.

A more straight forward approach then, was to look at the trimuon mass distribution. The trimuon invariant mass was used in this search since it did not depend on any vertex information like M_{TT}. Figure 6 shows the three muon invariant mass distribution after the detector and the trigger simulation [13]. This data sample is different from the sample that was used to study the transverse mass (it has more statistics). The P_t distribution of the $J/\psi + \mu$ and the muon from the B_c is shown in Fig. 7. The sharp cutoff in the P_t spectrum of the muon from the B_c at 3 GeV/c is due to the fact that we cut on the P_t of this muon at 3 GeV/c . Figure 8 shows the pseudo-$c\tau$ and the L_{xy} distribution for the $J/\psi + \mu$. The impact parameter and the impact parameter significance for the muon from the B_c is shown in Fig. 9.

3 Data Analysis

The data sets used in this analysis were the inclusive J/ψ datasets on cdfsga. For Run 1a we used the data with 7_11 tracking (files with extension *.psix_5b) and for Run 1b we used the Production data with the 7_12 version of DO_SVX_PAD with Internal3 SVX alignments (files with extension *.psia_7b) . The aim of the analysis was to look for events with three muons from a secondary vertex. For the purpose of this analysis the invariant mass range of interest for the three tracks was defined to be between 4 and 6 GeV/c^2. This range was chosen after looking at the three track invariant mass distribution from the monte-carlo. The primary vertex for the events was obtained from the run average beam position and the errors on it were set to 40 μm. The vertex fitting was done using CTVMFT [8]. In CTVMFT the two J/ψ muons were mass constrained to the world average J/ψ mass. However, since these event are not fully reconstructed there CTVMFT was not required to do the pointing constrain. The cuts used in this analysis are shown in Table 1.

The combined Run 1a and Run 1b J/ψ mass distribution is shown in Fig. 10. There are 194431 $\pm$ 1371 events under the peak. Figure 11 shows the invariant mass distribution of J/ψ and the third muon for Run 1a and Run 1b for a $c\tau^*$ cut of 60 μm. In Fig. 12 the P_t spectrum of the $J/\psi + \mu$ is plotted. Figure 13 shows the pseudo $c\tau$ and the L_{xy} distribution of $J/\psi + \mu$ and Fig. 14 show the impact parameter and impact parameter significance distribution for the third muon. The number of events in the signal region with different $c\tau$ cuts are summarized in Table 2

Table 1: Summary of the cuts used in the analysis.

	Cuts
Muon Selection	$\chi^2_x < 9$ and $\chi^2_z < 12$ for type 1, 3, and 5 muons $\chi^2_x < 9$ For type 4 muons Muon $P_t > 1.4$ GeV/c
J/ψ Selection	Muon types allowed 1, 3, 4, and 5 Di-muon pair should pass the J/ψ trigger Both the muons should be SVX muons. J/ψ mass should be within 50 GeV of the PDG J/ψ mass. J/ψ $P_t > 4.0$ GeV/c CTVMFT is used to fit the muons to a vertex.
Cuts on the third muon.	Third muon should be CMU/CMP (type 3) muon. Third muon $P_t < 3.0$ GeV/c It should be a SVX muon.
Cuts on the three track vertex	CTVMFT is used to fit the two tracks to a vertex. J/ψ muons are mass constrained to the PDG J/ψ mass The three tracks are vertex constrained. Prob(χ^2) > 1% *J/psi* and the muon are required to be in the same hemisphere $c\tau^* > 60, 85, 100, 150$ μm.
Cuts on $J/\psi K$	K $P_t > 3.0$ GeV/c K should point to the CMU/CMP fiducial region K should be a SVX track Prob(χ^2) of the vertex fit be > 1% J/ψ and K be in the same hemisphere $c\tau > 100$ μm.
Covariance scaling	In Run-1a the scale factor is set to 2.0 In Run-1b the scale factor is set to 2.4

4 Background

The irreducible background in this channel is likely to come from fake muons (punch-trough and decay in flight), mis-measured tracks and the normal $b\bar{b}$ events. Fake J/ψ's too contribute to the background. The fake J/ψ's can contribute in two ways, (1) fake J/ψ and fake muon and (2) fake J/ψ and a good muon. Case (1) is automatically included in our background estimates for the fake muons. Case (2) is too small (<.2 events) and is ignored in the overall estimate of the background. The overall shape of the three track invariant mass distribution for the background will be given by the the plot in Fig. 15.

Table 2: Summary of the Events in the Signal Region for Run 1a and Run 1b

$c\tau^*$ cut μm	Run 1a	Run 1b	Run 1a + Run 1b
60μm	3	14	17
85μm	3	11	14
100μm	2	11	13

4.1 $B\bar{B}$ Background

The signature of the $B_c \rightarrow J/\psi + \mu + X$ signal is a displaced vertex with three muons. $B\bar{B}$ pairs produced during the $p\bar{p}$ collision can fake such a signature. This happens when one of the B's produced, decays into J/ψ + X and the other B decays into μ + X. Further if the J/ψ decays into a $\mu\mu$ pair then there would be three muons in the event. In a few cases these muons may make a vertex that passes our vertex cuts. If such an event also passes the other cuts of our analysis, it would be an irreducible background to the B_c signal.

This background was estimated by using monte-carlo. $B\bar{B}$ pairs were generated using BGENERATOR [15], CLEOMC [16] was used to decay the particles. One of the B's was forced to decay into J/ψ + X and the other was allowed to decay naturally. The detector was simulated using QFL and the simulated data was required to pass the dimuon trigger. The analysis code was run on the simulated data and the events picked up by the analysis code were checked for the third muons which came from decay in flight or punch through. Any such contribution was removed from the set of events that were picked up. The resulting number of event was then the $B\bar{B}$ background for the generated monte-carlo.

The number of J/ψ's from B's in actual data was used to normalize the $B\bar{B}$ background obtained from monte-carlo to Run 1a or Run 1b data. We define the normalization factor as,

$$R = \frac{N_{J/\psi}^{data}}{N_{J/\psi}^{MC}} \times F_B$$

where, F_B is the fraction of the J/ψ's in data that come from B's, $N_{J/\psi}^{data}$ is the number of J/ψ's passing our cuts in data and $N_{J/\psi}^{MC}$ is the number of J/ψ's in the monte-carlo sample. $F_B = 19.6 \pm 1.5\%$ [20].

Since the SVX and the triggers are different for the two runs the $B\bar{B}$ monte-carlo data was generated for both Run 1a and Run 1b. We get R as 0.117 for Run 1a and 0.357 for Run 1b. The number of the background events is obtained by using the following formula:

$$\text{Number of Background events} = N^{MC}_{J/\psi+\mu} \times R$$

Where $N^{MC}_{J/\psi+\mu}$ is the number of events picked up by the analysis code when it was run on $B\bar{B}$ monte-carlo. Table 3 summarizes the $B\bar{B}$ background for various $c\tau^*$ cuts for both the runs.

Table 3: Summary of the $B\bar{B}$ Background for Run 1a and Run 1b

$c\tau^*$cut	Run 1a	Run 1b	Run 1a + Run 1b
60μm	0.23±0.16	1.07±0.62	1.30±0.64
85μm	0.23±0.16	1.07±0.62	1.30±0.64
100μm	0.23±0.16	0.71±0.51	0.94±0.53

4.1.1 Systematic error on the $B\bar{B}$ background

The major systematic errors in this estimate come from F_B and the trigger simulation. The systematic error due to F_B is 7.7% and due to the trigger simulation it is 4% . Hence the total systematic error for this estimate is 17.4%.

4.2 Punch-through Background

One of the backgrounds that can fake a $B_C \rightarrow J/\psi + \mu + X$ signal is due to the fact that other particles in a J/ψ event can travel through the calorimeter and the CMP steel without showering. This probability is about one in 500; however, there are a large number of tracks meeting the cut requirements and this tends to offset the fact that most of them will be absorbed before reaching the CMP.

In order to estimate the punch-through background the analysis code was first run on the data without requiring that the third track be a muon. All of the analysis cuts that make sense to apply to a non-muon third track are then applied to the resulting sample of J/ψ+track events, including the requirement that the track be pointing in a direction that could intercept the CMU+CMP fiducial region.

Shown in Figure 15 is the J/ψ+track distribution where the additional track is assumed to be a muon for the purposes of determining its properties. The data in this histogram are from Run 1b only and the J/ψ was required to pass the dimuon trigger. One can see the definite peak due to $B \rightarrow J/\psi + K$ events where the kaon has been assigned a muon mass.

An accounting of the amount and kinds of materials in the detector through the CMU has been done and implemented in the subroutine CMWINT.[10] This program uses the cross sections from the Particle Data Group (PDG)[12] to obtain the shape of the nuclear interaction lengths in CDF as a function of the particle energy. In this case, we expect to only receive significant punch-through backgrounds from kaons and pions. The subroutine output is normalized at high energy to the particle cross sections measured in Caroll, et al.[11] and returns the number of nuclear interaction lengths traversed by a particle at normal incidence to the calorimeter. This code was modified to account for the upgrades that have taken place since the 88-89 run. The modification includes the additional steel in the CMP and was done by scaling the interaction lengths at 100 GeV/c by the values indicated in PDG[12] for an additional 60cm of steel. The energy lost by a minimum ionizing particle in the detector material can also have an effect by slowing the particle down and changing the probability with which it interacts. This effect was also included in the punch-through probability calculation.

Using Figure 15 as a starting point, the events were weighted by the probability that each would punch through the detector to produce a fake CMP muon. This was done according to the formula:

$$P(\lambda) = exp(-\frac{\lambda}{\sin\theta})$$

where $\lambda(E)$ represents the number of interaction lengths for a particle of energy E at normal incidence and θ is the angle of the track with respect to the calorimeter along the beam-line. As of this writing, the angle of the track with respect to the muon upgrade walls in the $r-\phi$ projection is not taken into account. All tracks are assumed to punch through the CMP at normal incidence in the $r-\phi$ projection.

It is assumed that all particles faking muons will reconstruct regardless of the offline CMP reconstruction efficiency. The resulting weighted distributions are shown in Figure 16. In the upper histogram, it is assumed all the tracks in Figure 15 are pions. The lower two histograms show what happens when all the observed tracks are assumed to be kaons. The interaction probability per unit material is smaller for the positive kaon and this causes the positive kaons to be approximately ten times more likely to punch through the CMU and CMP over negative kaons or pions.

Adding up the weighted events in the B_C signal region yields 1.77 ± 0.08 events if one assumes all of the tracks are kaons and 0.23 ± 0.01 events for the pion assumption. The uncertainties quoted here are statistical. It is clear that assuming all of the tracks come from kaons is incorrect, however it is not clear what fraction should be applied. Nearly all of the tracks in the miss-identified $J/\psi + K$ peak are kaons. The background below an invariant mass of 5.1 GeV/c^2 consists of J/ψ+track from other B meson decays. Consequently, production of strange quarks is preferred causing an abundance of kaons over normal $J/\psi+X$ background. In the absence of more detailed

information, this analysis will assume that all of the punch-through candidates are kaons. Furthermore, to determine whether the calculation is correct and understand the systematic uncertainties, we shall focus on the region of the $J/\psi + K$ excess where the particle type is well understood. This region is from 5.15 to 5.30 GeV/c^2, which is below the true B meson mass because the third track has been assigned a muon mass here.

4.3 Punch through background systematic uncertainties

There are two dominate sources of uncertainty in this calculation. The first involves the lack of knowledge of the interaction cross sections of the punch-through candidates with the materials in the detector. The second is uncertainty in the kind and amount of matter encountered by a particle as it traverses the calorimeter. A crosscheck can be done to determine the overall systematic error in the calculation of the punch-through probability by examining the predictions for the invariant mass region around the $J/\psi + K$ mass peak and comparing this to the data.

The code that allows one to predict the number of punch-through fakes in the signal sample will also predict how many tracks would punch through to the CMU alone. Without requiring the added steel in the CMP one would expect most of the positively charged events in the B^+ region to be punch-through events.

Duplicating the procedure outlined above for the tracks in the $B \rightarrow J/\psi + K$ region in Figure 15 we require only the acceptance and material through the CMU. The following predictions for the mass region from 5.15 to 5.30 GeV/c^2 are obtained:

- 3.32 ± 0.46 positive events.
- 0.65 ± 0.08 negative events.

Figure 17 shows the numbers and event distributions for kaons from the calculation of the punch through probability. This was applied to the initial number of tracks pointing toward the CMU. The data from run 1b, requiring at least a CMU muon for the third track, are shown in Figure 18. The data yield 3.0 $J/\psi + K^+$ events and 1.0 $J/\psi + K^-$ event in the $B^\pm$ mass region.

One problem with this comparison is that the CMU data in the $J/\psi + K$ region, though enriched in punch-through, will also contain possible backgrounds. For example, the kaon can decay into a muon and if the tracking chamber picks up the kaon track instead of the muon, then the decay would still reconstruct in the $J/\psi + K$ region. This is also near the most likely location for actual B_C signal events to appear in the distribution. To get some idea of how much of the data in the $J/\psi + K$ mass region is background we can look in the same mass region but require

a CMP muon as well. We obtain 2 positive events and that same negative event having CMU/CMP stubs which pass the cuts. It is approximately 10 times less likely that a K^- would punch thorough the CMP than a K^+. Consequently there is an indication that approximately one event of background exists in the CMU data in the B^+ mass region based on the fact that one event is present in the B^- region.

The systematic error is set as the difference between the predicted number of events between 5.15 and 5.3 GeV/c^2 for the positive tracks versus the actual punch through from CMU data of 2 events, or $\pm$39%. The final numbers for the punch through background in the mass region from 4.0 to 6.0 GeV/c^2 is obtained by assuming that all of the events are kaons. The whole exercise is then repeated for Run 1a. The results of this estimate are summarized in Table 4

Table 4: Summary of the Punch-through Background for Run 1a and Run 1b

$c\tau^*$ cut	Run 1a	Run 1b	Run 1a + Run 1b
60μm	0.43$\pm$0.17	1.77$\pm$0.69	2.20$\pm$0.71
85μm	0.38$\pm$0.17	1.56$\pm$0.62	1.94$\pm$0.64
100μm	0.34$\pm$0.14	1.50$\pm$0.56	1.84$\pm$0.58

We believe that this is a conservative estimate. We have shown using a known sample of kaons that the calculation properly predicts their numbers within statistics given the total number of input tracks. Furthermore we have assumed that all of the tracks are kaons for the purposes of calculating the punch through background. Since the positive kaon has a much better chance of faking a muon, this is the worst case.

We can support the conclusion that our estimate of all kaons is conservative by again turning to the CMU only sample and looking at the charge asymmetry in the data in the mass region of interest. The point being that if the background in the entire mass region is dominated by Kaon punch through there would be a large asymmetry in the CMU only data. As pointed out earlier there are 3 positive events and one negative event in the $J/\psi + K$ mass region indicating some excess expected of positive over negative events. However, the CMU data have 16 positive events and 16 negative events from 4.0 to 6.0 GeV/c^2 as shown in Figure 18. The pion punch through probability is the same as the K^- punch through probability, so it is unlikely that the lack of charge asymmetry is due to an excess of symmetric pion punch-through. This evidence in the data supports our conclusion that the estimate of the punch through background is a conservative one.

4.4 Decay in Flight

Pion or kaon decay in flight can contribute to the background to the decay $B_c^{\pm} \rightarrow J/\psi + \mu^{\pm} + X$. This happens when a daughter muon from a pion or a kaon decay makes a good vertex with a J/ψ from a secondary vertex.

In the search for B_c, one of the cuts required that the P_t of the muon decaying from the B_c be greater than 3 GeV/c. With this cut on the P_t, the probability for a pion or a kaon to decay before reaching the muon chambers is small. However there are a large number of pions and kaons present in an event, hence decay in flight makes a significant contribution to the total background. The decay in flight background has the following two components:

- Pions or kaons from the primary vertex that decay in flight and make a good vertex with a J/ψ from a secondary vertex.
- Pions or kaons from a displaced B that decay in flight and make a good vertex with the J/ψ from the B. This usually happens when the pion or the kaon decay towards the end of the CTC or beyond the CTC volume.

4.4.1 Background due to the Pions or Kaons from the Primary Vertex

The estimate of the background due to the decay of the pions or kaons which come from the primary vertex was made using data. CTC tracks in a data event with a J/ψ were selected and were assumed to be pions or kaons. These tracks were forced to decay before the end of the CMU volume. Hadronic interactions was turned on in CDFSIM so that the probability of the particle to interact with the material in the detector before it decayed was taken care of. The decayed tracks were reconstructed and fitted to a vertex with the two muons from the J/ψ. The resulting three track combinations were subjected to all the cuts that were applied to the data. Combinations that passed the cuts were weighted by the probability for the third track to decay before the end of the CMU volume. The background was calculated by summing up the weights of all the three track combinations whose invariant mass falls between 4 and 6 GeV/c^2. This process is described in detail in the following steps:

- Select events from data that have passed the dimuon trigger [13] and have a J/ψ with its two muons in the SVX.
- Select CTC tracks with $P_t > 2.0$ GeV from events selected above and require that these tracks point to the CMU and the CMP fiducial regions.

- The pions and the kaons have different decay kinematics and decay probability, hence the background is first calculated by assuming that all the selected CTC tracks are pions and then it is calculated again by assuming that all the tracks are kaons.

- Depending on what the tracks are assumed to be (pion or kaon), they are allowed to decay using PDECAY[14]. The momenta of the tracks and their daughters are put into a GENP bank.

- A new bank (PVTX) is created and the primary vertex of the event is written to this bank.

- The GENP bank is input to CDFSIM [14] which simulates the passage of the decayed tracks through the detector. The routine SMRVTX[14] in CDFSIM is changed so that it fixes the simulated event vertex to the value written in the PVTX bank.

- TRAKST[14] routine was changed to force the tracks to decay before the end of the CMU volume, and the probability of each track for such a decay was recorded.

- The output from CDFSIM was processed using the 7_12 version of offline reconstruction (Production) .

- The analysis code was then run on the subset of the run 1b dataset that contained the J/ψ's selected earlier. A three track vertex is formed from the simulated track and the two muons from the J/ψ.

- Each three track combination is subjected to the analysis cuts. The combinations that pass all the cuts and have their invariant mass in the signal region (4 and 6 GeV/c^2) are weighted by the probability of the third track to decay before the end of the CMU volume.

- Sum of the weights was the total number of background events.

The CTC tracks selected have a $P_t > 2$ GeV/c and not 3 GeV/c as in the analysis cut for this search. This is done because when a track is decays, it develops a kink, where the kink is larger for the kaons than for the pions. Because of this kink the reconstruction program reconstructs these tracks, with a momentum that is some times higher than the actual momentum of the track. Thus it is possible for a track with $P_t < 3$ GeV/c to pass the 3 GeV/c P_t cut, if it is reconstructed after it decays within the CTC. This effect is shown in Fig. 19. The solid lines in these plots are the P_t of the track before the decay and the dashed ones are the P_t of the track after the decay and the reconstruction. In the top plot all the tracks were assumed to be kaons and in the bottom they are assumed to be pions. It should be noted that more

tracks reconstruct as stiffer tracks after the decay if they are assumed to be kaons as compared to the assumption that they are pions. This is because the muons from a kaon decay have a greater kink than the muons from a pion decay. This "feedup" in the momentum motivated the requirement that the P_t cut on the selected tracks be much below 3 GeV/c. However in this estimate this cut is set at 2 GeV/c. This is done because of the following reason: The third muon is required to be a CMU/CMP muon. A track with a $P_t < 2$ GeV/c would decay into muons with $P_t < 2$ GeV/c. Due to the dE/dX losses a muon with $P_t < 2$ GeV/c would not be able to traverse as far as the CMP. Hence, even though a 1 GeV/c tracks may decay and get reconstructed as a track with $P_t > 3$ GeV, the actual momentum of the daughter muon would be less than 1 GeV/c. A muon with this P_t be unable to reach the CMP and therefor such an event will be rejected.

Figure 20 shows the result of the estimate for this background for about one third of the run 1b data set. The top plot in this figure shows the three track invariant mass distribution when all the tracks are assumed to be pions. The lower plot shows the same thing when the tracks are assumed to kaons. It should be noted that the number of kaon events are less than the number of the pions events. This is because the reconstruction efficiency for a decayed pion is more than the reconstruction efficiency for a decayed kaon. In both these cases one of the most discriminating factors against this background is the requirement that the third track be a SVX track. After weighting the entries in the two plots in Fig. 20 and summing them up for the signal region we get .21 events for the pions and .17 events for the kaons. Since the kaons and the pions in this case are prompts, we used the kaon to pion ratio as 4:1 [22]. Reference [22] give the kaon to pion ratio in $p\bar{p}$ collisions at $\sqrt{s}=$ 1.8 TeV. Assuming the pion to kaon ratio as 4:1, and using the fact that we looked at about one third of the run 1b data, we can calculate the number of background events for Run 1b. This result is scaled to Run 1a, by scaling the Run 1b results by the number of J/ψ's in Run 1a. The results of this calculation are summarized in Table 5.

Table 5: Summary of the Decay in Flight Background from Prompts for Run 1a and Run 1b

$c\tau^*$ cut	Run 1a	Run 1b	Run 1a + Run 1b
60μm	0.14±0.10	0.64±0.49	0.78±0.50
85μm	0.13±0.10	0.61±0.46	0.74±0.47
100μm	0.10±0.08	0.58±0.37	0.68±0.38

4.4.2 Background from Pions or Kaons from Displaced B's

B's which decay into $J/\psi + X$ where the X may contain pions and kaons, if the pions or the kaons decay in flight and still pass the vertex cuts with the J/ψ along with all the other data cuts, the corresponding B event will then contribute to the background. The most likely scenario for this is when the particle decays towards the end of the CTC or decays in the calorimeters before it could shower. In these cases it is likely that the CTC will reconstruct the original particle, yet the muon from the decay will yield a stub in the muon chambers. This stub could be assigned to the reconstructed track.

This background was estimated using monte-carlo. BGENERATOR [15] was used to generate the B's. The generated B's were decayed using CLEO monte-carlo [16]. All the B's were forced to decay into $J/\psi + X$. CDFSIM was used to simulate the detector. The detector simulation was done twice. In the first case the pions and the kaons in the event were forced to decay before the end of the CMU volume with the hadronic interaction enabled in the simulation. In the other case the pions and the kaons were not forced to decay, but were allowed to decay naturally.

The analysis code was run on the two data sets generated above. In the case where the particles were not forced to decay all the analysis cuts were applied, however the requirement that the third track have a CMU/CMP stub was replaced by the requirement that it point to the CMU/CMP fiducial region. The top plot in Fig. 21 shows the three track invariant mass distribution, where the third track is assigned the muon mass. In this case the decays were not forced. There are 310 entries in this plot in the signal region, with 58 events under the mis-identified $J/\psi K$ peak. A similar plot for the run 1b data yields about 520 events in the signal region and 74 events under the mis-identified $J/\psi K$ peak, see Fig. 15. We use the number of events under the mis-identified $J/\psi K$ peak to normalize the monte-carlo to the Run 1b data. The bottom plot in Fig. 21 shows the three track invariant mass distribution for the case where the kaons and the pions were forced to decay. In this plot all the analysis cuts were applied, including the requirement that the third tracks have CMU/CMP stubs. 103 events were picked up in the signal region. To get the number of background events from this plot, the entries in the plot were weighted by the probability of their third track to decay before the end of the CMU volume. If all the tracks are assumed to be pions then the the number of the background events is 1.17 events. If the tracks are assumed to be kaons the number of the background events is 8.15 events. To estimate the background from Fig. 21 we will have to determine the K to π ratio for the third tracks in the bottom plot in Fig. 21. It should be noted that in this case we cannot use the kaon to pion ratio we used in the prompt case.The ratio for this case is determined as follows:

We took a sample of the $B \rightarrow J/\psi + X$ monte-carlo data which had passed the trigger simulation. In this data set we counted the number of K's and π's with $P_t >$

3.0 GeV/c using the information from the GENP bank. The K to π ratio obtained by such a counting gave us the ratio which would exist before any reconstruction was done. We call this ratio the ratio at birth. For our sample N_{kaon}/N_{pion} at birth was 1.38 .

Next we studied how the ratio at birth will be affected when the reconstruction is done. We generated one dataset with $B \rightarrow J/\psi K$ and another dataset with $B \rightarrow J/\psi\pi$. The number of events generated in the two datasets was the same. The kaons and the pions in each data set were forced to decay within any region upto the CMU and the events were simulated through the detector using CDFSIM. Our analysis code was run on the simulated data. After applying all the analysis cuts we got 238 events for the $J/\psi K$ case and 891 events for the $J/\psi\pi$ case, see Fig. 22. This means that if we start with a sample in which K to π ratio is 1:1 at birth, then after reconstruction N_{kaon}/N_{pion} becomes 0.27 . In our case N_{kaon}/N_{pion} at birth was 1.38, hence after the reconstruction N_{kaon}/N_{pion} will be 0.37 . This implies that the bottom plot in Fig. 21 has 27% kaons and 73% pions.

4.4.3 Scaling the Results to Run 1a and Run 1b

To get the estimate of this background for run 1b, the results will have to be scaled by a factor of 1.27. From monte-carlo we have already seen that the sample of the third tracks have 27% kaons and 73% pions. Using this ratio and then scale factor we obtain the number of background events for Run 1b. The Result is scaled to Run 1a by the number of events in the mis-identified $J/\psi K$ peak seen in Run 1a. The results of this estimate are summarized in Table 6.

Table 6: Summary of the Decay in Flight Background from B's for Run 1a and Run 1b

$c\tau^*$ cut	Run 1a	Run 1b	Run 1a + Run 1b
60μm	0.79±0.23	3.87±1.12	4.66±1.14
85μm	0.79±0.23	3.74±1.08	4.53±1.10
100μm	0.79±0.23	3.53±1.02	4.32±1.05

4.4.4 Systematic errors for the Decay in Flight Background

One of the major contribution to the systematic error in the calculation of the background from the decays in flight comes from the efficiency of reconstructing a track that decayed after entering or before exiting the CTC. This is due to the fact that most of the tracks that decay after the CTC will be reconstructed by the CTC and will

pass as good tracks. However when a track decays with in the CTC, depending on how far into the CTC did it actually decay, the track might or might not get reconstructed as a good track. Figure 22 shows that about 17% of the reconstructed tracks decayed with in the inner 80% of the CTC. We could therefore make a conservative estimate on the systematics due to the reconstruction as 17%. The contribution from the trigger simulation is 4%. There is an 8% systematic error on the K to π ratio. The systematic error due to the monte-carlo statistics is 17%. Thus the total systematic error is 24%.

4.5 Summary of the Total Background

The total background to the search can be summed up in Tables 7, 8 and 9:

Table 7: Background for Run 1a and Run 1b at $c\tau > 60\mu$m.

Background type	Run 1a	Run 1b	Run 1a + Run 1b
$B\bar{B}$	0.23±0.16	1.07±0.62	1.30±0.64
Punch-through	0.43±0.17	1.77±0.69	2.20±0.71
Decay in Flight from Prompts	0.14±0.10	0.64±0.49	0.78±0.50
Decay in Flight from B's	0.79±0.23	3.87±1.12	4.66±1.14
Total Background	1.59±0.34	7.53±1.53	8.94±1.57
Data events	3	14	17

Table 8: Background for Run 1a and Run 1b at $c\tau > 85\mu$m.

Background type	Run 1a	Run 1b	Run 1a + Run 1b
$B\bar{B}$	0.23±0.16	1.07±0.62	1.30±0.64
Punch-through	0.38±0.17	1.56±0.62	1.94±0.64
Decay in Flight from Prompts	0.13±0.10	0.61±0.46	0.74±0.47
Decay in Flight from B's	0.79±0.23	3.74±1.08	4.53±1.10
Total Background	1.53±0.34	6.98±1.46	8.51±1.50
Data events	3	11	14

5 Efficiencies

To determine the efficiencies, B_c's were generated using BGENERATOR and were simulated through the detector using QFL. The trigger was simulated using

Table 9: Background for Run 1a and Run 1b at $c\tau > 100\mu$m.

Background type	Run 1a	Run 1b	Run 1a + Run 1b
$B\bar{B}$	0.23±0.16	0.71±0.51	0.94±0.53
Punch-through	0.34±0.14	1.50±0.56	1.84±0.58
Decay in Flight from Prompts	0.10±0.08	0.58±0.37	0.68±0.38
Decay in Flight from B's	0.79±0.23	3.53±1.02	4.32±.1.05
Total background	1.46±0.32	6.32±1.32	7.78±1.36
Data events	2	11	13

Table 10: Relative Efficiency calculations

B_c Lifetime (ps)	$c\tau^*$ cut (μm)	$1/\varepsilon_{rel} = \frac{\varepsilon_{B_u}}{\varepsilon_{B_c}}$ (Errors are stat + Sys.)
0.25	60	3.11±.36
0.50	60	1.96±.19
0.75	85	2.30±.23
1.00	85	1.90±.23
1.20	100	1.82±.18
1.55	100	1.59±.14

DIMUTG. The efficiency for the B_c was defined as follows:

$$\varepsilon_{B_c} = \frac{Number\ of\ B_c\ picked\ up\ by\ the\ analysis\ code}{Number\ of\ events\ passing\ the\ dimuon\ trigger}$$

In this analysis we used the relative efficiencies instead of absolute efficiencies. The relative efficiency was calculated with respect to the B_u, where the efficiency of the B_u is defined in the same manner as that for the B_c. The relative efficiency can be written as follows:

$$\varepsilon_{rel} = \frac{\varepsilon_{B_c}}{\varepsilon_{B_u}}$$

For the purpose of this calculation the B_c were generated at various assumed life times of .25, .50, .75, 1.0, 1.2 and 1.55 ps. The B_u was generated at 1.55 ps. The results of the the relative efficiency calculations are shown in Table 10.

Comparing the efficiencies and the relative efficiencies between the $B_c \to J/\psi + \mu + X$ and the $B_c \to J/\psi + e + X$ analysis would be a good check of the consistency of the two calculations. Table 11 show the comparison of the efficiencies and the relative efficiencies for the two cases. For the purpose of comparison the P_t cut on the third track was raised to 3 GeV/c in the electron analysis. When no fiducial cuts, and no lepton I.D cuts are applied, the various efficiencies and the relative efficiencies are the same (within statistical errors) for the two cases. After applying the fiducial cuts, but no lepton ID cut the efficiencies change according to the change in the

fiducial, however the relative efficiencies remain the same within statistical errors, which is expected. Finally when the lepton ID cuts are applied the two analysis have the same efficiency for the B_c. This is due to the fact that the increase in the efficiency in the $J/\psi e$ case due to the increased fiducial is compensated by the electron identification efficiencies.

Table 11: Fiducial cut and lepton ID efficiency for B_c^+ lifetime = B_u^+ lifetime.All the cuts except for fiducial cut and lepton ID were applied.The P_t cut on the the third track was increased to 3.0 GeV/c in the electron analysis to be consistent with the muon analysis.

Cuts on 3rd track	electron mode			muon mode		
	$\varepsilon(B_c^+)$	$\varepsilon(B_u^+)$	Rel. Eff.	$\varepsilon(B_c^+)$	$\varepsilon(B_u^+)$	Rel Eff.
no fid. cut,no ℓ ID	$4.5 \pm 0.2\%$	$7.6 \pm 0.2\%$	1.7 ± 0.1	$4.3 \pm 0.2\%$	$7.5 \pm 0.1\%$	1.6 ± 0.1
with fid. cut,no ℓ ID	$3.1 \pm 0.2\%$	$5.3 \pm 0.2\%$	1.7 ± 0.1	$1.7 \pm 0.2\%$	$3.2 \pm 0.1\%$	$1.5 \pm .10$
ℓ ID, fid cut on K	$1.9 \pm 0.1\%$	$5.3 \pm 0.2\%$	2.8 ± 0.2	$2.0 \pm 0.1\%$	$3.2 \pm 0.1\%$	1.6 ± 0.2

The systematic error for this calculation is listed in Table 12. The individual sources of the systematic errors in Table 12 are described as follow:

- There is a 2.5% error due the finite statistics of the monte-carlo used.
- The calculation of the error due to the b quark production spectrum was calculated by the $J/\psi e$ analysis [21]. Since this result would be the same for both the analyses, we used the number obtained by them.
- The uncertainty due to the peterson's fragmentation parameter is only for the B_u's. We used the number obtained by the $J/\psi\pi$ analysis [17].
- The difference in Run 1a and Run 1b accounts for a 3.4% uncertainty. We therefore assign a 3.4% error to the detector simulation.
- The error due to the trigger simulation was estimated to be 4%.

6 Limit of the Relative B_c Production

The limit on the $B_c^+ \to \psi + \mu^+ + X$ production is calculated relative to the $B_u^+ \to \psi + K^+$. The method employed in this calculation is similar to the one used by Carol Anway-Wiese in the analysis of the rare B decays [18].

The limit results from Table 13 is plotted in Fig. 23. the dotted line in the plot shows the theoretical predictions for limit using the QCD sum rules and the dashed line is predicted curve using the potential model [19].

Table 12: Systematic Errors for the Efficiency Calculations

Source of Error	Contribution
Monte-carlo Statistics	2.5%
Production Spectrum	5.0%
Fragmentation Parameter	2.3%
Detector Simulation	3.4%
Trigger Simulation	4.0%
Total	**8.0%**

Table 13: This table shows the 95% C.L. limit on the production of $\psi\mu + X$ from B_c to ψK from B_u.

Results at various assumed B_c lifetimes
$N(\psi K) = 80 \pm 9$
B_u lifetime = 1.55 ps.

B_c lifetime(ps)	$c\tau^*$ cut μm	$1/\varepsilon_{rel}$ (stat+sys)	$N_{\psi\mu X}$	N_{bkg} (stat+sys)	$\frac{\sigma.BR(B_c^+)}{\sigma.BR(B_u^+)}$ 95% C.L.
0.25	60	3.11 ± .36	17	8.94 ± 1.57	0.71
0.50	60	1.96 ± .19	17	8.94 ± 1.57	0.44
0.75	85	2.30 ± .23	14	8.51 ± 1.50	0.42
1.00	85	1.90 ± .23	14	8.51 ± 1.50	0.35
1.20	100	1.82 ± .18	13	7.68 ± 1.36	0.32
1.55	100	1.59 ± .14	13	7.68 ± 1.36	0.28

7 Conclusion

We have searched for the $B_c \to \psi + \mu + X$ in the Run 1a and 1b data. The result is not significant if we look at the $B_c \to \psi + \mu + X$ results independent of the $B_c \to \psi + e + X$ results. Therefore the 95% C.L. upper limit on the $\sigma.BR(B_c^+)/\sigma.BR(B_u^+)$ was obtained. The results are plotted in Fig. 23 and also shown in Table 13

References

[1] W. Kwong and J. Rosner, Phys. Rev. D44, p212, 1991.

[2] E. J. Eichten and C. Quigg, Preprint, FERMILAB-PUB-94/032-T.

[3] R. Roncaglia, A. Dzierba, D. B. Lichtenberg and E. Predazzi, Preprint, IUHEP 278.

[4] E. Braaten and K. Cheung, Phys. Rev. D48, r5049, 1993.

[5] A. K. Likhoded and S. R. Slabosptsky, Preprint IHEP 93-23.

[6] CDFNOTE 1626

[7] CDFNOTE 2655

[8] CDFNOTE 1996

[9] CDFNOTE 2360

[10] D. Smith, Ph.D. Thesis, University of Illinios, Urbanna, 1989.

[11] A.S. Carroll, I-H. Chiang, T.F. Kycia, K.K. Li, M.D. Marx, and D.C. Rahm. *Physics Letters*, **80B**(3):319, Jan. 1979. See also S.P. Denisov, et al. *Nuclear Physics*, **B61**:62, 1973.

[12] Particle Data Group, *Phys. Rev. D*, **50**:3, 1335, August 1, 1995.

[13] CDFNOTE 3070

[14] C$DOC:SIMGUIDE.MEM and C$DOC:CDFSIM_TUTORIAL.PS

[15] CDFNOTE 2655

[16] CDFNOTE 2724

[17] CDFNOTE 3541

[18] Carol Anyway-Wiese, Ph.D. Thesis UCLA, May 1995.

[19] C. Quigg, FERMILAB-Conf-93/265-T

[20] Result obtained from Vaia.

[21] CDFNOTE 3287 version 2.2

[22] T. Alexopoulos et. al., Phys. Rev. Lett **64** 991(1990)

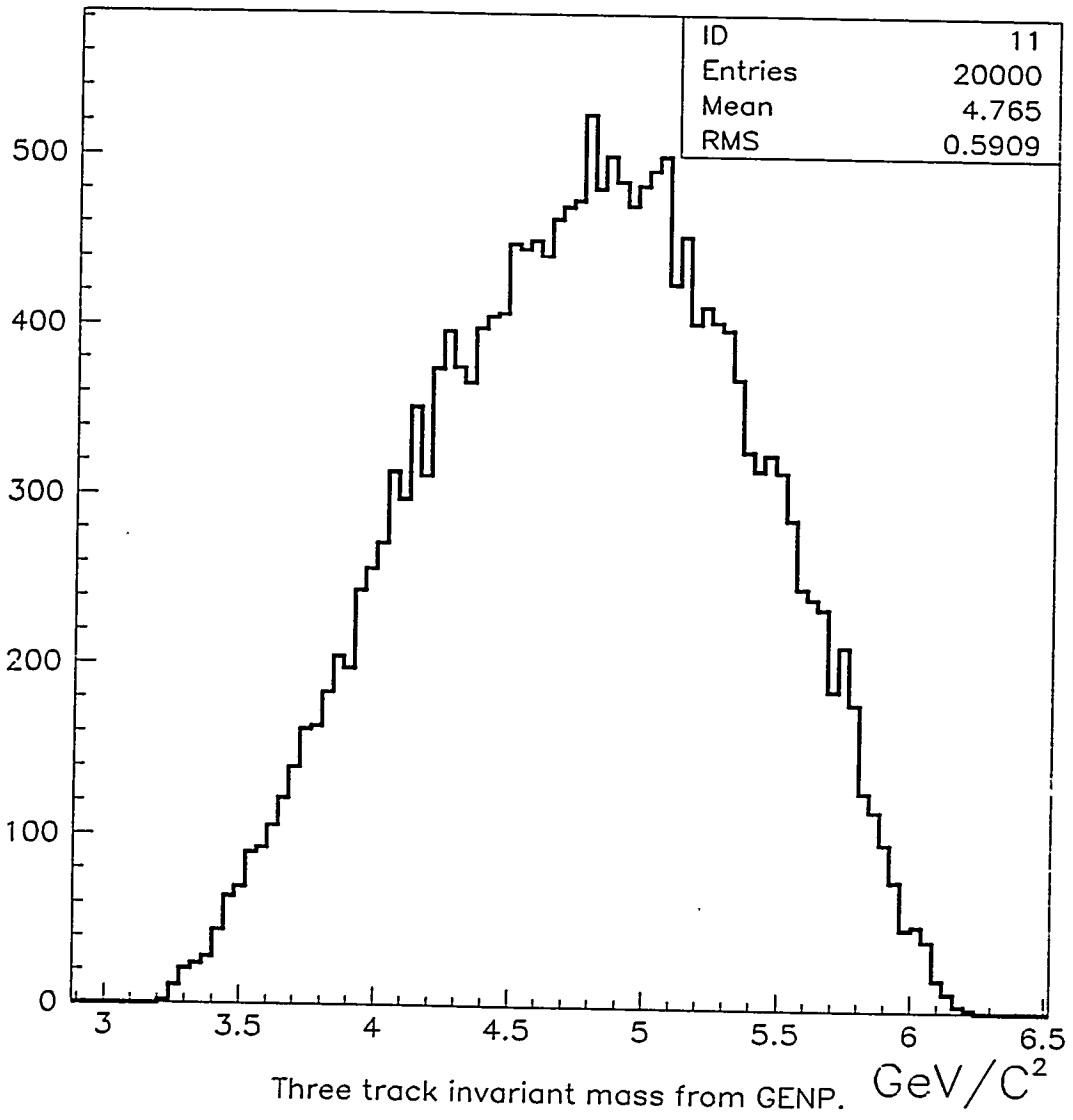

Figure 1: The three muon invariant mass from the GENP information.

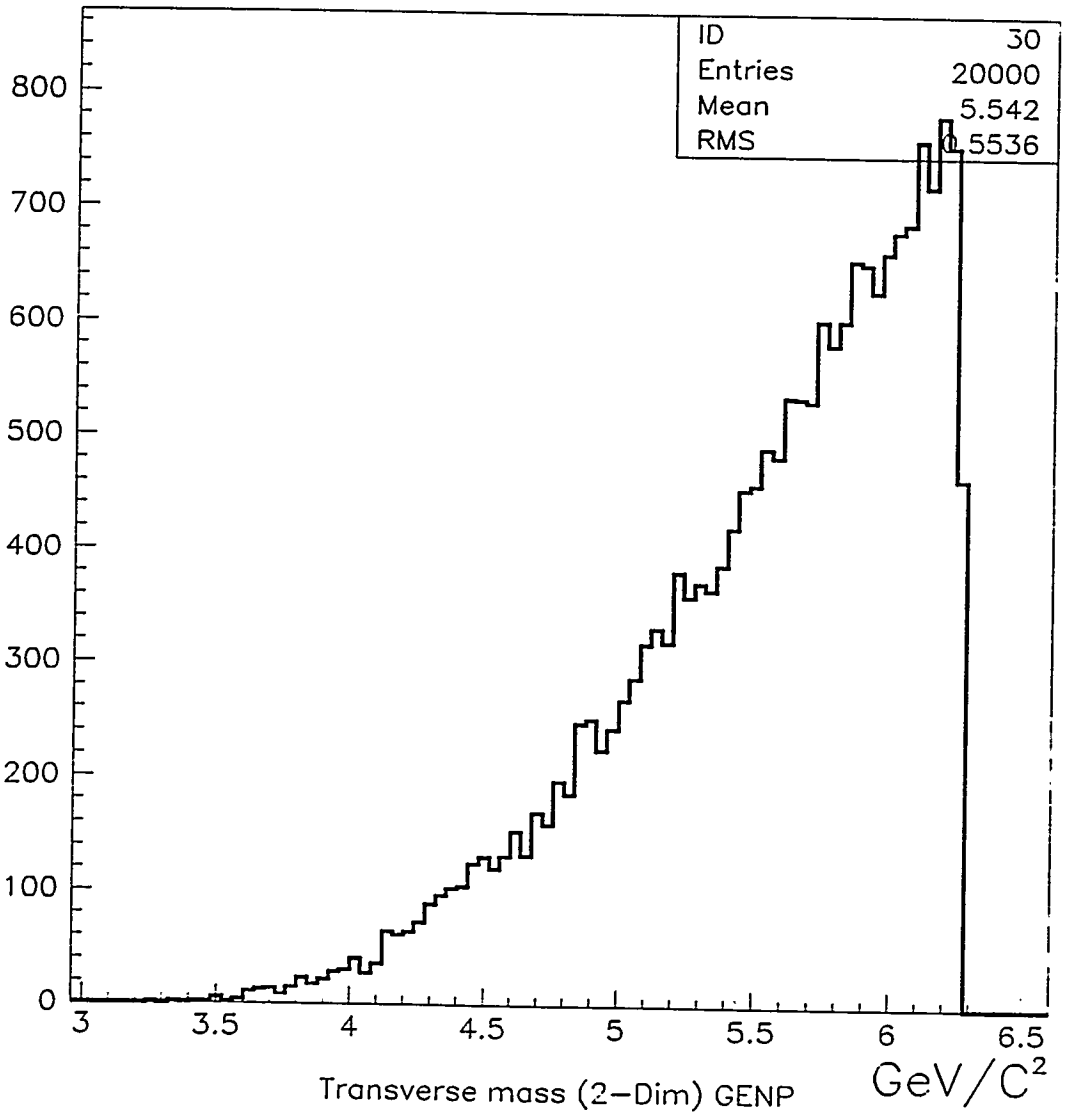

Figure 2: Two dimensional transverse mass of the B_c from the GENP information.

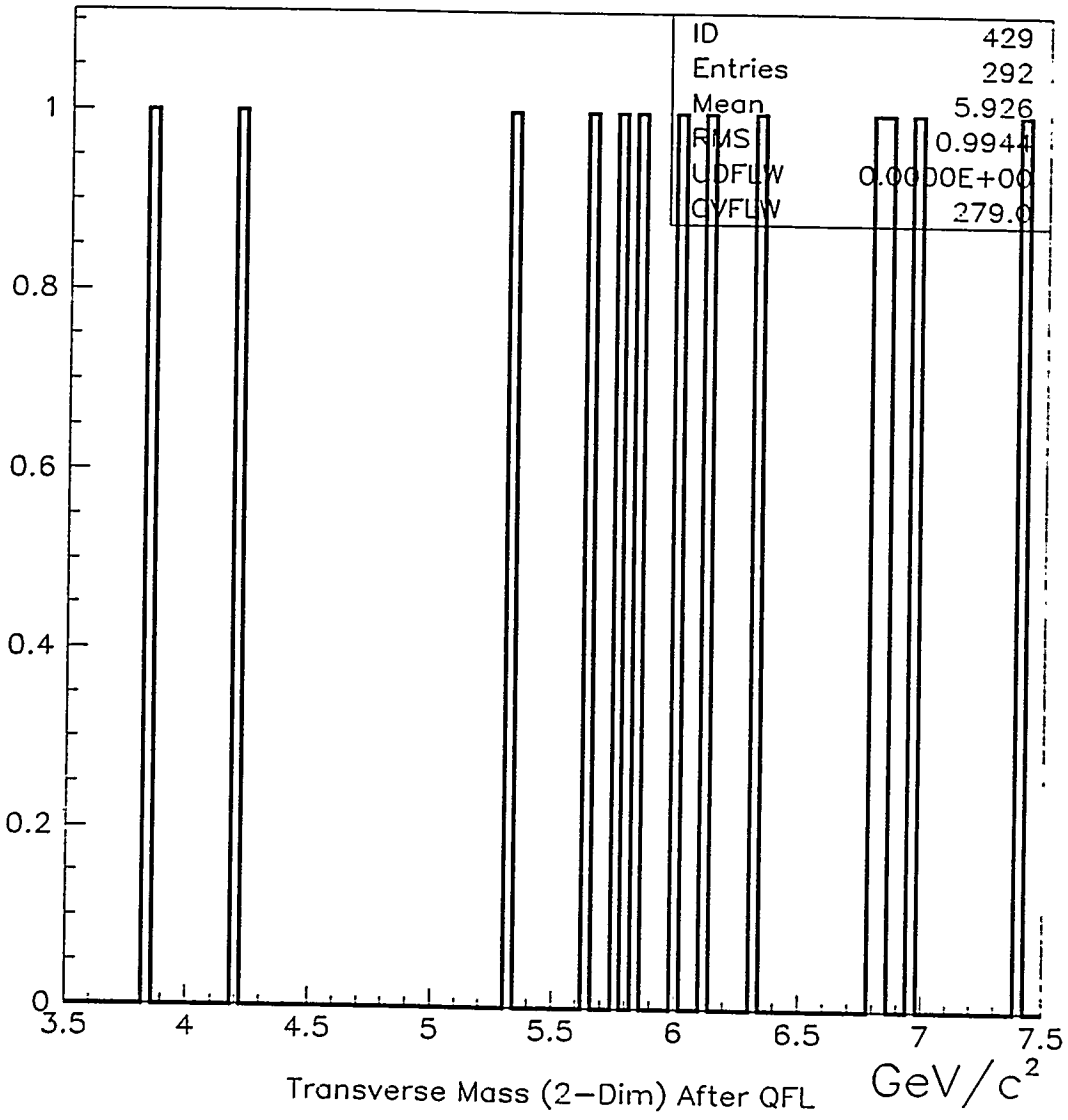

Figure 3: Two dimensional transverse mass of the B_c after the QFL simulation. It should be noted that in this plot most of the reconstructed events overflow the signal region.

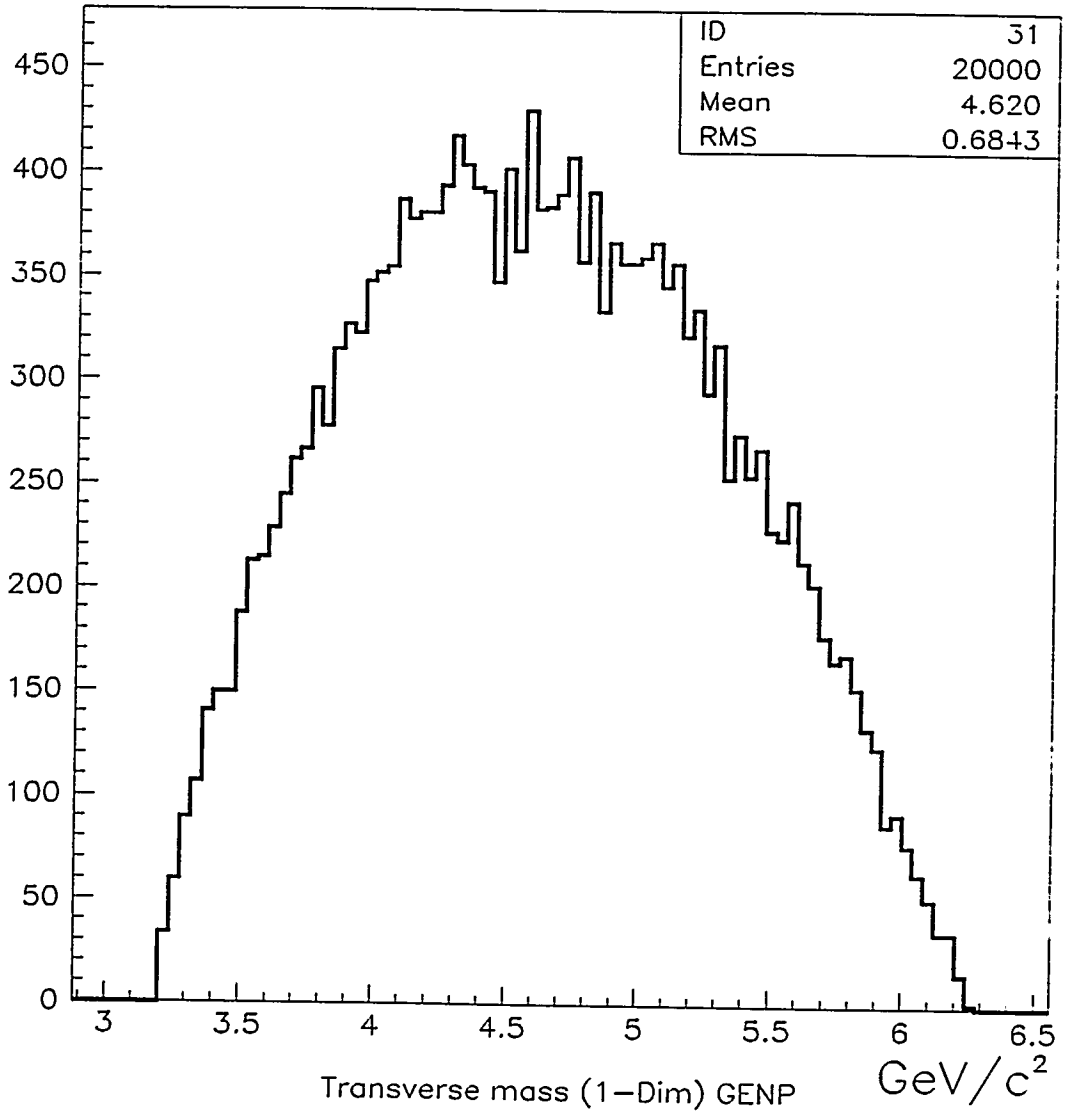

Figure 4: One dimensional transverse mass of the B_c from the GENP information.

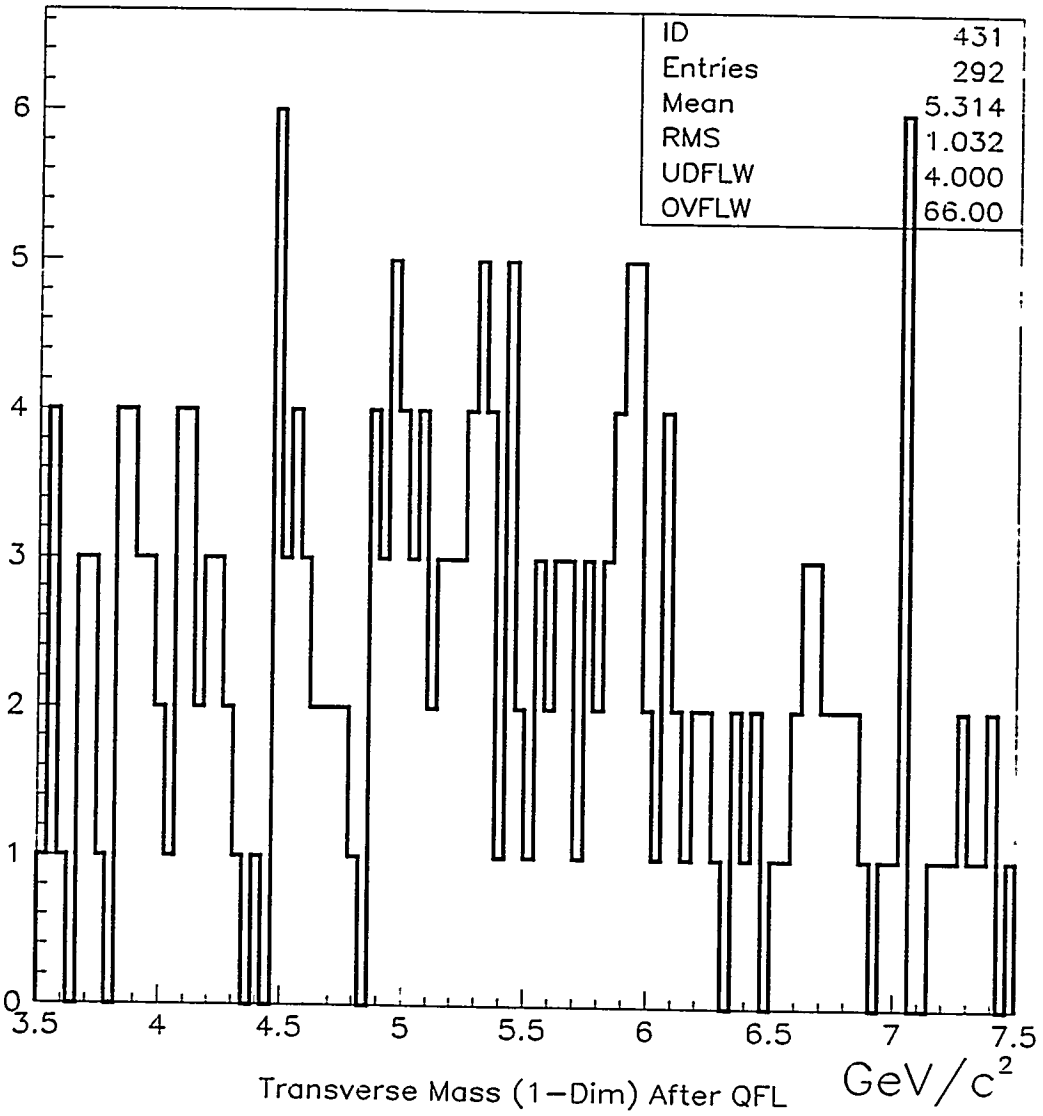

Figure 5: One dimensional transverse mass of the B_c after the QFL simulation.

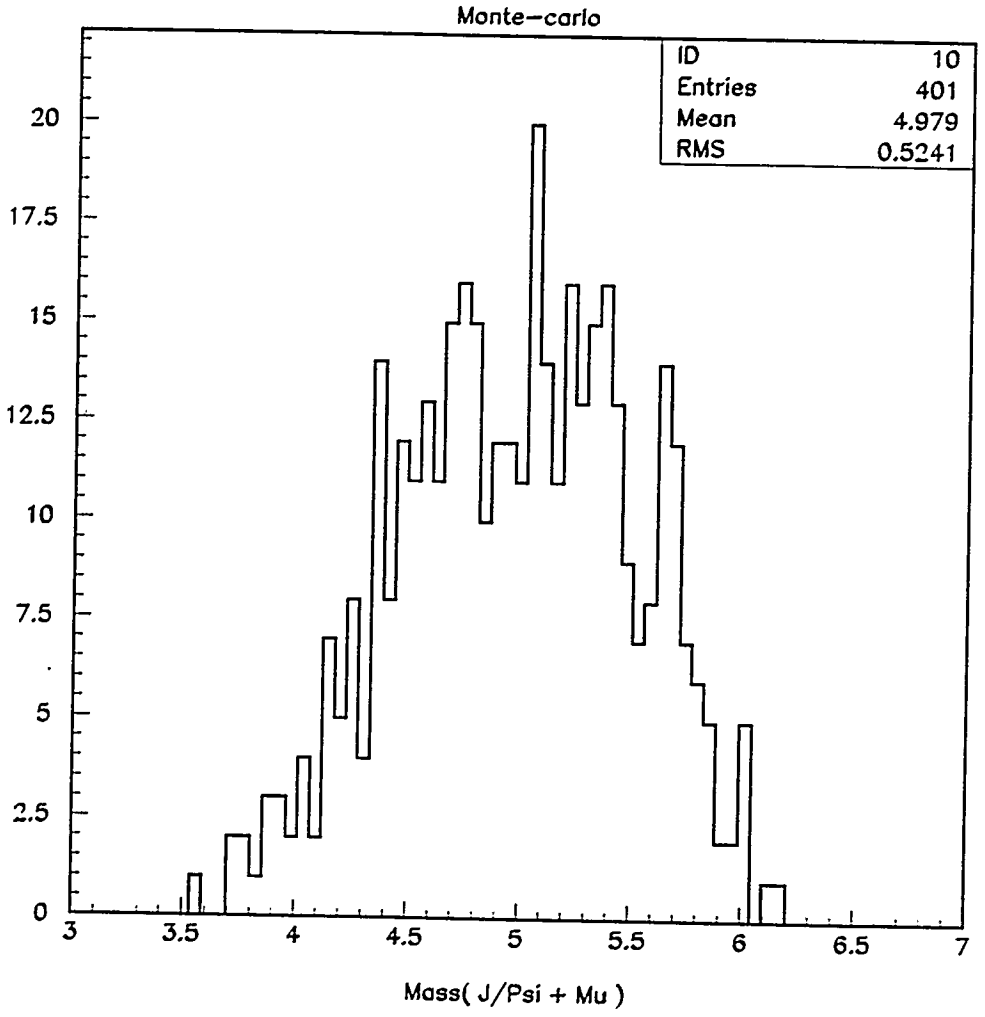

Figure 6: The three muon invariant mass after the QFL simulation.

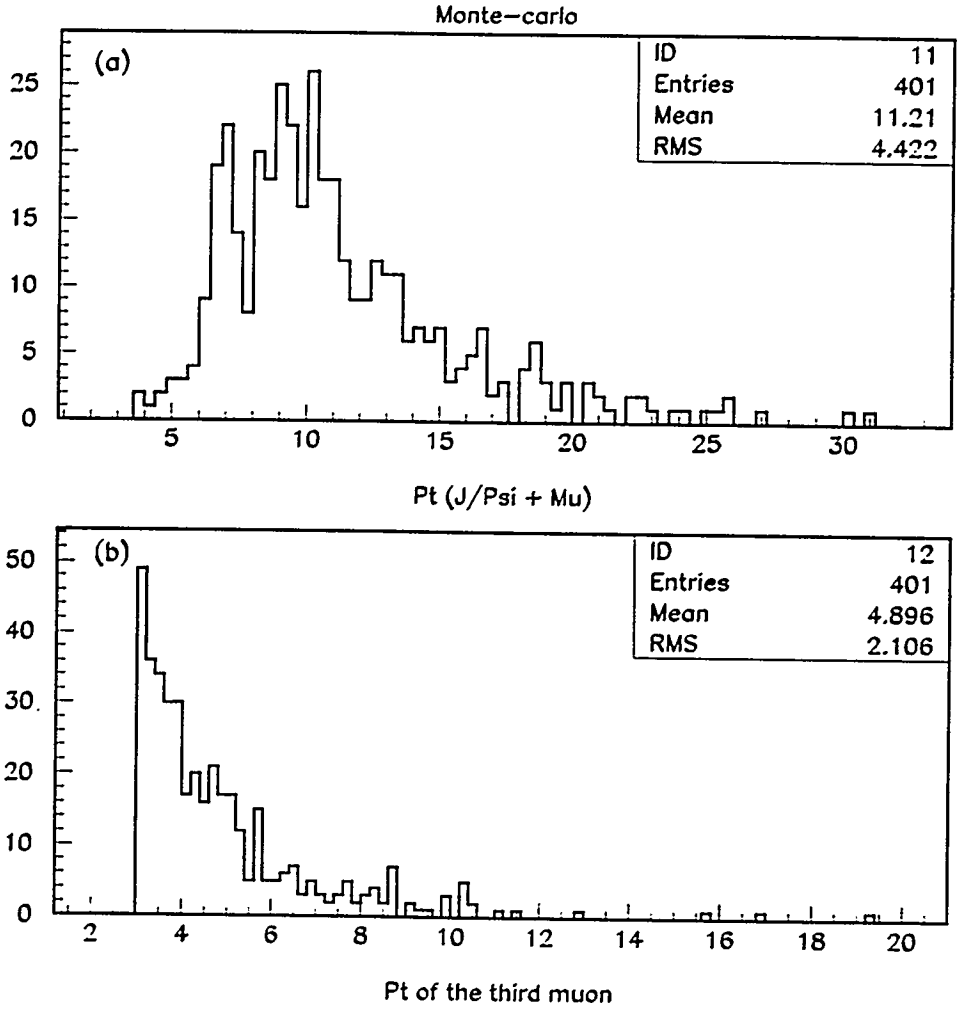

Figure 7: (a) P_t spectrum of $J/\psi + \mu$ from monte-carlo. (b) P_t spectrum of the third muon from monte-carlo.

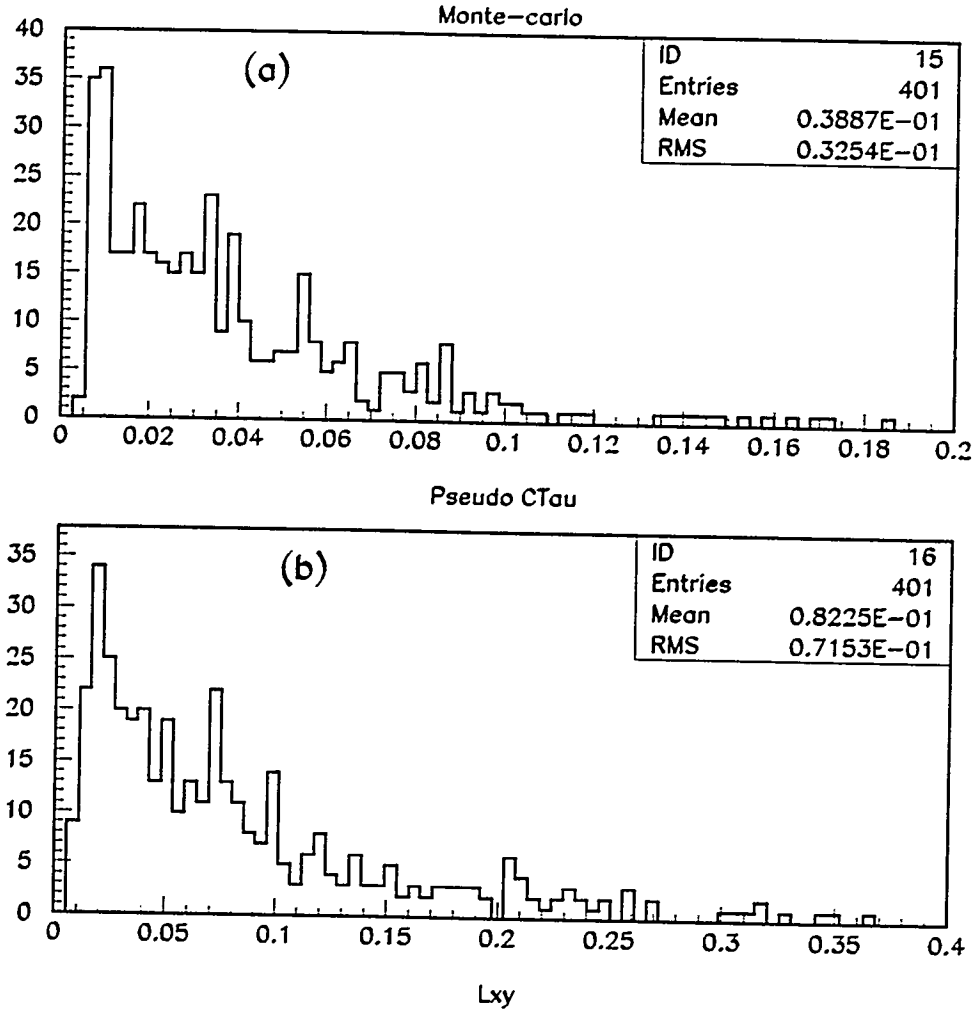

Figure 8: (a) The pseudo $c\tau$ distribution for $J/\psi + \mu$ from monte-carlo. (b) The L_{xy} distribution for $J/\psi + \mu$ from monte-carlo.

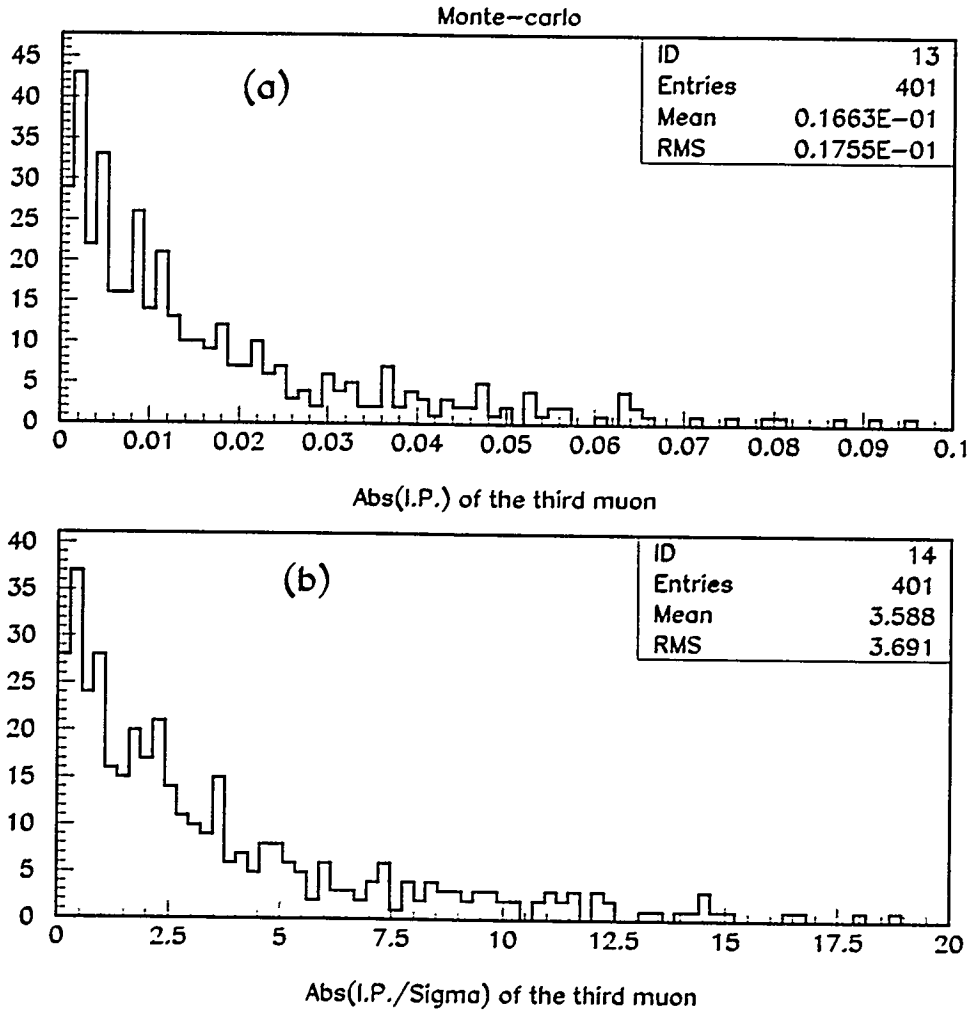

Figure 9: (a) The impact parameter distribution of the third muon from monte-carlo. (b) The impact parameter significance distribution of the third muon from monte-carlo.

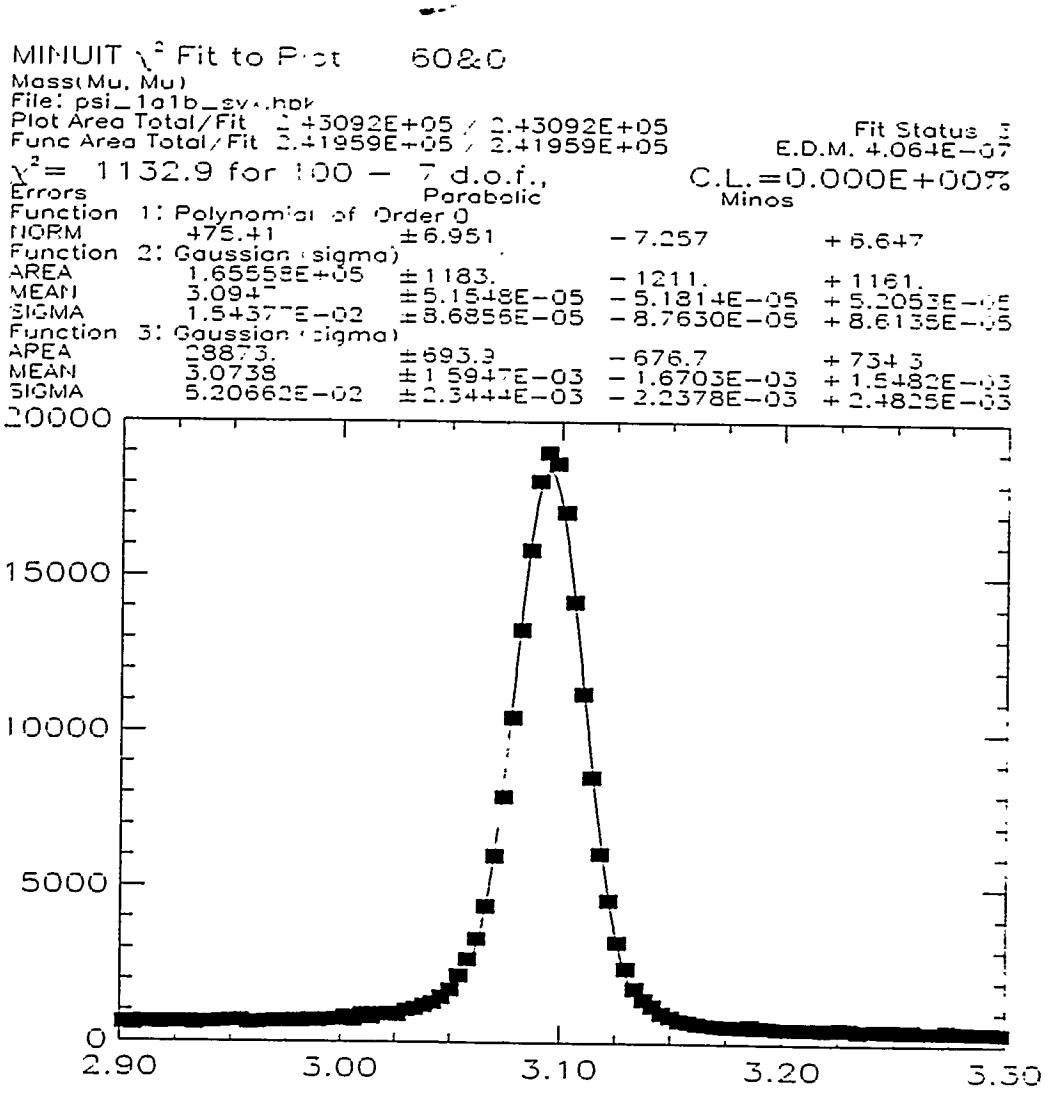

Figure 10: The J/ψ mass plot for Run 1a + Run 1b, the J/ψ's are required to pass all the cuts described for the J/ψ's in Table 1. There are 194431 $\pm$ 1371 events under the peak.

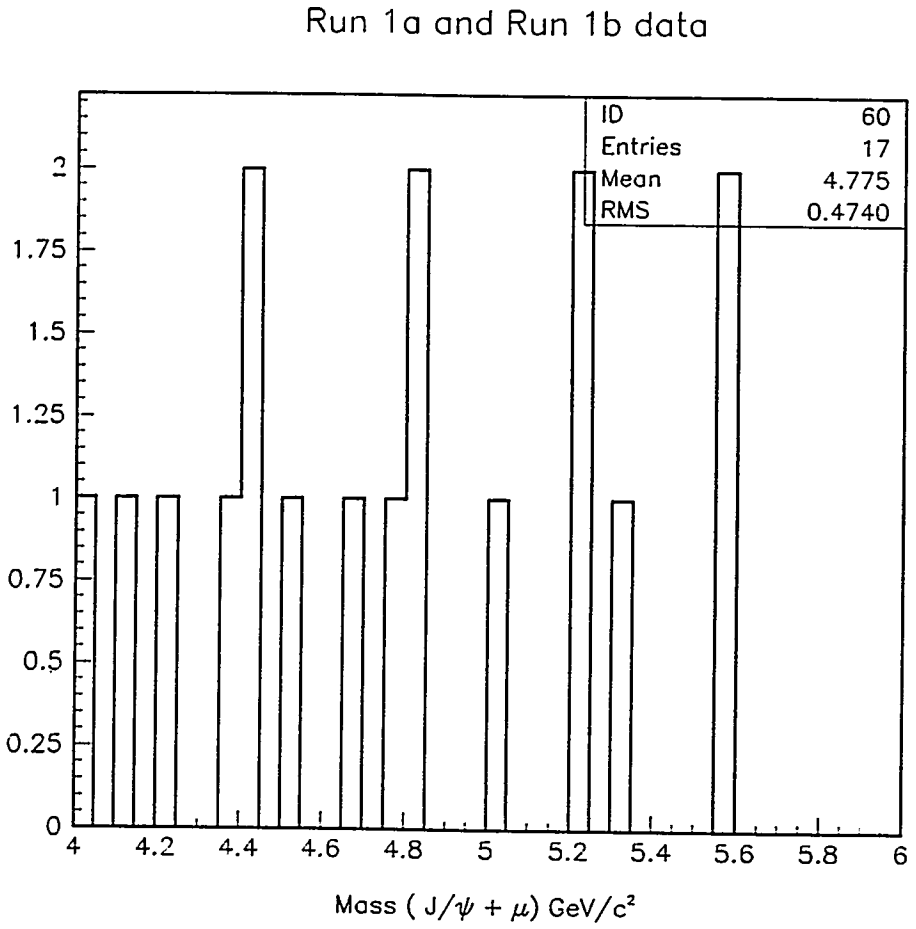

Figure 11: The three track invariant mass plot for Run 1a and 1b. There are 17 events in the signal region. The $c\tau^*$ cut is 60μm.

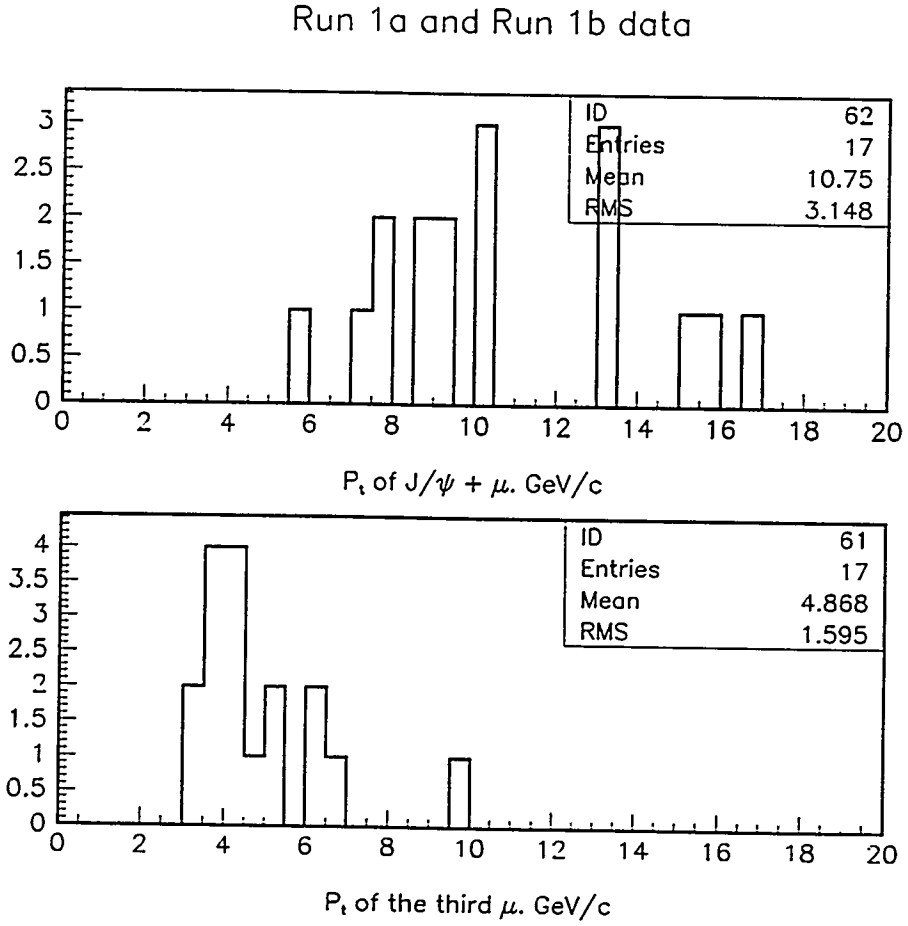

Figure 12: (a) The P_t spectrum of $J/\psi + \mu$ for Run 1a and 1b data. (b) The P_t spectrum of the third muon for Run 1a and 1b data.

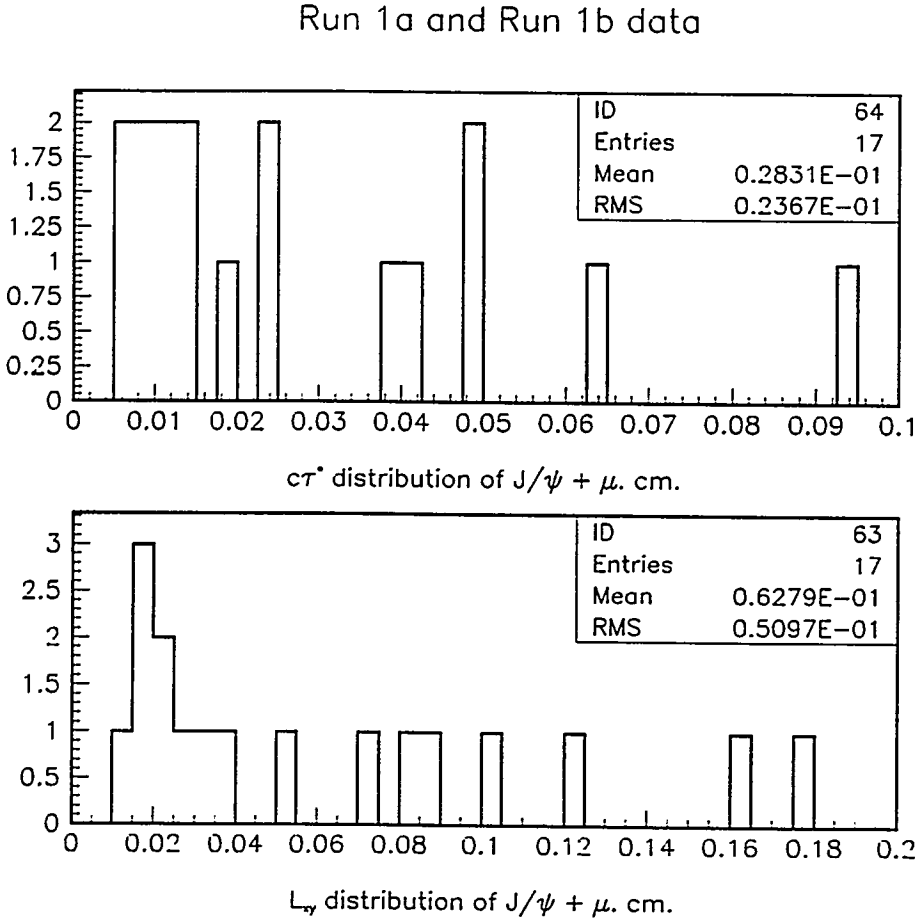

Figure 13: (a) The pseudo $c\tau$ distribution for $J/\psi + \mu$ vertex for Run 1a and 1b data. (b) The L_{xy} distribution for $J/\psi + \mu$ vertex for Run 1a and 1b data

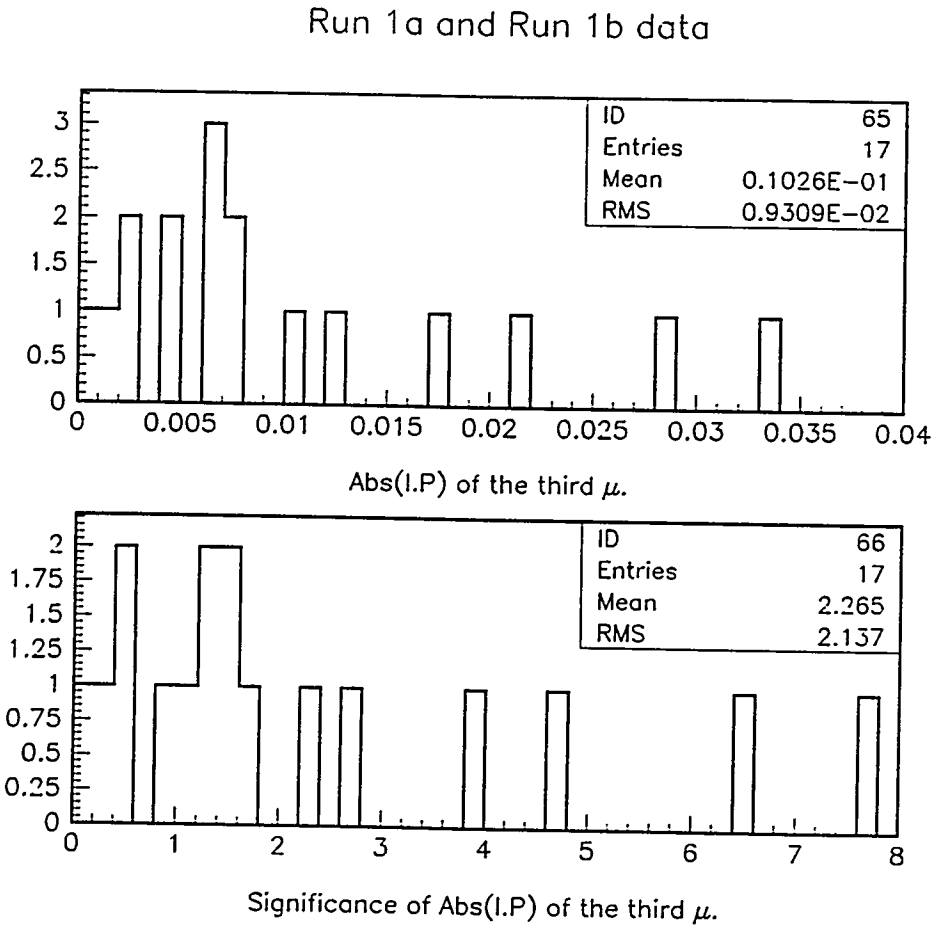

Figure 14: (a) The impact parameter distribution of the third muon for Run 1a and 1b data. (b) The impact parameter significance distribution of the third muon for Run 1a and 1b data

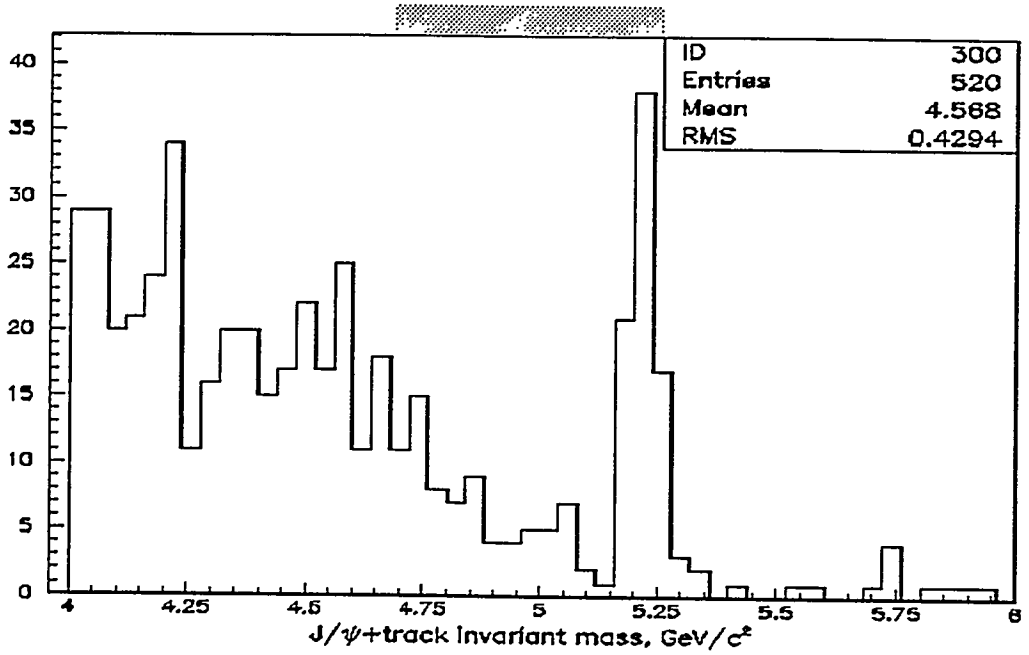

Figure 15: The total number of $J/\psi + \mu$ candidates prior to requiring hits in the muon chambers. These events are the potential contributors to the punch-through and the decay in flight background. One can clearly identify the peak caused by $B \rightarrow J/\psi + K$ events where the kaon has been called a muon. The overall shape of this curve would also be the shape of the three track invariant mass distribution for the background.

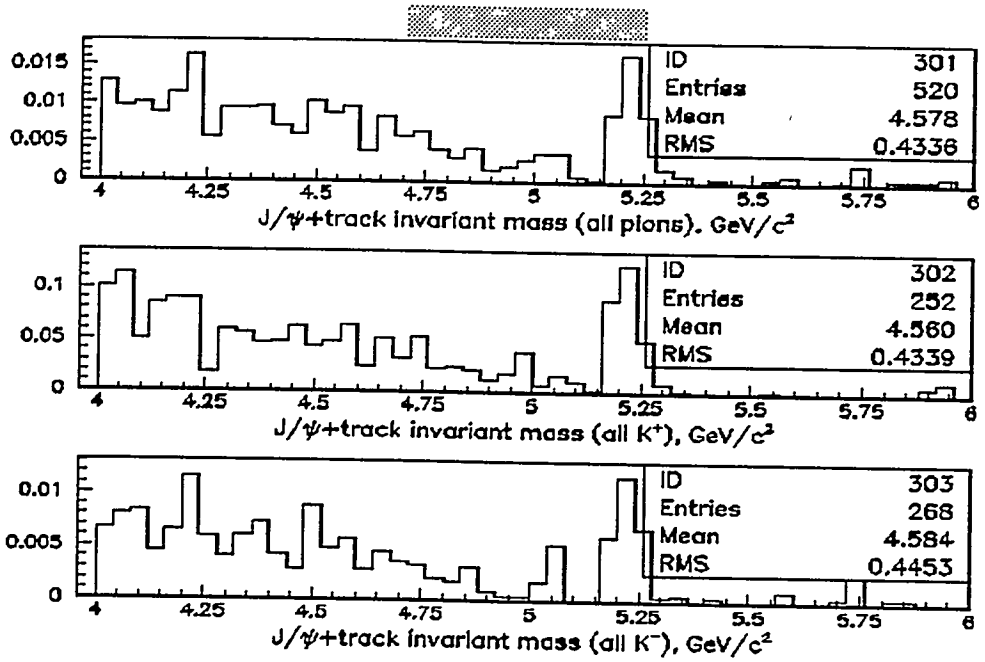

Figure 16: The total number of $J/\psi + \mu$ candidates expected from fake muon background due to punchthrough. The top histogram assumed all the tracks are pions whereas the middle and lower plot assume all of the third tracks are kaons (positive and negative respectively). The events are weighted by the punch through probability for each track. Adding up the weighted entries in each plot we get 0.23 events if we assume that all the tracks were pions and 1.77 events if we assume that all the tracks were kaons.

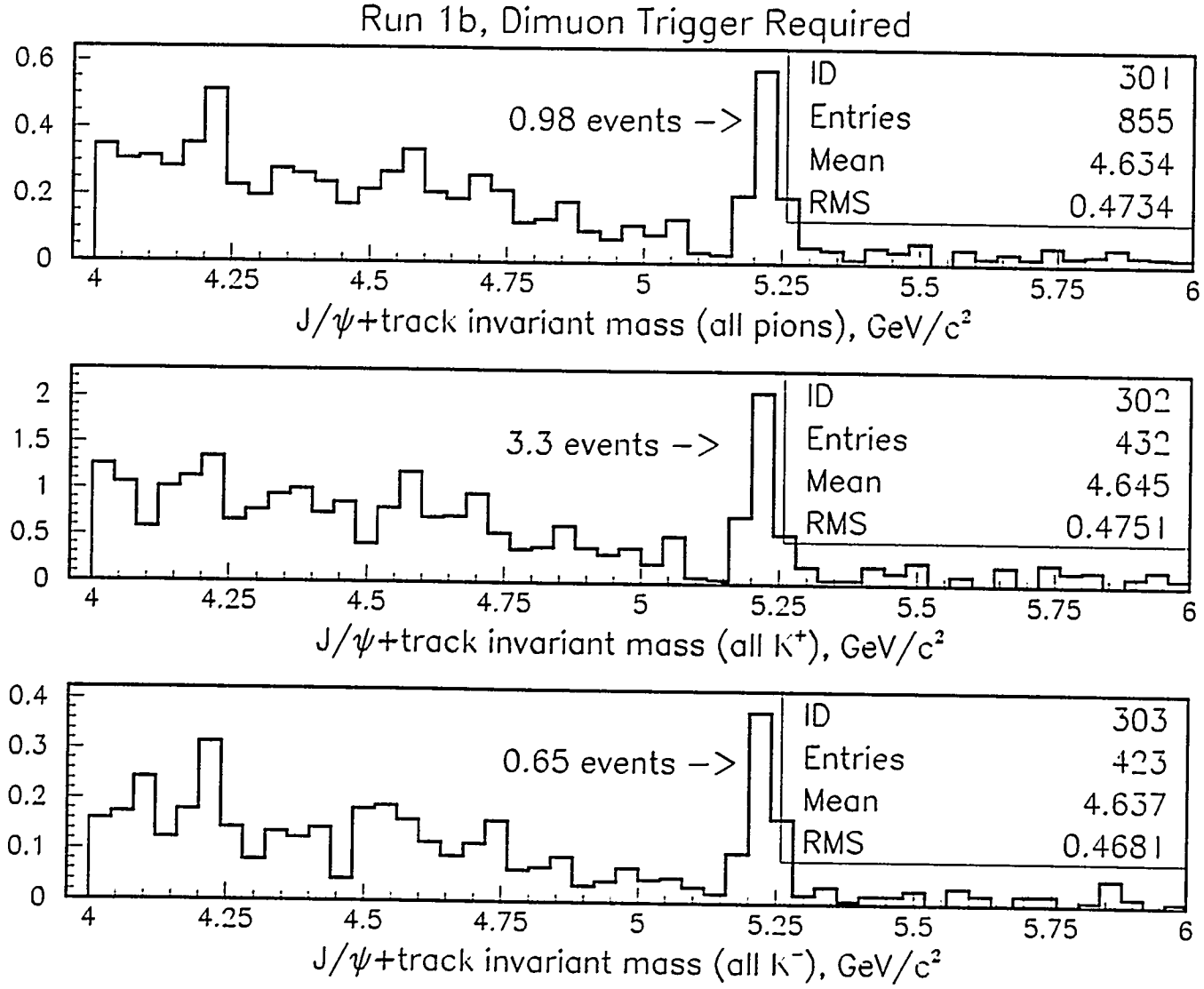

Figure 17: These figures show the punch through calculation but only the material through the CMU was required of the third track. The upper plot shows the assumption of only pions. The next two plots show the calculation for positive and negative kaons respectively. Indicated on the plots are the estimated punch through in the $J/\psi + K$ peak region.

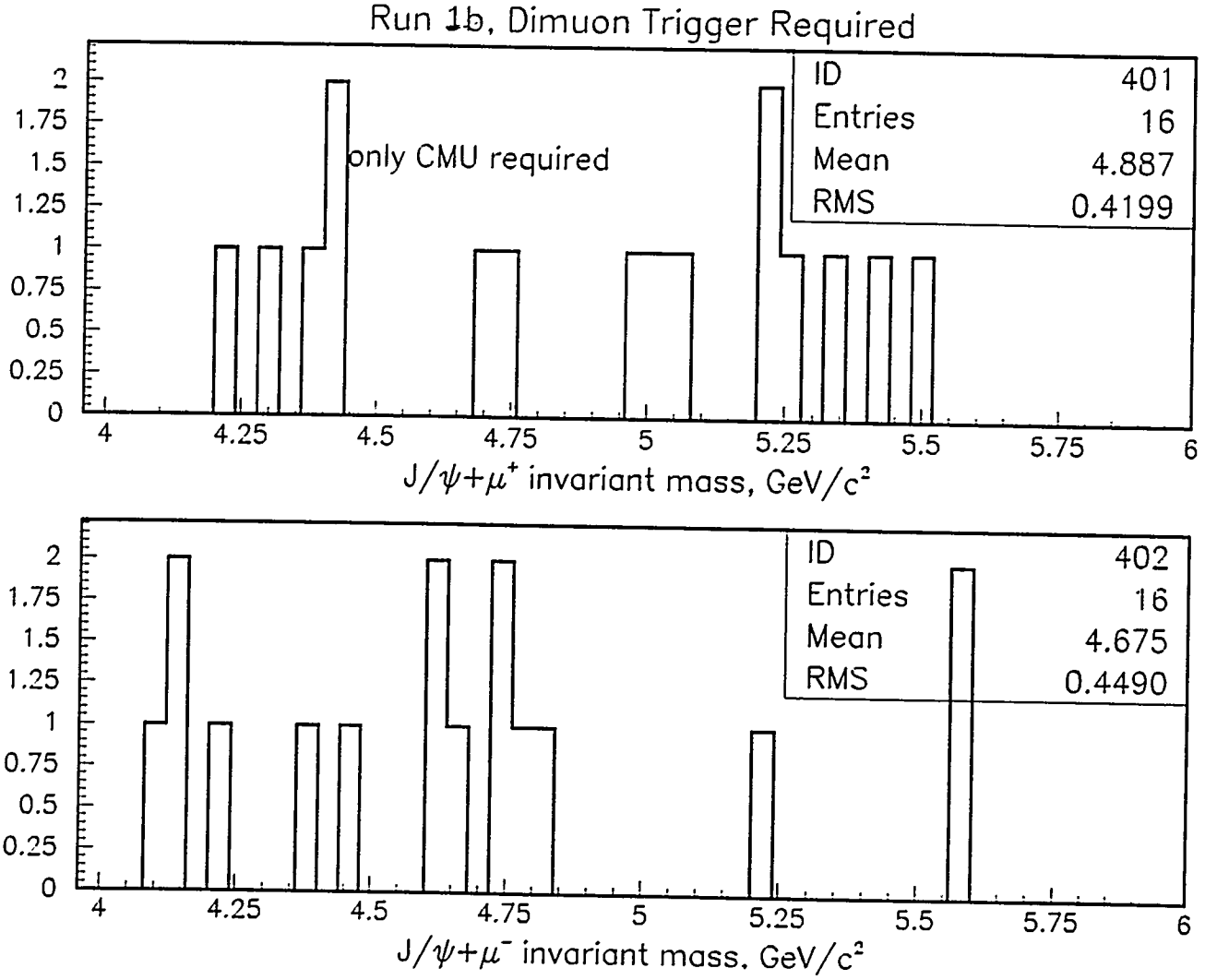

Figure 18: This figure shows the data where all of the analysis cuts have been applied but only a CMU muon was required of the third track. The upper plot shown the cases with positive third CMU's and the lower plot is the negative CMU tracks. The $J/\psi + K$ mass region is from 5.15 to 5.30 GeV/c^2.

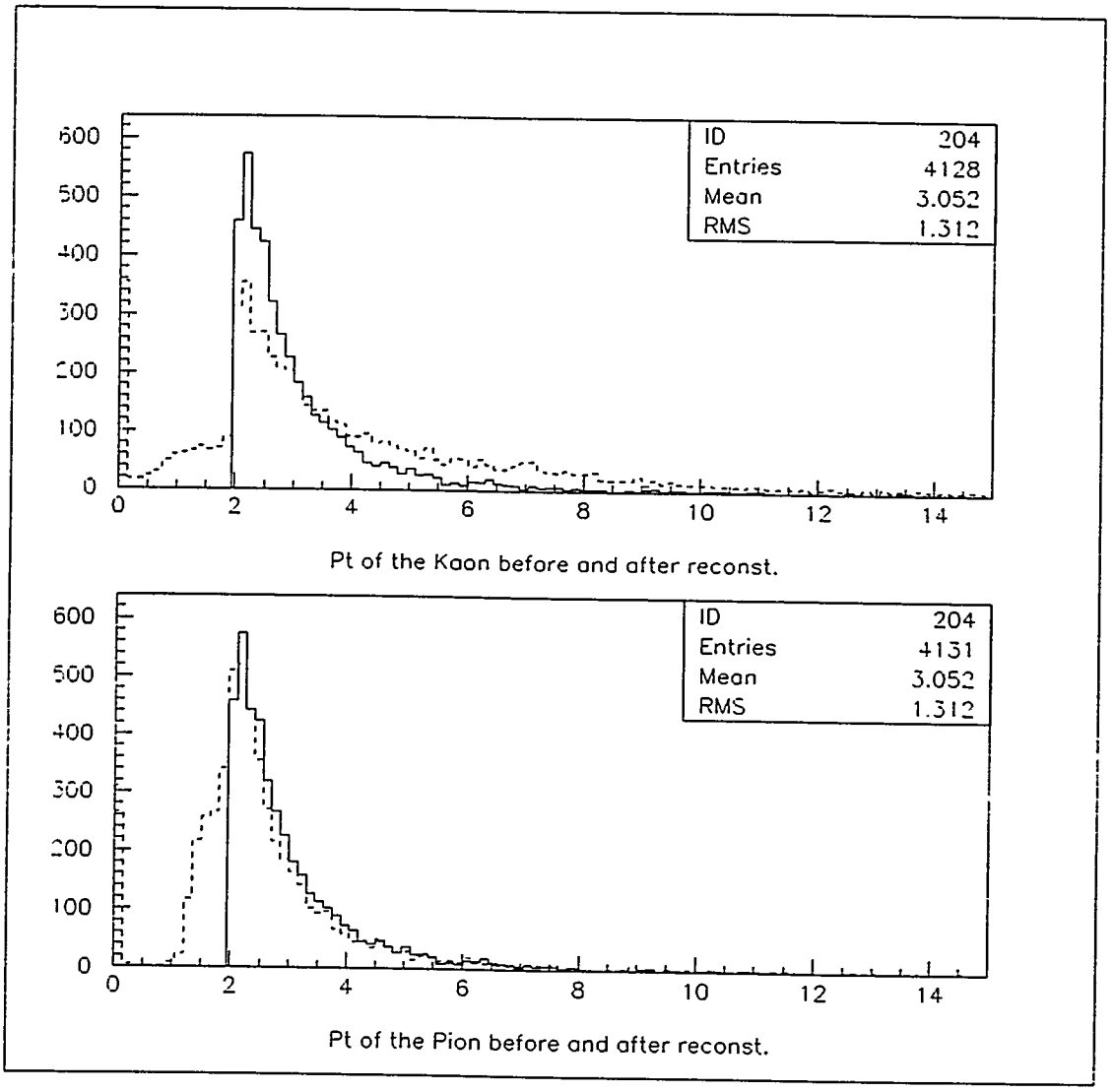

Figure 19: The top plot shows the momentum spectrum of the kaon before decay (solid line) and after decay and reconstruction (dashed line), the bottom plot shows the same for the pions.

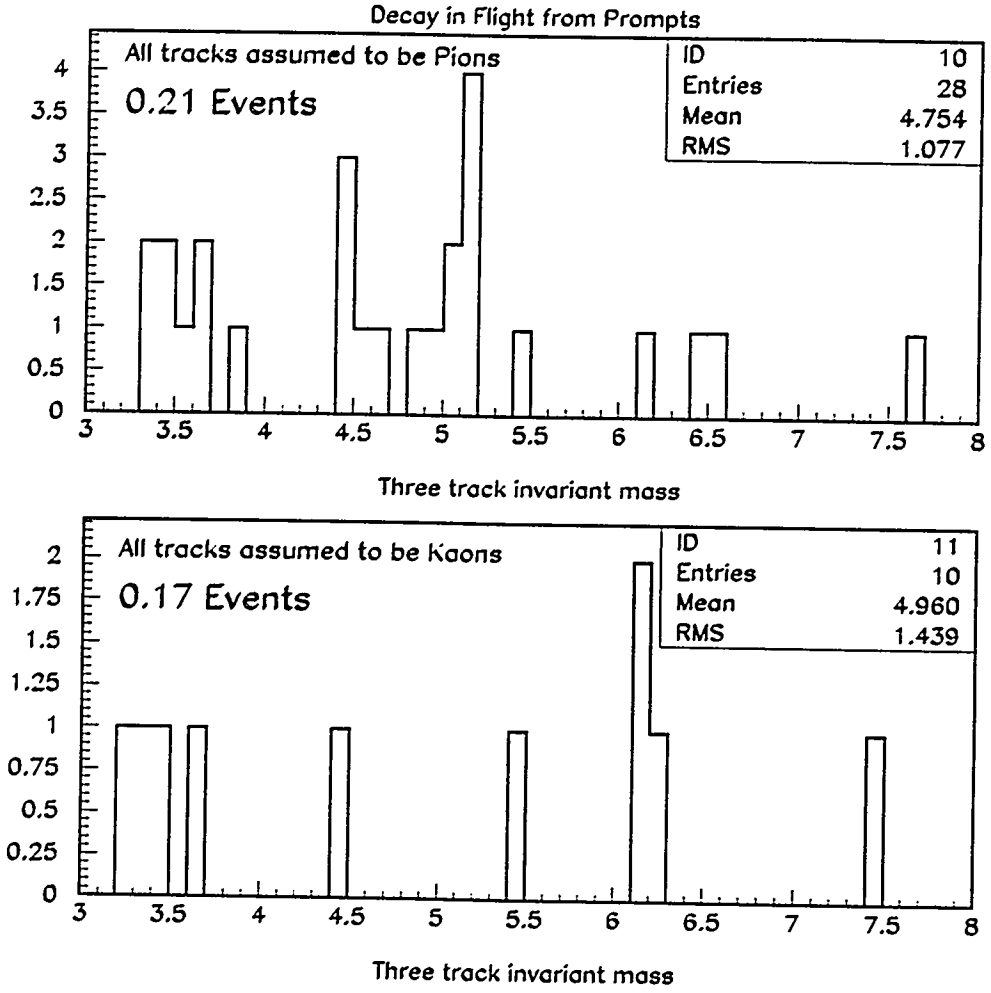

Figure 20: The top plot shows the three track invariant mass distribution when the third track is assumed to be a pion. The bottom plot shows the same thing when the third track is assumed to be a kaon. These plots are for about one third of the Run 1b. After weighting the probability of the third track to decay and summing it up for all the entries in the signal region there will be .21 events when the tracks were assumed to be pions and 0.17 events when the tracks were assumed to be kaons.

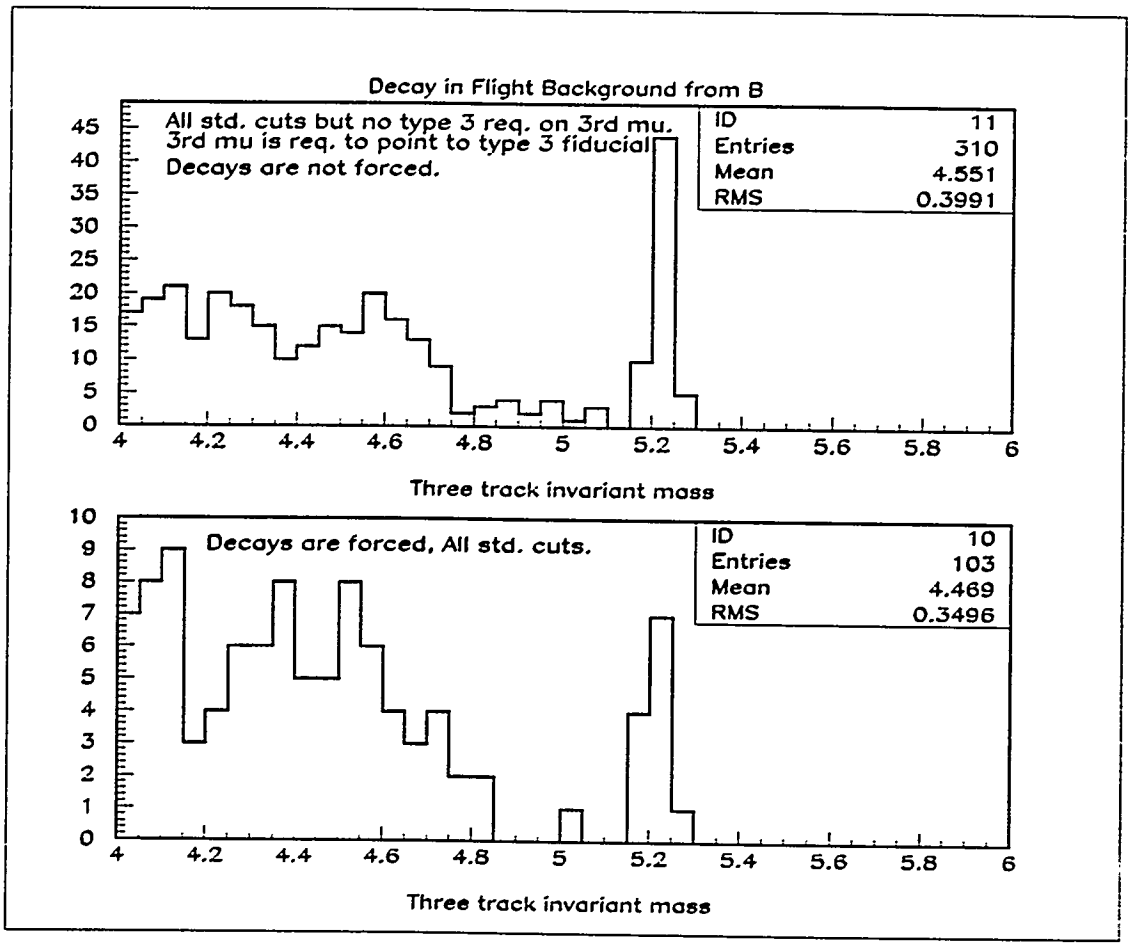

Figure 21: The top plot shows the three track invariant mass distribution for the $B \rightarrow J/\psi + X$ monte-carlo data set, where the kaons and the pions were not forced to decay. All the analysis cuts were applied, however the third track was not required to have a CMU/CMP stub but was just required to point to the CMU/CMP fiducial region. The lower plot is made from the same data set when the pions and the kaons were forced to decay before the end of the CMU volume. If the entries in this plot are weighted by the probability of their third track to decay, then they add up to 1.17 events if the tracks are assumed to be pions and 8.15 events if the tracks are assumed to be kaons.

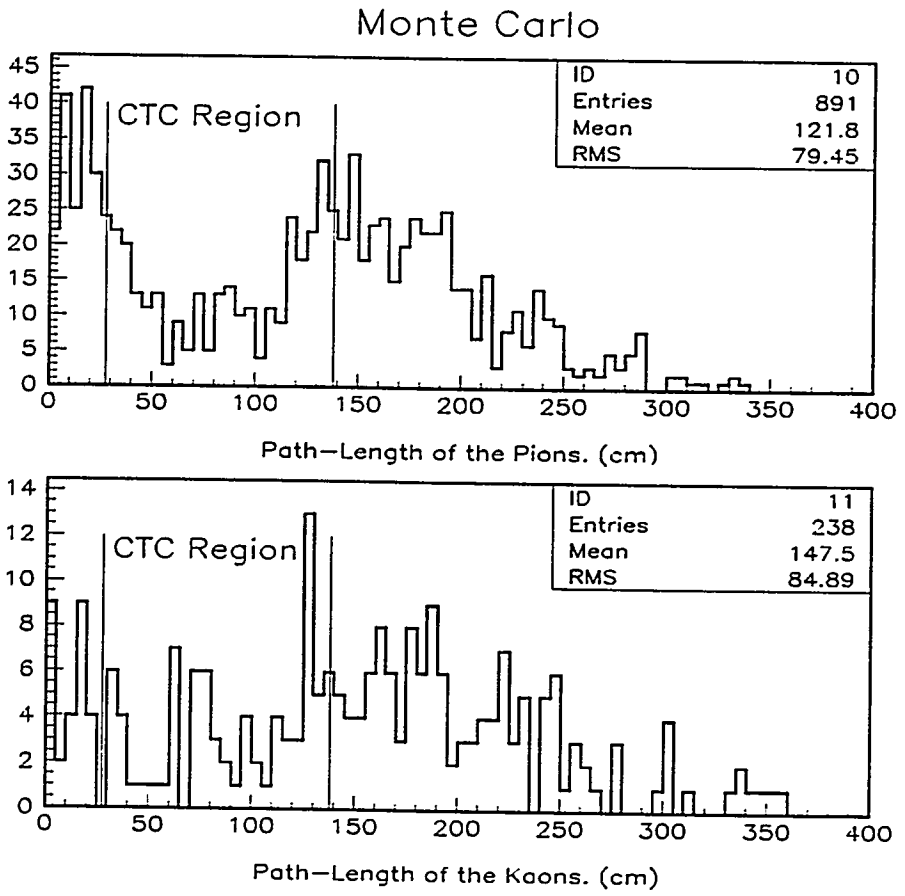

Figure 22: The top plot shows the path-length of the pions for a MC sample of $B \rightarrow J/\psi + \pi$ events, where the pions were forced to decay within any region up to the CMU. The sample has all the analysis cuts applied on it. The bottom plot shows the path-length distribution of the kaons for a MC sample of $B \rightarrow J/\psi + K$, the kaons were forced to decay within any region up to the CMU. This sample too has all the analysis cuts applied to it.

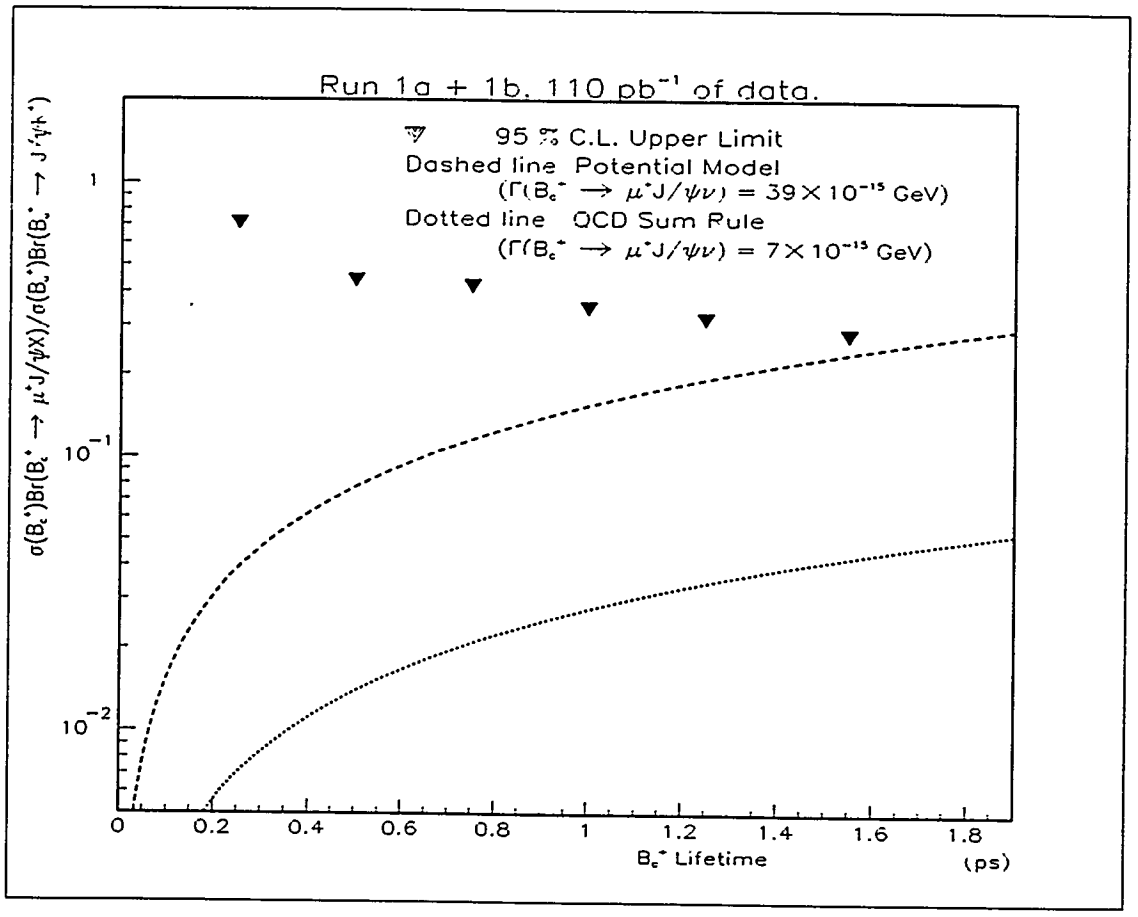

Figure 23: 95% C.L. upper limit on the $\sigma \times Br(B_c \to \psi\mu X)/\sigma \times Br(B \to \psi K)$ for the Run 1a and 1b data.